Impact Detection Techniques Using Fibre-Optic Sensors for Aerospace & Defence

Ryan Nichols John

Submitted for the degree of Engineering Doctorate

Heriot-Watt University

School of Engineering and Physical Sciences

March 2015

ABSTRACT

Impact detection techniques are developed for application in the aerospace and defence industries. Optical fibre sensors hold great promise for structural health monitoring systems and methods of interrogating fibre Bragg gratings (FBG) are investigated given the need for dynamic strain capture and multiplexed sensors.

An arrayed waveguide grating based interrogator is developed. The relationships between key performance indicators, such as strain range and linearity of response, and parameters such as the FBG length and spectral width are determined. It was found that the inclusion of a semiconductor optical amplifier could increase the signal-to-noise ratio by ~300% as the system moves to its least sensitive. An alternative interrogator is investigated utilising two wave mixing in erbium-doped fibre in order to create an adaptive system insensitive to quasistatic strain and temperature drifts. Dynamic strain sensing was demonstrated at 200 Hz which remained functional while undergoing a temperature shift of 8.5 °C.

In addition, software techniques are investigated for locating impact events on a curved composite structure using both time-of-flight triangulation and neural networks. A feature characteristic of composite damage creation is identified in dynamic signals captured during impact. An algorithm is developed which successfully distinguishes between signals characteristic of a non-damaging impact with those from a damaging impact with a classification accuracy of 93 – 96%.

Finally, a demonstrator system is produced to exhibit some of the techniques developed in this thesis.

DEDICATION

This work could not have been carried out without the help and support of my supervisors, Ian Read at BAE Systems Advanced Technology Centre and William MacPherson at Heriot-Watt University. Thank you for the many ideas, the helpful feedback and tireless reading of my work. I'd also like to thank Eoin Murphy and Peter Foote for their advice and help at different points over the last few years.

I'd also like to thank my parents for their love and support during my life which has certainly helped me get to where I am today. Finally, I'd like to thank Lynsey for being there for me all the time and for the constant encouragement which kept me going until the end.

Name:	
School/PGI:	

Version: *(i.e. First, Resubmission, Final)*		Degree Sought (Award and Subject area)	

Declaration

In accordance with the appropriate regulations I hereby submit my thesis and I declare that:

1) the thesis embodies the results of my own work and has been composed by myself
2) where appropriate, I have made acknowledgement of the work of others and have made reference to work carried out in collaboration with other persons
3) the thesis is the correct version of the thesis for submission and is the same version as any electronic versions submitted*.
4) my thesis for the award referred to, deposited in the Heriot-Watt University Library, should be made available for loan or photocopying and be available via the Institutional Repository, subject to such conditions as the Librarian may require
5) I understand that as a student of the University I am required to abide by the Regulations of the University and to conform to its discipline.

* *Please note that it is the responsibility of the candidate to ensure that the correct version of the thesis is submitted.*

Signature of Candidate:		Date:	

Submission

Submitted By *(name in capitals)*:	
Signature of Individual Submitting:	
Date Submitted:	

For Completion in the Student Service Centre (SSC)

Received in the SSC by *(name in capitals)*:			
Method of Submission (Handed in to SSC; posted through internal/external mail):			
E-thesis Submitted (mandatory for final theses)			
Signature:		Date:	

iv

TABLE OF CONTENTS

LIST OF PUBLICATIONS

R. N. John, I. Read, and W. N. MacPherson, "Design considerations for a fibre Bragg grating interrogation system utilizing an arrayed waveguide grating for dynamic strain measurement", Meas. Sci. Technol. **24** 075203 (9pp) (2013).

R. N. John, I. Read, and W. N. MacPherson, "Adaptive dynamic FBG interrogation utilising erbium-doped fibre" Proc. SPIE 8692, Sensors and Smart Structures Technologies for Civil, Mechanical, and Aerospace Systems 2013, 869220 (April 19, 2013).

R. John, I. Read and W. N. MacPherson, "Discrimination Between Damaging and Non-damaging Impact Events on Composite Structure using SHM Sensor Signal Analysis," SAE Aerotech Congress & Exhibition, Toulouse, France, (Oct. 18-21, 2011).

R. John , I. Read and W. N. MacPherson, "Impact Damage Assessment by Sensor Signal Analysis" Proceedings of IWSHM Conf., Stanford University, USA, (Sept. 2011).

Patent Application "Data Processing", Application No GB1114418.5, Date Lodged, 22.08.2011, Applicant(s) BAE SYSTEMS plc.

OTHER DISSEMINATION ACTIVITIES

R. John, I. Read, and W. N. MacPherson, "*Impact Damage Assessment by Sensor Signal Analysis*", IOP Instrument Science and Technology Group, Half-day meeting on Structural Health Monitoring , Institute of Physics, London (10th May 2012).

LIST OF ABBREVIATIONS

A/D	Analogue to digital
AE	Acoustic emission
ANN	Artificial neural network
ASE	Amplified spontaneous emission
AWG	Arrayed waveguide grating
BVID	Barely visible impact damage
CBM	Condition based maintenance
CCD	Charge coupled device
CFBG	Chirped fibre Bragg grating
DAQ	Data acquisition device
ECM	Electronic counter measures
EDF	Erbium doped fibre
EDFA	Erbium doped fibre amplifier
EFPI	Extrinsic Fabry-Perot interferometric
ELED	Edge emitting light emitting diode
FBG	Fibre Bragg grating
FFT	Fast Fourier transform
FP	Fabry-Perot
FSR	Free spectral range
FTS	Fourier transform spectroscopy
FWHM	Full width at half maximum
ICGI	Identical chirped grating interrogation
IFPI	Intrinsic Fabry-Perot interferometric
InGaAs	Indium gallium arsenide
InP:Fe	Iron doped indium phosphide
LED	Light emitting diode
LPG	Long period grating
NDE	Non-destructive evaluation
NDI	Non-destructive inspection
NDT	Non-destructive testing
OBR	Optical backscatter reflectometry
OC	Optical coupler
OLM	Operational load monitoring
OPD	Optical path difference
OSA	Optical spectrum analyser
PD	Photodiode
PRC	Photorefractive crystal
PZT	Lead zirconate titanate
SCM	Spectrally coded multiplexing
SFS	Superfluorescent source
SHM	Structural health monitoring
SLD	Superluminescent diode
SMF-28	Corning proprietary single mode fibre.
SNR	Signal to noise ratio
SOA	Semiconductor optical amplifier
TDM	Time division multiplexing

TWM	Two wave mixing
UAV	Unmanned air/aerial vehicle
USB	Universal serial bus
WDM	Wavelength division multiplexing

Chapter 1 – Introduction

1.1. Structural Health Monitoring

1.1.1. Commercial justification

Structural health monitoring (SHM) is the process of damage prediction and detection in a structure (such as a bridge, aircraft or ship) and the monitoring of its evolution in time. Structural health is directly related to structural performance and as such is a major parameter with regard to safety of operation [1.1]. This is especially important in areas such as transportation where the potential cost of structural failure extends to human lives.

In the modern age, the quantity of aerospace, naval and other structures has reached a level where traditional inspection techniques are overly time-consuming and expensive. Aging structures are required to continue operating past their original projected lifetime which has left large fleets requiring increased inspection and maintenance. For instance, the number of US and European built civil aircraft older than 25 years rose from 1900 in 1997 to 2130 in 1999 [1.2]. The situation with military aircraft is even more serious; an increasing number of aircraft exceed the age of 40 years such as the F4, T-38 and MiG-21 aircraft. The Boeing KC-135, for example, was introduced in 1957 as an in-flight refuelling tanker. It is expected to still be in service until 2035 with many aircraft exceeding 80 years old [1.3]. In 2000, over 75% of US Air Force aircraft were more than 25 years old. These facts are illustrative of the growing need for improved structural health monitoring to maintain aging fleets in a cost effective and reliable way.

Many air forces are moving towards upgrading existing aircraft rather than designing and manufacturing completely new ones. Freighter aircraft are being created by converting aging civil passenger aircraft while fighters are being upgraded with new weapon loads, engines as well as upgraded communications and electronics systems. The upgraded aircraft may be experiencing larger forces and performing different manoeuvres leading to an increased risk of damage as it ages.

The testing of structural health and making the appropriate repairs incurs direct costs due to labour and parts. In addition, there are indirect costs as the system is taken out of service due to the reduction in production volume or the cost of a replacement system. As such, minimising the frequency a system has to be out of action is desirable. A military aircraft may often need 6000 man-hours a year for maintenance of which

inspection may easily account for as much as 50%. The overall cost of this huge inspection effort can reach into the multi-billion US$ range for a single air force such as the US Air Force or the Royal Air Force. This effort increases dramatically with the age of the aircraft for instance the number of man-hours required for inspecting and repairing one EF-111A fighter has increased from 2200 in 1985 to 8000 in 1996 [1.4].

1.1.2. Composite materials and damage

Composite materials are being increasingly employed in advanced structures such as military aircraft due to their properties, including lightweight and layered structure allowing them to be designed to exhibit desired characteristics. For instance, they can be designed to be stiffer in one direction which is advantageous for some advanced designs. Composite materials are made out of a thermosetting matrix such as epoxy or polyimide interlaced with a reinforcing material such as carbon fibre manufactured in layers which can be oriented to produce desired properties.

There are significant differences in the damage development of metallic and composite structures; in metals, cracking is generally a gradual and predictable process which can be monitored by regular inspection and manual testing. However, in composite materials there is a much higher risk from discrete traumas such as accidental damage which is inherently unpredictable. Even relatively small impacts can be sufficient to cause delamination of the structure which could lead to structural failure. This suggests that an alternative structural health monitoring strategy may be required.

The most common types of damage in composite materials are matrix cracking, fibre breakage, fibre-matrix debonding and delamination. The matrix is the resin that holds the fibres together and forms the structure of the material. Delamination is the debonding of adjacent layers that make up the composite structure causing a significant loss of mechanical strength. Composites are especially prone to delamination due to their weak transverse tensile and interlaminar shear strengths when compared to their in-plane components. It can occur due to accidental impacts by hard objects during maintenance, repair or operation. For thin laminates, damage is usually subsurface and is not often visually apparent from the outside and is therefore termed 'barely visible impact damage' (BVID). This is particularly difficult to detect externally by simple visual inspection; therefore non-destructive testing methods must be employed to assess and ensure the structural integrity of composites [1.5]. Further theory of composite materials and damage mechanisms is presented in §2.1.

1.1.3. Smart structures

An integrated structural health monitoring system consisting of sensors for damage detection combined with advanced signal processing capabilities could be used to automate the inspection process. Structures and materials which are able to sense and potentially react to changes in their environment are known as 'smart'. Smart structures have great potential for structural health monitoring, by integrating sensors and signal processors into the structure a damage monitoring system can be created. If the monitoring system is dependable then the structure only needs to be inspected and repaired when required (condition based maintenance) reducing the amount of wasted inspection time which results in a 'no-fault-found' situation.

Introducing such a system allows the operational availability of the structure to be maximised and therefore a reduction of the operating costs due to improved availability. It also allows determination of the structures residual value as an accurate knowledge of the structures condition allows the remaining lifetime to be estimated. Also, an integrated system allows inspection of structural zones that are extremely difficult to access and require special measures in the design stage such as moving wiring to allow a section to be removable.

A possible drawback of this technique is the addition of mass due to the SHM system which is a concern for some structures such as aircraft in which case a system must be designed to have minimal detrimental effect on the aircraft. In addition, the system itself must require little maintenance otherwise the whole ideology of the system is compromised. Finally, the cost of the system must be acceptably low so that it leads to an overall reduction in costs. If this was not the case then the system would only be purposeful if it demonstrated a genuine increase in safety.

1.1.4. Prognosis and diagnosis

Structural health monitoring can be split broadly into two categories; prognostic and diagnostic. Prognosis is concerned with predicting the future health of the structure through gathering data about its usage while diagnostic is concerned with detecting the current health of the structure to identify damage or merely ascertain that the structure is still fit for purpose. An important prognostic technique is to monitor the loads experienced by a structure during its life cycle such as performing manoeuvres for an aircraft or while fully laden for a bridge. By comparing this data with usage data of components and systems tested in a laboratory environment the lifespan of the

components and system as a whole can be determined. With this information action can be taken pre-emptively, if required, to prevent failure or plan for replacement.

In addition, by monitoring the loads experienced during use, events which overload a component past its design limit can be detected allowing action to be taken to ensure the structure has not been damaged. An example of this situation is a hard landing for an aircraft, if it is detected that the load on the landing gear was above the design threshold then remedial actions can be performed before the aircraft is allowed to depart.

Other diagnostic activities include acoustic emission sensing to detect stress waves characteristic of damage such as cracks and delamination [1.6, 1.7]. This form of sensing can also be used for impact detection to measure the location and severity of an impact and then determine whether damage is likely to have occurred. Corrosion can also be measured as part of a structural health monitoring programme to determine if it is currently causing a structural problem especially in aircraft operating in coastal environments where corrosion can be accelerated.

1.2.   Optical Fibre Technology

Optical fibres are increasingly being considered for use on aircraft due to their numerous advantages over the incumbent electrical systems. Most importantly they are very light weight which can lead to significant savings in fuel over the lifetime of an aircraft, enough to comfortably offset the higher initial costs. Not only is one fibre lighter but, because of wavelength division multiplexing, many channels can be routed through an aircraft using one fibre hence removing the need for multiple electrical cables. Next generation avionic networks require much higher bandwidth both for in-flight entertainment systems on commercial aircraft and for systems which produce high bandwidth data on military aircraft. Fibre optic networks are best placed to cope with this increased bandwidths and much development is going into environmental testing and ruggedising connectors; long seen as a disadvantage of fibre optic systems in a difficult environment. Development of fibre optic networks, both for terrestrial use and avionic has led to favourable conditions such as cheap telecommunications components for fibre optic based structural health monitoring systems i.e. at an operating wavelength of 1550nm. They allow multiple sensors to be placed on each fibre minimising the weight and therefore cost and minimise the potential impact on the aircraft by removing the spark hazard of electrical cables and they do not produce electromagnetic interference. A full comparison of fibre optic and electrical sensors is given in §2.5.

4

1.3.   Aim of Thesis

The aim of the work presented in this thesis is to develop technologies related to impact detection for aircraft and unmanned air vehicles. This includes interrogation schemes for fibre-optic sensors to allow multiplexed detection at high enough measurement speeds to allow high frequency components of dynamic impact events to be captured. In addition to hardware considerations, the relevant techniques are investigated in order to locate impacts on a complex structure accurately given the anisotropic nature of a general surface. Finally, determining the severity of an impact is very important to such a system in order to differentiate between damaging and non-damaging impacts either through estimating the impact intensity or detecting the onset of damage directly.

1.4.   Aerospace Operating Requirements

An aerospace environment is typically harsher than that of, for instance, a commercial telecommunications network. This includes a large temperature range, vibration and mechanical shock which places limitations on the design. Table 1.1 lists the conditions aboard both civil and military aircraft.

Vibration and mechanical shock restrict the choice of equipment, for instance bulk optics require expensive ruggedizing which seriously harms the commercial viability of such a technique. The operational temperature ranges can be large and can vary widely across the airframe due to the proximity of hot components, the engines and surfaces heated by air friction. Unconditioned areas of the air frame can experience even higher temperature ranges than those listed in Table 1.1, operational temperature ranges of -60 °C to 160 °C [6.8] or -60 °C to 100 °C [6.9] have been reported in the literature.

The typical requirements for an aerospace structural health monitoring load monitoring application specify a strain range of $\pm$ 3500 $\mu\varepsilon$ [6.8,6.9]. This suggests that the quasi-static strain that the sensors will experience can reach those two extremes, even if an impact detection system does not intend to measure the load it must be able to operate over that range.

As an emerging area, the requirements for an aerospace impact detection system are still being explored. The frequency content of impact detection signals ranges from the tens of Hz to approximately 200 kHz for low-velocity impacts [1.10]. Whether or not the operating bandwidth has to cover the full frequency range is uncertain and depends on whether the higher frequency content provides valuable information for the application; this is explored in chapter 4. The dynamic strain resolution requirements will depend

on the frequency of interest; the strain reached in low-velocity impacts has been recorded as 1000 µε [1.11] and 2700 µε [1.12]. This is mainly due to the low-frequency flexing of the material as the impact deflects it with dynamic strain over 1 kHz being much lower. The strain values corresponding to the dynamic components are not reported in the literature which may be due to the difficulty in measuring the strain directly at high operating bandwidth. In order to attempt to partially answer this questions the relative magnitude of different frequency ranges are investigated in chapter 4. Finally, the number of sensors to be interrogated simultaneously will depend on the application. Some potential applications require just a few sensors around at-risk components such as the leading edge of the wing. However, more sensors would always be useful to allow greater coverage of a structure, to provide redundancy in case of damage or used in different orientations to better address the directionality of many fibre-optic sensors.

Table 1.1. Conditions on board both civil and military aircraft [1.13].

Condition.	Civil Aircraft, Flight deck and passenger cabin.	Civil Aircraft, Flight control surfaces and landing gear.	Military Aircraft, Conditioned avionics bay.
Temperature			
Operating	-15 to +55 ℃	-55 to +70 ℃	-40 to +70 ℃
Short term operation	+70 ℃	+70 ℃	+90 ℃
Survival	-55 to +85 ℃	-55 to +85 ℃	-55 to +90 ℃
Temperature Shock	2 ℃ / min	10 ℃ / min	5 ℃ / min
Steady State Pressure	57.2 to 107 kPa	4.4 to 107 kPa	3.6 to 115 kPa
Pressure Variation	226 kPa /min decreasing	Unpressurised zone	318 kPa – 400 kPa/ min
Acceleration	Not specified	Not specified	Linear 9.6g
Mechanical Vibration	0.003 g^2 / Hz	0.16 g^2 / Hz	0.04 g^2 / Hz
Acoustic Vibration	Not specified	Not specified	140 dB
Mechanical shock			
Operational	6g half sine wave in 11ms	6g	20g sawtooth in 11ms
Crash Safety	15g half sine wave in 11ms	15g	20g sawtooth in 11ms
Humidity	85% at 38 ℃	95% at 55 ℃	27 g/kg water/air mix

Additionally, size and weight are very important for an aerospace application, any extra weight increases fuel costs significantly. Large and heavy laboratory equipment is therefore uneconomical in such an environment, higher initial costs for lighter components and techniques can typically be offset by large savings over the lifetime of the aircraft.

All of these conditions must be considered carefully when developing techniques for an impact detection system on an aircraft and they will be considered throughout this thesis.

1.5.   Outline of Thesis

Chapter 2 contains an introductory overview of a number of topics relevant throughout the rest of the thesis. These topics are: composite materials and their damage mechanisms, electrical and fibre optic sensors, interrogation techniques for optical fibre sensors and important measurement parameters for structural health monitoring. Chapter 3 experimentally investigates impact location techniques on a curved composite leading edge structure. Time-of-flight triangulation using a look-up table technique is compared to that of a neural network. Piezoelectric sensors are compared to a simple chirped fibre Bragg grating (FBG) interrogation scheme. In Chapter 4 a method for differentiating between damaging and non-damaging impacts in composite materials is developed from analysis of acoustic waves. A large dataset of impact signals is created and analysed leading to the identification of characteristic damaging features and an automated detection algorithm. An arrayed waveguide grating (AWG) based FBG interrogator is developed in Chapter 5. Using experiments and computational modelling, design parameters such as FBG and AWG spectral widths are varied in order to determine their effect on key performance indicators, such as the strain range and linearity of the system. The effect of FBG length on the temporal bandwidth of the system is investigated as well as the stability over short and long timescales. An alternative FBG interrogation technique is investigated in Chapter 6 utilising erbium doped fibre as a non-linear medium for two wave mixing in order to create a temporary dynamic grating. This dynamic grating allows for an adaptive system that is not affected by quasi-static strain or temperature drifts. The creation of a dynamic grating is verified before dynamic signals are captured and shown to be unaffected by quasi-static drifts. Wavelength division multiplexing is demonstrated by interrogating two sensors simultaneously. Chapter 7 describes the development of a demonstrator system

utilising techniques developed in this thesis to allow multiplexed interrogation of four FBG sensors using an AWG to locate impacts via a neural network on a curved composite structure. The final chapter concludes the findings of the thesis and gives information on possible further work that could be undertaken to progress these further.

1.6. References

[1.1] W. Staszewski, C. Boller and G. Tomlinson, *"Health Monitoring of Aerospace Structures,"* Chichester, UK, Wiley (2004) ch.1.

[1.2] W. Staszewski, C. Boller and G. Tomlinson, *"Health Monitoring of Aerospace Structures,"* Chichester UK, Wiley (2004) ch.35.

[1.3] C. Brand and C. Boller, *"Identification of life cycle cost reduction in structures with self-diagnostic devices,"* NATO Symposium on Design for Low Cost Operation and Support, Ottawa, Canada, 21-22 October (1999).

[1.4] C. P. Sampath, *"Aging combat aircraft fleets – long-term applications,"* AGARD Lecture Series, **206**, (1996).

[1.5] K. -H. Ip and Y. -W. Mai, *"Delamination detection in smart composite beams using Lamb waves,"* Smart Mater. Struct. Vol. **13**(3) pp544-551 (2004).

[1.6] P. J. de Groot, P. A. M. Wijnen, and R. B. F. Janssen, *"Real-time frequency determination of acoustic emission for different fracture mechanisms in carbon/epoxy composites,"* Composites Science and Technology, Vol. **55** pp. 405-412 (1995).

[1.7] J.-R. Lee, S.-S. Lee and D.-J. Yoon, *"Simultaneous multipoint acoustic emission sensing using fibre acoustic wave grating sensors with identical spectrum,"* Journal of Optics A: Pure and Applied Optics pp. 1-9 (2008).

[1.8] I. J. Read, and P. D. Foote, *"Sea and flight trials of optical fibre Bragg grating strain sensing systems,"* Smart Mater. Struct. **10**, 1085–1094 (2001).

[1.9] H. Guo, G. Xiao, N. Mrad, and J. Yao, *"Fiber Optic Sensors for Structural Health Monitoring of Air Platforms,"* Sensors 2011, **11**, 3687-3705 (2011).

[1.10] G. Kirikera, O. Balogun and S. Krishnaswamy, *"Fiber Bragg Gratings and Two Wave Mixing Spectral Demodulator System for Impact Detection and Localization,"* 4th European Workshop on Structural Health Monitoring, Crakow, Poland, pp. 841–848 (2008).

[1.11] C. Y. Park, B.-W. Jang, J. H. Kim, C.-G. Kim, S.-M. Jun, *"Bird strike event monitoring in a composite UAV wing using high speed optical fiber sensing system,"* Composites Science and Technology **72** pp. 498–505 (2012).

[1.12]   S. Takeda, Y. Aoki, and Y. Nagao, *"Monitoring of Buckling Behaviours in Composite Stiffened Panel With Impact Damages Using Fiber-Optic Sensors,"* Asia-Pacific Workshop on Structural Health Monitoring, The University of Tokyo, Tokyo, Japan, 1A1 pp. 1-8 (2010)

[1.13]   R. D. Gardner, I. Andonovic, D. K. Hunter, A. J. McLaughlin, J. S. Aitchison, J. H. Marsh, *"PHONAV – A Photonic WDM Network Architecture for Next Generation Avionics Systems,"* Aerospace Conference, pp. 451-466 (1999).

Chapter 2 – Background Theory and Literature Review

2.1. Composite Materials

Composite materials are increasingly being used for aerospace structures and have some notable differences to metals in both their structural properties and damage mechanisms which must be considered when contemplating a structural health monitoring system. The structure of common composite materials, their properties, differences to metals and damage mechanisms are detailed below.

2.1.1. Introduction

A composite material is formed by the combination of two or more distinct materials to form a new material with enhanced properties [2.1]. Unlike metallic alloys, each material retains its separate chemical, physical, and mechanical properties. A typical composite material used in aerospace is composed of long fibres which are placed in a liquid resin and then cured, usually by heating, in order to solidify and form a plate. The resin holds the fibres together and provides the shape and stability while the fibres provide a high tensional strength.

There are generally two key components in a composite material: the reinforcement and the matrix. The reinforcing structure provides the strength and stiffness and is usually a fibre or a particulate: typical fibres include glass, aramid and carbon. Fibres can be either long and continuous or short and discontinuous, several types of fibre reinforcement are shown in Figure 2.1 [2.2]. Continuous-fibre composites are the most common and have various configurations such as unidirectional or woven cloth. They are more expensive to make but provide much greater performance. Single sheets of continuous fibres in different orientations are usually stacked to form laminates in order to obtain the desired strength and stiffness.

The matrix is the continuous material, the resin in the previous description, in which the reinforcing agent (typically fibre) is contained. It can be a polymer, ceramic or metal [2.3]. Ceramics are generally used to increase the toughness rather than the strength and stiffness and tend to have weak bonds with the fibres. Both metal and polymer matrix composites form a strong bond between the fibres and the matrix allowing the load to be transferred efficiently to the fibres. Metals have relatively high strength and stiffness along with high ductility. Polymer matrix composites are very common as they tend to be much cheaper to manufacture although they do have lower strength and stiffness.
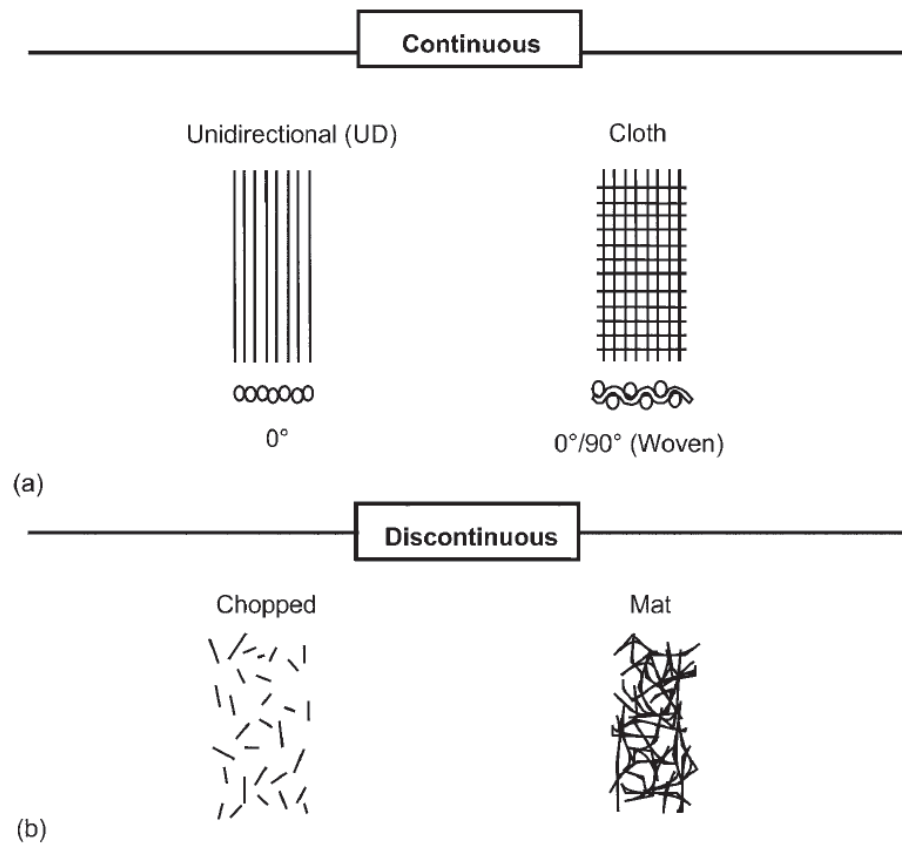
Figure 2.1. Comparison of different types of fibre reinforcement. Long, continuous fibre type are shown in (a) while short, discontinuous fibre types are shown in (b) adapted from [2.2].

Two common types of polymer matrices are thermoset and thermoplastic. A thermoset is a low-viscosity resin that reacts and cures during processing, forming an intractable solid. A thermoplastic, however, is a high-viscosity resin that is processed by heating it above its melting temperature. It can be reheated above its melting temperature for additional processing unlike a thermoset resin which cannot be reprocessed by reheating once the resin has cured. Another purpose of the matrix is to protect the fibres from environmental attack; due to the excellent resistance of polymer matrices to environmental and chemical attack composites have replaced many traditional materials.

A single ply or a lay-up in which all layers or plies are stacked in the same orientation is called a lamina. If instead the plies are stacked at various angles, the lay-up is called a laminate. Continuous-fibre composites are usually laminated materials in order to increase strength in the primary load direction. Unidirectional laminae are extremely strong and stiff in the fibre direction, however, perpendicular to the fibre orientation the load must be carried by the much weaker polymeric matrix. A high strength fibre can have a tensile strength of 3500 MPa or more, a typical polymeric matrix has a tensile strength of $35 - 70$ MPa [2.2]. A comparison of a unidirectional lay-up and a quasi-

isotropic lay-up in which fibres are oriented in four different directions is shown in Figure 2.2. Although a quasi-isotropic laminate can handle multidirectional loads, the strength and stiffness per unit weight of the laminate on a given direction are lower than the corresponding values for a unidirectional composite. Other materials can be added to create a hybrid structure of which sandwich construction is the most common. A sandwich composite is created by adding a lightweight core, such as foam or honeycomb between two strong, stiff faces. This creates a separation between the two faces so that the moment of inertia of the faces is large. This results in high bending stiffness while adding less weight and cost than a thicker non-sandwich construct [2.1].
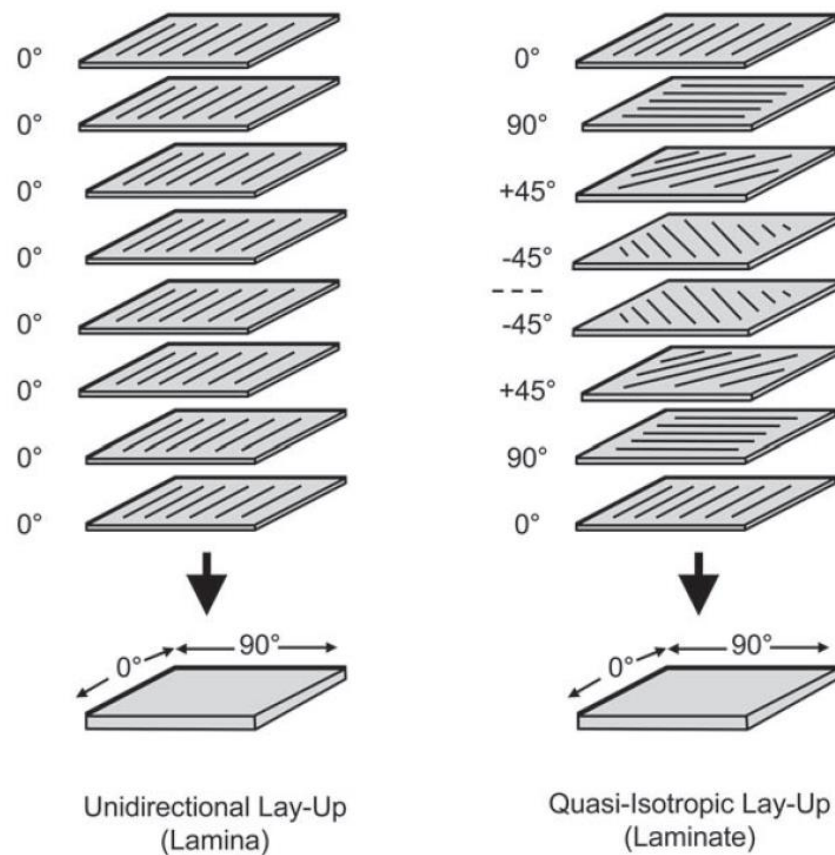
Figure 2.2. Comparison of a unidirectional lay-up (lamina) and a quasi-isotropic lay-up (laminate) in which fibres are oriented in four different directions [2.2].

2.1.2. Comparison to other materials

A major advantage of fibre reinforced composite materials is the high specific strength and modulus when compared to metals such as steel and aluminium. Composite materials are strong and stiff but lightweight, especially important for weight critical applications such as aviation, resulting in improved performance, greater payloads, longer range, and fuel savings. Composites also have improved fatigue life and excellent corrosion resistance which can lead to major savings in structural life costs.

13

Composite materials can be expensive and time consuming to produce due to the material costs, labour intensive manufacturing process and long fabrication time. A further disadvantage of composite materials is the difficulty associated with repair, subsurface damage can be generated which has an adverse effect on the performance of the material and is not easy to detect. The number of joints and fasteners in a part made from composites materials can be dramatically reduced when compared to a similar metallic part however joining composite materials is difficult [2.4]. Finally, they have poor strength in the out-of-plane direction as the matrix carries the primary load causing susceptibility to impact damage and delamination.

2.1.3. Composite damage

Impact damage is not generally considered to be a threat in metal structures because large amounts of energy can be absorbed due to the ductile nature of the material. Composites, however, may fail in a wide variety of modes leaving barely visible impact damage (BVID) which nevertheless severely reduces the structural integrity of the component. There are also other failure modes with non-impact causes such as over-stressing and thermal damage but this description will focus on those directly related to low-velocity impacts. Low-velocity impact is a term used to signify non-ballistic projectiles such as bird strikes, runway stones and falling tools. This is in contrast to high-velocity impacts and hypervelocity impacts which include ballistic munitions and micrometeorites etc. [2.5, 2.6].

The anisotropic and heterogeneous nature of fibre reinforced laminates contributes to different modes of failure. In most cases, these include; (1) matrix cracking that occurs parallel to the fibres due to tension, compression or shear; (2) debonding and/or delamination between the layers as a result of interlaminar stresses; (3) fibre breakage and buckling; and (4) penetration. The interaction between failure modes influences damage mode initiation and propagation [2.7].

Matrix damage is the first type of failure induced by transverse low-velocity impact and usually occurs as matrix cracking but also includes debonding between fibre and matrix. Matrix cracks are usually oriented in planes parallel to the fibre direction in unidirectional fibre composites.

A delamination is a crack which runs in the resin-rich area between plies of different fibre orientation and not between lamina of the same ply group. It is caused by the mismatch of bending stiffness between adjacent layers. The greater the mismatch (0/90

being the worst case fibre orientation), the greater the delamination area will be. Delamination caused by transverse impact only occurs after a threshold energy has been reached and it has been observed that delamination only occurs in the presence of a matrix crack [2.8].

Fibre failure usually occurs much later in the fracture process than matrix cracking and delamination and is a precursor to catastrophic penetration mode. It occurs under the impact point due to locally high stresses and indentation effects and on the non-impacted face due to high bending stresses.

Finally, penetration is a macroscopic failure mode and occurs when the fibre failure reaches a critical extent, allowing the impactor to completely penetrate the material. The impact energy penetration threshold rises rapidly with specimen thickness and is also affected by the diameter of the impactor as well as fibre sizing and orientation [2.9].

Currently the only proven method for damage detection in composite materials is ultrasonic/acoustic non-destructive technology (NDT). This is also sometimes referred to as non-destructive evaluation (NDE), non-destructive examination (NDE) or non-destructive inspection (NDI). Utilising this method requires aircraft to stop service and be manually checked point-to-point by skilled technicians. In addition some aircraft sections may need to be dissembled to provide access for the inspection which can itself lead to accidental damage. This leads to a labour intensive and very costly effort due to the amount of man hours and time out of service for the aircraft. On-board impact detection methods could lead to a reduction in scheduled maintenance which would reduce costs significantly [2.10].

2.2. Acoustic Waves

Acoustic waves are an important topic in NDE and are used actively and passively to detect events or to probe for damage. For aerospace applications this typically takes place in plates and therefore the most important class of acoustic waves are Lamb waves. Rayleigh waves, which relate to wave propagation along a guided surface were discovered in plates and subsequently named Lamb waves [2.11]. They refer to waves in thin plates, those whose planar dimensions are far greater than that of the thickness and also with the wavelength being of the order of the thickness. They include symmetric (longitudinal) and anti-symmetric (flexural) modes. The fundamental symmetric mode has a displacement which is mainly longitudinal as the frequency

approaches zero [2.12]. This corresponds to a stretching of the plate without bending. The antisymmetric mode, in contrast, corresponds to a transverse displacement and therefore corresponds to bending without stretching. An event such as an impact on the plate will create Lamb waves which will have a mix of modes which will then propagate through the plate from the initial impact point. For an impact perpendicular to the plate the largest component will likely be flexural and therefore the antisymmetric mode will have the greatest magnitude. Lamb waves are dispersive and therefore the phase and group velocities vary with frequency which complicates their use for locating sites of impact or damage.

2.3.   Electrical Sensors

In order to detect the loads and strain that composite panels are experiencing, as well as acoustic emission and other signifiers of damage electrical sensors are commonly employed. Strain gauges and piezoelectric transducers are two such established sensors currently used in engineering environments.

2.3.1. Strain gauges

Electric resistance strain gauges commonly used for experimental strain analysis for aircraft and other structures. They are based on the principle that the electrical resistance of a wire changes when it is subject to load discovered by Lord Kelvin in 1856 [2.13]. Strain sensitivity, *F*, (defined as the *gauge factor* for a strain gauge) is a dimensionless relationship which can be expressed as

$$F = \frac{\Delta R}{R} \div \frac{\Delta l}{l} \qquad (2.1)$$

where *R* is the initial resistance, ΔR is the change in resistance, *l* is the initial length and Δl is the change in length [2.14]. The electrical resistance, *R*, of a conductor is given by

$$R = \frac{\rho l}{A} \qquad (2.2)$$

where ρ is the resistivity and *A* is the cross-sectional area [2.14]. Strain sensitivity is a combination of the effects of geometric change and a resistivity change due to changing internal stresses. Beyond the elastic limit, the changes in stress approach zero and the strain sensitivity approaches 2.0, therefore a material with a sensitivity of approximately 2.0 in the elastic range as well will remain essentially linear over both ranges. Therefore it will operate over a wide strain range making it ideal for use in a strain

gauge. Changes in the length of the gauge due to strain will lead to a linear change in the resistance of the gauge which can then be measured.
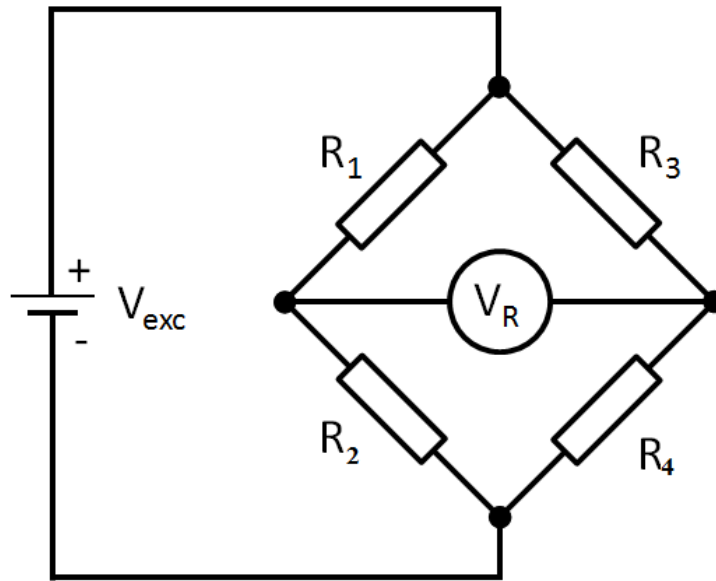

Figure 2.3. Diagram of a Wheatstone bridge arrangement for measuring a small change in resistance.

The Wheatstone bridge is the most commonly used for converting the small resistance change into a voltage suitable for amplification and measurement, it is illustrated in Figure 2.3. An excitation voltage, V_{exc}, is placed across the resistor arrangement and if $R_1/R_2 = R_3/R_4$ then the output voltage, V_R, will be zero when the bridge is balanced. If one of the resistors is a strain gauge of equal starting resistance then any deviation due to applied strain will lead to a measurable output voltage.

Foil strain gauges are essentially small printed circuits, with a conductor typically 3 – 5μm thick and made from alloys such as copper-nickel or nickel-chrome. Major advantages of electric resistance strain gauges are accuracy and versatility. Commercial foil gauges are normally accurate to within 1 percent, if the gauge is calibrated after installation accuracies better than 0.1 % have been maintained over many years [2.15]. They have the basic limitation that each gauge element is capable of monitoring the strain in only one locations and in only one direction. While the gauge itself is cheap and lightweight the associated electronics may be costly and elaborate for multisensor amplification and measurement.

2.3.2. *Piezoelectric transducers*

The piezoelectric effect, which occurs in certain materials when subject to mechanical stress, produces a voltage which is linearly related to the applied stress [2.16]. This

allows the material to function as a sensor and measure local perturbations such as acoustic waves travelling through the material. Similarly, if a voltage is applied across the piezoelectric material stress will be created accordingly, this is the reverse piezoelectric effect. Therefore, applying an oscillating voltage across a suitable material will lead to a dynamic, repeatable size change of the material dimensions allowing it to be used as an actuator [2.17].

The piezoelectric effect is characteristic of single crystals of certain insulators such as quartz and lithium sulphate, some semiconductors such as cadmium sulphide and certain ceramic materials such as barium titanate and lead zirconate titanate (PZT). PZT is the most commonly used and performs better than naturally occurring piezoelectric materials [2.18].

An ultrasonic transducer can be created which normally consists of several parts. The active element is a piezoelectric ceramic such as PZT with electrodes on each face that are connected to ground and the signal lead. Behind the active element there is usually a backing material which loads the active element and can be designed to produce a less resonant device [2.19]. This may be useful for sensing or actuating a broadband signal but a more resonant device will be more sensitive of certain frequencies and will be preferable for other applications where the frequency of interest is well defined and narrowband.

The thickness of the active element largely controls the frequencies at which the transducer has the highest sensitivity. For acoustic emission sensing using common piezoelectric materials the thickness would typically be several millimetres, producing a first resonance of about 0.5 MHz.

The transducer must be coupled to the material of interest either through permanent adhesive bonding or temporary couplant to allow good transfer of acoustic waves between the transducer and the material. Alternatively, piezoelectrics transducers can be embedded into a composite material during manufacture which can produce higher outputs due to the improved strain transfer. However, this may affect the material causing a reduction in strength and complicating the manufacturing process.

2.4. Optical Fibres

Optical fibres are increasingly being used as an alternative to electrical cables in many applications such as telecommunications and they may soon see increased use on board aircraft.

Total internal reflection is a useful but simple model which will be covered here, a more complete analysis can be afforded via analysis of Maxwell's Equations. For further information on fibre optic theory see [2.20, 2.21].

An optical fibre is a flexible, cylindrical structure used as a waveguide to transmit light from one end to the other with minimal loss. Step-index fibres consist of a central core of high refractive index material surrounded by a cladding layer of lower refractive index. Light is guided by total internal reflection at the interface subject to the condition that the ray enters the fibre within the acceptance angle φ_{acc} which, for multimode fibre, is given by

$$n_0 \sin \varphi_{acc} = \sqrt{n_1^2 - n_2^2} \tag{2.3}$$

where n_0, n_1 and n_2 are the refractive indices outside the fibre, in the core and in the cladding, respectively [2.22]. The numerical aperture of a fibre is defined as $n_0 \sin \varphi_{acc}$ which is often quoted as a measure of the acceptance angle of a given fibre.

The light is guided down the fibre as the light is reflected repeatedly at the boundary with very low loss for light which has an angle of incidence less than the critical angle for total internal reflection. As the light travels, a wave interference effect will occur. Light arriving at a point in the core via different optical paths will interfere causing bands of constructive and destructive interference to be created. This means that only certain optical paths, known as spatial modes, can actually travel along the fibre.

Fibres may support one or more optical transverse modes depending on the characteristics of the fibre such as the diameter of the core and the refractive index contrast between the core and cladding. Fibres which support only one such mode are known as single mode fibres and have a core diameter of ~10 μm depending on the wavelength of light to be guided. If more than one mode is supported then the fibre is known as a multimode fibre and typically has a core diameter of ≥ 50 μm. Due to the larger cross-section of the core, multimode fibres have a greater light-gathering ability and as such are easier to align and splice. Single mode fibres exhibit fewer dispersion effects compared to multimode fibres which have increased dispersion because light in different modes travel with a different group velocity. While the phase velocity of the light is constant for n_{core} the path length travelled through the fibre will differ between modes leading to dispersion. This allows single mode fibres to transmit data over longer distances without the signal quality degrading.

Higher order modes can exist in an optical fibre which are not restricted to the area of the core and are known as cladding modes. A percentage of the light directed onto the end face of a fibre will not propagate through the core but will instead travel as cladding modes. These modes will usually have higher losses and be attenuated by leakage into the fibre jacket coating and will therefore not propagate over large distances.

Alternatively, optical fibres can be made with a radially varying refractive index profile known as graded index fibres. This profile causes light to refract continuously as it propagates through the fibre rather than reflect at the core-cladding interface. This design reduces the modal dispersion of a multimode fibre as the high angle rays travel more through the lower index periphery of the core which compensates for the longer distance travelled.

Connections between optical fibres are more complicated than electrical cables as they need to be aligned with an accuracy better than 1 μm. Fibres can be permanently spliced together by first cleaving the end faces and then splicing together either mechanically or through fusing with an electric arc. Alternatively, many connectors are commercially available which, once attached, provide easy, reproducible connections which accurately align the two fibres for efficient light coupling.

Single mode step-index fibres are used in the following chapters due to their advantages as listed above as well as the prevalence of cheap, optical components which are designed for such fibres.

2.5. Optical Fibre Sensors

Optical fibre sensors may be defined as devices through which a physical, chemical or biological measurand interacts with light, either guided in an optical fibre (intrinsic sensor) or guided to an interaction region by an optical fibre (extrinsic sensor), to produce an optical signal related to the parameter of interest [2.23]. Many different optical fibre sensors have been developed to measure a variety of different parameters over both short and long range with appropriate resolution for the application. This section gives an overview of the main categories of sensor including fibre Bragg gratings, chirped and long period gratings, interferometric based sensors and distributed sensing techniques.

2.5.1. Intensity based sensors

The simplest optical fibre sensors are intensity based and are often made of multimode fibre with small sensors that can measure parameters at certain localised points. The

optical carrier is delivered to the remotely located sensor and the return signal is modulated in intensity by the sensor. Intensity sensors can be divided into two groups; hybrid sensors and internal effect sensors. Hybrid sensors treat the optical fibre as a 'light pipe' only and all intensity modulation is performed by attaching a miniaturised device to the end face of the fibre, this technique can be less rugged due to the external sensor. Alternatively, internal effect sensors use an intensity modulation mechanism within the optical fibre such as microbend losses [2.24] or the fiberdyne modal intensity modulation effect [2.25].
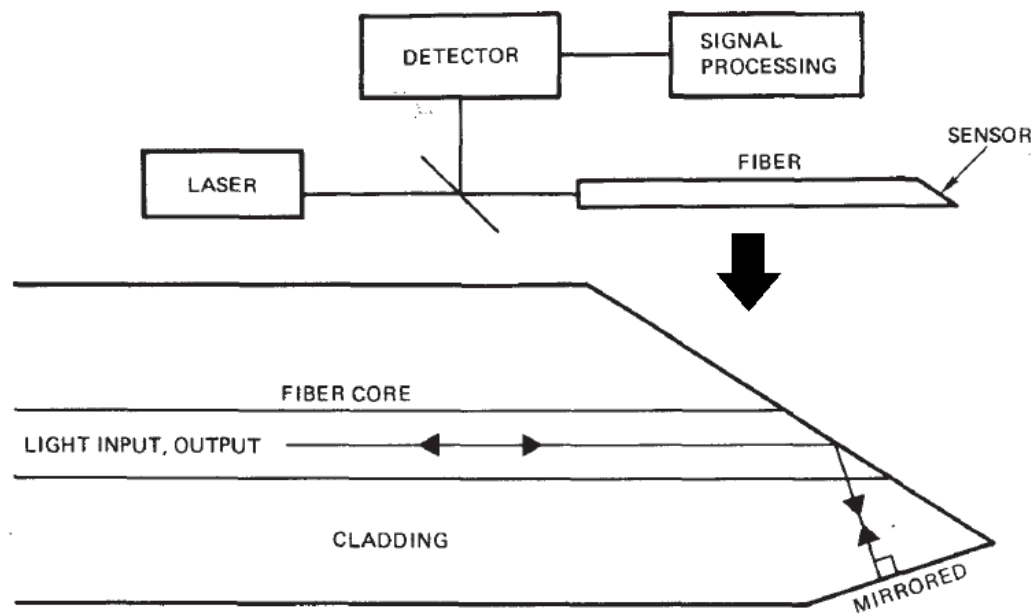

Figure 2.4. An intensity based hydrophone sensor. Acoustic perturbations in the surrounding water change the critical angle and lead to a change in intensity [2.2726].

An example of an intensity based hydrophone sensor is shown in Figure 2.4. Light reflects off a total internal reflective surface and is then reflected off a mirrored surface back to a detector. If an acoustic wave passes through the water surrounding the sensor it alters the refractive index of the water more than that of the optical fibre causing a change in the critical angle as well as internal reflectivity leading to an intensity drop at the detector [2.26].

The main limitation of this technique is downlead/source loss; fluctuations in the source and attenuation within the fibre limit the sensitivity and reliability of this technique as well as limiting the maximum range [2.27].
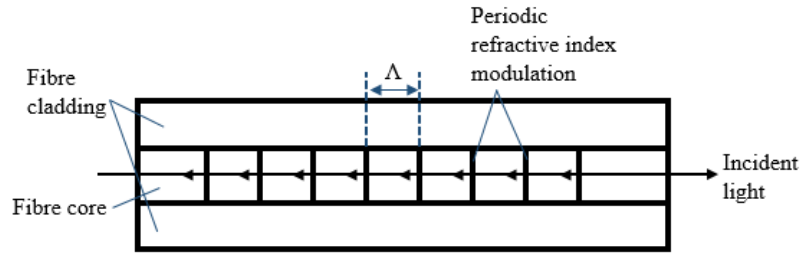
2.5.2. Fibre Bragg gratings

Figure 2.5. Diagram of a fibre Bragg grating showing the multiple reflections from the periodic refractive index modulation of period Λ.

Figure 2.5 shows a fibre Bragg grating (FBG), formed by inscribing a periodic refractive index modulation, usually between 1 – 20 mm in overall length, along a length of optical fibre. Upon broadband illumination the FBG reflects a narrow band of wavelengths determined by the spacing of the index modulation which, when perturbed by strain or temperature, will shift according to the perturbation. The reflectivity can approach 100% for the corresponding stopband with only a relatively small refractive index modulation ($\sim 10^{-4}$) required to achieve high reflectance [2.28]. For some applications, such as time-division multiplexing, the reflectivity is required to be significantly lower and the grating can be designed as such by reducing the refractive index modulation accordingly. For efficient fibre Bragg grating fabrication the photosensitivity has to be increased from that of standard telecommunication fibre. This can be achieved in several ways such as increasing the germania (GeO_2) concentration from the standard 3 mol% or by loading the fibre with hydrogen. Co-doping with elements such as boron or tin can compensate for the increased germania concentration and lower the refractive index [2.29]. The modulation of the refractive index is created by exposure to UV light between 244 – 248 nm by the photorefractive effect in the germania oxygen-vacancy defect band.

In the following treatment the assumption has been made that the refractive index modulation is constant across the along the length of the grating which would not be the case for chirped gratings (see §2.5.3).

The high reflectance occurs because the period of the grating has been chosen to cause maximum constructive interference between subsequent reflections as the light passes from high to low refractive index as given by

$$\lambda_B = 2n\Lambda \qquad\qquad (2.4)$$

where λ_B is the Bragg wavelength, which is the wavelength of maximum reflection, n is effective core index of refraction and Λ is the period of the index modulation.

The reflectivity, R, of the fibre Bragg grating at the Bragg wavelength is given by

$$R = \tanh^2 \Omega \qquad (2.5)$$

where

$$\Omega = \pi n(L/\lambda_B)(\Delta n/n)\eta(V) \qquad (2.6)$$

with L as the length of the grating, Δn is the refractive index modulation and $\eta(V)$ as the fraction of the integrated fundamental mode stored within the core [2.30].

Fibre Bragg gratings can be used to detect many parameters such as temperature [2.31], strain [2.32], pressure [2.33], dynamic magnetic fields [2.34], acceleration [2.35] and many others. As equation (2.4) shows the Bragg wavelength is dependent on both the refractive index and the grating spacing which may be both affected by the above parameters. The Bragg wavelength may be dependent on many of these parameters simultaneously and even small changes will result in a measurable shift in the Bragg wavelength. To detect the desired parameter, the system will have to be carefully designed to isolate the sensor from changes in the other variables or otherwise decouple the required characteristic, for instance by use of a reference sensor. Figure 2.6 shows a simple fibre Bragg grating setup to detect strain with a broadband optical source, the reflected signal is a narrowband peak which is shifted from the Bragg wavelength by an amount related to the strain [2.36]. This peak is missing from the transmitted spectrum and could be detected directly, however, the reflected signal usually has a better signal to noise ratio and is therefore more useful for sensing. Also, in this case the fibre only needs to be accessed from one end which makes the system simpler, requiring fewer connectors which are a weakness of optical fibres.
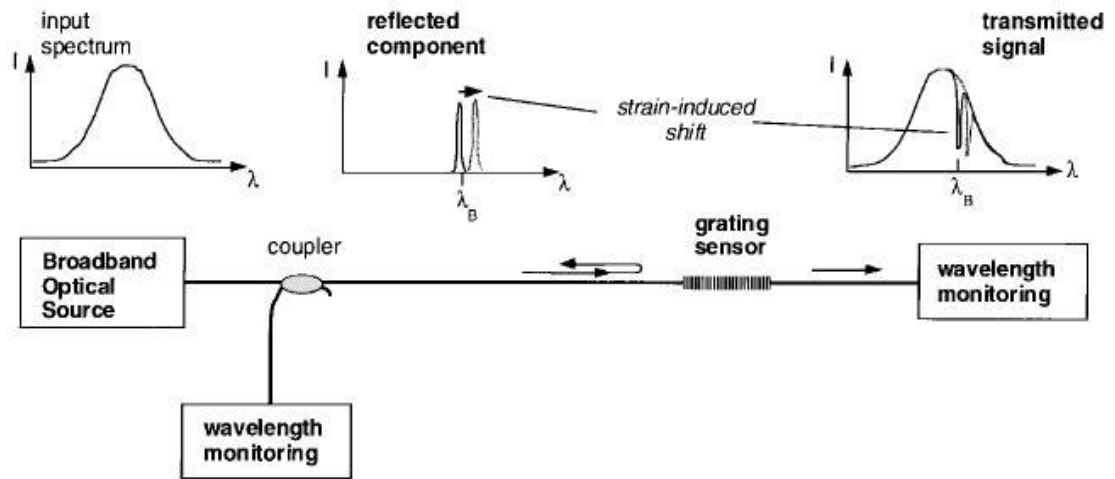
Figure 2.6. Simple fibre Bragg sensor setup to detect strain in either reflection or transmission [2.36]

One of the main advantages of the fibre Bragg grating sensor is that the measured parameter is wavelength, an absolute parameter; it does not depend directly on the light level, input intensity or losses due to connectors and couplers. Thus the sensor is almost immune to the uncertainty in those parameters. Wavelength encoding allows the use of wavelength division multiplexing (WDM); multiple sensors can be written into a single fibre and assigned a section of the input spectrum by varying the grating period used (see § 2.8.1). This leads to quasi-distributed sensing, for a WDM system the upper limit to the amount of sensors attached to one source is a function of the source spectral bandwidth and the operational spectral bandwidth required for each sensor. This depends on the maximum strain expected, and hence maximum wavelength shift, together with the reflection bandwidth of each Bragg grating sensor, which is typically 0.1 nm.

A further consideration for the use of FBG sensors is their directionality. They have a higher sensitivity to perturbations which are in the fibre axis direction and a lower sensitivity to those orthogonal to this. Several studies have used this fact to determine the direction of travel of a detected acoustic wave using a rosette of, typically three, FBG sensors at various angles [2.37, 2.38, 2.39].

2.5.3. Chirped grating sensors

Chirped fibre Bragg gratings (CFBG) were first developed for dispersion compensation in high bit-rate telecommunications but have now found applicability in sensing [2.40]. These gratings can be created by axially varying either the period of the grating, the refractive index of the core or both (see Figure 2.7). As such, they may be considered to

24

be made up of a series of smaller length uniform Bragg gratings increasing in period which produces a broadband reflector. Chirped Bragg gratings with a broadband, step-function chirp profile may also be used as sensors.
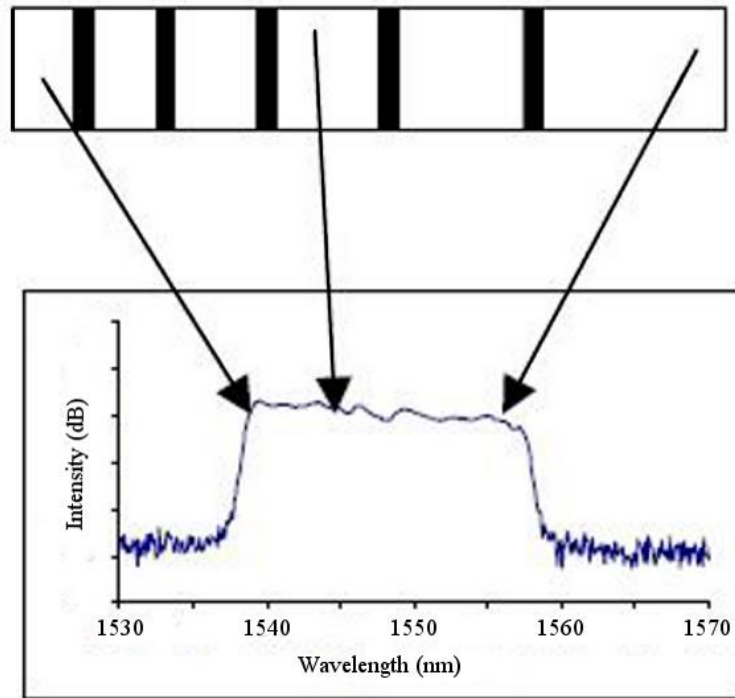

Figure 2.7. A chirped fibre Bragg grating showing the axially varying period of the grating (exaggerated for clarity) and the resultant broad reflectivity spectrum [2.40].

2.5.4. Long period gratings

A long-period fibre grating (LPG) is a periodic modulation of the core index of refraction written into a single mode fibre. A typical LPG has a period, Λ, in the region of hundreds of microns, a length of 1-3 cm and an index modulation depth of $\sim 10^{-4}$. The index modulation can be written using several different techniques such as using UV exposure through an amplitude mask to induce a permanent change via the photorefractive effect [2.41]. Alternatively, for fibres that contain significant residual stress in the core, a CO_2 laser can be used to relax this stress by laser heating and thus lower the refractive index [2.42]. LPGs can also be created by non-optical means by mechanically stressing the fibre at the required location.
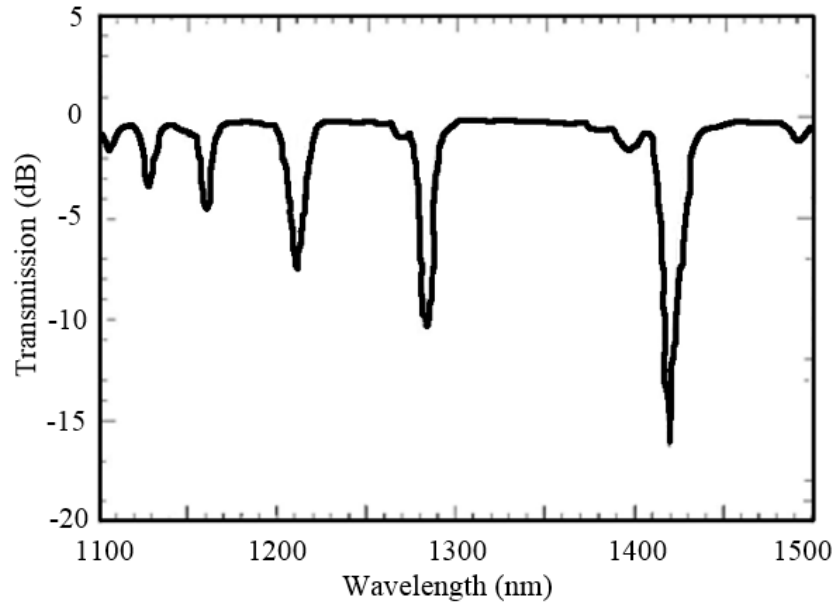
Figure 2.8. Representative transmission spectrum for a long period grating showing the multiple resonances which exist for a single grating.

LPG structures couple the guided fundamental mode in a single-mode fibre into the forward propagating cladding modes. These cladding modes decay rapidly as they propagate along the fibre axis due to scattering losses at the cladding-air interface and bends in the fibre; this leaves a series of loss bands or resonances in the guided mode as shown in Figure 2.8. Due to the wavelength-selective nature of the coupling, the fibre grating acts as a wavelength-dependent loss element [2.43]. The LPG couples light out of the core and into the cladding at specific wavelengths, λ_i, according to the expression

$$\lambda_i = \left(n_{01} - n_{clad}^{(i)}\right)\Lambda \tag{2.7}$$

where n_{01} is the effective index of the core mode and $n_{clad}^{(i)}$ is the effective index of the ith axially symmetric cladding mode. The section of fibre where the grating is located is usually stripped of its polymer coating as $n_{clad}^{(i)}$ is dependent on the index of the medium surrounding the cladding. The phase-matching condition that dictates the coupling of one mode into another determines the exact periodicity to be used. For two forward-propagating modes, the difference between the propagation constants is very small leading to the requirement that the grating periodicity be long.

LPGs can be used as fibre optic sensors due to the dependence of the centre wavelength of the LPG resonance on the index difference between the core and the cladding. Any variations in strain, temperature or external refractive index can cause large wavelength shifts in the resonance due to their effect on the refractive index difference.

26

LPGs have a unique characteristic amongst fibre gratings in that an LPG resonance can have a very different sensitivity with regard to strain and temperature depending on the fibre type and the grating period. The temperature and strain response can be either positive or negative depending on the differential responses of the core and the cladding. These properties mean that LPGs are particularly useful for multi-parameter sensing such as strain and temperature. Two LPG resonances can be used with a single grating to provide simultaneous measurement of strain and temperature.

Advantages of LPGs include the capability to design the grating so that its response fits the specific application, cheap fabrication techniques, they are compatible with inexpensive demodulation techniques [2.44] and the multiple resonances can be used for multiple parameter sensing.

Some areas in which these sensors require improvement are the development of coatings to protect the fibre, refined interrogation techniques of the resonances and narrowing the LPG resonance bands to allow multiplexing [2.36]. In addition, the cross-sensitivity to a number of parameters such as strain, temperature and fibre bending makes it difficult to differentiate between them and measure the parameter of interest. Due to these limitations they do not currently offer sufficient advantages over standard FBGs to be used in this work further.

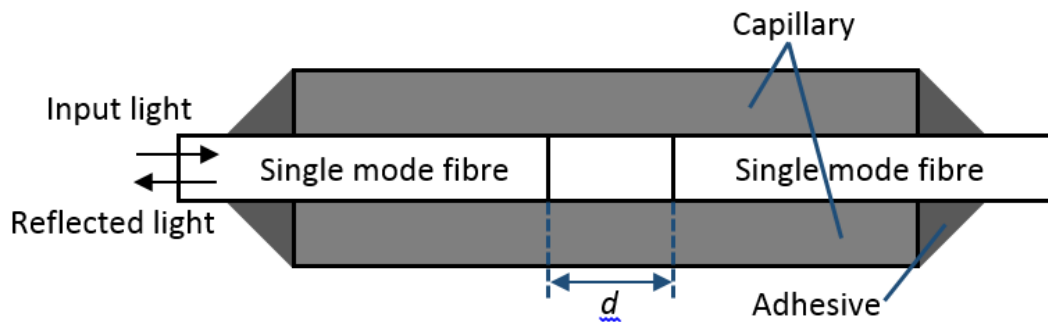### 2.5.5. *Fabry-Perot interferometric sensors*

Figure 2.9. Diagram of an extrinsic Fabry-Perot interferometric sensor constructed from two single mode fibres separated by a cavity of length, *d*, using a capillary.

An extrinsic Fabry-Perot interferometric (EFPI) sensor consists of a Fabry-Perot cavity illuminated by a single mode laser diode through a fused biconical tapered coupler. The cavity consists of a single-mode input fibre and a single-mode or multimode reflecting fibre which are aligned using a hollow-core silica fibre alignment tube as illustrated by Figure 2.9 [2.45]. A 4% Fresnel reflection results at both fibre faces for uncoated fibre ends [2.46]. The first reflection is used as a reference reflection as it is independent of

the applied perturbation. The second reflection, the sensing reflection, is dependent on the length of the cavity, d, which is modulated by the applied perturbation. The two reflections interfere and the intensity, I, at the detector is given by the following expression:

$$I = I_0 \cos\left(\frac{4\pi}{\lambda} d\right) \tag{2.8}$$

where λ is the wavelength of the laser diode and I_0 is the maximum output intensity.

The output is cosinusoidal in nature with the phase related to the cavity length. Hence, any external perturbation that changes the length of the cavity can be detected.

Most fibre optic strain sensors such as fibre Bragg gratings have a large cross-sensitivity between strain and temperature due to the dependence of the output on the finite thermal coefficient of refractive index. However, because the sensing air cavity is external to the lead-in/lead-out fibre, temperature changes and input polarisation have no noticeable effect on the output signal unless the alignment tube is made from a thermally conductive material such as metal. In addition, strain components transverse to the sensor longitudinal axis have negligible effect on the axial strain sensitivity allowing EFPI sensors to be more ideally suited to some embedded applications in smart structures.

One major limitation of this technique is the non-linearity of the output signal requiring complex and expensive systems to be used to detect larger signals. A highly stable laser diode is needed as a source and even small wavelength drifts due to temperature fluctuations can degrade the strain sensitivity. Expensive optical isolators may have to be employed to eliminate back-reflections from the EFPI cavity and parasitic cavities at connectors causing fluctuations in the laser wavelength [2.47, 2.48].

An intrinsic Fabry-Perot Interferometric sensor is an all-fibre sensor composed of two partial reflectors inside the fibre. The length of fibre between the two reflectors acts as the sensor and by control of their reflectivities sensor multiplexing can be achieved [2.49, 2.50, 2.51].

Compared to their extrinsic counterparts, IFPI sensors are usually more difficult and expensive to fabricate due to the equipment needed, they have found applicability for distributed sensing and in harsh environments where an all fibre solution is preferable [2.52].

2.5.6. *Distributed sensing*

In addition to point sensing, distributed sensing techniques also exist allowing measurements to be taken continuously along a fibre. Many parameters (strain, temperature, compression etc.) can be detected along the length of an optical fibre using time-of-flight information with an optical time-domain reflectometer technique. Backscattered radiation from defects is detected providing a detailed picture of the attenuation mechanisms or other inhomogeneities in the fibre as a function of length down the fibre. The backscattered light consists of different spectral components due to different interaction mechanisms including Rayleigh, Brillouin and Raman peaks as shown in Figure 2.10.
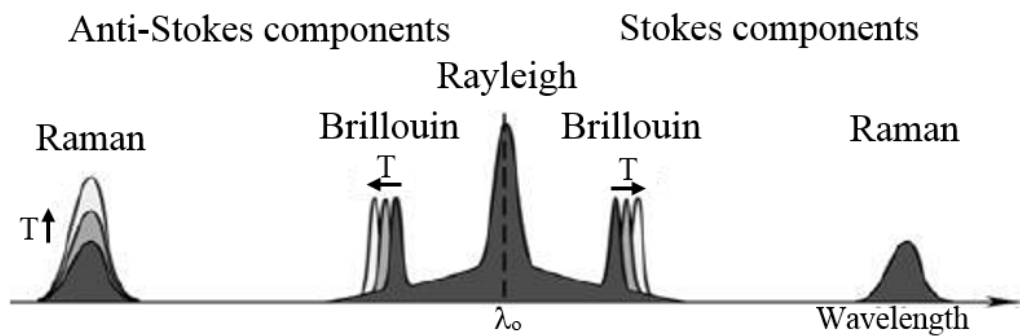

Figure 2.10. Spectral components of backscattered radiation in an optical fibre. The high intensity Rayleigh component is unshifted, one Raman component is red-shifted while blue-shifted component has a temperature dependent intensity. The wavelength of the Brillouin component is also temperature dependent [Adapted from 2.53]

As the strongest interaction, the Rayleigh component can be used to detect breaks and inhomogeneity in the fibre such as refractive index fluctuations. A small percentage of photons are Raman scattered exchanging energy with the molecular energy levels in the fibre producing Stokes photons (lower energy) and anti-Stokes photons (higher energy). The anti-Stokes interaction is dependent on local temperature and therefore by taking a ratio of these two components a temperature profile along the fibre can be determined. This system can be used over distances upto 50 km with a resolution of 0.1 °C [2.53].

Brillouin scattering occurs when light travelling down the fibre interacts with time dependent density fluctuations such as phonons. The Brillouin component can be used in an alternative technique known as Brillouin optical time domain reflectometers to resolve the strain or temperature from a single pulse [2.54]. Brillouin optical time domain analysis, however, uses stimulated Brillouin scatter. Brillouin scattering occurs between the optical pulse and the acoustic waves present in the silica fibre producing frequency shifted components. These Brillouin techniques are frequency based and as

such are more accurate and reliable in the long term than the intensity based Raman techniques which are affected by sensor degradation. True distributed temperature and strain sensing using Brillouin scattering has been developed to the point of commercial availability and is used in application areas such as pipeline, bore hole and geophysical monitoring with spatial resolutions of the order of 1 m, for fibre lengths of upto a few km or even upto 20 km with lower spatial fidelity [2.55]. As such this technique is unsuitable for short range, high fidelity sensing such as for SHM of aircraft.

An alternative Brillouin technique based on coherence can be used to give higher resolution over a shorter range. This technique is based on Brillouin loss and uses two counterpropagating laser beams; a combination continuous and pulsed light beam as the probe beam and a continuous pump beam which exchange energy through an induced acoustic field. Using this technique an accuracy of 15 $\mu\varepsilon$ and a temperature resolution of 1.3 °C were shown along with a crack detection system capable of detecting centimetre cracks [2.56].

Optical backscatter reflectometry (OBR) using Rayleigh scattering bridges the gap in sensitivity between Brillouin scattering distributed sensing techniques and FBG based sensing. This technique allows very high resolution measurement of distributed Rayleigh backscatter along a single mode optical fibre and records a 'finger print' scatter pattern as a function of length. Strain and temperature variations result in a shift of the periodicity of this fingerprint and the magnitude and location of these perturbations can be recovered with suitable algorithms with a sub-mm resolution along with sensitivities of a fraction of 1 °C and a few microstrain with fibre lengths of upto 70 m [2.57].

Advantages of distributed sensing techniques when compared to point sensing include fewer requirements for fibre preparation, increased range and the possibility to sense in any section of the fibre. However, they require more complex information handling, have a slower response time and usually a higher input optical power requirement.

2.5.7. *Sensor choice*

For the design of a sensor system the target performance specifications must be identified to allow the best choice of sensor and system architecture to be made. The required sampling rate is an important consideration, some sensors are only suitable for quasi-static systems while others can be interrogated at high frequency and can be used to detect transient events. For instance, FBGs interrogated using a swept laser

interrogator typically have a bandwidth of between a few Hz to 1 kHz [2.58] while a fibre Fabry-Perot sensor may have a bandwidth of 100 kHz to 1 MHz depending on the signal processing [2.59]. The operational temperature range of the sensor is also important in some situations such as in aircraft where both low and high temperatures can be experienced. This is also a concern for the signal processors which may be operating in uncontrolled avionics bays.

The maximum and minimum detectable strains (or other parameter of interest) are also important as this will define which sensors can be used in a given application and will also influence multiplexing choices. The reliability and lifetime needed for the sensors will also have to be taken into account which will depend on the conditions they are expected to operate in. For some applications sensors will be subject to strong vibrations and accelerations which would make some sensing architectures unreliable.

Another factor is the ambient noise level which is especially important for sensors designed to detect sound such as acoustic emission based detection of defects in which case the frequency of the various signals becomes important to allow differentiation between signal and noise background.

A further important consideration is the size of the area to be interrogated, large structures such as pipelines will either require a distributed sensing system or a multiplexed set of hundreds or thousands of sensors which will limit the possible sensor and interrogation techniques. If the area is a small, safety critical area then a technique using one or several sensors will be preferable and would allow greater sensitivity or larger bandwidth to be achieved.

Fibre Bragg gratings are the most commonly used optical sensors and their characteristics make them the best choice for the task of impact detection in an aerospace environment. They can be easily multiplexed allowing many sensors to be used to cover all necessary areas of interest in contrast to some sensors such as interferometric sensors that are difficult to multiplex. If certain areas require higher fidelity monitoring then more sensors can be placed in that area. An important consideration is that of measurement speed, and therefore temporal bandwidth, distributed sensing systems cover large areas excellently but their measurement speed is usually limited and limits their applicability for dynamic measurements. FBGs will therefore form the basis for the majority of the optical sensing presented in this thesis.

2.6. Comparison of Electrical and Optical Fibre Sensors

A major advantage of optical fibre sensors over electrical sensors such as strain gauges is that many designs can be wavelength encoded so a loss of intensity as the signal passes along the fibre does not correspond to a drop in the strain measured at the end.

Many fibre optic sensors can be written onto a single fibre; this technique is known as multiplexing and allows a sensor network to be created without the need for separate connections and cables for each sensor.

Strain gauges can also be affected by corrosion and debonding leading to degradation of the signal quality. Optical fibre sensors are expected to offer improved reliability and accuracy as the technology matures. Due to their dielectric nature, optical fibre sensors are immune to electromagnetic interference allowing them to operate in places that would be unsuitable or impractical for electrical sensors. This is very important in some military aircraft applications where the platform has a suite of electromagnetic devices such as radar and electronic counter measures (ECM) which can all interfere with each other. In some situations where there is a fire or explosion risk electrical wiring is undesirable and therefore using optical fibres which carry no current is preferable. In many aircraft the wings include the fuel tank and as such adding an electrical sensor network to this vulnerable area would risk ignition from a spark due to faulty wiring. Fibre optic sensors can have all connections, power and signal processing at a non-critical location and only the electrically inert fibre is needed at the sensing location which leads to a system which is intrinsically safer.

They also have very long range due to the low loss of optical fibres allowing fibres to reach to the end of the wing without the need for amplifiers or repeaters and without excess noise pickup. This reduces the weight, cost and potential for complications due to extra electrical devices in the wings as discussed above. A large reduction in weight is anticipated over electrical wiring due to the low mass of optical fibre and the need for fewer cables due to their multiplexing capabilities which is advantageous in aerospace structures and other weight critical designs.

The embedding of sensors into the structure is an important concern, sensors must accurately register the strain, temperature etc. of the structure at the sensors location. Embedding optical fibres between layers of the composite during manufacture is an attractive solution which ensures good coupling between the strain in the structure and the fibre. The effect of the embedded fibres on the structure is another important

consideration as they should not harm the microstructure and cause substandard performance. It has been found that by aligning the optical fibre with the reinforcing fibres in the composite the impact of the fibre inclusion is reduced [2.60].

Initial uptake of fibre optic sensing technologies was slow due to the higher costs involved; however the widespread adoption of fibre optic technology in the telecommunications industry has increased the availability of many key components. This has advanced the technology and driven down the costs to a level where fibre optic sensing is a credible and inviting option.

This information is summarised in Table 2.1.

Table 2.1. Comparison of fibre optic and electrical sensors.

	Fibre Optic	Electrical
Multiplexing	Hundreds of Sensors *	One
Lifetime	Expected Good	Average
Range	Extremely Long	Short
Accuracy	Excellent	Excellent
Electromagnetic Interference	None	Yes
Explosion Risk	None	Yes
Weight	Very Low	High
Initial Costs	High	Low

* With some types of sensors and interrogation schemes

2.7. Interrogation Systems

2.7.1. Comparison of techniques

A wavelength detection system must be used to interrogate the FBG sensors. To be of commercial use this must use small, packaged electro-optics units rather than laboratory based equipment such as optical spectrum analysers and large, tunable lasers. An early demonstrated system in 1992 by Melle *et al.* used a simple ratiometric technique [2.61].

The narrowband reflected signal from the Bragg grating is split into two beams of equal intensity. One beam is filtered by an edge filter with a transmittance which has a linear wavelength dependence over the full scale measurement range of the signal and is then detected by a photodetector. This is illustrated in Figure 2.11; as the Bragg grating spectrum shifts horizontally between the dashed positions the relative overlap with the edge filter varies. The proportion of light emerging from the edge filter to the detector therefore varies along with the strain the grating experiences.
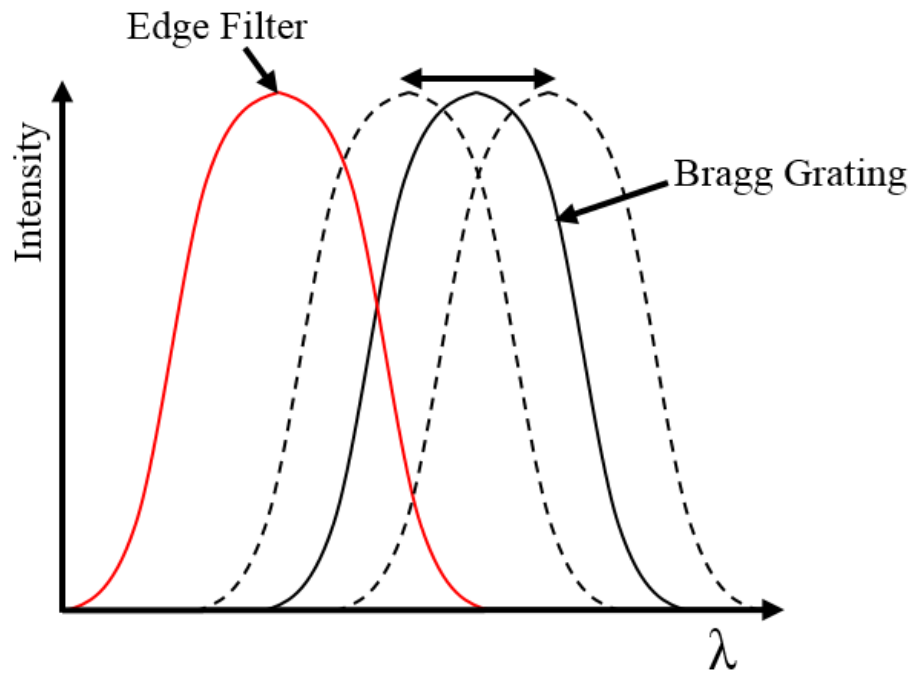
Figure 2.11. Bragg grating and edge filter spectra. As the grating spectrum shifts horizontally into the dashed positions the relative overlap with the edge filter varies.

The other beam is used as a reference signal and is measured unfiltered by a similar photodetector. The ratio of the filtered beam over the reference provides the wavelength information of the signal without being affected by the intensity variations of the source spectrum, power fluctuations or attenuation by fibres and connectors. A relatively limited sensitivity is obtained due to the use of bulk-optic filter/collimation components and associated alignment stability.
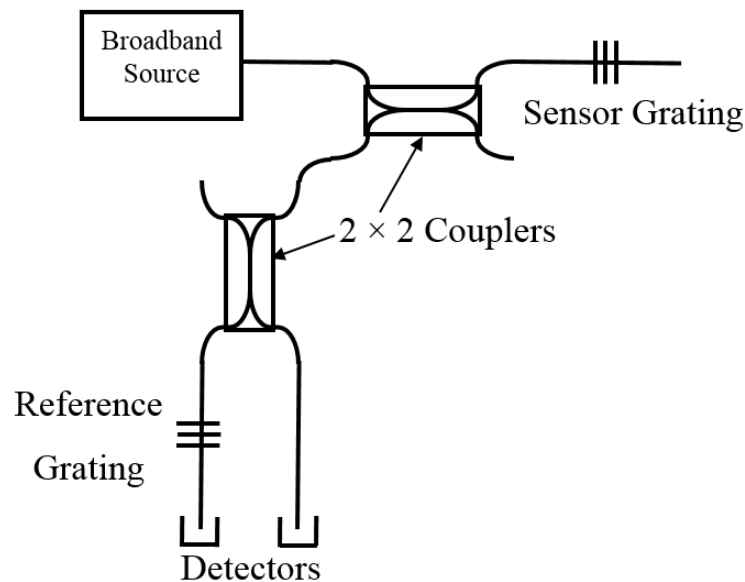

Figure 2.12. Diagram of a simple identical chirped grating interrogation setup with a broadband source, a sensing grating and reference grating.

A similar interrogation scheme can be created using all fibre components to overcome this issue. For instance, demodulation can be achieved by the mismatching of two identical, broadband, chirped gratings known as identical chirped grating interrogation (ICGI). This technique does not require high quality piezoelectric actuators or tunable filters and as such is very attractive for aerospace applications as it is a passive demodulation technique with no moving parts. Figure 2.12 illustrates the principle of the technique; light from a broadband source, incident on the sensor grating, is reflected to the reference grating, which acts as a rejection filter minimally transmitting to the detector. When a perturbation acts on the grating the spectral profile will be linearly shifted causing a fraction of the light from the sensing grating to fall outside of the rejection band of the reference grating and be transmitted to the detector [2.62]. The quasi-square reflection profiles permit a linear relationship between the change in strain or temperature encoded in the Bragg wavelength and the intensity of light transmitted by the reference grating. The ICGI can be extended to a multiple sensor multiplexed system with sensors arranged in serial, parallel or both. As the sensors are simultaneously interrogated, interrogation speed can be very high unlike tunable filter or switching approaches. The disadvantage is that multiple broadband sources may be required to increase total bandwidth and light intensity [2.63].

More sensors can be easily interrogated with the use of a fibre device with a wavelength dependent transfer function such as a fibre wavelength-division multiplexing (WDM) coupler or biconical fibre filters.
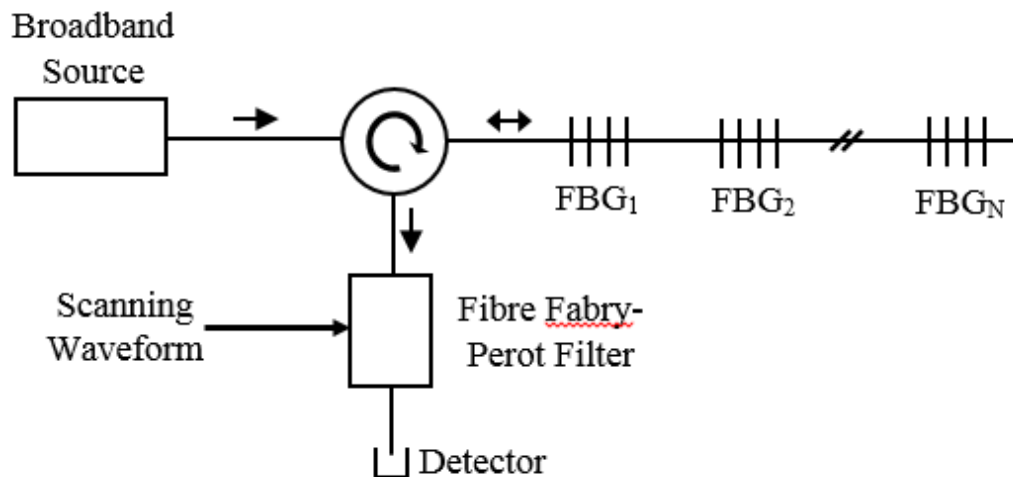

Figure 2.13. A typical fibre Fabry-Perot filter based interrogation system allowing a narrowband wavelength component to pass to the detector which is dependent on the spacing in the FP filter which is controlled by the applied voltage.

One of the most successful techniques for FBG interrogation is based on the use of a tunable passband filter to track the FBG signal. Fabry-Perot (FP) filters, acousto-optic filters and FBG filters are all suitable for this technique; however FP filters are the most common. Figure 2.13 shows a typical fibre FP filter based interrogation system that allows a narrowband wavelength component to pass to the detector which is dependent on the spacing of the mirrors in the FP filter. The mirror spacing is varied by piezoelectric stacks which are controlled by a scanning waveform, as the filter is tuned the passband moves over the return signals from the gratings and the voltage and optical signal recorded at each point to produce a spectrum. Typical characteristics of this type of FP are a free spectral range (FSR) of 50 nm and a filter passband of ~0.3 nm. This allows as many as 16 sensors to be used with ~3 nm spacing, allowing over $2000\mu\varepsilon$ strain range before crosstalk. In this case using a 16 bit digital-to-analog converter produces a minimum resolvable wavelength shift of ~0.8 pm which is equivalent to a strain resolution of 0.8 μstrain and with scan rates of upto ~1 kHz [2.36].

An alternative interrogation method is through parallel detection of the entire spectrum with a linear-array detector such as a charge coupled device (CCD) [2.64, 2.65]. In this system a dispersive element such as a prism or grating converts wavelength into position as the degree to which the light is diffracted will depend on the wavelength. This light distribution is incident onto a CCD detector which detects the intensity as a function of position and therefore a spectrum can be produced. The main advantage of this method is that all of the light is collected over the whole scan period for every FBG which is in contrast to scanned detection techniques which have a much lower detectable energy caused by the scanning filter.

Fourier transform spectroscopy (FTS) is another form of direct spectroscopic tool for analysing the return signals. The signal from an array of FBGs is fed into an interferometer in which one arm has the length linearly changed creating an interferogram at the output. The Fourier transform of the interferogram is then taken to obtain an accurate representation of the source spectra. Fibre Fourier transform spectroscopy systems were developed to remove the problems inherent in bulk optics systems for portable use. Instead of mirrors mounted on piezostacks which are inaccurate in an environment which may include large amounts of vibration and temperature variation a fibre stretcher is used to vary the length of the reference arm. No bulk optical components or speciality fibres are required for this system, providing the potential for a low cost, robust and compact Fourier transform spectrometer with a

resolution of ~0.015 nm [2.66]. However, due to the fibre stretching apparatus the measurement speed will be limited meaning that this technique will not capture the full dynamics of an impact.

Table 2.2 shows a comparison of some interrogation techniques for wavelength demodulation [adapted from 2.67].

Table 2.2. Summary of Bragg grating sensor interrogation techniques [adapted from 2.67].

	Edge Filter	Tunable Filter	Interferometric	Tunable Laser	CCD-Spectrometer
Range to resolution	10^2-10^3	10^3-10^4	10^3-10^4	10^3-10^5	10^3-10^4
Measurement speed	> MHz	~1 kHz	> 100 kHz	> MHz	~1 kHz
WDM compatibility	Low	High	High	Low	High
Potential cost	Low	Medium	Low	High	Medium

2.7.2. Light sources

Interferometric sensors are generally illuminated by highly coherent laser sources such as single mode laser diodes. Fibre Bragg gratings however usually require a broadband source for most applications. One commonly used source is an edge emitting light emitting diode (ELED) which have a structure similar to an edge emitting semiconductor laser in that they emit from the edge of a cleaved wafer where the active region meets the cleaved surface [2.68]. This structure allows more efficient fibre coupling than surface emitting diodes. They are cheap, lower power sources with a high bandwidth sufficient for some sensing applications.

A variant of this device is the superluminescent diode (SLD), which emits light through luminescence which experiences significant optical gain within the diode due to waveguiding techniques (superluminescence) [2.69]. An SLD is similar in construction to a laser diode however it lacks optical feedback preventing lasing from occurring. They have very high spatial coherence and beam quality and hence can easily be coupled into an optical fibre.

Amplified spontaneous emission sources (ASE) are optical amplifiers in which spontaneous emission, or fluorescence, is amplified in a single or double pass of the device to give an output which is primarily due to stimulated emission but is broadband. ASE sources in general produce low coherence emission with high brightness which can be important for multiplexing large numbers of sensors. They also exhibit excellent

wavelength stability which is crucial for systems measuring wavelength shifts with high accuracy [2.70].

Tunable fibre lasers typically use rare-earth doped fibres as the gain medium with a tunable reflector to create optical feedback for the correct wavelength. This is typically achieved with a fibre Bragg grating which has a period tunable via application of strain or temperature. They are tunable over a range of upto 10 nm and a high output power but at a relatively high cost compared to other light sources [2.71].

An alternative type of tunable source is an external cavity diode laser which consists of a diode laser and a laser resonator [2.72]. In order to tune the wavelength of the output a diffraction grating is typically used in the external resonator which can be rotated to vary the output wavelength. State of the art commercial systems are available which can be tuned over 80 nm with a sweep frequency of 1 kHz [2.73].

Table 2.3 shows a summary of light sources used for optical fibre sensing comparing their optical power, FWHM bandwidth and cost.

Table 2.3. Summary light sources used for illumination of optical fibre sensors [2.28].

	ELED	SLD	ASE	TFL
Optical Power*	1-10µW	0.1-2mW	1-10mW	0.1-10mW
FWHM Bandwidth	40-100nm	15-30nm	20-40nm	1-10nm**
Device Cost	Low	Medium	High	High

* Optical power coupled into a single mode fibre

** Tunable range

2.7.3. Light amplification

In some situations it is preferable to amplify an optical signal, either to allow more accurate detection or when high intensities are required such as for non-linear effects. The two most common approaches used to achieve this are erbium doped fibre amplifiers (EDFA) and semiconductor optical amplifiers (SOA). An EDFA features an optical fibre with an erbium doped core, which is then pumped with a lightsource with a wavelength of 980 nm or 1450 nm. The pump light excites erbium ions (Er^{3+}) into a higher energy state which allows them to amplify light in the important 1550 nm wavelength region [2.74, 2.75]. The 1550 nm wavelength region is commonly used for telecommunications and many other applications due to the extremely low loss allowing long fibre links to be created. For further information on EDFAs see [2.76] as well as further theory relating to erbium doped fibre in §6.2.

An SOA is very similar in structure to a laser diode except there is no optical feedback as the end mirrors are replaced with anti-reflection coatings. The semiconductor gain medium is pumped with an electric current and typically operates at signal wavelengths near 1300 nm or 1500 nm. For further information on SOAs see [2.77].

There are several differences between SOA and EDFA devices which should be considered when choosing the best device for a given application. An SOA is simpler and much more compact however the saturation power is a lot lower than an EDFA and the noise figure is often higher due to losses at the glass/silicon interfaces. SOAs also have a smaller gain bandwidth although devices can be made to operate in different wavelength regions. SOAs have a much smaller upper-state lifetime which allows the gain to react to changes in pump or signal power in nanoseconds as opposed to milliseconds with an EDFA, which allows SOAs to be used as amplitude modulators at GHz rates. Finally, SOAs are polarizarion-sensitive and can have larger nonlinear distortions such as four-wave mixing and self-phase modulation. In summary, an SOA is typically a cheaper and simpler device but if very high powers or exceptional noise performance are required then an EDFA may be a better solution.

2.8. Multiplexing

2.8.1. Wavelength division multiplexing

Many sensors can be embedded into a single optical fibre to create a simple sensor network without the need for many fibres and connectors. In this case a method of separating the signals from each sensor must be employed; one such method is wavelength division multiplexing (WDM). The source spectrum is separated into bands and a band is assigned to each sensor, illustrated in Figure 2.14. For the case of grating based sensors each sensor is then written with a refractive index modulation such that it reflects this wavelength band. To measure parameters such as strain, the displacement of the central peak in wavelength space due to the applied strain is used and as such the band assigned to each sensor must be sufficient to measure the maximum strain expected [2.78].
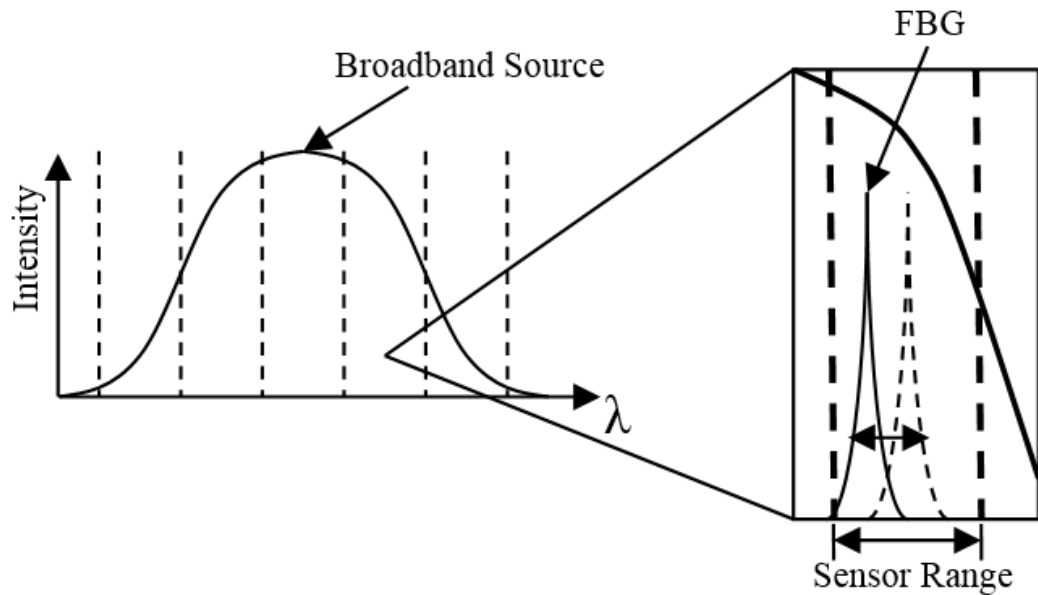
Figure 2.14. A lightsource spectrum divided into bands for wavelength division multiplexing. For each band a sensor is assigned which is written (for the case of grating based sensors) so that the central wavelength of its stopband (dashed curve) is in the middle of the band.

2.8.2. *Time-division multiplexing*

In time-division multiplexing (TDM) each signal may occupy the entire bandwidth of the source spectrum but each sensor has a limited time window in which the reflected light from that sensor is sampled. Light arriving from the sensor outside of that window will contribute to crosstalk in the next sensor window so care must be taken to separate the signals via time-of-flight methods and a sufficient delay between windows.
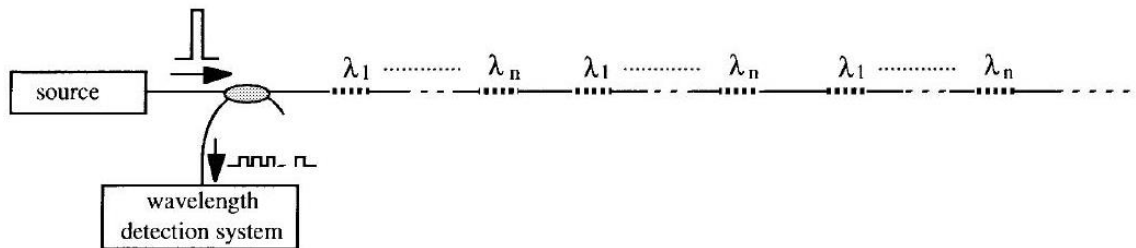

Figure 2.15. A WDM/TDM system with the source spectrum split between sensors 1 to n in a WDM scheme. Several sets of sensors are then multiplexed using time-of-flight to create a hybrid WDM/TDM system capable of supporting a large number of sensors [2.36]

Wavelength division multiplexing allows tens of sensors per fibre by splitting up the spectrum of the source between the sensors. TDM can multiply this number several times by re-using the source spectrum. In a mixed WDM/TDM system several arrays of WDM sensors are embedded in a fibre at progressively greater distance as shown in Figure 2.15. A short pulse of light is used which will cause a set of reflections to be detected at a range of times dependent on the distance to the sensor. For the case of FBGs their reflectivities are specifically designed to be low so that only a small portion

40

of the intensity is reflected, allowing light to propagate through and reach the subsequent gratings. By configuring the detector to acquire the signal for each set of sensors within the window of time corresponding to the time of flight from the sensor the signal from each sensor array can be demodulated [2.79]. In such a way large sensor systems can be created for large structures and produce a quasi-distributed sensor system [2.80, 2.81]. As the light is sampled for a small amount of time the detected light level will be much lower requiring more sensitive detectors. In addition, the time it takes to sample all of the sensors will put a limit on the sample rate of the system which will reduce the temporal bandwidth.

2.8.3. *Spectrally coded multiplexing*

Spectrally coded multiplexing (SCM) is a technique which adds a further degree of freedom and provides additional flexibility and channel capability needed for fibre and fibre grating based sensor systems. For large civil structures such as bridges and tunnels a SHM system could easily require hundreds of sensors even for single parameter monitoring. For multiple parameter monitoring the required amount of multiplexing will increase and as such traditional multiplexing techniques such as TDM and WDM will not provide a sufficient channel count. To demultiplex a sensor it must have at least one particular parameter or feature that is uniquely identifiable to allow the signal corresponding to that sensor to be separable from that of other sensors. For TDM this is the time of arrival of the sensor signal at the detector. For SCM this identifiable parameter is in some way coded into the spectral signature allowing the signal to be uniquely identifiable even if they are spectrally overlapped with the same Bragg wavelength and bandwidth [2.82].

This can be achieved in several ways, one technique uses chirped Bragg gratings which have had a unique index modulation function applied to them such that their reflection spectra are amplitude modulated. Each sensor is identifiable by the number of periods of its amplitude modulation and as such can be distinguished even when completely spectrally overlapped.

SCM is fully compatible with TDM and WDM and can be used in conjunction to significantly increase the amount of channels available which is very useful for long distance sensing and large structures.

2.8.4. *Further multiplexing techniques*

In addition to these methods, other multiplexing techniques also exist including coherence multiplexing and frequency–division multiplexing. Coherence multiplexing can be used to interrogate interferometric sensors by using sensors with varying cavity lengths and then altering the path length of the system to allow constructive interference at each sensor in turn [2.83]. Frequency-division multiplexing can be used with similar sensors by modulating the frequency of the source so that each sensor in turn matches the constructive interference condition due to the length of the cavity. These techniques have not thus far found widespread applicability in structural health monitoring [2.84].

2.9. Measurements

Optical fibre sensors have found applications in a variety of structural health monitoring applications in the aerospace sector and beyond. Operational Load Monitoring (OLM) systems can be created by bonding optical fibre sensors onto the skin of an aircraft to monitor the loads experienced by the structure during use [2.32]. In this way it can be used for prognosis, which uses information about the lifetime of the various components and usage data from the OLM system to predict the aircraft degradation. In addition, optical fibre sensors can be used for impact detection by measuring the impact location and energy and hence can predict damage as damage is correlated with impact energy. Unlike electrical strain gauges optical fibre sensors can also be used to measure temperature and as such can be used to document the conditions in which the structure is operating and also any temperature anomalies which could be indicative of a problem such as electrical damage. Optical fibre sensors can also be used for acoustic emission detection to detect the characteristic signals emitted by defects when they are loaded.

An important consideration which places restrictions on the type of interrogation technique to be used is the measurement speed required. The frequency content of strain signals for various applications varies greatly, a comparison is shown in Figure 2.16 along with the FBG interrogation techniques applicable for each frequency range [2.10].
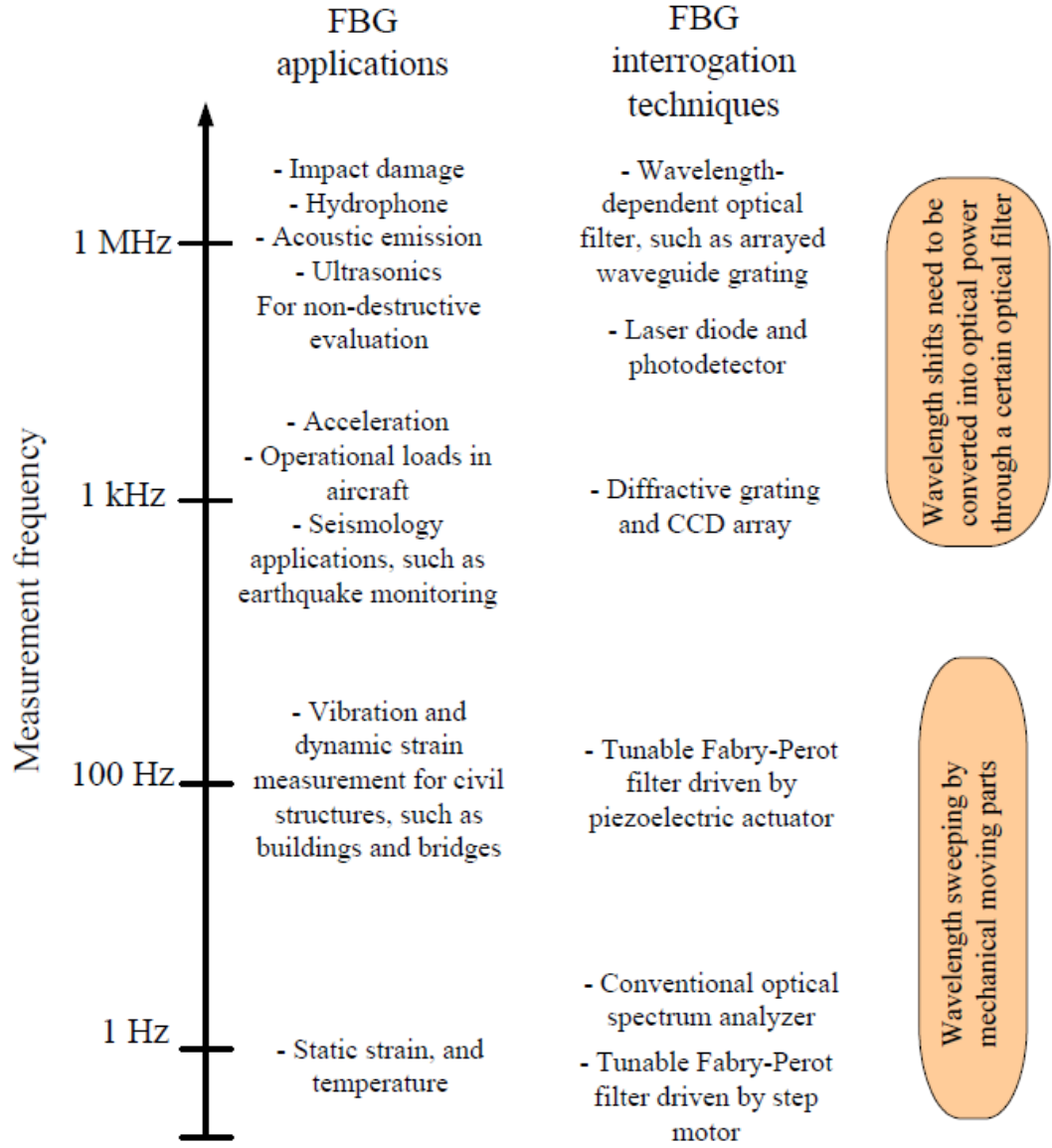
Figure 2.16. Comparison of the measurement frequency required for various applications and the interrogation techniques suitable for these frequencies [2.10].

2.9.1. *Operational load monitoring*

Operational load monitoring is the act of investigating the characteristics of a structure in its normal operating environment, typically including the installation of strain gauges to measure loads. An FBG sensor can be used to detect strain due to the change in the refractive index grating spacing, Λ, as well as the refractive index when the grating is strained. As equation (2.4) shows, the change in the grating spacing causes a shift in the wavelength of light reflected by the sensor. Therefore by measuring the fractional change in peak reflection wavelength, $\Delta\lambda$, the fractional change in Λ, and therefore strain, can be determined by

$$\frac{\Delta\lambda}{\lambda} = \left(1 - \rho_\alpha\right)\frac{\Delta\Lambda}{\Lambda} = \left(1 - \rho_\alpha\right)\varepsilon \tag{2.9}$$

where ρ_α is the photoelastic coefficient of the fibre given by

$$\rho_\alpha = \frac{n^2}{2}\left[\rho_{12} - \nu(\rho_{11} + \rho_{12})\right] \tag{2.10}$$

where ρ_{11} and ρ_{12} are the components of the fibre-optic strain tensor and ν is Poisson's ratio [2.85]. Typical values are $\rho_{11} = 0.12$, $\rho_{12} = 0.275$ and $\nu = 0.17$ [2.86].

A significant limitation of FBG sensors is their dual sensitivity to strain and temperature, for a typical aerospace temperature operating range of 150 °C thermal effects contribute an additional apparent strain of upto 1000 μstrain. One solution is to place a sensor in thermal equilibrium with the structure but keep it isolated from changes in strain allowing it to be used as a reference point for thermal compensation [2.87]; this is analogous to the inclusion of compensating gauges in bridge circuits for electrical strain gauges. This is commonly achieved using a sensor patch of 4 sensors, 3 strain sensors are arranged with principal sensitivities aligned along axes separated by 120° and the 4th sensor is strain isolated. A minimum of 3 independent strain measurements along differing angles are required to resolve all principal directions of planar strain and thereby fully determine the strain at a location [2.88, 2.89]. This technique provides some compensation for thermal fluctuations when measuring strain however it is not always a desirable system design choice. Another technique involves the use of two collocated sensors with very different responses to strain and temperature [2.90]. In this case, the ratio of the strain responses is very different to that of the temperature allowing the temperature and strain to be determined at each location without requiring that a section of the fibre be isolated. Backing patches are often used to act as a substrate to hold the fibre sensor array together and transmit strain from the underlying structure to the optical fibre itself. The shear modulus of the backing material must be large enough to faithfully transmit strain from the structure to the sensors especially at elevated temperatures. It also has to balance rigidity with the ability to comply with curved surfaces.

Strain sensing can also be achieved using chirped Bragg gratings based on the change in the effective change in reflection point, $\delta\lambda_b$, which is given by

$$\frac{\delta\lambda_b}{\delta l} = -\frac{\lambda}{\Delta\lambda_c} \tag{2.11}$$

where $\Delta\lambda_C$ is the width in wavelength space of the bandpass filter caused by the chirped grating. δl is the optical length change for a fibre of length B which is given by

$$\delta l = \Delta\varepsilon B\zeta \qquad (2.12)$$

and ζ is a constant determined by the photoelastic properties of the fibre. Due to the fact that $\delta\lambda_b >> \delta l$ and $\lambda >> \delta\lambda_C$ the chirped Bragg grating gives a very high response to changes in strain and therefore strain sensing with chirped gratings can be achieved with a high sensitivity [2.48].

By embedding optical fibre sensors in a composite structure or bonding to the surface in a retrofit procedure allows an operational load monitoring system to be created. The sensors monitor the local strain and using multiplexing techniques a sensor network is created allowing the strain to be measured at many points across the structure. This OLM system can then be used to monitor the loads experienced by individual sections of the aircraft allowing a prognostic approach to be taken to predict the lifetime of components due to their usage.

2.9.2. Temperature

A fibre Bragg gratings sensitivity is given by

$$\frac{\Delta\lambda_B}{\lambda_B} = C_\varepsilon\varepsilon_z + C_T\Delta T \qquad (2.13)$$

where $\Delta\lambda$ is the change in the Bragg wavelength, λ due to a temperature change ΔT and strain ε_z, C_ε and C_T are material constants relating the materials response to strain and temperature respectively and can be determined by experiment [2.91]. The temperature response of a FBG is typically 10 pm/°C. Temperature measurements can therefore be made by isolating an FBG from strain to leave only the temperature component. This measurement of temperature can be used as a reference for another sensor measuring strain or used directly to measure the temperature variation over a structure. This can be useful to identify extraordinary temperatures which could be indicative of a failure in the electrical wiring or similar. In addition, recording the temperatures experienced by areas of the structure during use can enable prognostic techniques to be used based on performance tests of components at high and low temperatures.

2.9.3. Acoustic Emission

Processes such as cracking, deformation, debonding and delamination all produce localized transient changes in stored elastic energy [2.92]. This change in energy causes transient elastic waves to be created in a process known as acoustic emission (AE). Therefore by detecting these acoustic emission events and by measuring the rate of occurrence damaged areas which are likely to fail can be located. These internal sources of AE represent a passive, static sensing technique as the AE sources regularly emit. As such a passive AE system need not have the same high level of detection reliability required for an impact detection system as there are many opportunities to detect an AE source as it re-emits.

When compared to common temperature and strain sensing systems the requirements for an AE system are different. Firstly, the frequency is much higher with typical frequencies of acoustic emissions in the range of 100 kHz to 1 MHz. Additionally, the strain levels are lower, typically in the microstrain order of magnitude.

One technique for detecting acoustic emission uses fibre Bragg gratings interrogated by a narrow-linewidth laser diode [2.93]. A typical Bragg reflectance spectrum is shown in Figure 2.17, the optical power reflected by the grating, P_r, is related to the input power P_{in} by

$$P_r(\lambda) = P_{in}R(\lambda) \tag{2.14}$$

where $R(\lambda)$ represents the reflectance spectrum of the grating. This spectrum is approximated to be linear between ~20-80% and by applying the interrogation technique to this part of the system a linear dependence between the reflected power and wavelength can be achieved. In this region on both sides of the peak the slope is a constant given by the value of $dR/d\lambda$. The laser is tuned to the wavelength at FWHM labelled as λ_0 to give the maximum range of detection in both directions. The acoustic wave travelling through the structure will create a time dependent strain field, $\varepsilon(t)$, which causes a shift in the reflectance spectrum. This shift corresponds linearly to the power reflected and therefore captured by a detector placed along the return line. Hence the detected power is linear with strain with high sensitivity allowing detection of acoustic emission events characteristic of damage.

AE detection as a SHM technique has several advantages such as high sensitivity, real-time measurement, the ability to locate damage and sensitivity to any mechanism that produces stress waves [2.94].
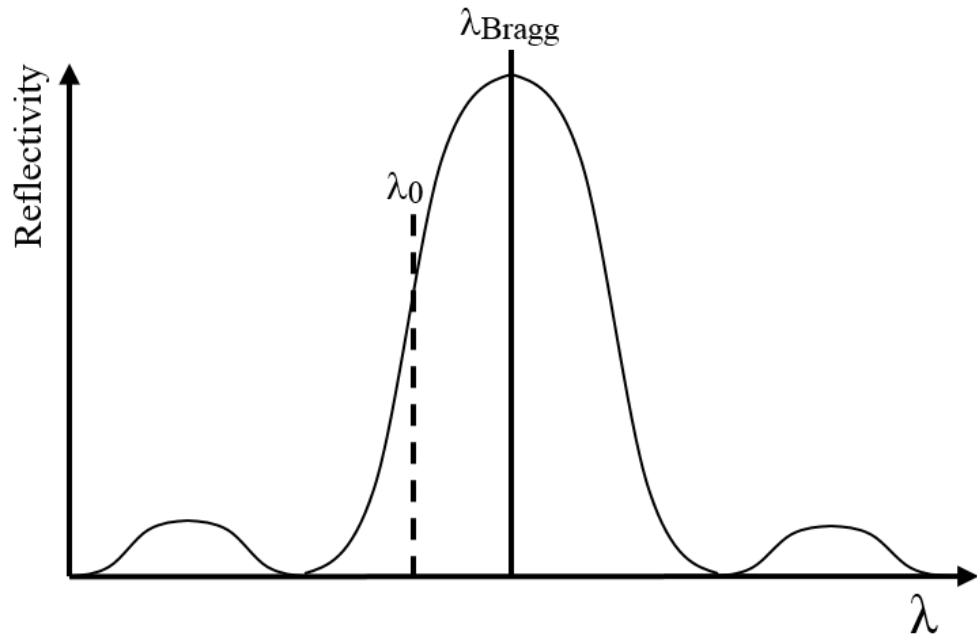
Figure 2.17. The reflectance spectrum of an FBG showing the initial position of the laser, λ_0, to allow maximum detection range in both directions.

2.9.4. Impact detection

As well as the detection of internal events such as cracking, acoustic emission can be used as a technique for impact detection. When a composite structure is impacted, an acousto-ultrasonic wave spreads across the surface which can be detected by sensors as above. The impact loading also give rise to local and global deformation, the mechanical deformation changing the Bragg wavelength considerably makes it difficult for a bonded FBG to detect the pure acousto-ultrasonic wave. FBG sensors can be attached to a structure in certain ways so that they are strain-free and thus capable of detecting the acousto-ultrasonic wave without mechanical strain-induced Bragg wavelength change [2.95]. Alternatively, as long as the interrogation scheme is capable of accommodating the full strain change induced by the impact then the signal can be high-pass filtered to remove the low frequency mechanical deformation and leave the acousto-ultrasonic wave signal [2.5].

The type of sensor is an important consideration when analysing an impact induced signal. A typical piezoelectric transducer is an out-of-plane sensor and will have the greatest response to the flexural mode wave. However, an FBG sensor is an in-plane sensor and will have the greatest response to the longitudinal mode wave. A further consideration is the non-resonant nature of the FBG sensor which differs from the piezoelectric transducer which will have a degree of resonance which depends on the

47

sensor construction as described in §2.3.2. These two features will result in the same impact signal appearing to be different when captured by the two sensor types [2.95].

Impact signals are reported to contain frequency components upto 100 kHz [2.96], in order to capture these components high speed FBG interrogation techniques must be used. Optical spectrum analysers and other techniques that employ scanning components cannot operate fast enough and some method of passive wavelength to intensity conversion is usually required. This may be achieved with a tunable laser as described for acoustic emission detection in §2.9.3 although the maximum strain occurring during the impact needs to be considered as this will be significantly larger than a standard acoustic emission. The maximum strain will depend on many factors including the energy of the impact, the angle of the impact, the location in relation to the support structure beneath the panel as well as other factors.

By measuring the time of arrival of the leading edge of the signal and comparing to each of the other sensors a relative timing can be determined. Using this information the location of the impact can be determined using a triangulation method. The energy of the impact can also be ascertained by measuring the intensity of the signal detected by the sensor and correcting for the attenuation due to the distance travelled through the structure.

This type of system is very useful for aircraft to allow collisions to be detected during use such as impacts from stones on the runway, birdstrike or potentially gunfire. This will allow the pilot to decide to take appropriate action in the case of an impact magnitude likely to have caused damage or if less severe the location can be stored to be investigated for damage upon landing. This kind of impact detection system is even more crucial for the use of unmanned aerial vehicles (UAVs) which require a mechanism to detect that they have been hit allowing the control mechanisms to take action appropriate to the situation.

2.10. Conclusion

Changes in the aerospace sector over the past few decades including increased use of composites and a move towards upgrading and refitting existing aircraft has created a need for a different approach to structural health monitoring. With increasing demand the standard manual inspection techniques such as ultrasonic non-destructive testing have become too time consuming and costly. 'Smart' structures which have on-board sensors and can detect and analyse their own structural health are desired.

Optical fibre sensors are a prime candidate for use in smart structures due to their low mass, immunity to electromagnetic interference and multiplexing ability allowing sensor networks to be created. Many different types of optical fibre sensor exist, such as intensity based sensors, fibre Bragg gratings, long period gratings and interferometric sensors. In addition to these point sensing techniques distributed sensing techniques exist such as optical time domain reflectivity allowing continuous sensing over very large distance which is of use in the monitoring of bridges and pipelines. For impact detection applications FBG sensors are the most promising due to their multiplexing capability, ability to operate at high measurement speeds and high sensitivity.

Multiplexing techniques can be used to create a sensor network using a single optical fibre and lightsource; for instance by splitting up the input spectrum between sensors (wavelength division multiplexing) or by interrogating each sensor in turn (time division multiplexing) or by more advanced combinations.

These techniques can be used to make an embedded sensor network capable of operational load monitoring of an aircraft for prognostic and diagnostic purposes. This is achieved with a set of optical fibre sensors measuring the local strain at several points on the aircraft which can be used to predict the lifecycle of the aircraft as well as monitor operational abnormalities such as overloading. In addition, a sensor network can be created to detect acoustic emission signatures characteristic of damage growth such as delamination. In this way the evolution of damage on the structure can be monitored autonomously leading to condition based maintenance. Acoustic emission sensors can also be used to detect impacts on the structure, which can be located using triangulation methods which can provide early warning of likely damage due to runway collision or birdstrike.

The overall aim of the smart structure methodology is to create a structure with a system akin to a nervous system, able to sense its structural health and usage to create a safer and more reliable aircraft without the need for expensive and regular manual testing enabling the aircraft to continue operating with minimal disruption.

The techniques discussed in this chapter have focussed on the structural health monitoring application, many other optical sensing approaches exist. For further information see the following references [2.97, 2.98, 2.99].

2.11. References

[2.1] E. J. Barbero, *"Introduction to Composite Materials Design Second Edition"* (CRC Press, 2011) pp1.

[2.2] F. C. Campbell, "*Structural Composite Materials*", ASM International, Materials Park, Ohio, USA (November 30, 2010).

[2.3] L. A. Pilato, and M. J. Michno, *"Advanced Composite Materials"* (Springer-Verlag, Berlin, 1994) pp9.

[2.4] V. K. S. Choo,*"Fundamentals of Composite Materials"* (Knowen Academic Press, Delaware, 1990) pp3.

[2.5] E. I. Madaras, W. H. Prosser, and M. R. Gorman, "*Detection Of Impact Damage On Space Shuttle Structures Using Acoustic Emission*", Review of Nondestructive Evaluation Vol. **24** (2005).

[2.6] E. I. Madaras, W. H. Prosser, G. Studor, M. R. Gorman, and S. M. Ziola, "*Structural Health Monitoring of the Space Shuttle's Wing Leading Edge*", Review of Nondestructive Evaluation Vol. **25** (2006).

[2.7] U. K. Vaidya, "*Impact response of laminated and sandwich composites*", Impact Engineering of Composite Structures, CISM International Centre for Mechanical Sciences Volume 526, pp 97-191 (2011).

[2.8] H. Y. Choi, R. J. Downs and F. –K. Chang, *"A new approach toward understanding damage mechanisms and mechanics of laminated composites due to low-velocity impact: Part I Experiments,"* J. Compos. Mater. **25** pp. 992-1011 (1991).

[2.9] M. O. W. Richardson, and M. J. Wisheart, "*Review of low-velocity impact properties of composite materials*", Composites Part A **27A** pp. 1123-1131 (1996).

[2.10] H. Guo, G. Xiao, N. Mrad and J. Yao, "*Fiber Optic Sensors for Structural Health Monitoring of Air Platforms*", Sensors 2011, **11**, pp. 3687-3705 (2011).

[2.11] Z. Su, L. Ye, *"Identification of Damage Using Lamb Waves: From Fundamentals to Applications"*, (Springer Science & Business Media, 2009) pp. 15.

[2.12] J. D. N. Cheeke, *"Fundamentals and Applications of Ultrasonic Waves, Second Edition"*, CRC Press (2012) pp. 141.

[2.13] W. Thompson (Lord Kelvin), "*On the electrodynamic qualities of metals*", Proc. Roy. Soc., **146** (1856).

[2.14] A. L. Window, and G. S. Holister, "*Strain gauge technology,*", Applied Science Publishers, 1982).

[2.15] R. C. Juvinall, "*Engineering considerations of stress, strain and strength*", (McGraw-Hill, 1967).

[2.16] A. A. Vives, *"Piezoelectric Transducers and Applications",* (Springer Science & Business Media, 2008).

[2.17] J. Blitz, G. Simpson, "*Ultrasonic methods of non-destructive testing*", (Chapman and Hall, 1996).

[2.18] J. Szilard, "*Ultrasonic Testing*". (Wiley, Binghamton, USA, 1982).

[2.19] R. K. Miller, E. v.K. Hill, and P. O. Moore, "*Acoustic Emission Testing*", (American Society for Nondestructive Testing, 2005).

[2.20] S. E. Miller, and A. G. Chynoweth, "*Optical Fibre Communications*" (Academic Press, 1979).

[2.21] S. E. Miller, and I. P. Kaminov, "*Optical Fibre Communications II*" (Academic Press, 1988).

[2.22]   C. Yeh, "*Handbook of Fibre Optics, Theory and Applications*", (Academic Press, 1990).

[2.23] A. B. Lobo Ribeiro, J. L. Santos, J. M. Baptista, L. A. Ferreira, F. M. Araújo, and A. P. Leite, "*Optical Fiber Sensor Technology in Portugal*", Fiber and Integrated Optics vol. **24** (3-4) pp171-199 (2005).

[2.24] N. Lagokos, W. J. Trott, and J. A. Bucaro, "*Microbending fiber optic sensor design optimisation*" Proc. CLEO, (1981).

[2.25] M. R. Layton and J. A. Bucaro, "*Optical fiber acoustic sensor utilising mode-mode interference*" Appl. Opt. , Vol. **18**, pp 666-670 (1979).

[2.26] R. L. Phillips, "*Proposed fiber optic acoustical probe*", Optics Letters, Vol **5**, pp. 318-320 (1980).

[2.27] S. -K. Yao, and C. K. Asawa, "*Fiber Optical Intensity Sensors*", IEEE Journal On Selected Areas In Communications, Vol. **1**, No. 3 (1993).

[2.28]   Y. -J. Rao, "*In-fibre Bragg grating sensors*", Meas. Sci. Technol., **8**, pp. 355–375 (1996).

[2.29]   A. Othonos, and K. Kalli, "*Fiber Bragg Gratings: Fundamental and Applications in Telecommunications and Sensing*" (Artech House, London, 1999) p.10

[2.30]   D. K. W. Lam, and B. K. Garside, "*Characterization of single-mode optical fiber filters*", Applied Optics, Vol. **20**, No. 3, pp. 440-5 (1981).

[2.31]   H. B. Liua, H. Y. Liua, G. D. Penga, P. L. Chu, "*Strain and temperature sensor using a combination of polymer and silica fibre Bragg gratings*", Optics Communications **219** pp. 139–142 (2003).

[2.32]   I. J. Read, and P. D. Foote, "*Sea and flight trials of optical fibre Bragg grating strain sensing systems*", Smart Mater. Struct. **10** pp. 1085–1094 (2001).

[2.33]   M. G. Xu, H. Geiger and J. P. Dakin, "*Optical in-fibre grating high pressure sensor*", Electron. Lett. Vol. **29** No. 4, pp. 398–399 (1993).

[2.34] A. D. Kersey and M. J. Marrone, "*Fibre Bragg high-magnetic-field probe*" Proc. 10th Int. Conf. on Optical Fibre Sensors (Glasgow, UK, October 1994) (SPIE) pp. 53–56 (1994).

[2.35]   S. Theriault, K. O. Hill, F. Bilodeau, D. C. Johnson and J. Albert "*High-g accelerometer based on an in-fibre Bragg grating sensor*", Proc. 11th Int. Conf. on Optical Fibre Sensors (Sapporo, Japan, May 1996) (IEICE and IEEJ) pp. 196–9 (1996).

[2.36]   A. D. Kersey, M. A. Davis, H. J. Patrick, M. LeBlanc, K. P. Koo, C. G. Askins, M. A. Putnam, and E. J. Friebele, "*Fiber Grating Sensors*", Journal of Lightwave Technology, Vol. **15**, No. 8, pp. 1442-1463 (1997).

[2.37]   D.C. Betz, G. Thursby, B. Culshaw, W.J. Staszewski, "*Advanced layout of a fiber Bragg grating strain gauge rosette*", Journal of Lightwave Technology, Vol. **24**, No. 2, pp. 1019-1026 (2006).

[2.38] T.-Y. Chang, H.-L. Cui, "*Determination of Direction of Arrival of Seismic Wave by a Single Tri-axial Fiber Optic Geophone*", Defence Technology, Vol. **9**, No. 1, pp. 1-9 (2013).

[2.39]   A. Laudati, F. Mennella, M. Esposito, A. Cusano, M. Giordano, G. Breglio, S. Sorge, "*A fiber optic Bragg grating seismic sensor*", In Third European Workshop on

Optical Fibre Sensors, International Society for Optics and Photonics, pp. 66191C-66191C (2007).

[2.40] J. Palaniappan, H. Wang, S. L. Ogin, A. Thorne, G. T. Reed, S. C. Tjin, and L. N. McCartney, "*Prediction of the reflected spectra from chirped fibre Bragg gratings embedded within cracked crossply laminates*", Meas. Sci. and Technol. Vol. **17**(6) pp. 1609-1614 (2006).

[2.41] S. A. Vasiliev, and O. I. Medvedkov, "*Long-period refractive index fiber gratings: properties, applications, and fabrication techniques*", Proc. SPIE **4083**, Advances in Fiber Optics, 212 (2000).

[2.42] H. W. Lee, and K. S. Chiang, "*CO2 laser writing of long-period fiber grating in photonic crystal fiber under tension*", Optics Express Vol. **17**, No. 6, 4533 (2009).

[2.43] A. M. Vengsarkar, P. J. Lemaire, J. B. Judkins, V. Bhatia, T. Erdogan, and J. E. Sipe, "*Long-period fiber gratings as band-rejection filters*", Tech. Dig. Conf. Opt. Fiber Commun., San Diego, CA, 1995, postdeadline paper PD4-2.

[2.44] V. Bhatia and A. M. Vengsarkar, "*Optical fiber long-period grating sensors*", Optics Letters, Vol. **21**, No. 9 (1996).

[2.45] V. Bhatia, K. A. Murphy, R. O. Claus, T. A. Tran, and J. A. Greene, "*Recent developments in optical-fiber-based extrinsic Fabry-Perot interferometric strain sensing technology*", Smart Mater. Struct. **4** 2446251 (1995).

[2.46] R. O. Claus, M. F. Gunther, A. Wang, and K. A. Murphy, "*Extrinsic Fabry-Perot sensor for strain 1 and crack opening displacement measurements from -200 to 900 °C*", Smart Mater. Struct. **1** pp. 237-242 (1992).

[2.47] D. -H. Kim, B. -Y. Koo, C. -G. Kim and C. -S. Hong, "*Damage detection of composite structures using a stabilized extrinsic Fabry–Perot interferometric sensor system*", Smart Mater. Struct. **13** pp. 593–598 (2004).

[2.48] Y. -J. Rao, "*Recent progress in fiber-optic extrinsic Fabry–Perot interferometric sensors*", Optical Fiber Technology **12** pp. 227–237 (2006).

[2.49] A. Wang, S. Gollapudi, K. A. Murphy, R. G. May, and R. O. Claus, "*Sapphire-fiber-based intrinsic Fabry-Perot interferometer*", Optics Letters, Vol. **17**, No. 14 (1992).

[2.50] W. -C. Du, X. -M. Tao, and H. -Y. Tam, "*Fiber Bragg Grating Cavity Sensor for Simultaneous Measurement of Strain and Temperature*", IEEE Photonics Technology Letters, Vol. **11**, No. 1 (1999).

[2.51] T. Yoshino, K. Kurosawa, K. Itoh, and T. Ose, "*Fiber-Optic Fabry-Perot Interferometer and Its Sensor Applications*", IEEE Transactions on microwave theory and techniques, Vol. **MTT-30**, No. 10 (1982).

[2.52] X. Chen, F. Shen, Z. Wang, Z. Huang, and A. Wang, "*Micro-air-gap based intrinsic Fabry–Perot interferometric fiber-optic sensor*", Applied Optics, Vol. **45**, Issue 30, pp. 7760-7766 (2006).

[2.53] A. Guemes, and B. Soller "*Optical Fiber Distributed Sensing: Physical Principles and Application*" Proc. 7th Int. Workshop on Structural Health Monitoring, Stanford University, September 9-11 (2009).

[2.54] T. Kurashima, T.Horiguchi, H. Izumita, S. I. Furukawa and Y. Koyamada,. "*Brillouin optical-fiber time domain reflectometry*". IEICE Transactions on Communications, **76**(4), pp. 382-390 (1993)

[2.55] R. R. J. Maier, W. N. MacPherson, and J. S. Barton, "*Distributed transverse load sensing in polarisation maintaining fibres using Rayleigh backscatter*", Proc. SPIE 20th Int. Conf. on Optical Fibre Sensors, Edinburgh, UK, Oct. 2009, vol. 7503.

[2.56] L. Zou, X. Bao, Y. Wan, and L. Chen, "*Coherent probe-pump-based Brillouin sensor for centimeter-crack detection*", Optics Letters, Vol. **30**, No. 4 pp. 370-372 (2005).

[2.57] A. Bueno, K. Nonaka, and S. Sales, "*Novel system to interrogate distributed fiber strain sensors and point temperature sensors based on pulse correlation and FBGs*", Proc. SPIE 20th Int. Conf. on Optical Fibre Sensors, Edinburgh, UK, Oct. 2009, vol. 7503

[2.58] C. -Y. Ryu, J. -R. Lee, C. -G. Kim and C. -S Hong, "*Buckling behavior monitoring of a composite wing box using multiplexed and multi-channeled built-in fiber Bragg grating strain sensors*", NDT&E International **41** pp. 534– 543 (2008).

[2.59] J. Frieden, J. Cugnoni, J. Botsis, T. Gmür, D. Coric, "*High-speed internal strain measurements in composite structures under dynamic load using embedded FBG sensors*", Composite Structures **92** pp. 1905–1912 (2010).

[2.60] X. W. Pan, D. K. Liang, and D. Li, "*Optical fiber sensor layer embedded in smart composite material and structure*", Smart Mater. Struct. Vol. **15**(5) pp. 1231–1234 (2006).

[2.61] M. S. Melle, K. Lui, and R. M. Measures, "*A Passive Wavelength Demodulation System for Guided-Wave Bragg Grating Sensors*", IEEE Photonics Technology Letters, Vol. **4**, No. 5 (1992).

[2.62] L. Zhang, R. W. Fallon, A. Gloag, I. Bennion, F. M. Haron, and P. Foote, "*Spatial and Wavelength Multiplexing Architectures for Extreme Strain Monitoring System Using Identical-Chirped-Grating-Interrogation Technique*", Proceedings of the Optical Fibre Sensors Conference (OFS-12), Williamsburg, VA, USA, 1997 pp. 452-455.

[2.63] A. Othonos, and K. Kalli, "*Fiber Bragg Gratings: Fundamental and Applications in Telecommunications and Sensing*" (Artech House, London, 1999) p.346.

[2.64] K. Zhou, A. G. Simpson, X. Chen, L. Zhang, I. Bennion, *"Fiber Bragg grating sensor interrogation system using a CCD side detection method with Superimposed blazed gratings,"* Photonics Technology Letters, IEEE , Vol. **16**, No. 6 (2004)

[2.65] A. G. Simpson, K. Zhou , L. Zhang, L. Everall, I. Bennion, *"Optical sensor interrogation with a blazed fiber Bragg grating and a charge-coupled device linear array"*, Appl Opt. Vol. **43** No. 1 (2004).

[2.66] M. A. Davis, and A. D. Kersey, "*Application of a Fiber Fourier Transform Spectrometer to the Detection of Wavelength-Encoded Signals from Bragg Grating Sensors*", Journal of Lightwave Technology, Vol. **13**, No. 7 (1995).

[2.67] A. Othonos, and K. Kalli, "*Fiber Bragg Gratings: Fundamental and Applications in Telecommunications and Sensing*" (Artech House, London, 1999) p.304.

[2.68] D. Goff, *"Fiber Optic Reference Guide"* (CRC Press, 2002) p.62

[2.69] L. Goldberg, and D. Mehuys, *"High power superluminescent diode source"*, Electron. Lett. **30**, 20 (1994).

[2.70] P. R. Morkel, K. P. Jedrzejewski, E. R. Taylor, and D. N. Payne, "*High-Gain Superfluorescent Neodymium-Doped Single-Mode Fiber Source*", IEEE Photonics Technology Letters, Vol. **4**, No. 7 (1992).

[2.71] P. Liu, F. -P. Yan, J. Li, L. Wang, T. G. Ning, T. -R. Gong, and S. S. Jian, "*A Continuously Tunable Erbium-Doped Fibre Laser Using Tunable Fibre Bragg Gratings and Optical Circulator*", Chin. Phys. Lett., Vol. **25**, No. 12, 4276 (2008).

[2.72] K. Harvey and C. Myatt, *"External-cavity diode laser using a grazing-incidence diffraction grating",* Opt. Lett. **16**, 910-912 (1991).

[2.73] Micron Optics, 1852 Century Place NE, Atlanta, GA 30345 USA

http://www.micronoptics.com/

[2.74] R. J. Mears, L. Reekie, M. Jauncey, and D. N. Payne, "*Low-noise erbium-doped fiber amplifier operating at 1.54 μm*", Electron. Lett. **26**, 1026 (1987).

[2.75]   E. Desurvire, J. R. Simpson, and P. C. Becker, "*High-gain erbium doped traveling wave fiber amplifier*", Optics Letters **12** (11), 888 (1987).

[2.76] P. M. Becker, A. A. Olsson, J. R. Simpson, "*Erbium-Doped Fiber Amplifiers: Fundamentals and Technology*", Academic Press (1999).

[2.77] M. J. Conelly, "*Semiconductor Optical Amplifiers*", Springer, 1st edn. (2002).

[2.78]   F. Slaveski, J. Sluss, Jr., M. Atiquzzaman, H. Nguyen, and D. Ngo, "*Optical Fiber Wavelength Division Multiplexing*", IEEE AES Systems Magazine, August 2003.

[2.79] T. A. Berkoff, M. A. Davis, D. G. Bellemore, A. D. Kersey, G. M. Williams, M. A. Putnam, "*Hybrid time and wavelength division multiplexed fiber grating array,*" Proc. SPIE, Vol. SPIE-2444. p. 288, (1995).

[2.80] W. H. Chung, Hwa-yaw Tam; P. K. A. Wai, A. Khandelwal, "*Time- and wavelength-division multiplexing of FBG sensors using a semiconductor optical amplifier in ring cavity configuration,*" Photonics Technology Letters, IEEE , Vol. **17**, No. 12, pp.2709 - 2711, (2005).

[2.81] Y. M. Gebremichael, W. Li, B.T. Meggitt, W. J. O. Boyle, K. T. V. Grattan, B. McKinley, L. F. Boswell, K. A. Aarnes, S. E. Aasen, B. Tynes, Y. Fonjallaz, T. Triantafillou, "*A field deployable, multiplexed Bragg grating sensor system used in an extensive highway bridge monitoring evaluation tests,*" Sensors Journal, IEEE , Vol. **5**, No. 3, pp.510-519, (2005).

[2.82] P. Childs, A. C. L. Wong, B. Yan, M. Li, and G. –D. Peng, "*Spectrally coded multiplexing for fibre grating sensor systems*" Proc. SPIE 20th Int. Conf. on Optical Fibre Sensors, Edinburgh, Oct. 2009, Vol. 7503.

[2.83] D. Inaudi, S. Vurpillot, S. LLoret "*In-line coherence multiplexing of displacement sensors: a fiber optic extensometer*", SPIE, Smart Structures and Materials, San Diego, USA (1996).

[2.84] L. J. Cimini, "*Analysis and Simulation of a Digital Mobile Channel Using Orthogonal Frequency Division Multiplexing*", Communications, IEEE Transactions on, Vol. **33**, No. 7, pp.665 - 675, (1985).

[2.85] C. D. Butter and G. B. Hocker, "*Fiber optics strain gauge*", Appl. Opt. Vol. **17** No. 18, pp.2867-2869, (1978).

[2.86] H. F. Taylor, "*Acoustooptic modulators for single-mode fibers*", J. Lightwave Technol., Vol. **LT-5**, pp. 990–992, (1987).

[2.87] J.-R. Lee, H. Tsuda, "*Acousto-ultrasonic sensing using capsular fibre Bragg gratings for temperature compensation*", Meas. Sci. Technol. **17** pp. 2920–2926 (2006).

[2.88] S. Magne, S. Rougeault, M. Vilela, and P. Ferdinand, "*State-of-strain evaluation with fiber Bragg grating rosettes: application to discrimination between strain and temperature effects in fiber sensors*" Appl. Opt. **36**, pp. 9437-9447 (1997).

[2.89] C. Ramos, R. de Oliveira, A. Marques, O. Frazao, "*Design and Experimental Evaluation of a Composite Strain Rosette Using Fiber Bragg Grating*" Microwave And Optical Technology Letters **53** 8 pp. 1853-1857 (2013).

[2.90] N. Tanaka, Y. Okabe and N. Takeda, "*Temperature-compensated strain measurement using fiber Bragg grating sensors embedded in composite laminates*", Smart Mater. Struct. **12** pp. 940–946 (2003).

[2.91] A. Othonos, and K. Kalli, "*Fiber Bragg Gratings: Fundamental and Applications in Telecommunications and Sensing*" (Artech House, London, 1999) p.99.

[2.92] C. C. Ciang, J. -R. Lee, and H. –J. Bang, "*Structural health monitoring for a wind turbine system: a review of damage detection methods*", Meas. Sci. Technol. Vol. **19** (12) 122001 (2008).

[2.93] D. C. Betz, G. Thursby, B. Culshaw, and W. J. Staszewski, "*Acousto-ultrasonic sensing using fiber Bragg gratings*", Smart Mater. Struct. **12**, pp. 122–128 (2003).

[2.94]   M. A. Hamstad, "*A Review: Acoustic Emission as a Tool for Composite Materials Studies,*" Experimental Mechanics, **26**(1), pp. 7-13 (1986).

[2.95] J. -R. Lee, H. Tsuda and N. Toyama, "*Impact wave and damage detections using a strain-free fiber Bragg grating ultrasonic receiver*", NDT&E International **40** pp. 85–93 (2007).

[2.96] W. H. Prosser, M. R. Gorman and D. H. Humes, "*Acoustic Emission Signals in Thin Plates Produced by Impact Damage*", Journal of Acoustic Emission, Vol. **17**(1-2) pp. 29-36, (1999).

[2.97]   J. Dakin and B. Dakin, "*Optical fiber sensors: principles and components*" Artech House, Boston and London (1988).

[2.98] J. Dakin and B. Dakin, "*Optical fiber sensors: systems and applications volume two*" Artech House, Boston and London (1989).

[2.99] J. Dakin and B. Dakin, "*Optical fiber sensors: applications, analysis and future trends volume four*" Artech House, Boston and London (1997).

Chapter 3 - Impact Location

3.1. Introduction

3.1.1. Aim

This work follows on from earlier studies at BAE Systems that demonstrated the ability to detect the occurrence of impacts on a carbon fibre composite test structure and simultaneously display the location on a graphical user interface representing the surface of the structure. In aerospace applications, the objective is to identify that an impact has occurred allowing targeted maintenance to be carried out. A major aim of this work was to improve the location accuracy which was unreliable and frequently represented the impact on an incorrect part of the structure. This was achieved by improving and further calibrating the time-of-flight triangulation location technique already in use before implementing a neural network system as an alternative technique and performing a comparative study. An additional aim was to extend the system capabilities to estimate the severity of the impact by estimating the intensity. Finally, the system was adapted to utilise some previously embedded chirped fibre Bragg grating sensors in the structure as an alternative to the piezoelectric sensors used in the rest of the study.

3.1.2. Impact detection

An aircraft can use an impact detection system to detect collisions that might occur from stones on the runway, birdstrikes or gunfire. This will allow the pilot to decide to take appropriate action in the case of an impact magnitude likely to have caused damage or, if less severe, the location and energy can be stored to be investigated for damage upon landing. This minimises maintenance time and therefore cost by narrowing down the area for investigation. Searching for impact damage is a slow and labour intensive process especially when composite materials are involved, as non-destructive testing is required to search for barely visible impact damage. Impact detection systems are even more crucial for unmanned air vehicles which require a method of detecting impacts allowing the control mechanisms to take action appropriate to the situation.

When a structure is subject to an impact the resulting acoustic wave spreads across the surface which can be detected by suitable sensors. By measuring the time of arrival of the leading edge of this acoustic signal and comparing it with each of the other sensors a relative timing can be determined. Using this information the location of the impact can be determined using a triangulation method based on the time of flight of the acoustic

signal. The energy of the impact can be ascertained by measuring the absolute intensity of the signal detected by each sensor and correcting for the attenuation due to the distance travelled through the structure. As damage likelihood increases with the impact energy, this measurement can allow a rough estimate of damage likelihood when combined with material damage tolerances.
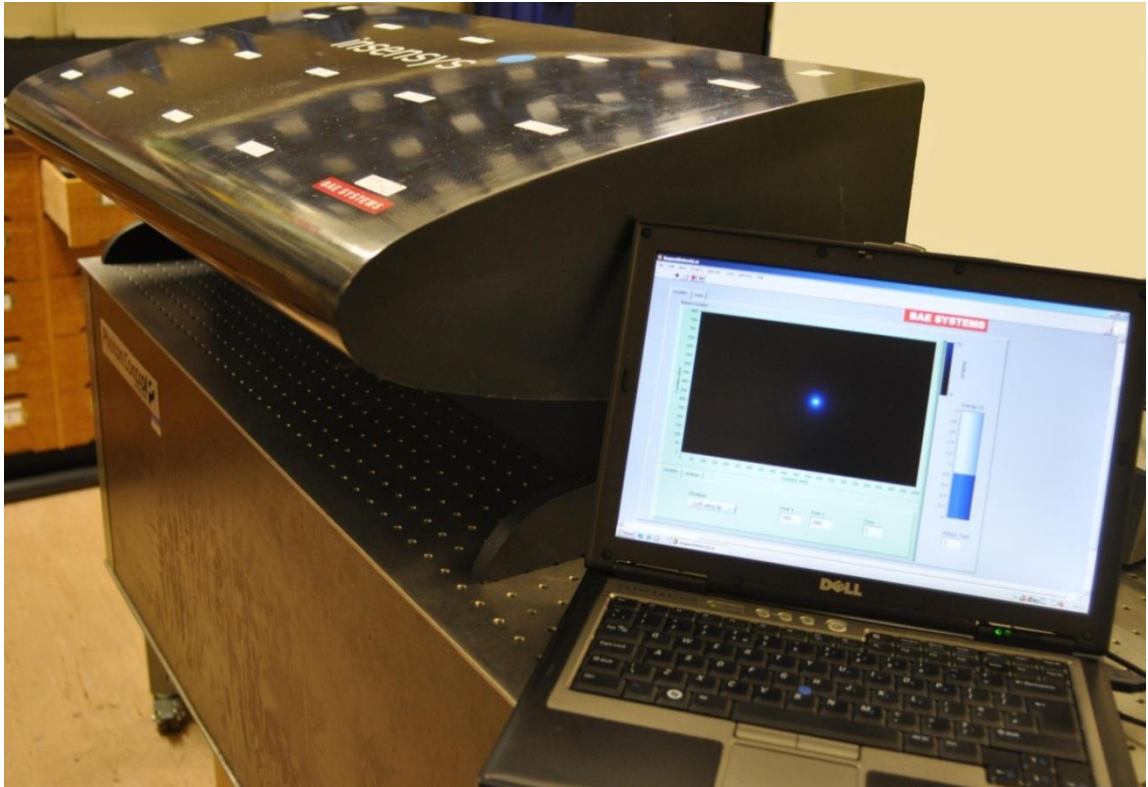
3.2. System Development

3.2.1. Test structure

Figure 3.1. Test structure made from carbon fibre composite and user interface.

The test structure, comprising a curved, carbon skin reminiscent of a section of wing leading edge, was manufactured by Insensys Ltd (Figure 3.1). The composite material is made using a fibre weave. The unfolded wing surface would be 991 mm wide and 796 mm high with the leading edge 260 mm from the bottom edge. The structure is instrumented with 4 piezoelectric strain gauge sensors bonded to the underside near the corners of the structure; the locations are marked on Figure 3.2. Each of the sensors was found to have a different magnitude response to an impact with approximately a factor of 10 difference between the weakest and strongest sensor. This is an issue that had to be considered and dealt with in the development of the system.
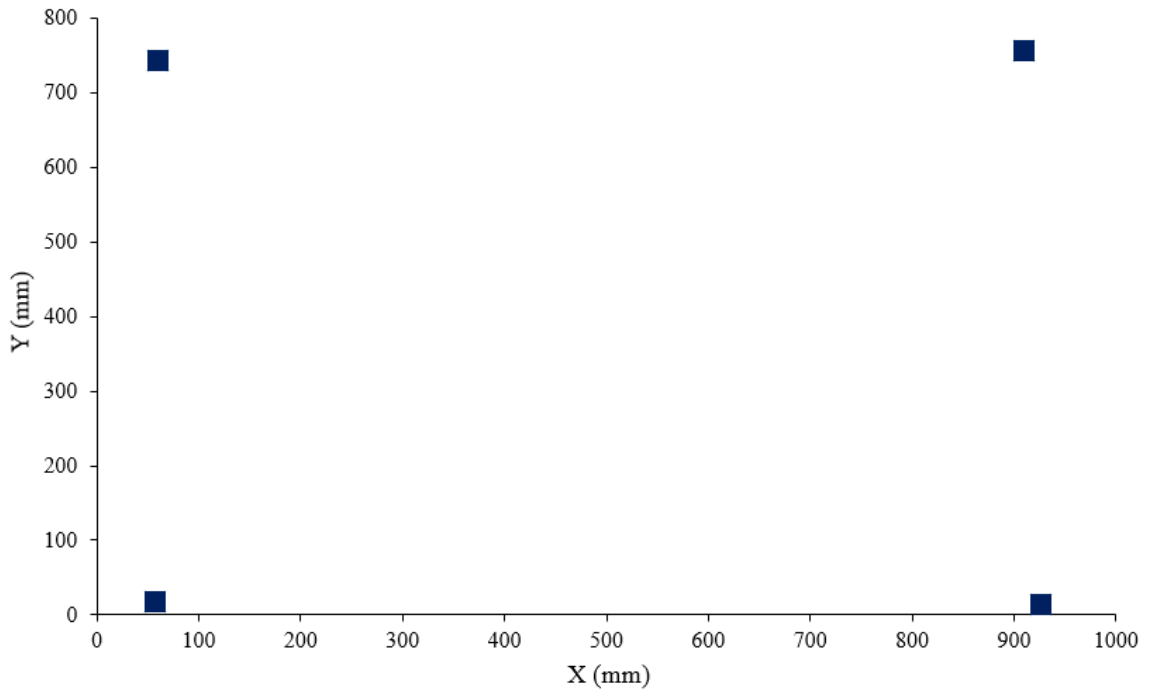
Figure 3.2. The four sensor locations marked on a 2D representation of the structure.

3.2.2. Data acquisition

A LabVIEW program, used in an earlier three sensor system, was adapted to control the demonstration system and provide a graphical user interface. The signals are acquired using a National Instruments USB 6259 data acquisition device (DAQ) set to trigger above a threshold of 0.1V. This threshold was determined through experimentation to avoid false triggering from the noise. It was found that there was significant electrical crosstalk between the channels in the DAQ; it was observed that channels following a large signal in the previous channel had the exact same form merely with a lower amplitude. This was causing the weaker signals to be overwhelmed resulting in the loss of the relative timing information which is vital to the location technique. Additionally, the signals were prone to drift which caused issues with the thresholding. To address these issues a pre-amplifier was constructed based on an op-amp with each circuit on a separate circuit board and a housing constructed with connectors to produce a flexible and reliable system.
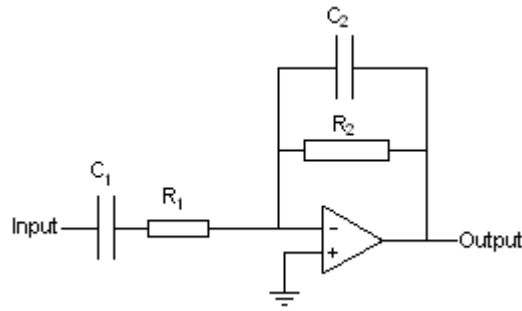
Figure 3.3. Pre-amplifier circuit diagram.

Figure 3.3 shows the circuit diagram with the values for the resistors and capacitors chosen to produce gain in the weaker signals and to pass the desired signal that was found to be upto 25 kHz. The values are given in Table 3.1. The op-amp used was a FET-input, low distortion device with a device number OPA604AP. The input is also AC coupled in order to address the issue of drift.

Table 3.1. Component values for pre-amplifier circuit.

Component	Sensor 1	Sensor 2	Sensor 3	Sensor 4
C_1	1μF	1μF	1μF	1μF
C_2	47pF	100pF	470pF	470pF
R_1	5kΩ	9kΩ	13.4kΩ	13.4kΩ
R_2	100kΩ	39kΩ	13.4kΩ	13.4kΩ

The PZT sensors have a high impedance which causes problems for the DAQ as it converts the analogue to digital signals sequentially and the measurement of a strong signal caused crosstalk in the next channel. The above circuit creates a lower impedance output that the DAQ can measure successfully as well as incorporating some filtering and gain to reduce the differences in signal strength between the different sensors. The electronics were found to almost completely eliminate the crosstalk and leave the signals from each sensor independent.

A set of four raw signals are shown in Figure 3.4 captured and displayed using the LabVIEW user interface.
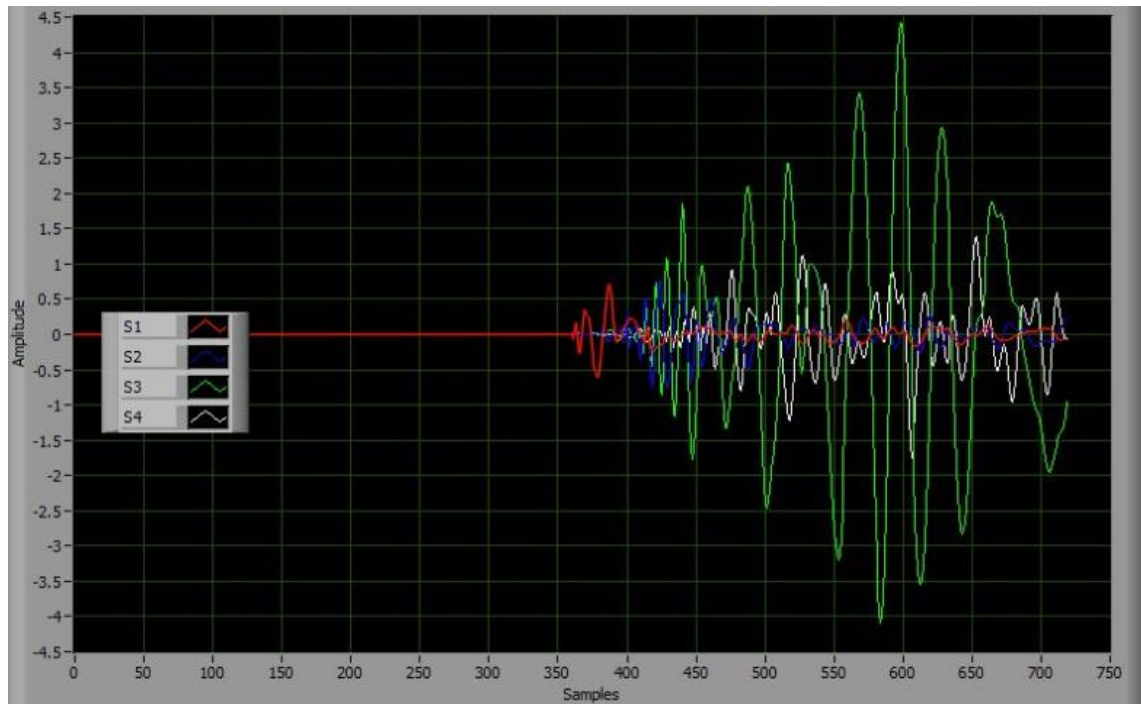
Figure 3.4. An example of a set of raw signals captured and displayed on the LabVIEW user interface

The LabVIEW program was developed to take the waveforms from the data acquisition device once triggered and analyse them to determine the intensity of the largest peak. The waveform is normalised by dividing by this value allowing the peak locations to be detected with the same relative threshold despite the large variation in magnitude of the signals. It was found that the noise was low enough for this to be viable without false identification of peaks. The difference between the time of arrival of the first peak for each pair of sensors is calculated. This is repeated for the 2nd and 3rd peak, Figure 3.5 illustrates this process and shows the three time differences. These three values are averaged to mitigate the effect of a peak from a weaker sensor just failing to reach threshold causing a later peak to be identified as the first and the location moved away from that sensor. This data is then used for the location.
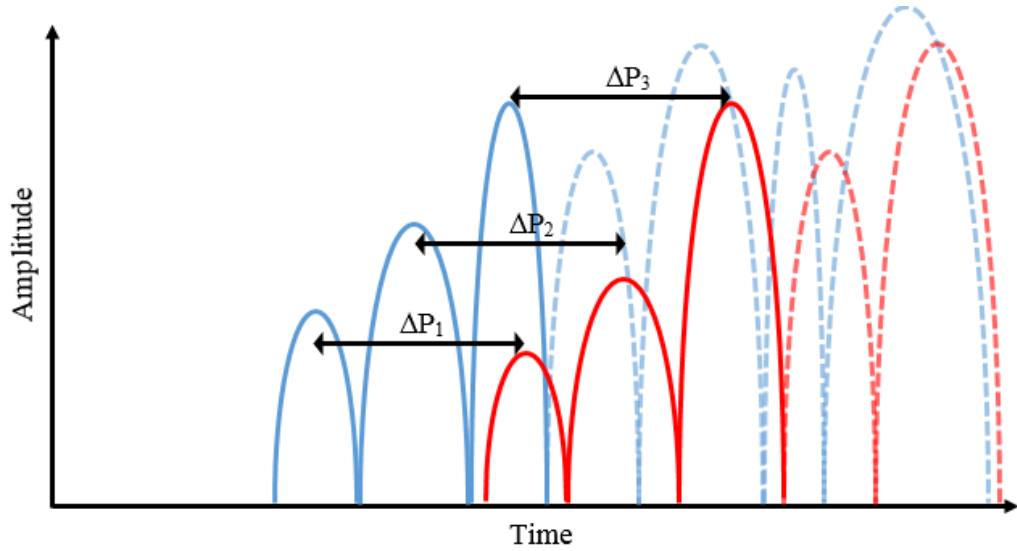
Figure 3.5. Diagram showing the peaks from one sensor (blue) and a second (red). The first three peaks are highlighted along with the time differences between each peak.

3.2.3. *Impact energy determination*

After an impact, the acoustic wave travels across the structure losing intensity due to attenuation. It was assumed that this intensity relationship can be approximated by:

$$I_i = I_0 \exp^{-\alpha x} \tag{3.1}$$

where I_i is the intensity measured by sensor i, I_0 is the intensity of the impact, x is the distance between the impact and sensor i and α is an attenuation coefficient to be determined. Due to the nature of the structure the attenuation coefficient is likely to be inhomogeneous. Therefore, a different coefficient was determined for each sensor to reflect the difference in its position on the structure. For example, it was expected that there would be higher attenuation to waves travelling around the curve of the structure. To determine these coefficients a 58 g weight was dropped multiple times from a height of 200 mm to produce a 0.114 J impact at 14 locations on the structure. The standard deviation of the calculated impact intensity was minimised with respect to the attenuation coefficient for each sensor in a method which is described more fully in §3.3.2.

Different approaches for quantifying the intensity of an impact were investigated to determine the most reproducible and robust technique for use by the system. These included the magnitude of the first peak, the magnitude of the largest peak and the sum of all peaks within a window of time at the leading edge of the signal, they are shown in Figure 3.6. The first peak is not reliable as the peaks build in intensity over a period of time and the threshold chosen to detect the peaks has a significant effect on the results.

64

Due to the shape of the structure, multiple reflections of acoustic waves occur and the largest peak is often due to constructive interference later than the leading edge of the signal. This is location dependent and therefore unsuitable as a robust measure. It was found that the sum of all the peaks within a 0.1 second window gave the most robust measure and is a good indication of the total intensity in the leading edge of the signal.
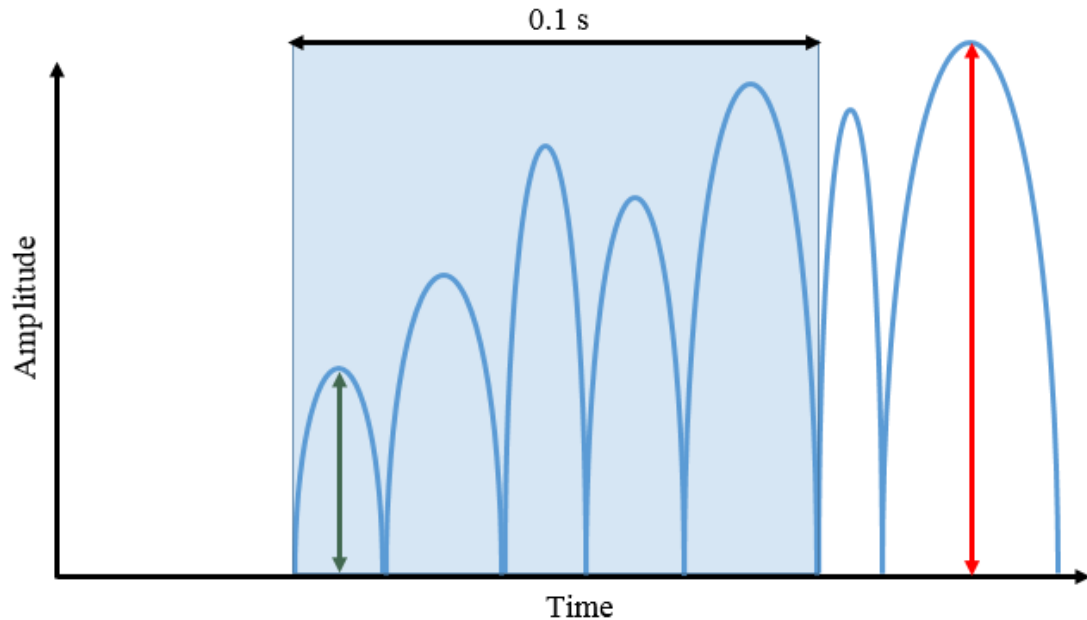

Figure 3.6. Diagram of possible intensity measures: magnitude of first peak (green), magnitude of the largest peak (red) and the sum of all peaks in a 0.1s time window at the leading edge of the signal (blue box)

The intensities are then normalised with previously determined calibration factors to make the sensor responses consistent with each other and on an arbitrary scale. Variation occurs between the different sensors due to a combination of several factors including the quality of sensor construction, the efficiency of the bonding and the sensor location. The structure cannot be assumed isotropic or homogenous and as such, an acoustic signal travelling the same distance in different directions to different sensors may arrive with a different amplitude. Further impact tests were carried out to verify the effectiveness of the impact intensity estimation. It was found that there was significant variation in the standard deviation of the impact intensity between the four sensors and a weighted average was used to produce the most reliable overall estimate of intensity. The weighting of each sensor is directly related to the standard deviation of the test data with sensor 4 receiving the weakest weighting, as the standard deviation is over three times greater than that of sensor 1.

Table 3.2. Impact intensity test data for each sensor.

Sensor	Attenuation Coefficient	Avg. Impact Intensity (a.u.)	Standard Deviation (a.u.)	Weighting
1	0.0014	0.155	0.039	3
2	0.0025	0.173	0.067	2
3	0.0016	0.169	0.040	3
4	0.0029	0.281	0.145	1

Table 3.2 shows a summary of the results of the impact intensity detection tests including the attenuation coefficient, average impact intensity, standard deviation and weighting corresponding to each of the four sensors. Sensors 1 and 3 are in the top corners of the structure and as such experienced less attenuation as the majority of impacts are on the larger top side and therefore the wave does not have to travel around the leading edge of the wing. Sensors 2 and 4 in the bottom corners suffer significantly increased attenuation due to the leading edge that makes the intensity estimation more complex. The LabVIEW program uses these attenuation coefficients for each of the sensors to mitigate the effect of the structural topography.

3.2.4. Integrated demonstration system

This system was part of a larger demonstration as part of a collaboration between several groups. This larger demonstration was of an integrated sensing system incorporating impact detection (my system as previously described), fuel management systems and wetness sensing (produced by other people). This demonstrated the advantages of a variety of sensor systems working together to allow corroboration of data and increase the ability to make decisions based on the available information. For this integrated system the impact detection system was required to send the location and intensity of any impact every second should one have occurred in that timeframe. Otherwise an "all clear" message was sent. The structure is split into 6 zones and the intensity is split into 4 categories from insignificant to penetrating.

The program was adapted to fulfil its role within the integrated demo. The program runs continuously and when an impact is detected, the zone that the impact occurred in and the category of impact are recorded. Once a second, the program sends a message to a control system within the integrated demo with the zone and category of an impact that occurred or a null message if no impact occurred. This message is consistent with the aerospace protocol being followed by the integrated demo. The impact detection system was tested as part of the integrated demo and successfully detected impacts and transmitted the relevant data allowing the information to be viewed on a remote

graphical user interface which could be used for a mission control system. This system was demonstrated to stakeholders and was a big success.

3.3. Time-Of-Flight Triangulation

3.3.1. Location algorithm

The carbon fibre composite structure is inhomogeneous and due to its woven nature the speed of propagation of an acoustic wave is also likely to vary with direction. If these speeds are known then the location of the acoustic wave source can be determined from the relative times of arrival of the wave. If the acoustic wave arrives at sensor 1 and 2 simultaneously then the delay is zero and the x co-ordinate of the source must be midway between sensor 1 and sensor 2. There are a set of points that satisfy this condition which form a straight line. If the differential delay is positive then the source lies closer to sensor 2. Again, there are a set of points that satisfy this condition and form a curved line and similar lines can be drawn between all of the sensor pairs. The location of the impact lies at the intersection of all of these lines. In a real system, the lines will not all perfectly overlap and the algorithm determines the most likely location using the following method.

The surface is split into a 100 by 100 grid that is assumed flat. A lookup table is calculated with the expected relative times of arrival, dt_{ij}, between each pair of sensors if an impact occurred in each grid square. This lookup table is then used in conjunction with the measured relative times of arrival, T_{ij}, to determine the most likely impact location. The function $F(x, y)$ is calculated for each grid square:

$$F(x, y) = \frac{A}{A + \left(dt_{12}(x, y) - T_{12}\right)^2 + \left(dt_{13}(x, y) - T_{13}\right)^2 + \dots} \tag{3.2}$$

where A is a sharpness factor to prevent the function tending to infinity when $dt_{ij}(x, y) \to T_{ij}$. All 6 combinations of sensors are included in the denominator, 1-2, 1-3, 1-4, 2-3, 2-4 and 3-4. The location where $F(x, y)$ is at a maximum is the most likely impact location, it is then displayed on a map on the user interface. When $F(x, y)$ has a sharp peak the location is more certain and the location is displayed as a small intense spot, when the peak is shallow the location is less certain and a larger diffuse area will be displayed. This indicates visually to the user the location of an impact and the degree of certainty attributed to this determination.
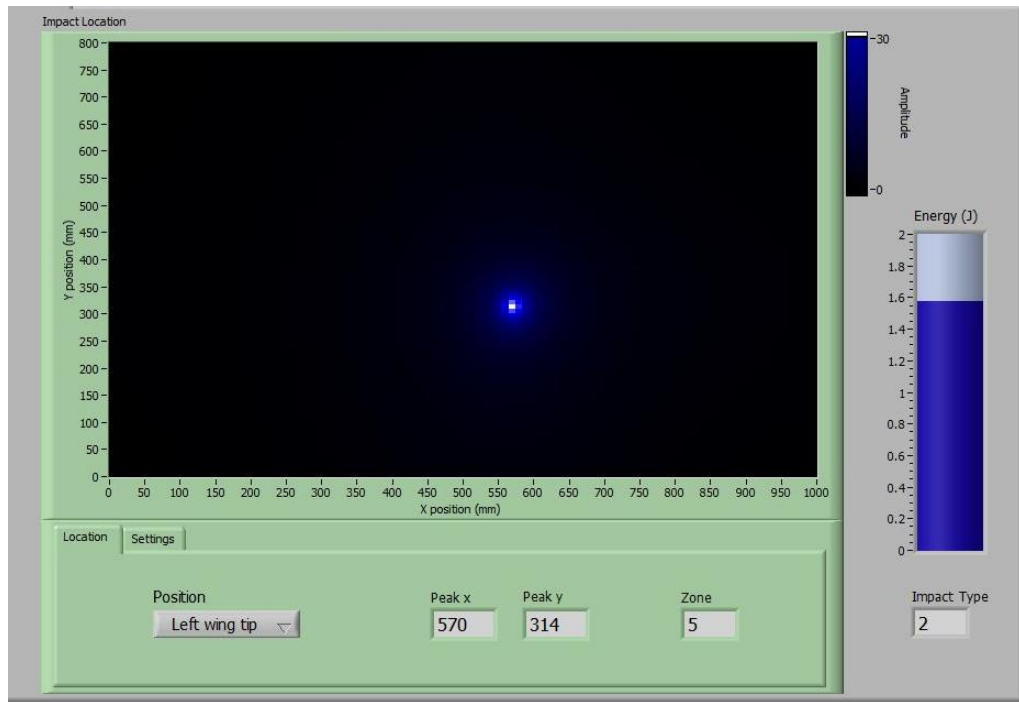
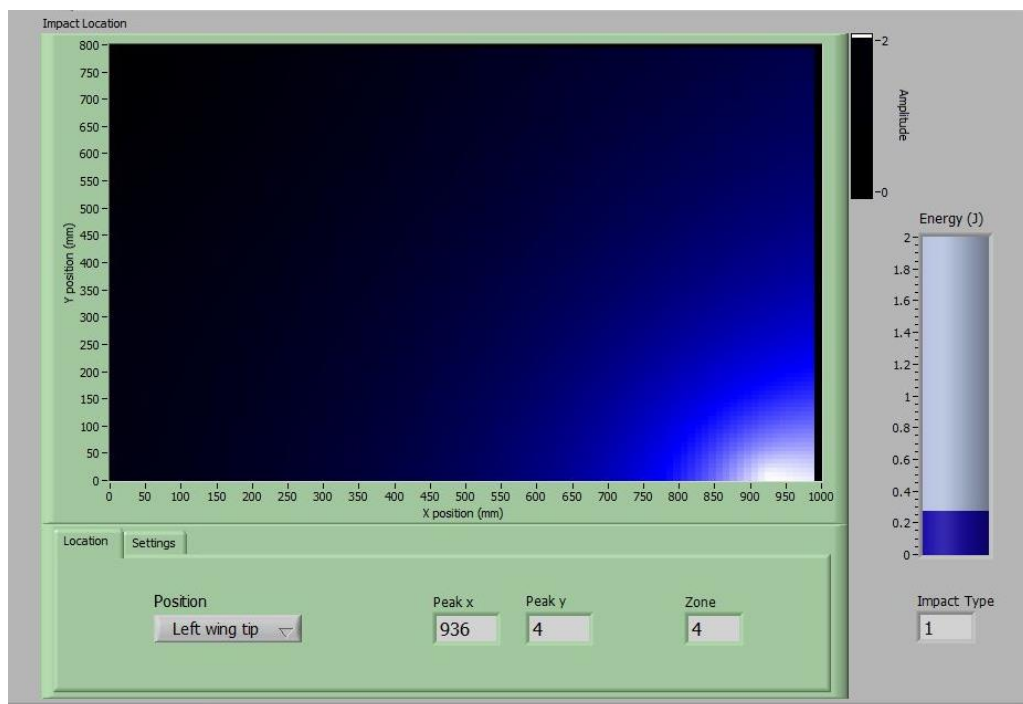**Figure 3.7. User interface showing a well-defined impact location.**

Figure 3.8. User interface showing a more uncertain impact location.

Figure 3.7 and Figure 3.8 show the user interface with two different impacts. A strong, central impact which has been located with higher certainty and a weaker impact in the bottom corner which has been located with less certainty.

A three dimensional, rotatable representation of the test structure was produced to allow easier visualisation and comparison with the real test structure. It is shown in Figure 3.9. It is a two dimensional surface that is shown curved in a three dimensional space to

approximate the shape of the real structure. The impact is located on the surface using the same method as the two dimensional visualisation. This representation can be used as an alternative to the two dimensional surface view and can be rotated to allow the impact point to be seen easily on any point of the three dimensional structure.
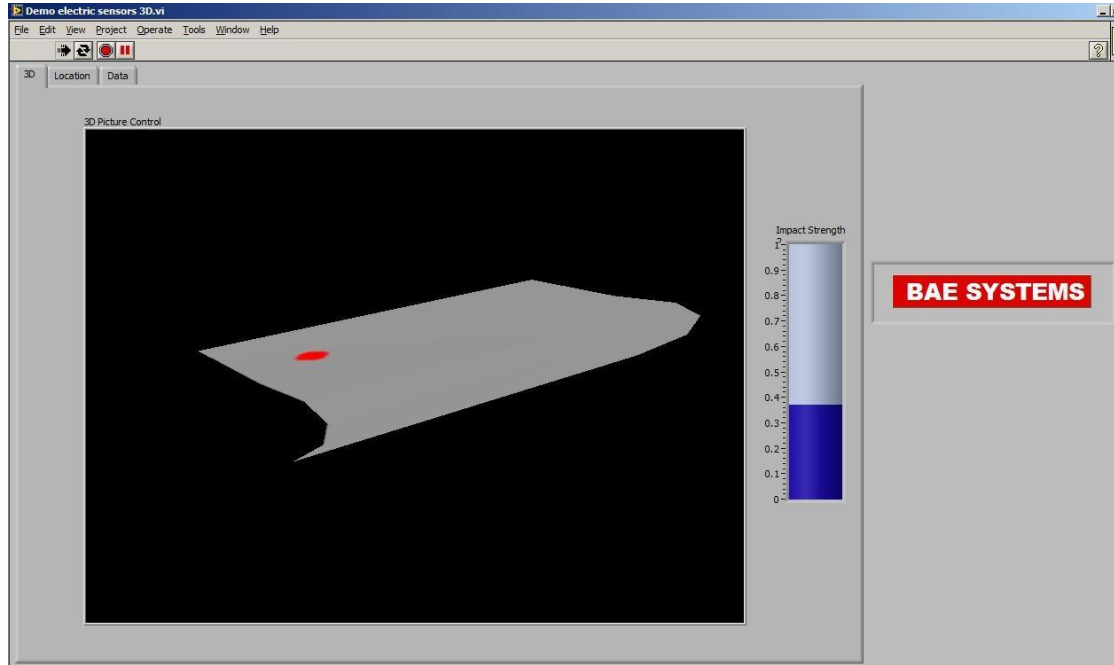
Figure 3.9. Three dimensional, rotatable visualisation of test structure showing detected impact point.

3.3.2. *Speed of acoustic waves*

This location technique relies on the knowledge of the speed of the acoustic wave across the structure. It was assumed that the speed may be different in the x and y direction. To determine these two speeds, v_x and v_y, impacts were carried out at known locations. Initial values of $v_x = v_y = 1000$ ms^{-1} were used as a reasonable estimate. Ten locations were marked on the structure and each was struck 5 times and the values of T_{ij} were recorded. These times were compared to the predicted times for that location and an error number calculated as a measure of the deviation from ideal. The sum of all of the errors from each location was minimised using a least squares approach with regard to v_x and v_y which were found to be $v_x = 1150$ ms^{-1} and $v_y = 1425$ ms^{-1}. The experiment was then repeated using these values and updated values of $v_x = 1220$ ms^{-1} and $v_y = 1400$ ms^{-1} were obtained and subsequently used by the LabVIEW program.

3.3.3. Results

Impacts with a range of energies were carried out on the system to calibrate the arbitrary impact intensity scale to energy. Only low energy impacts could be carried out to

ensure that the structure was not damaged and, despite the limited range, a good linear relationship was achieved and is shown in Figure 3.10. The relation between impact intensity and energy was then included in the program to display an estimate of the impact energy on the user interface.
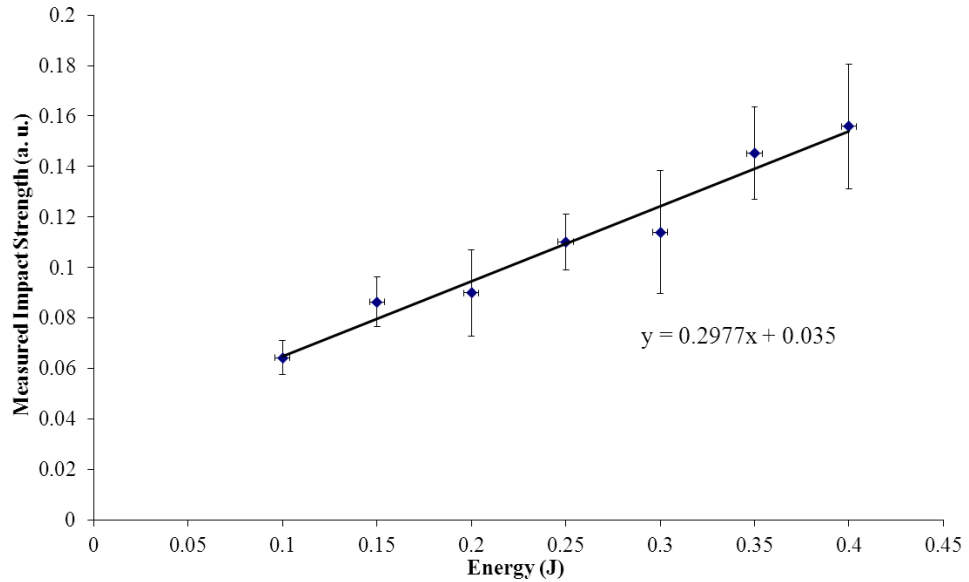
Figure 3.10. Calibration of impact intensity to impact energy.

An investigation into the accuracy of the system was undertaken. A 5×4 grid of points was marked on the structure with the first three rows on the top and the final row on the bottom. A 0.2201 kg metal tup (hemispherical impact head) was dropped from a height of 200 mm to create 0.432 J impacts. Fifteen impacts were carried out at each location. Figure 3.11 shows the average position acquired for each location along with error bars corresponding to plus/minus the standard deviation of the data for that location.
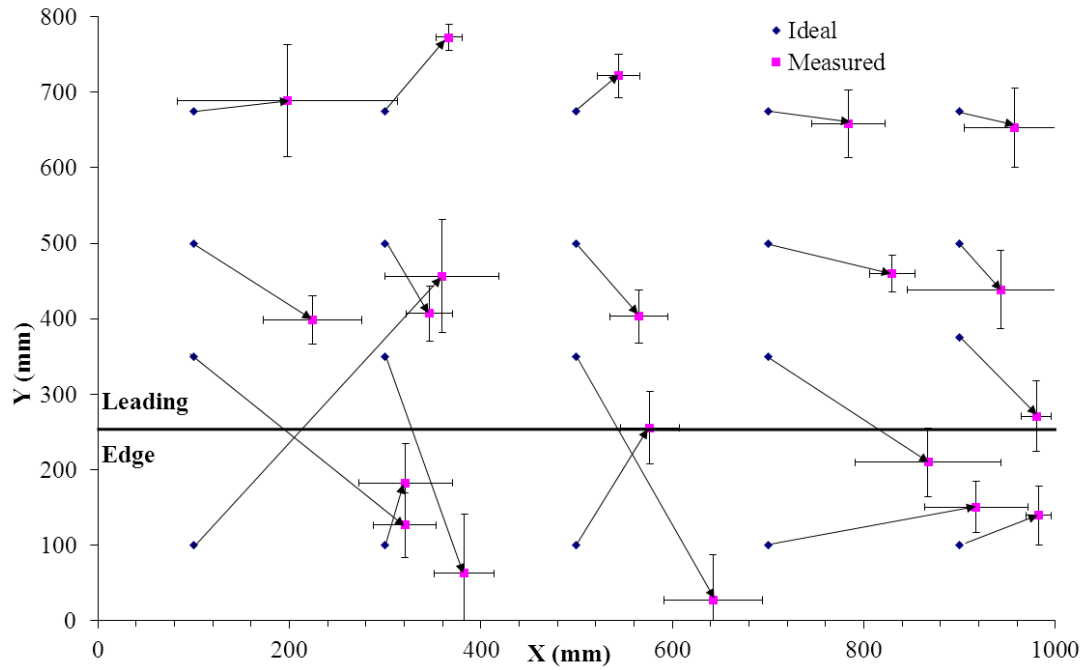
Figure 3.11. Average impact locations detected by the system and the corresponding actual impact point.

As can be seen in Figure 3.11, there is a systematic error in that all 20 impact locations had an average detected location to the right of the actual impact point. The average error in *x* was 105.5 mm while the *y* error was more scattered with the average error -33.4 mm. The leading edge is a major cause of error in the system. The average error for the top 10 locations is 102 mm while that of the second 10 positions, which surround the leading edge, is 233 mm. The locations of impacts in the vicinity of the leading edge can be mislocated to the other side of the edge. This may be caused by sound waves travelling through the walls or along the short side of the curve. This problem appears worse in the bottom left corner, exacerbated by the long distance to the top right corner that houses the weakest sensor. Therefore, an impact in the bottom left corner will have a very weak and noisy signal from that sensor lowering the location accuracy. This is illustrated by Figure 3.12 which is an error map for the structure.
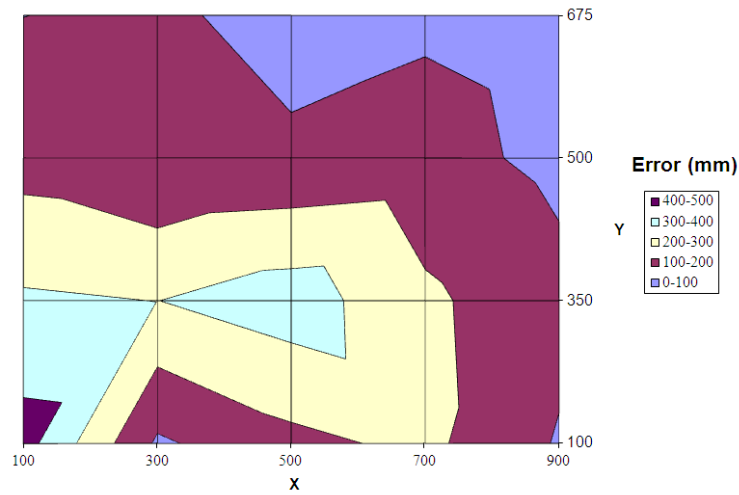
Figure 3.12. Error map of the structure constructed from the data in Figure 3.11.
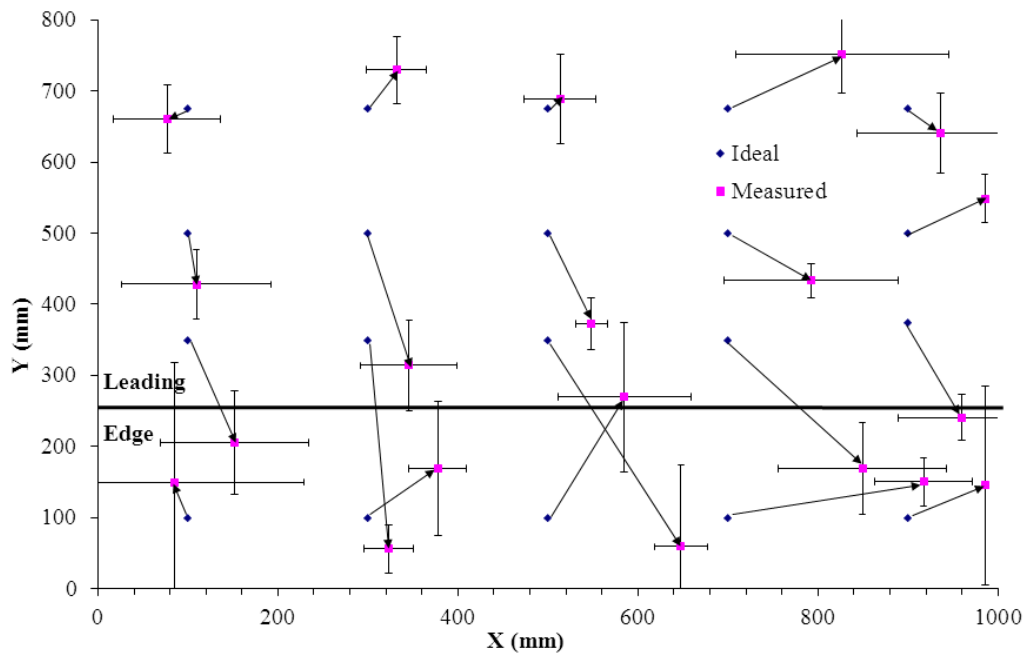
Figure 3.13. Average impact locations and the corresponding actual impact point obtained with the modified system.

It is clear that deviations from the model such as a curved structure and inhomogeneous wave speed are causing systematic errors. To counteract this, an Excel spreadsheet was created to use the same model to locate all of the impacts from this investigation. The spreadsheet allows the x and y wave speeds to be varied along with the positions of the sensors to see the effect of changing these parameters. To counteract the tendency of the system to place impacts to the right, the two left-hand sensors were virtually shifted 100 mm to the left. The wave speeds were also varied and the average error minimised to best map the data onto the correct points on the real surface. The optimum speeds were found to be $x = 1150$ ms^{-1} and $y = 1200$ ms^{-1}. These changes alter the lookup table and should lower the systematic error.

With these changes implemented in the system the same experimental procedure was repeated to obtain new data.
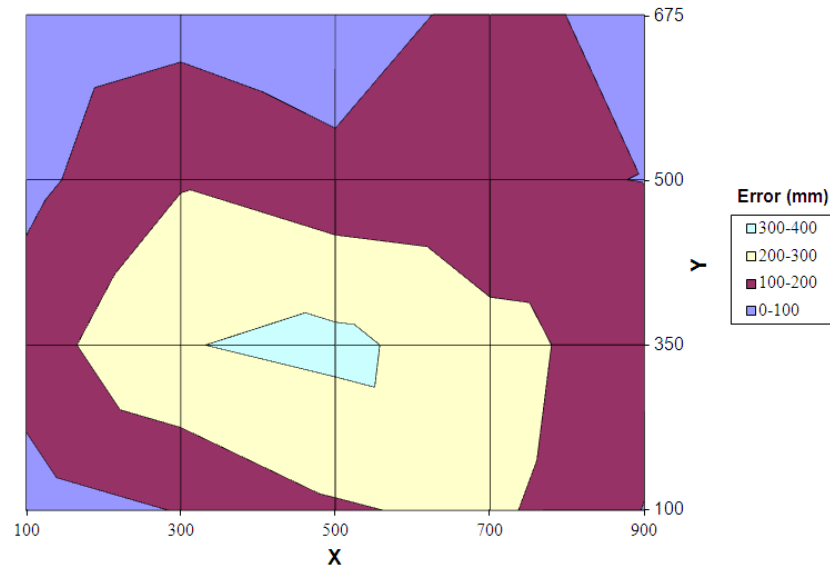
Figure 3.14. Error map of the structure from the data in Figure 3.13 for the modified system.

Figure 3.13 shows the average impact locations and their corresponding impact point detected using the modified system. These changes reduced the overall average error from 167 mm to 137 mm. Issues with the leading edge still exist, all of the impact locations immediately above the leading edge were placed on average below it. This effect is more significant near the centre and less pronounced near the sides. The distribution of the location error on the structure is illustrated in Figure 3.14. Similarly to the previous data, the average error for the top 10 locations was significantly lower than that of the lower 10 locations, 92 mm and 182 mm respectively. This further emphasises the significance of the leading edge on the accuracy of the system.

3.4. Neural Network

3.4.1. Theory

Knowledge of biological neural networks has inspired the development of artificial neural network (ANN) techniques which can be used to determine the relationship between input and output parameters [3.1]. The network is made up of a series of computing units or nodes which are connected by a set of connection strengths or weights. These connection strengths are parameters of the ANN, which are adjusted by a learning algorithm as a result of training [3.2]. The units are organised into layers: an input layer reacts to incoming information from outside of the system and an output layer generates the outputs of the system while any layers inbetween are known as

hidden layers. By training the system with example data, the weights between the layers can be determined allowing the system to produce an output from similar, but not identical, real data [3.3]. Neural networks have many applications typically where there is a need to approximate a complex relationship dependent on many parameters such as function approximation and pattern recognition [3.4,3.5,3.6].
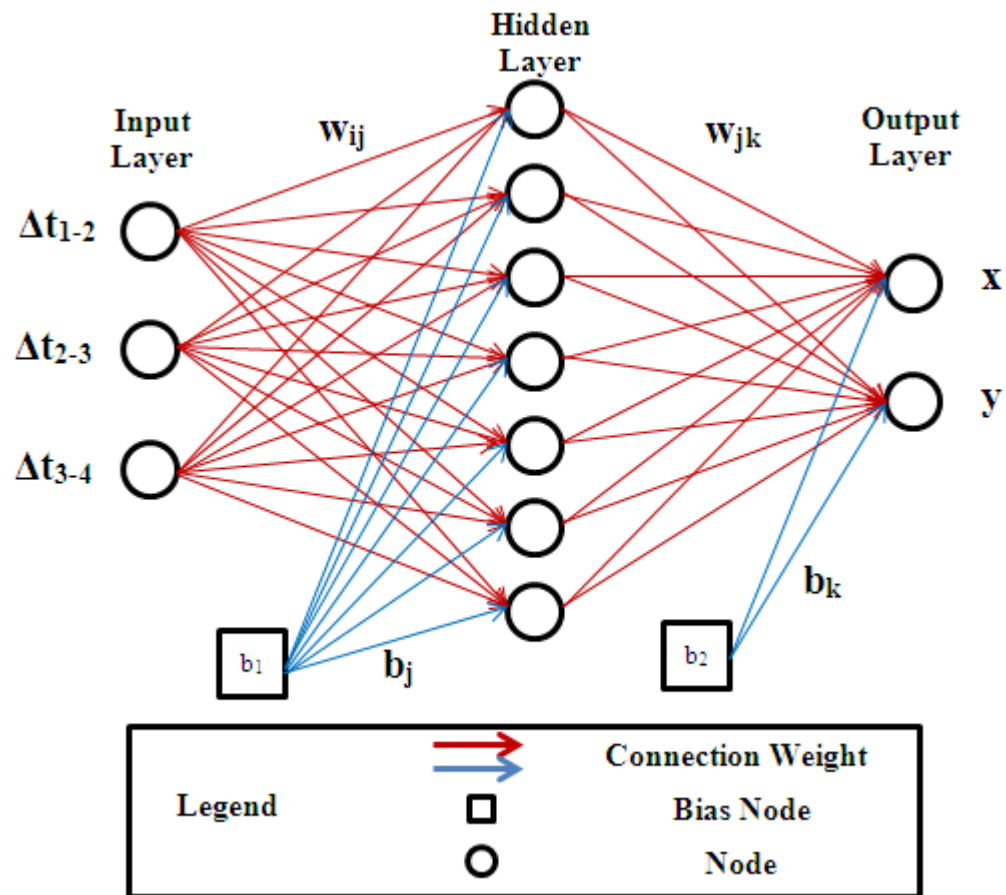
3.4.2. Implementation

Figure 3.15. Multilayer perceptron structure showing time inputs, position outputs and 7 node hidden layer.

Locating an impact on a complex surface shape using the time-of-flight information from several sensors is a problem that lends itself well to a neural network as it doesn't require an accurate model of the surface to be developed. The neural network implementation was developed using the Matlab neural network toolbox and run as a Matlab executable within a LabVIEW framework. The network was in the form of a multilayer perceptron structure with an input layer consisting of three input times, a hidden layer of 7 nodes and an output layer of two nodes which output the x and y co-ordinates of the determined impact location. The structure is illustrated in Figure 3.15.

The transfer function between layers is a hyperbolic tangent sigmoid:

74

$$\tan sig(n) = \frac{2}{1 + e^{-2n}} - 1 \qquad\qquad (3.3)$$

While the network is trained, all of the connection weights are recursively updated so that the network produces progressively closer to the desired output for a given input set. Through many training iterations the system "learns" the output location which corresponds to the distribution of input times without the need to understand the complex geometry itself. The network was trained using backpropagation learning in the form of the gradient descent momentum method with an adaptive learning rate. The training set comprised 262 input times and impact locations obtained from low energy impacts at 20 locations on the test structure with the mean squared error used as the performance function to test against. Following this, a further 40 inputs were presented to the system and the outputs simulated in order to test the performance using data that hadn't been used for training and resulted in an average position error of 79.6mm.

3.5.   Comparison of Location Techniques

A version of the LabVIEW program was produced that detected an impact and then simultaneously interpreted this data using both location methodologies allowing them to be compared in real time for identical data sets. Impacts were performed for 20 locations and the average location error was determined. The results for the triangulation method and the neural network method are displayed in Figure 3.16 and Figure 3.18 respectively. The triangulation method had an average location error of 130.9 mm and a standard deviation of 57.6 mm, which corresponds well to previous testing. The neural network method had an error of 89.8 mm and a standard deviation of 44.2 mm. This is a reduction in error of over 30% showing that the neural network technique produces a significant improvement.
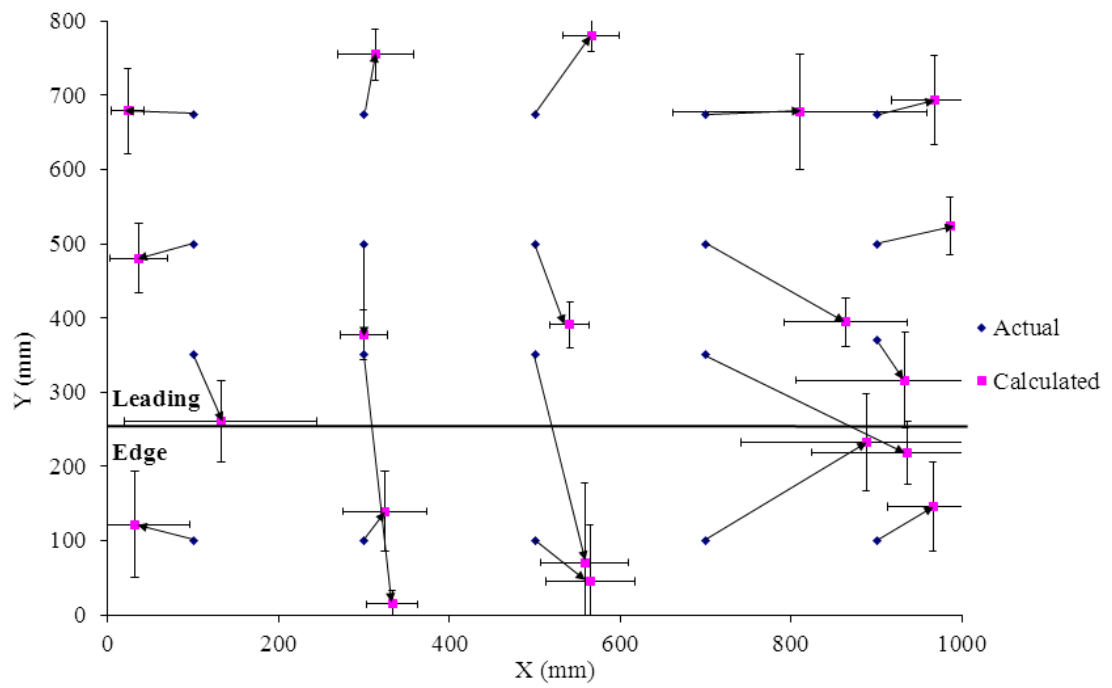
Figure 3.16. Calculated average impact locations and the corresponding actual impact point for the comparative data set using the triangulation method.
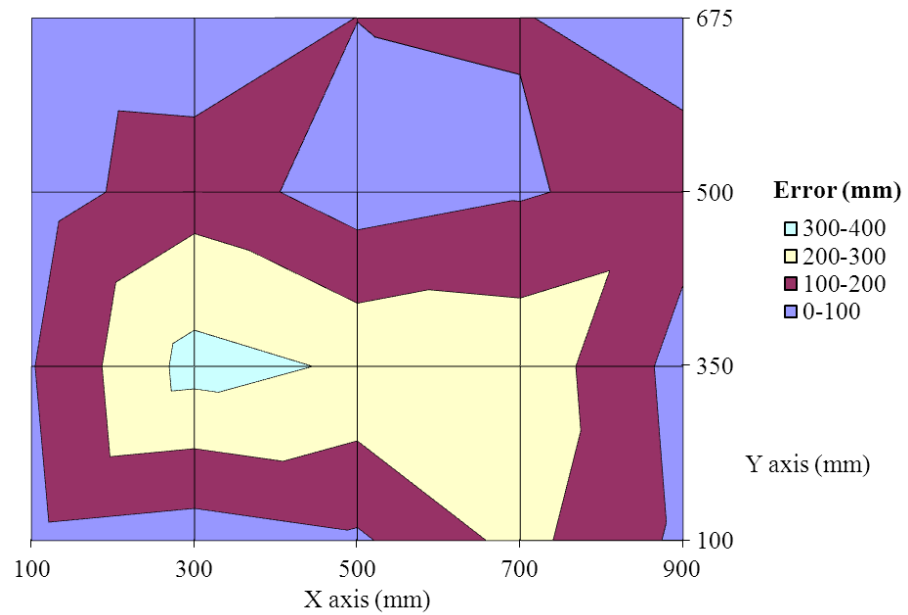

Figure 3.17. Error map computed for the triangulation method using the data represented in Figure 3.16 Error! Reference source not found.
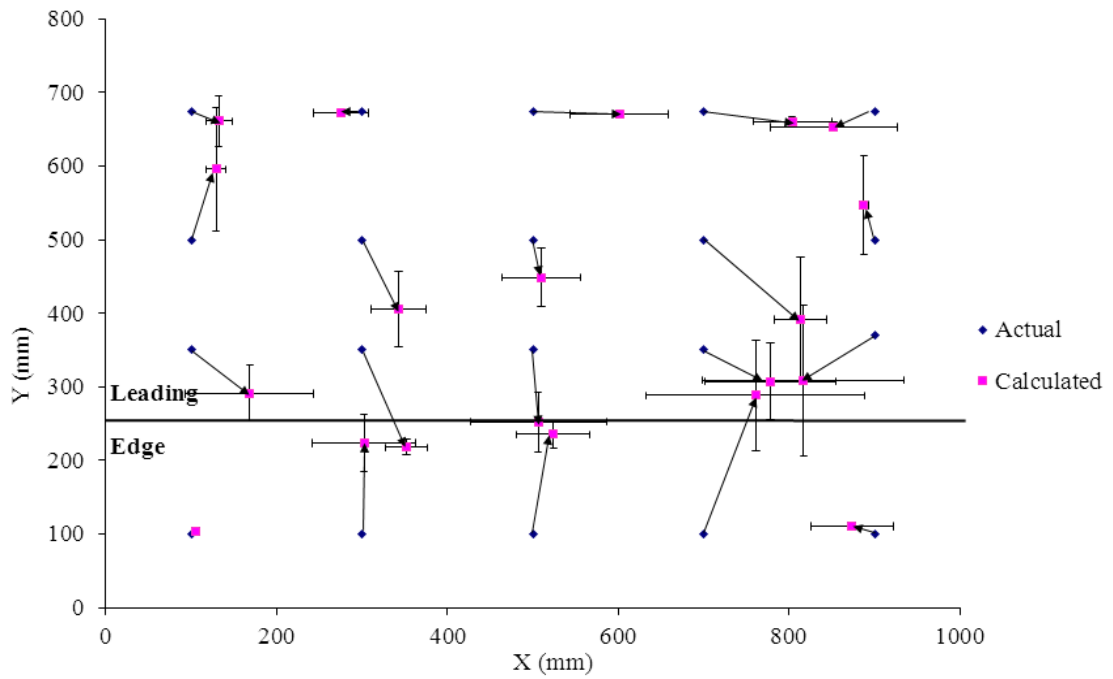
Figure 3.18. Calculated average impact locations and the corresponding actual impact point for the comparative data set using the neural network method.

This can be seen clearly by comparing Figure 3.17 and Figure 3.19 which are the error maps for the triangulation method and neural network method respectively. The adverse effect of the leading edge on the location accuracy has been reduced by the neural network method leading to a more consistent accuracy across the structure that is very beneficial in a real system.
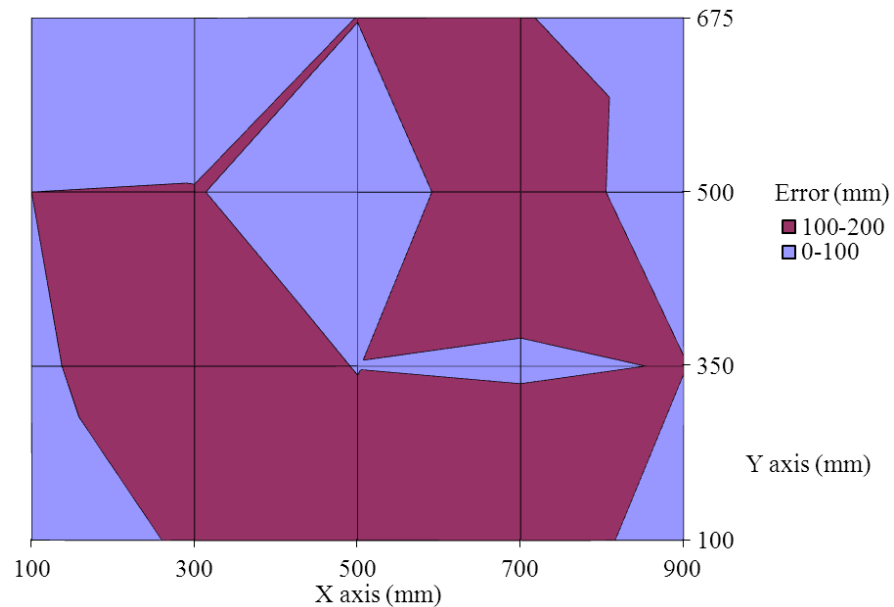
Figure 3.19. Error map computed for the neural network method using the data represented in Figure 3.18.

This improvement comes at the cost of a necessary training step including a large number of impacts on the structure in question. However, for a number of similar structures such as several aircraft of the same design, it is likely that the neural network developed and tested on one would be able to perform adequately on them all. This would require further study to prove and ascertain the accuracy of the system when operated on a different, but similar, structure.

3.6. FBG System

3.6.1. System design

The impact location system was also extended to allow the use of fibre optic sensors as an alternative to the piezoelectric sensors used thus far. An existing chirped fibre Bragg grating (CFBG) interrogation scheme with three sensors was expanded to include four sensors for this purpose using the technique pioneered in [3.7]. The principle of the technique is shown in Figure 3.20, the sensing grating spectrum, shown in red, shifts sideways across the fixed reference grating spectrum, shown in blue, as it is strained. This alters the amount of overlap between the two spectra and changes the amount of light reaching the detector. Figure 3.21 shows the optical diagram of the setup with a sensing grating and a matched interrogator grating highlighted, the signal of interest is measured at D1 (for sensor CFBG 1). An amplified spontaneous emission broadband lightsource is used to illuminate the gratings via a coupler tree arrangement to distribute the light to all gratings. If required, a second detector (D2 for CFBG 1) can be used to measure the light intensity reflected from the sensing grating allowing intensity variations to be compensated.
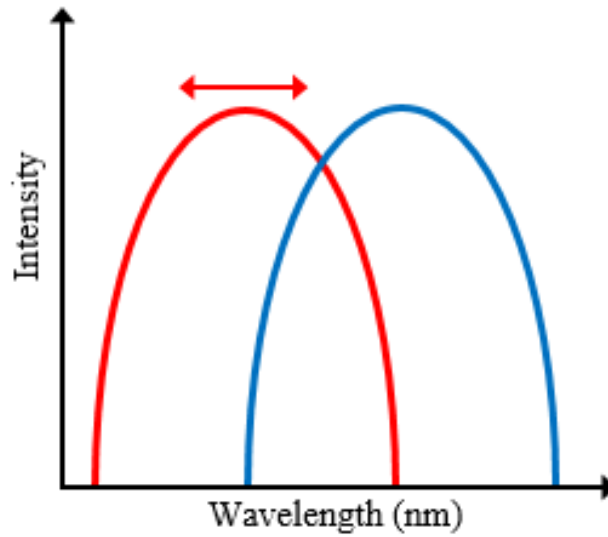
Figure 3.20. Diagram of interrogation principle, the sensing CFBG spectrum (red) will shift side to side across the fixed reference spectrum (blue) as the sensing grating is strained causing a change in intensity.
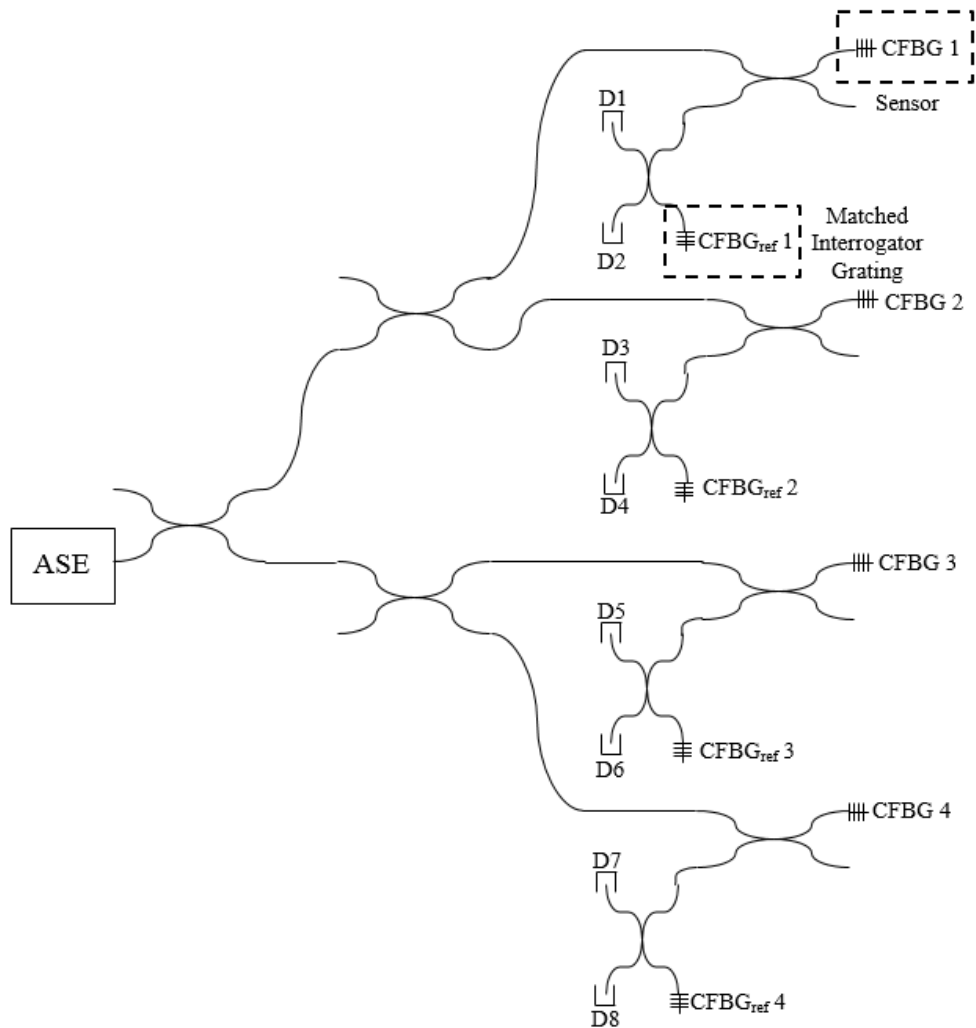

Figure 3.21. Optical diagram of chirped fibre Bragg grating (CFBG) interrogation scheme. ASE: amplified spontaneous emission broadband light source. D: detector.
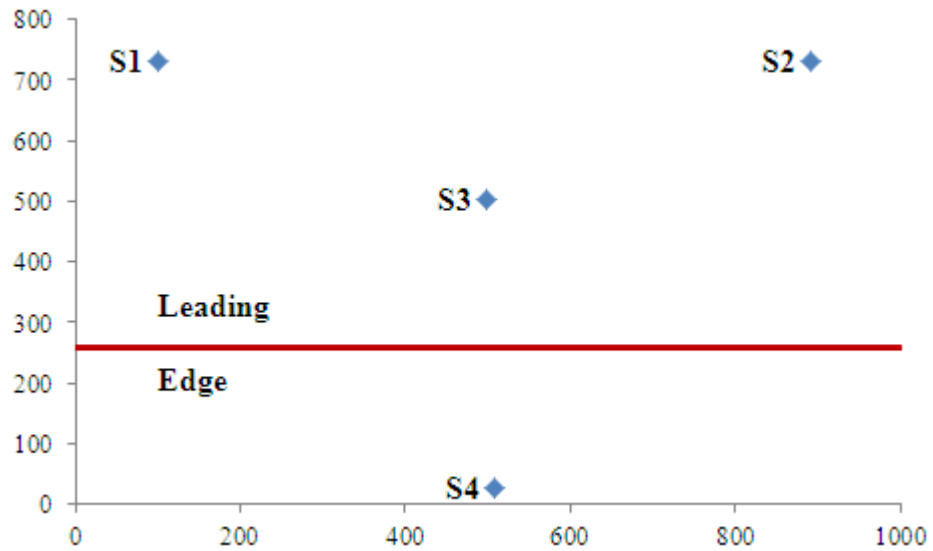
Figure 3.22. Locations of the four chirped fibre Bragg grating sensors on the test structure as well as the leading edge location.

The sensor gratings were embedded in the composite structure during manufacture for a different project and their position was not ideal for the current problem. The sensor locations are shown in Figure 3.22 along with the location of the leading edge.
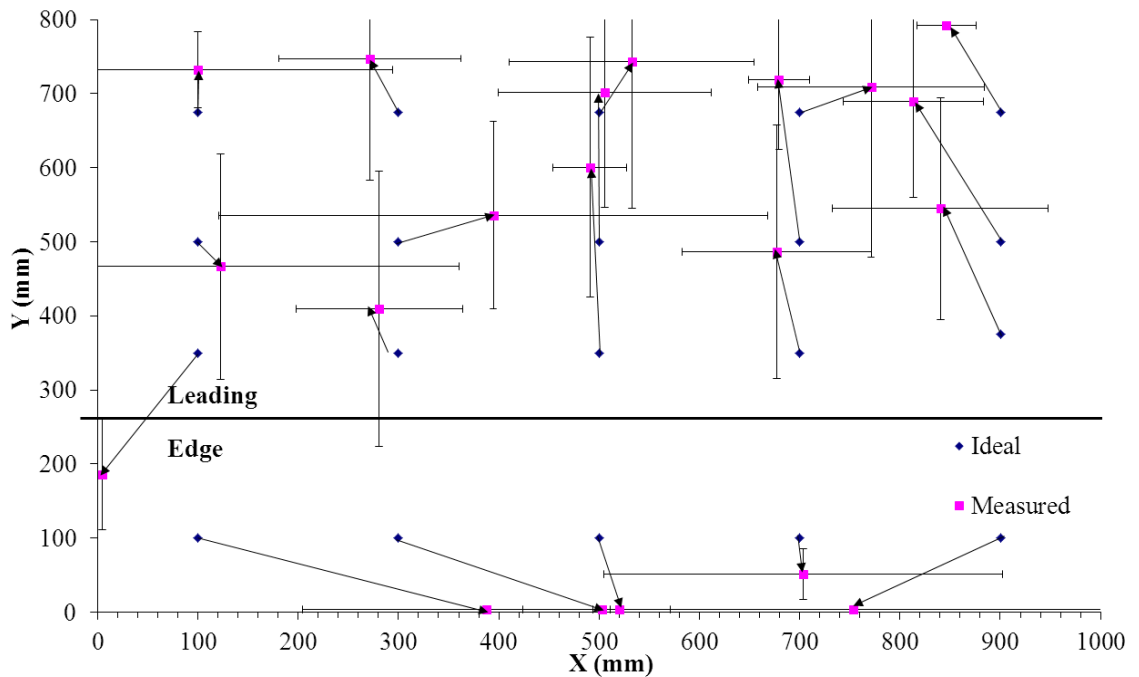
3.6.2. Results

Figure 3.23. Average impact locations and the corresponding actual impact point obtained with the optical sensor system and time-of-flight triangulation method.

To allow comparison with the results presented thus far utilising piezoelectric sensors the same experimental method was used and the results presented in Figure 3.23.

Notably, impacts below the leading edge were predicted to have occurred clustered towards the centre at the lowermost extent of the structure. This is likely caused by the presence of only one sensor below the leading edge meaning that all other signals will have experienced significant attenuation and the shortest path between impact and sensor will not be the same as the two dimensional model due to the strong curvature at the leading edge. The average position error was 143.0 mm and a standard deviation of 123.1 mm which is larger than that the results from the piezoelectric sensors which were 130.0 mm and a standard deviation of 57.6 mm. This is likely in large part due to the poor sensor positioning for the structure as locating impacts outside of the area encompassed by sensors is more imprecise than impacts within that area. Using sensors on the other side of the leading edge from the impact will lead to lower location accuracy and this should inform sensor placement decisions for complex structures such as this one. One configuration, which may help deal with this problem, would be two lines of sensors on the top surface of a wing and two lines on the lower surface leading to very accurate locations on the approximately flat surfaces and the two lines of sensors close to the leading edge would minimise attenuation by their small separation.

3.7. Conclusions

This work has demonstrated a laboratory based impact detection capable of detecting the position and energy of an impact. This has been achieved on a complex curved structure with similarities to a composite wing section without the need for a dense array of sensors. Reasonable location accuracy has been achieved using the time-of-flight triangulation technique with an average error of 67 mm in the *x*-direction, 7% of the width of the structure. In the *y*-direction, the average error was 49 mm, 6% of the height of the structure. A neural network based system was implemented for comparison and improved the overall location accuracy from 130.9 mm to 89.8 mm; an improvement of over 30%. This location accuracy was achieved with low energy impacts, well below the threshold for damage. In a real deployment, potentially damaging impacts would have a much higher energy and should therefore be easier to detect and locate. The error in the determination of the impact intensity corresponds to ±0.25 J. Although this error is quite significant for the low energy impacts used in this work the threshold for damage is in the tens of Joules and therefore the system is accurate enough to determine the energy of a potentially damaging impact.

The system was extended to use chirped fibre Bragg gratings and a reference grating based interrogation scheme utilising sensors that were already embedded in the test

structure. This system could also successfully detect and locate impacts though some areas, notably below the leading edge, had lower location accuracy due to the non-optimal sensor placement.

3.8. References

[3.1] C. Y. Park, B.-W. Jang, J. H. Kim, C.-G. Kim, and S.-M. Jun, "*Bird strike event monitoring in a composite UAV wing using high speed optical fiber sensing system*", Composites Science and Technology, **72**, pp. 498–505 (2012).

[3.2] R. M. Golden, "*Exploring the Diversity of Artificial Neural Network Architectures*", Journal of Mathematical Psychology, **41**, pp. 287-292 (1997).

[3.3] W. B. Lyons, C. Flanagan, E. Lewis, H. Ewald, and S. Lochmann, "*Interrogation of multipoint optical fibre sensor signals based on artificial neural network pattern recognition techniques*", Sensors and Actuators A, **114,** pp. 7–12 (2004).

[3.4] E. Lewis, C. Sheridan, M. O'Farrell, D. King, C. Flanagan, W. B. Lyons, and C. Fitzpatrick, "*Principal component analysis and artificial neural network based approach to analysing optical fibre sensors signals*", Sensors and Actuators A, **136**, pp. 28–38 (2007).

[3.5] S. E. Watkins, F. Akhavan, R. Dua, K. Chandrashekhara and D. C. Wunsch, "*Impact-induced damage characterization of composite plates using neural networks*", Smart Mater. Struct., **16**, pp. 515–524 (2007).

[3.6] Y. -G. Lee, B. -W. Jang, Y. -Y. Kim, C. -G. Kim, C. -Y. Park, and B. -W. Lee, "*Detection of Impact Locations on Composite Wing Structure Using FBG Sensors*", Asia-Pacific Workshop on Structural Health Monitoring 2010, The University of Tokyo, Tokyo, Japan (2010).

[3.7] R. W. Fallon, L. Zhang, A. Gloag, I. Bennion, *"Identical broadband chirped grating interrogation technique for temperature and strain sensing"*, Electronics Letters, **33**, (8), pp. 705-707 (1997).

Chapter 4 - Damage Classification

4.1.   Introduction

Laminated composites are widely used on aircraft as fuselage or wing skins because of their low mass, controllable geometry and adaptable properties, see §2.1. Low velocity impacts can weaken such composite structures, yet leave little visible sign of damage, for example composite delamination will significantly affect structural integrity but may not show external signs of damage [4.1]. Clearly, detection of such barely visible impact damage is an issue for the maintenance of aircraft employing composites. Manual inspection techniques to detect such damage can be costly, time consuming and risk overlooking damaged areas. An alternative approach is to have an automatic system to detect impacts. Ideally this should be able to distinguish between damaging impacts and those that can be safely ignored. Ultimately, such automated systems could reduce or remove the need for costly scheduled inspections altogether and allow for condition based maintenance (CBM).

Several studies have investigated impact interactions with composites including the contact force and strain experienced during the impact event [4.2,4.3,4.4].

These studies tend to use small test structures and reproducible test conditions to allow accurate comparisons between different materials or different composite stacking sequences. They often rely on instrumented impactors such as large test rigs fitted with accelerometers to determine the dynamics of the interaction. However, in a realistic impact scenario, such as a birdstrike, the impact shape and force will be unknown and sensing must be realised by the structure or sensors attached to it. Sensors capable of passively detecting dynamic strain such as piezoelectric [4.5,4.6] or fibre-optic sensors [4.7,4.8] can be bonded to the surface or incorporated into the composite material itself to monitor the strain during an impact.

The work in this chapter focuses on the development of a technique to differentiate between damaging and non-damaging impact by analysis of dynamic strain signals captured during the impact event. This was achieved with the generation of a large dataset of signals captured using a piezoelectric sensor during low velocity impact. Both damaging and non-damaging impacts were carried out so that the signals could be analysed for reproducible differences. Finally, a method to automatically analyse an impact signal and determine whether the impact was damaging was developed based on this imformation. Large composite panels (0.5 m by 0.5 m and larger) were used to

closely emulate a realistic scenario with impacts carried out at many locations with varying distance from the sensor. This is important because laminated composites can be highly attenuating. Attenuation of plate waves is typically ~ 40 dB over the first few centimetres due to geometric spreading while in the far field the attenuation of the flexural mode may be as high as 83 dB m^{-1} [4.9].

4.2.   Impact Tests

Impact tests were carried out using a drop-tower allowing a weight to be dropped from a wide range of fixed heights in order to change the energy of the impact. Two different weights were used with the same, removable hemispherical impact point to give a repeatable interaction with the composite panel. A 1.02 kg weight was used for impact energies up to 10 J while a 5.09 kg weight was used for higher energy impacts upto 50 J. The impactor is considered as a free falling rigid body. It is assumed that all of the energy from the change in gravitational potential goes into the impact energy and that there are no losses due to friction between the weight and the tower.

A low profile piezoelectric sensor was permanently bonded to the underside of each of the panels tested using quick setting epoxy adhesive. The sensor is a broadband, non-resonant sensor created from a packaged PZT disk with a 10 mm diameter and 0.2 mm thickness. It is designed to detect the acoustic wave caused by the impact and is sensitive from d.c. to several hundred kilohertz. The unprocessed sensor output and a 50-450 kHz passband filtered signal were recorded at 5 Msamples s^{-1} with an 8 bit resolution A/D. The filtered data was captured in order to allow the small high frequency components of the signal to be investigated without them being buried in the large low frequency strain signal. The filter transmission characteristic is shown in Figure 4.1, it was measured by measuring the input and output from the filter as the input frequency was varied using a signal generator.
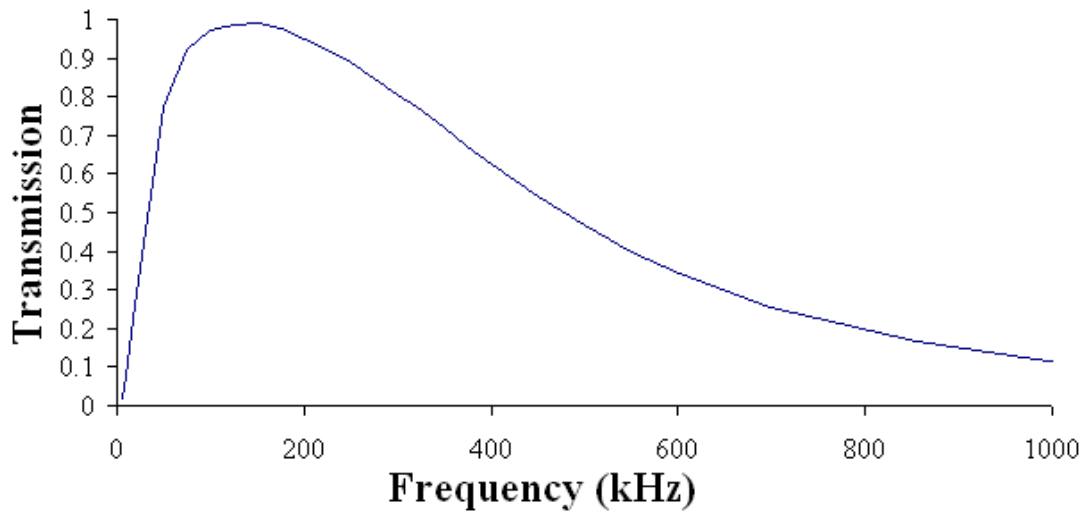
Figure 4.1. Transmission characteristic for the passband filter.

For panel 2 (see below) the sample rate was reduced to 2.5 Msamples s^{-1} to double the signal length, which was limited by the data capture apparatus, as preliminary impacts showed that some features appeared later due to the larger panel size. This may be because the larger panel took longer to reach maximum deflection and therefore maximum force. The passband filter was employed to improve bit resolution on the high frequency content which is small when compared to the large low frequency component.

Two composite panels were tested in this study:

Panel 1

Glass fibre and LM100 resin flat panel with a foam insert in the centre section, shown in Figure 4.2. The panel is 535 mm square with a 2 mm thickness at the edge section and 7 mm thick in the centre section. The panel was marked for impact at 31 locations in a grid excluding the corners at which points the panel was supported.
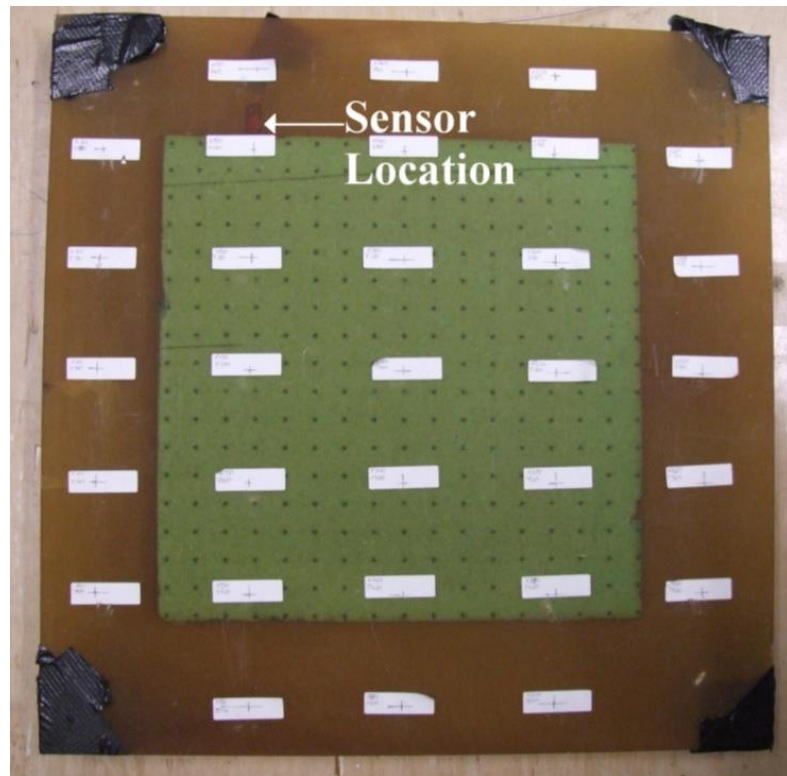
Figure 4.2. Image of the glass fibre panel used in this study. 535 mm square with foam insert (green) in centre section.

Panel 2

This is a monolithic carbon fibre and MTM46 resin panel, shown in

Figure 4.3, it is 700 mm square and approximately 4.5 mm thick. In this case the panel supports were designed to more realistically emulate aircraft substructure with the panel affixed to a frame constructed from aluminium 'C'-section supports.
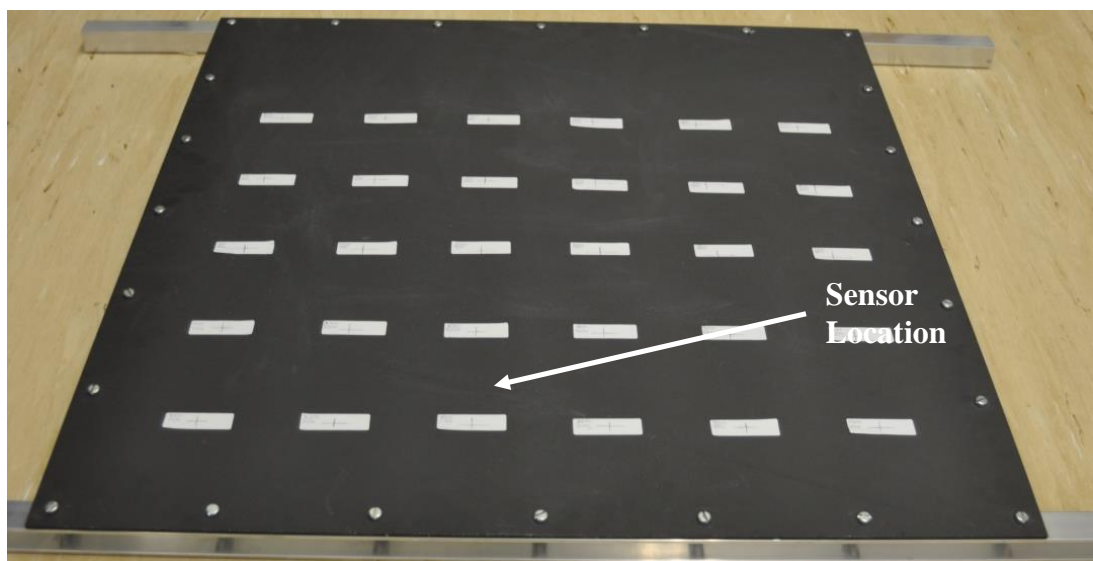

Figure 4.3. Image of composite panel used in this study. Here panel 2 is a carbon fibre panel bolted to a frame constructed from aluminium C-section (along all sides).

Initially both panels were subjected to non-damaging low energy impacts. At each grid position one or more impacts of different energies were performed. Recording these impacts provides data to assess signal variation due to impact energy or distance to the sensor. The panels were then subjected to higher energy impacts designed to cause damage. Fewer high energy impacts were recorded for each panel as an impact site cannot be reused once damage has occurred.

For the glass fibre panel (panel 1), the emphasis was on building up a large dataset of non-damaging impacts over a range of energies upto 10 J which could be used to differentiate between effects due to damaging impacts. 217 impacts were carried out of which 13 were damaging. The emphasis for the carbon fibre panel (panel 2) was to create a more realistic scenario by using a larger panel bolted to a metal supporting frame and to perform a larger proportion of damaging impacts. This was intended to corroborate results from the first panel, investigate the generality of the technique and to put into practice improvements based upon knowledge gained from the earlier experiments on panel l. 88 impacts were carried out of which 24 were damaging over a range of distances (50-500 mm) between sensor and impact site. A number of impacts on panel 2 were captured using a hi-speed camera operating at 440 frames per second. This data was then used to determine the dynamics of the impact in particular the overall contact time and time to maximum panel deflection, the results are shown in §4.3.1.
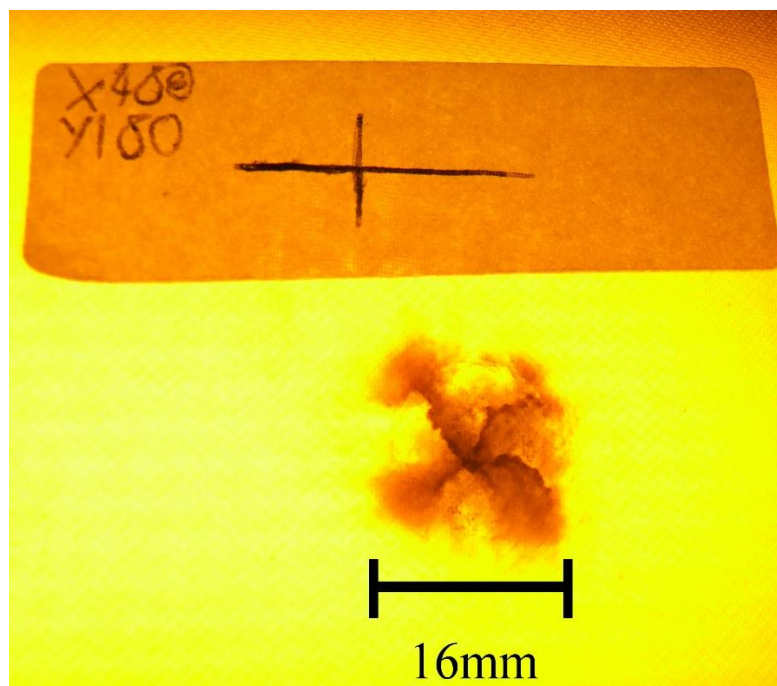

Figure 4.4. Visible impact damage from 40 J impact on panel 1, backlit with a lamp. Translucent panel becomes locally opaque.

The undamaged glass fibre composite used in panel 1 was translucent; impact damage caused the local region to become opaque. Thus, it was relatively easy to determine when damage had occurred and to what extent, see Figure 4.4. However this is not true for the opaque, carbon fibre composite. Here, once all the impact tests had been completed, an ultrasonic non-destructive testing technique ('C'-scan [4.10]) was used to determine the presence and size of damage, shown in Figure 4.5.
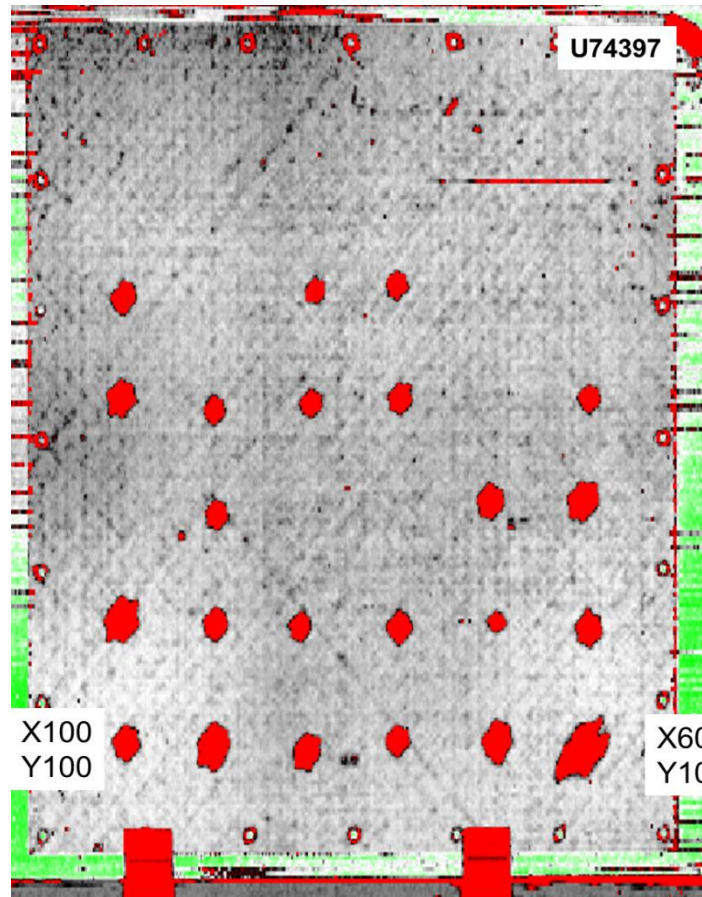

Figure 4.5. Ultrasonic testing results for panel 2 with red indicative of damage. Two red rectangles are clamps.

4.3. Experimental Results

4.3.1. Impact signals

Typical unfiltered signals vary considerably due to the dynamics of the impact location and impact energy and are dominated by low-frequency components, a low energy impact is shown in Figure 4.6. For comparison, Figure 4.7 shows an unfiltered damaging impact that has a much larger amplitude than the low energy, non-damaging impact. The measured voltage is related to the surface strain, larger impacts will therefore produce a higher voltage though this may not necessarily signify damage. They have few obvious definable features that could provide a 'fingerprint' confirming damage and, as such, they are weak candidates for a reliable damage detection system.
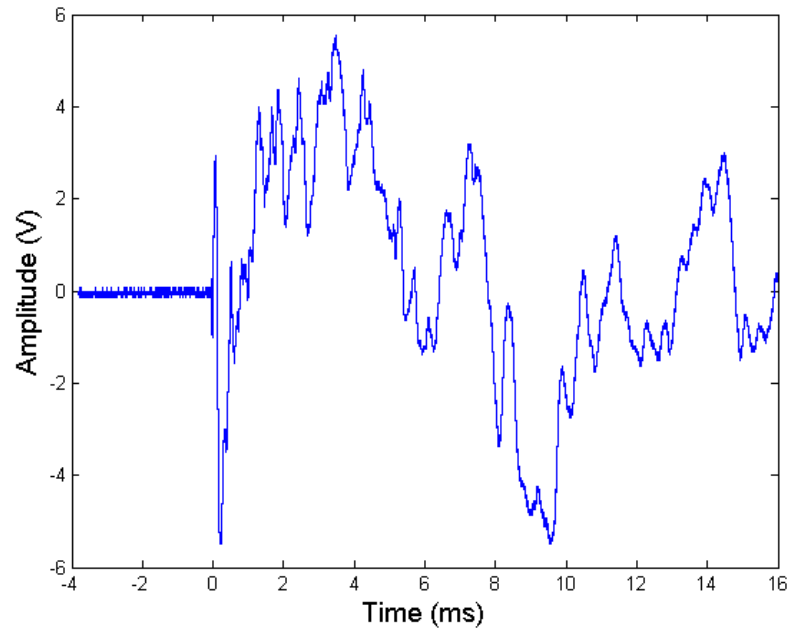
Figure 4.6. Unfiltered signal from a 1 J non-damaging impact on panel 2.
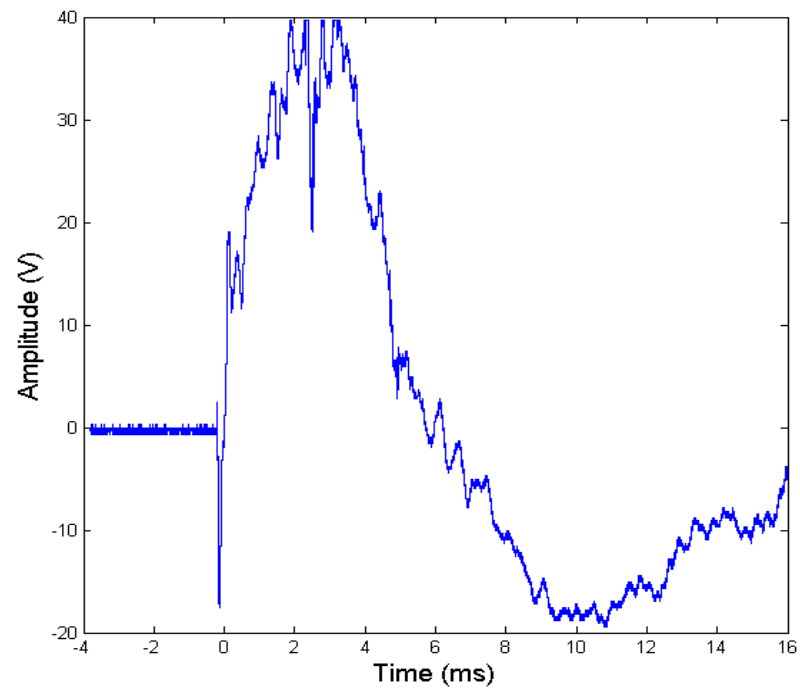

Figure 4.7. Unfiltered signal from a 30 J damaging impact on panel 2.

The filtered signals appear to be more useful and all have an initial 'burst' corresponding to the impact event. It was found that for higher energy impacts, one or more secondary pulses are present whose magnitude does not appear to level off with increasing energy.
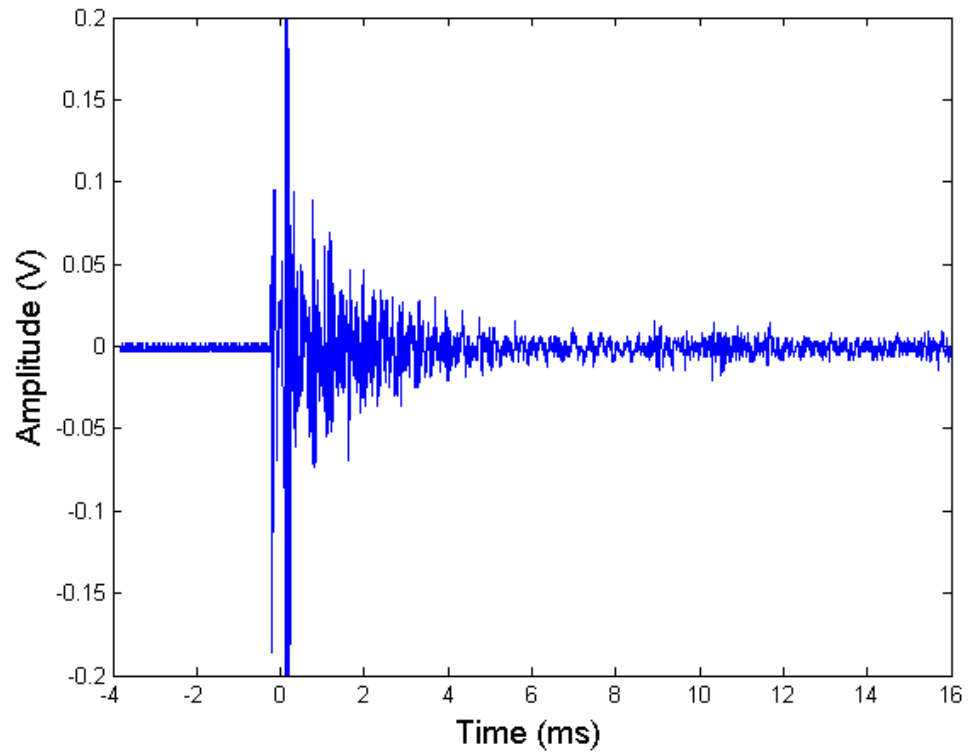
Figure 4.8. Bandpass filtered signals from a 1 J non-damaging impact.
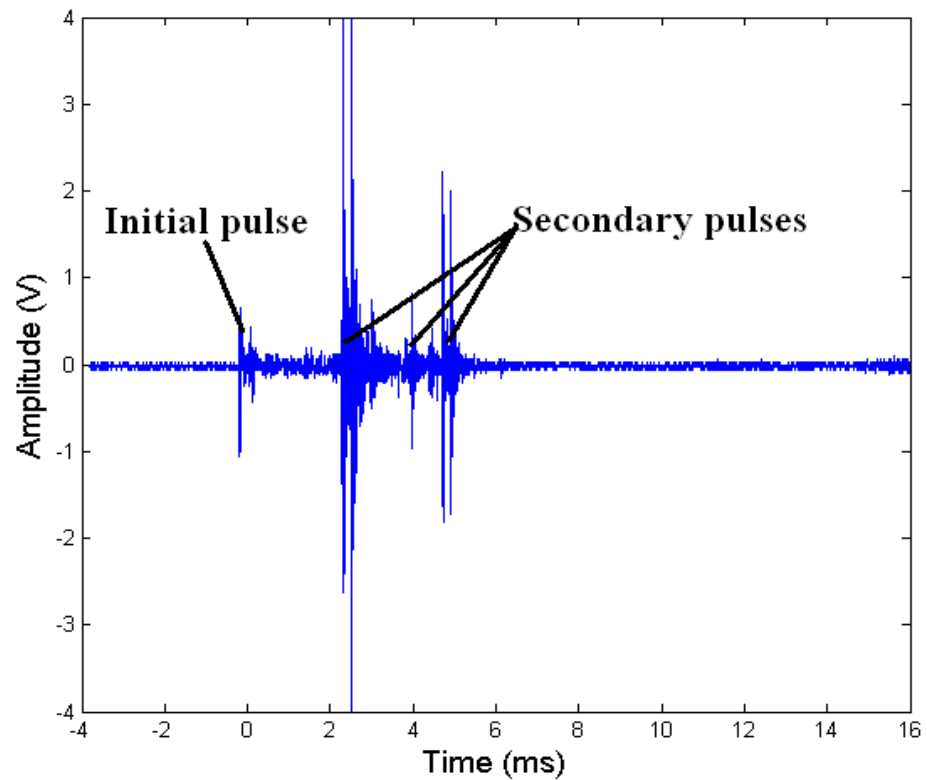

Figure 4.9. Bandpass filtered signals from 30 J damaging impact with initial and secondary pulses labelled.

Figure 4.8 shows the bandpass filtered signal from a low energy damaging impact featuring an initial burst while Figure 4.9 features both initial and secondary pulses and is from a 30 J damaging impact. Figure 4.10 provides more damaging impacts at a range

90

of locations for comparison and demonstrates the variation in the time between initial and secondary pulses.
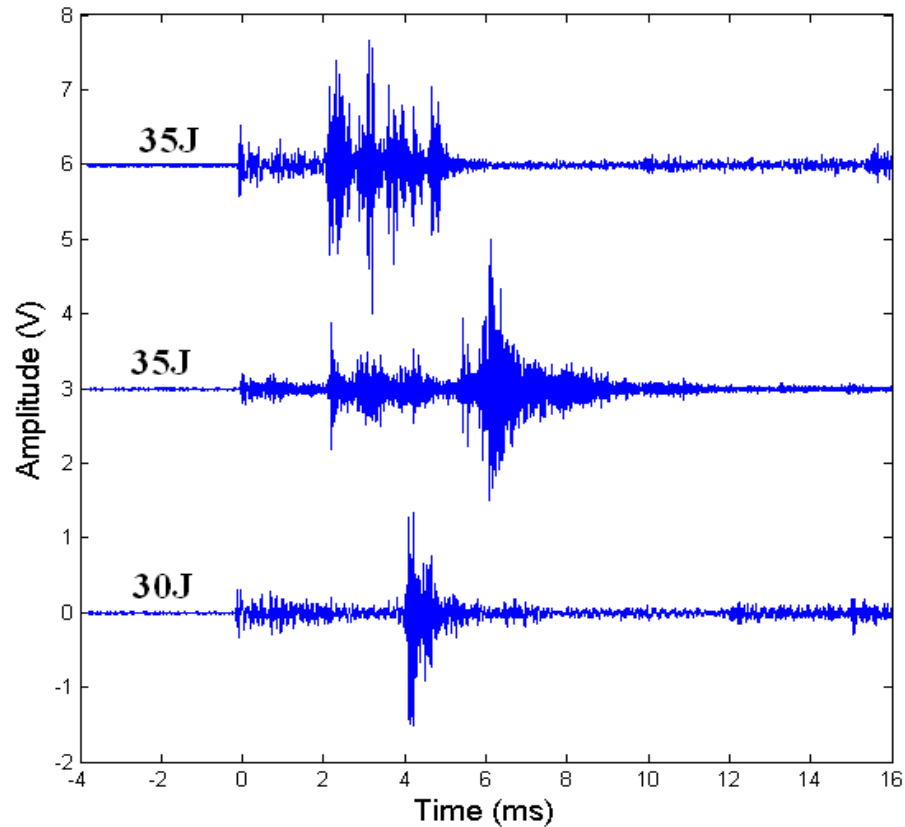

Figure 4.10. Three examples of damaging impacts, 30 J – 35 J at different locations on panel 2, showing significant secondary pulses (vertically offset for clarity).

Figure 4.11 shows 10 low energy impacts from 1-10 J for two locations away from the foam insert on panel 1, the two colours represent the two locations. Also included is a 40 J highly damaging impact from each of the locations allowing comparison between non-damaging and damaging impacts. The magnitude of the initial burst increases with increasing energy before levelling off and approaching a saturation point. It can be seen that the initial pulse increases in both duration and intensity with increasing energy until it appears to saturate above 5 J. Even the initial pulse of the 40 J impact has a similar amplitude and duration confirming that this initial pulse saturates well below the threshold for damage. For the damaging impact at both locations the secondary pulse can also be identified. The secondary pulse at location 1 (red) had a significantly greater amplitude than the initial pulse while both pulses at location 2 (blue) were approximately equal. This may indicate that the damage was more servere at location 1 or perhaps occurred over a shorter time frame. It can be seen that the secondary pulse of the impact at location 2 (blue) arrived approximately 5 ms after the impact while that of the impact at location 1 (red) arrives about 4 ms after the impact.
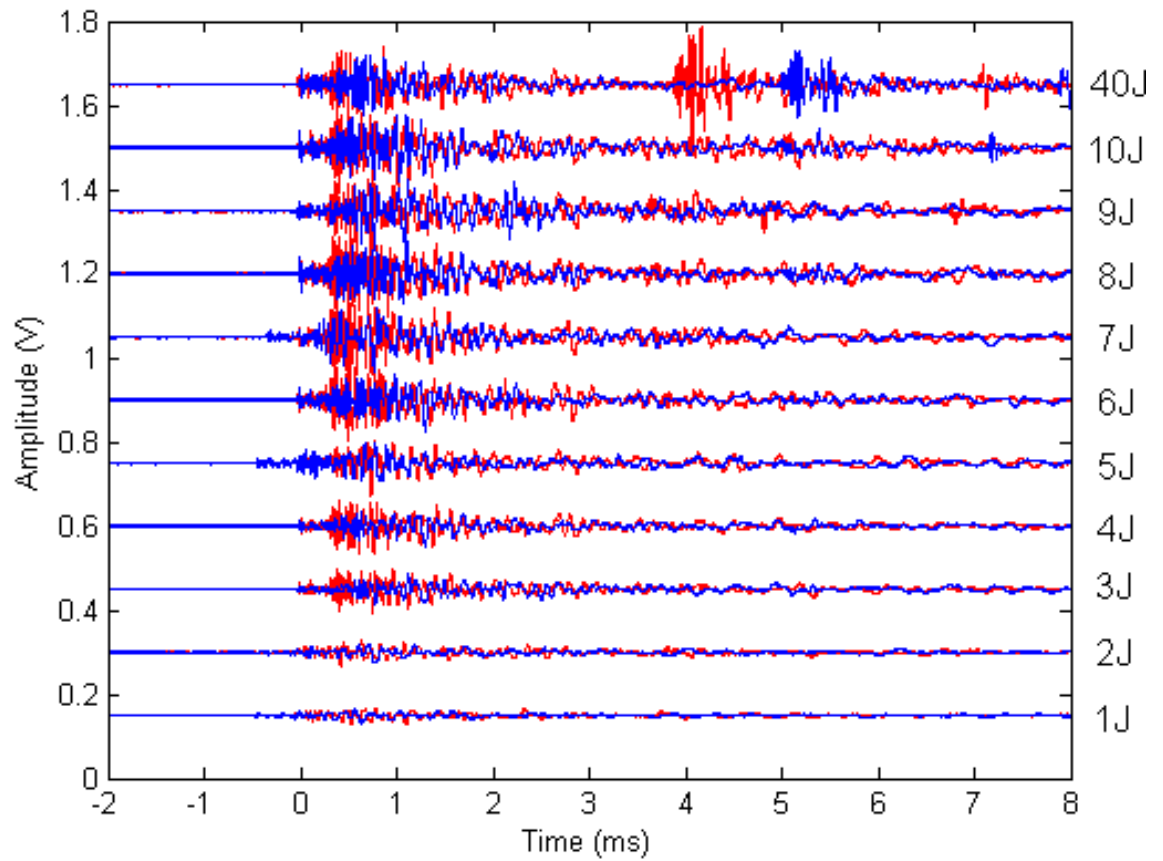
Figure 4.11. Filtered signals (blue) from 10 low energy impacts and one high energy damaging impact (40 J) on panel 1, all repeated at another location (red). Vertically offset for clarity.

To investigate whether repeated damaging impacts at the same location would show the same characteristics, one non-damaging and then two successive damaging impacts were performed at one location, shown in Figure 4.12. The first damaging impact (23 J) has a single secondary pulse while the second damaging impact (35 J) produced a similar secondary peak in the same temporal location as well as a pulse both before and after. It appears that the second damaging impact damaged that location further and showed even more intense secondary features than the first.
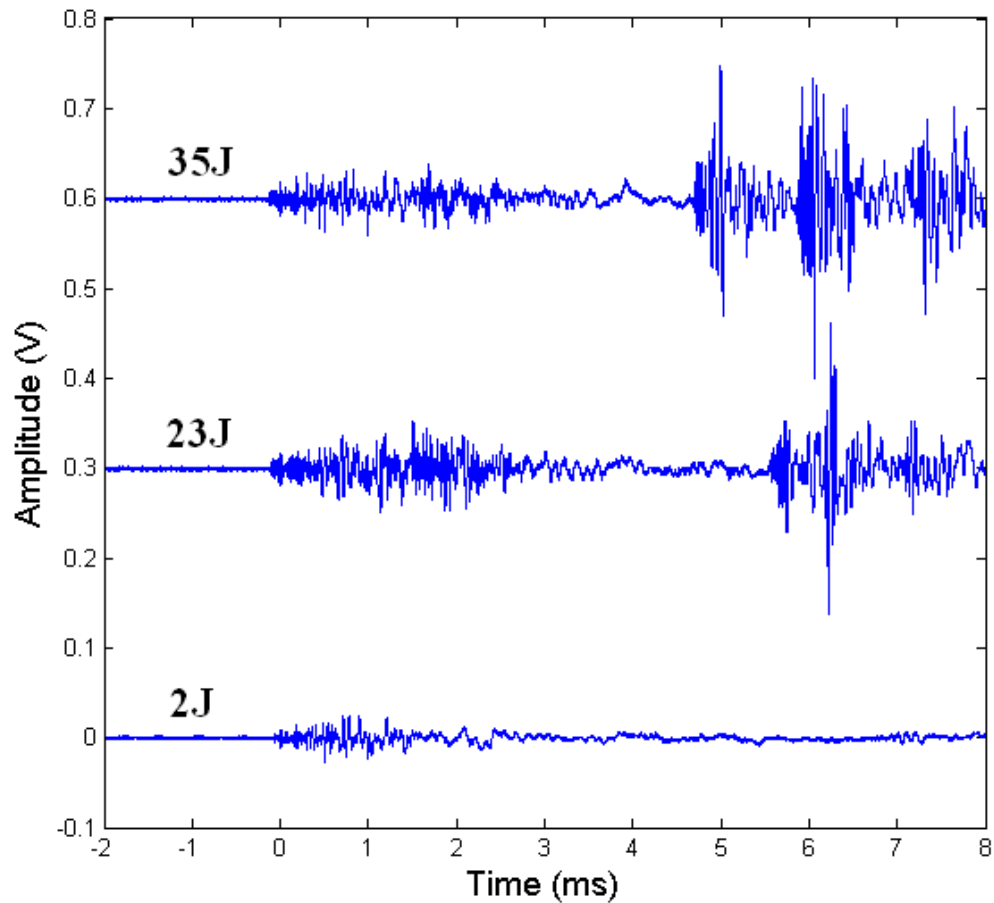
Figure 4.12. A non-damaging impact (2 J) followed by two successive damaging impacts at the same location on panel 2, showing the appearance of secondary pulses (offset for clarity).

We believe that this secondary pulse occurs due to acoustic emission during damage creation through one of several failure mechanisms. Damage will occur when a certain force threshold is exceeded in the material causing release, via acoustic emission, of a proportion of the stored energy in the panel. Several studies have investigated acoustic emission during quasi-static and cyclic tensile tests of composite panels; acoustic emission was found to occur during composite damage creation including matrix cracking, fibre breakage, fibre pull-out and delamination [4.11, 4.12].

The time difference between the initial and secondary pulses varies significantly and appears to depend on the material properties, the impact location and the velocity of the impactor. High-speed video (Figure 4.13) indicates that the maximum panel deflection for panel 2 occurred between 5-9 ms after initial contact, where the longest delay corresponded to impacts near the centre of the panel. This is largely due to the difference in local stiffness across the panels resulting from the location and nature of the supports. The high-speed video also confirmed that the secondary pulses definitely could not be due to any secondary impacts as these occur much later, after the signal acquisition has been completed.
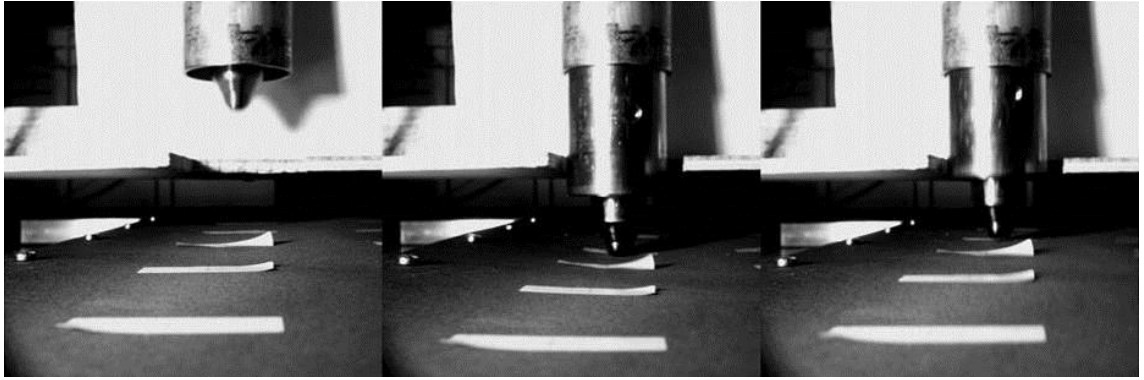
93

Figure 4.13. High speed camera footage of an impact captured at 440 frames per second. Left image shows the impactor falling, it is at maximum deflection in the centre and just releasing from the panel on the right.

4.3.2. Frequency analysis of strain data

To investigate the frequency distribution of the signal, spectrograms (sonograms) were produced from all of the damaging impacts and the corresponding non-damaging impacts at those locations. In these spectrograms the frequency of the signal is shown horizontally, the time vertically and the intensity of the signal is indicated by colour (on a decibel scale). The spectrograms were produced with a Hamming window length of 1024 samples with an overlap of 768, this means that every time band corresponds to 0.05 ms. The fast Fourier transform (FFT) length (number of frequency bands) was chosen to be 1024 samples to ensure any fine detail could be distinguished.

Figure 4.14 shows a spectrogram created from a 10 J non-damaging impact on panel 1. The initial pulse can be seen beginning at 2ms and has the highest intensity of the signal as well as higher frequency content upto 80 kHz. For comparison, Figure 4.15 shows a 40 J damaging impact at the same location. The secondary pulse can be seen and includes the highest intensity section of the signal which is between 15-30 kHz as well as even higher frequencies similar to those present in the initial pulse. The spectrograms are useful to investigate the high frequency content of the signals and see the differences in different sections of the signal. The higher intensity of high frequency content in the secondary pulses gives further evidence that the secondary pulses are caused by a different mechanism than that of the initial pulses. The initial pulse may be created in the initial impact process when the impactor grinds into the surface or due to minimal matrix cracking or crushing that is too small to be found through NDT. As described in §2.1.3 there are several damage modes for composite materials during impact, for instance, delamination occurs after a threshold energy has been reached in the presense of a matrix crack. As the damaged locations show signs of delamination in the NDT results it seems plausible, or even likely, that once the force becomes large

94

enough as the panels flexes under impact, delamination occurs releasing a burst of acoustic waves which is being detected as the secondary pulse feature.
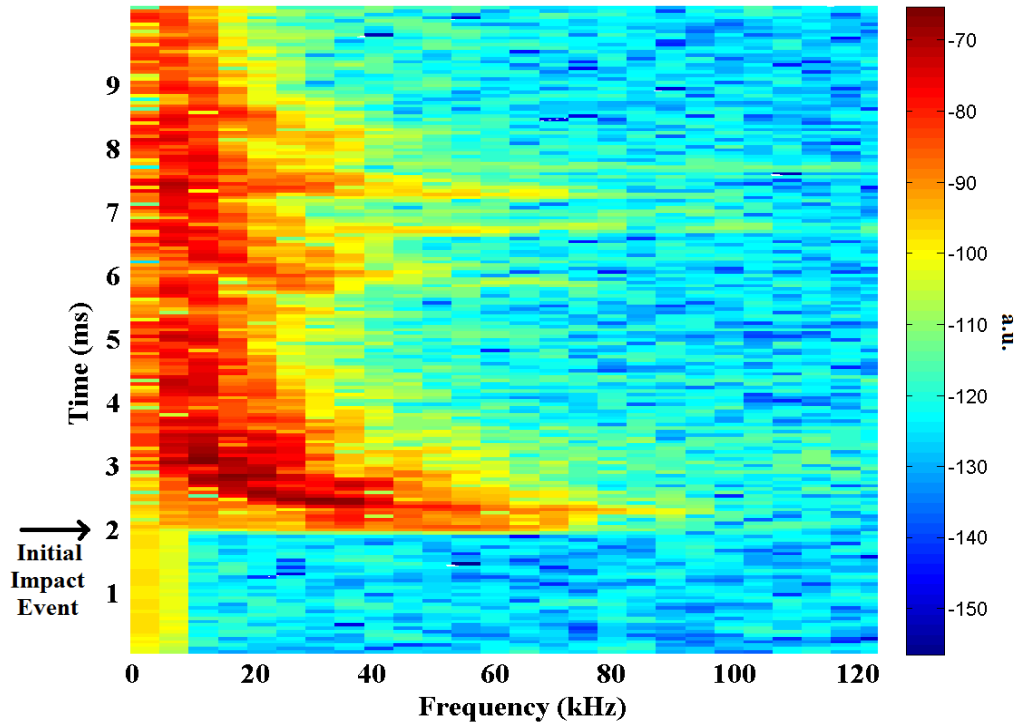

Figure 4.14. Spectrogram of a 10 J non-damaging impact on panel 1 showing the frequency distribution of the signal as it evolves with time. The logarithmic colour scale shows intensity with arbitrary units.
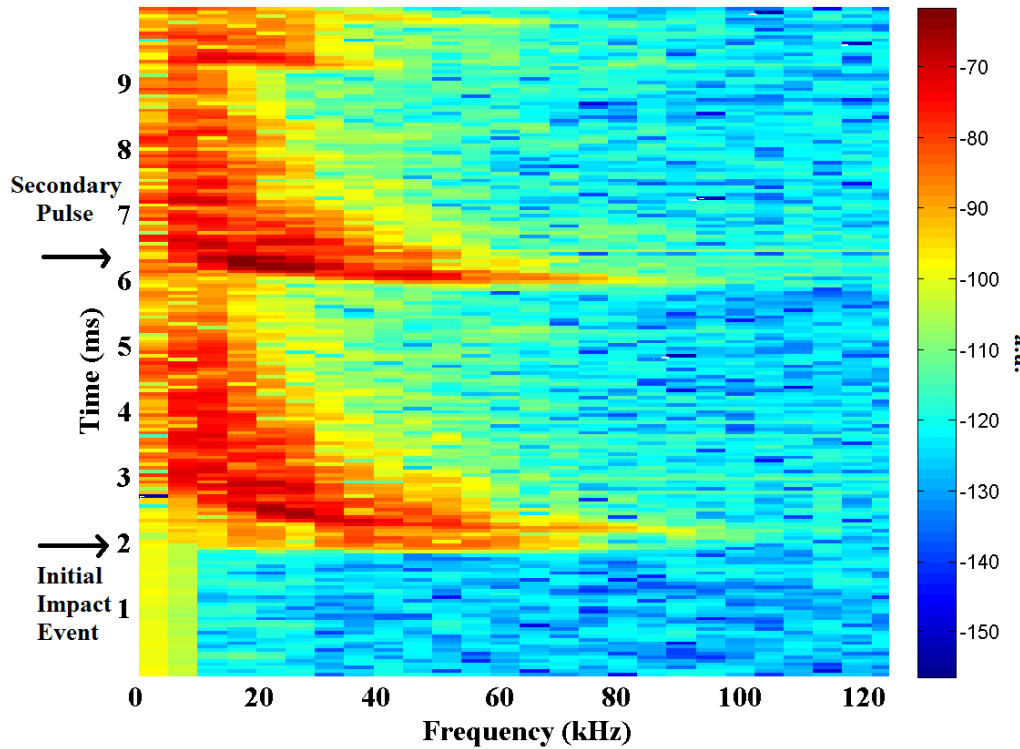

Figure 4.15. Spectrogram of a 40 J damaging impact on panel 1 showing the frequency distribution of the signal as it evolves with time, it can be seen that there is a high intensity secondary pulse feature, most intense between 15-30 kHz. The logarithmic colour scale shows intensity with arbitrary units.

95

4.4.   Impact Damage Classification

It is proposed that the presence of the secondary pulse feature identified in §4.3 could be used as a signature of potentially damaging impacts and algorithms to achieve automated classification of these were developed. Interpretation of data in comparison to visual inspection for damage and post experimental NDT reveals that the mere presence of a secondary pulse is not sufficient to identify damage. When the impact is close to the sensor then the signal-to-noise ratio is good and the initial and any subsequent pulses can be easily identified, however, when the separation increases the signal-to-noise ratio drops significantly due to the highly attenuating composite material. In extreme cases, the initial impact peak has been attenuated to the noise level during its travel to the sensor. This can make it appear that there are secondary pulses even for lower energy non-damaging impacts but those peaks are just noise. Therefore, a measure is required to test the significance of such secondary peaks, the most robust measure of damage was found to be the ratio between the magnitudes of the largest secondary peak and the initial peak. This ratio was termed the 'Damage Rating'.
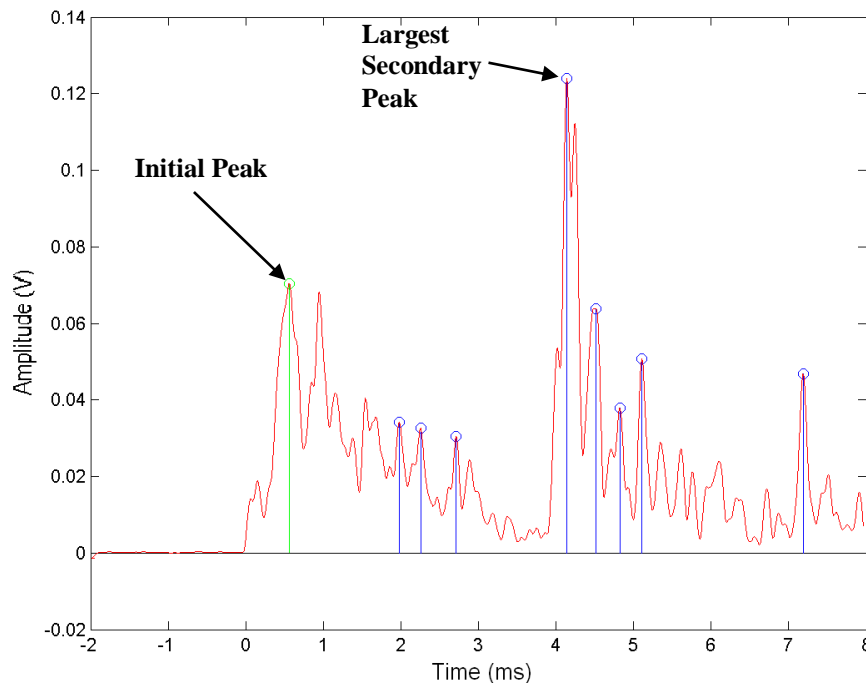

Figure 4.16. Envelope plot of a 40 J damaging impact on panel 1 with peaks indicated corresponding to a Damage Rating of 1.76.

To achieve automated calculation of this ratio, the envelope of the signal was first computed. This was done by squaring the signal to make all peaks positive and then low pass filtering the result to leave just the significant peaks. This was then corrected using the pretrigger data to give a consistent baseline at 0 V. A peak detection function is then used to detect a peak above a certain threshold and designate it as the initial

96

peak. This threshold was determined by analysing the noise level and determining a good compromise between being able to measure signals from distant impacts and falsely detecting peaks from the thermal noise. The peak detection function looks for points which are larger than its two neighbouring points, if one of those neighbouring points are equal then it moves to the next point, allowing for the detection of flat topped peaks. A time window is then created following this initial peak in which any subsequent peaks are deemed part of the initial pulse and are not falsely classified as secondary and hence indicative of damage. After analysing the duration of the initial pulses of many different impacts it was determined that 1 ms was the optimum time window in which to classify the initial pulse. Peak detection is then carried out for the remainder of the signal with only the largest peak identified in a cluster of peaks. The largest secondary peak magnitude is then divided by the magnitude of the initial peak to give the Damage Rating for that signal. Figure 4.16 shows an example envelope plot from panel 1 with the detected peaks labelled corresponding to a Damage Rating of 1.76.
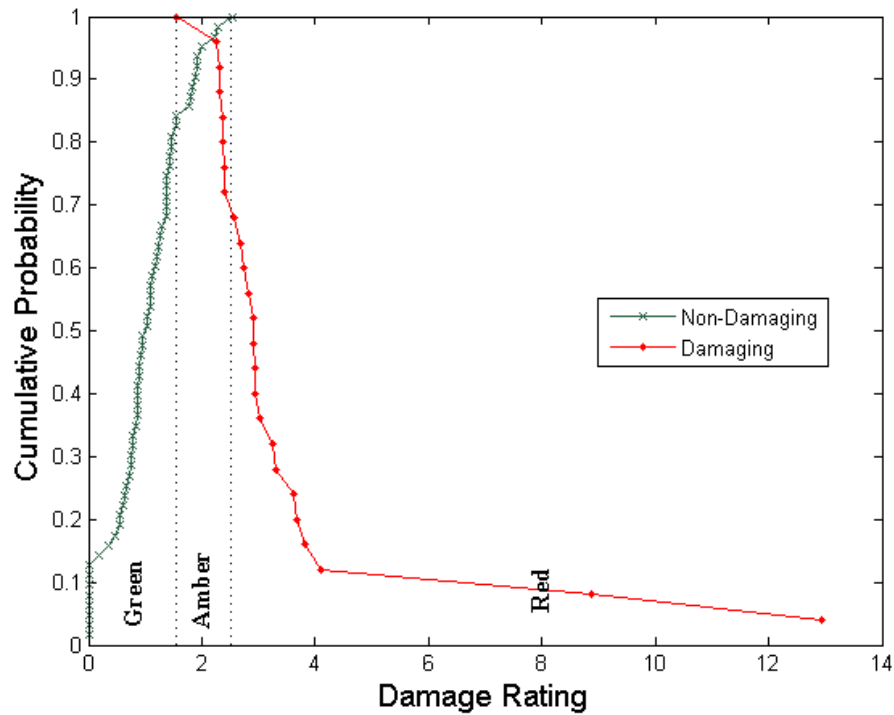

Figure 4.17. Threshold optimisation graph for panel 2 showing that for equal probability of correct classification between the two cases the probability of correct classification is 96%. Green, Amber and Red classification zones are labelled.

To determine the relevant threshold for the Damage Rating, a threshold optimisation graph was produced for each panel, Figure 4.17 shows this for panel 2. The cumulative probability is plotted against ascending damage rating for the non-damaging impacts and descending damage rating for the damaging impacts in order to determine a

threshold. It shows that if the threshold was set so that there was an equal probability of correctly identifying damaging and non-damaging impacts then 96% of impacts would be classified correctly. The results for panel 1 are similar with a correct classification probability of 93%. There is a range of Damage Rating's which came from both damaging and non-damaging impacts; therefore a traffic light system is proposed in which this section is the Amber zone and designated a possibly damaging impact. The Red zone consists of all Damage Rating's above this range and indicates damaging impacts while the Green zone includes all Damage Rating's below this range and indicates non-damaging impacts. Looking again at Figure 4.17 it shows that 70% of damaging impacts were classified in the Red zone while the remaining 30% were Amber. 85% of non-damaging impacts were classified as Green while the remaining 15% were Amber. These Damage Rating thresholds would have to be determined for each individual application as they will be different for different materials; however the rest of the method is general. A system can be imagined in which an impact is detected by a sensor and the signal is then classified using this technique into Green, Amber or Red which can then corroborate information about the energy of the impact inferred from the signal amplitude leading to improved reliability and actionable information.

4.5. Conclusions

A large number of impacts were carried out on two large composite panels and signals captured using a piezoelectric sensor. This data was then analysed and it was found that significant secondary pulses occur in the filtered data which may correspond to acoustic emission upon damage creation. An automatic classification algorithm was produced to differentiate between damaging and non-damaging impacts using the 'Damage Rating'; the ratio between the magnitudes of the largest secondary pulse and the initial pulse. This gave a correct classification probability of 93-96% and a traffic light system was proposed to differentiate between non-damaging, potentially damaging and damaging impacts.

4.6.   References

[4.1] C.F. Li, N. Hu, Y.J. Yin, H. Sekine, H. Fukunaga, "*Low-velocity impact-induced damage of continuous fiber-reinforced composite laminates. Part I. An FEM numerical model*", Composites: Part A **33** pp. 1055–1062 (2002).

[4.2] Z. Aslan, R. Karakuzu, and B. Okutan, *"The response of laminated composite plates under low-velocity impact loading"*, Composite Structures **59**: 119–127 (2003).

[4.3] G. Belingardi, and R. Vadori, *"Low velocity impact tests of laminate glass-fiber-epoxy matrix composite material plates",* International Journal of Impact Engineering **27**: pp. 213–229 (2002).

[4.4] G. A. O. Davies, and X. Zhang, "*Impact Damage Prediction In Carbon Composite Structures*", Int. J. Impact Engng Vol. **16**, No. 1, pp. 149-170 (1995).

[4.5] E. I. Madaras, W. H. Prosser, and M. R. Gorman, "*Detection Of Impact Damage On Space Shuttle Structures Using Acoustic Emission*", Review of Nondestructive Evaluation Vol. **24** (2005).

[4.6] W. H. Prosser, M. R. Gorman and D. H. Humes, "*Acoustic Emission Signals in Thin Plates Produced by Impact Damage*", Journal of Acoustic Emission, Vol. **17**(1-20) pp. 29-36 (1999).

[4.7] B. –W. Jang, Y. -G. Lee, Y. -Y. Kim, C. -G. Kim, C. -Y. Park, and B. –W. Lee, "*A study on low-velocity impact induced damage assessment of composite laminates using fiber Bragg grating sensors*", Asia-Pacific Workshop on Structural Health Monitoring, November 30, to December 2, 2010, The University of Tokyo, Tokyo, Japan. (2010).

[4.8] C. Park, K. Peters, M. Zikry, T. Haber, S. Schultz, and R. Selfridge, "*Peak wavelength interrogation of fiber Bragg grating sensors during impact events*", Smart Mater. Struct. **19** 045015 (2010).

[4.9] W. H. Prosser, "*Applications of Advanced, Waveform Based AE Techniques for Testing Composite Materials*", Proceedings of the SPIE Conference on Nondestructive Evaluation Techniques for Aging Infrastructure and Manufacturing: Materials and Composites, December 2-5, 1996, Scottsdale, Arizona, pp. 146-153 (1996).

[4.10] H.-Y. T. Wu, G. S. Springer, "*Measurements of Matrix Cracking and Delamination Caused by Impact on Composite Plates*", Journal of Composite Materials Vol. **22** No 6 pp. 518-532 (1988).

[4.11] K. Komai, K. Minoshima, and T. Shibutani, "*Investigations of the fracture mechanism of carbon epoxy composites by AE signal analyses*", JSME International Journal, Series I, Vol. **34**, No. 3 (1991).

[4.12] P. J. de Groot, P. A. M. Wijnen, and R. B. F. Janssen, "*Real-time frequency determination of acoustic emission for different fracture mechanisms in carbon/epoxy composites*", Composites Science and Technology **55** pp. 405-412 (1995).

Chapter 5 - Arrayed Waveguide Grating Interrogator

5.1. Introduction

Optical fibre sensors offer significant advantages over conventional electrical sensors for many challenging measurement problems and have seen commercial exploitation for distributed strain and temperature measurement [5.1], strain sensor arrays [5.2], and miniaturised sensor heads [5.3]. Transducers exploiting fibre Bragg gratings (FBGs) as the optical sensing element are one of the most promising technologies, with advantages that include small size, light weight, ability to embed in composite materials (§2.1), ease of multiplexing (§2.7), high durability and immunity to electromagnetic interference [5.4, 5.5]. Another major advantage of this approach is that the measurement becomes wavelength encoded, thereby avoiding issues with intensity based optical fibre sensors (§2.4.1), and allowing simple multiplexing in the wavelength domain.

FBG sensors have been widely reported for structural health monitoring applications; especially for large structures, such as bridges, where the long range multiplexing capability enables real time strain monitoring on a massive scale. For instance, the Dongying Yellow River Bridge in China has been instrumented with over 1800 FBG sensors for this purpose [5.6].

Many structural monitoring applications are interested in low bandwidth or 'quasi-static' strain measurement, with typical bandwidths below 1 kHz. In such cases sensor interrogation typically relies on wavelength scanning to monitor the grating wavelengths. Common approaches to do this exploit tunable laser sources [5.7, 5.8], or scanning spectrometers [5.9]. Commercially available interrogation systems suitable for monitoring FBG arrays currently operate up to 20 kHz (Ibsen Photonics [5.10]) which is more than adequate for many structural monitoring applications. For some interrogation systems an increase in measurement bandwidth can be afforded by reducing the number of FBG sensors monitored, with single grating monitoring systems capable of 100 kHz (Fiberpro [5.11]). Unfortunately for high frequency transient strain events, on the microsecond timescale, such as impacts and acoustic emission (AE) monitoring, the majority of commercially available interrogators are unsuitable, particularly where multiple sensors must be monitored simultaneously.

Where higher measurement bandwidth is important, methods for measuring FBG wavelengths based upon scanning components are unsuitable with typical sampling rates below 1 kHz [5.9, 5.8, 5.9]. Alternative techniques have been developed to

address this shortcoming using some form of wavelength-to-intensity mapping to allow high speed FBG interrogation based upon intensity rather than spectral measurement.
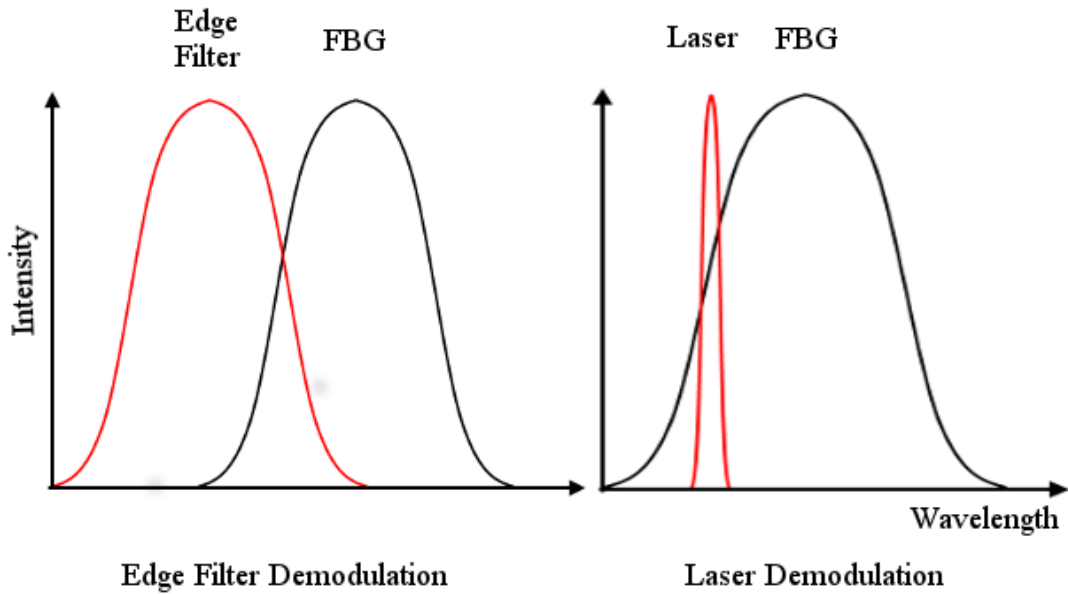

Figure 5.1. Two demodulation techniques are shown; an edge filter partially overlaps the FBG spectrum (left) and a laser spectrum is tuned to be at the full width at half maximum point (right). A wavelength shift of the FBG will alter the overlap with either the edge filter or the laser and cause an intensity change which can then be measured by a photodetector.

For example, passive components such as edge filters can be used to provide wavelength-to-intensity mapping [5.12], or narrow linewidth laser sources can be tuned to operate at the full width at half maximum point on the side of the grating spectrum which results in large changes in reflected light intensity for small wavelength shifts [5.13]. Figure 5.1 illustrates these two techniques.

Such approaches have an impressive temporal bandwidth which is only limited by the sample rate of the photodetector and associated electronics which can be beyond a MHz. However, these configurations typically suffer from a lack of scalability, poor strain range, and errors resulting from unknown or time varying intensity variations being indistinguishable from a true signal. This chapter explores a technique based upon an arrayed waveguide grating (AWG) to overcome these issues. The AWG is a passive device designed for wavelength (de)multiplexing in optical communications systems (§5.1.1). A series of such 'narrowband' wavelength filters can be used to interrogate FBGs which are written so that the FBG reflection spectrum overlaps with more than one channel of the AWG. Analysis of power measured from two (or more) AWG channels can be related to the grating wavelength, while offering some immunity to common mode intensity noise.

One study used the tunable laser demodulation technique shown in Figure 5.1 with an AWG for wavelength division multiplexing allowing several Bragg gratings with different Bragg wavelengths to be addressed with a measurement error of ±4 με [5.14]. However, this technique can only be used for active sensing when a signal is measured at a known time and cannot be used for passive sensing of impacts as each grating is addressed sequentially after the laser is tuned to the correct wavelength band. Other studies used a larger number of channels for each sensor and effectively use the AWG as a coarse spectrometer by fitting a parabola to the output achieving a measurement error of 4.8 με [5.15,5.16,5.17]. Application of these techniques include the interrogation of tilted FBGs for measuring refractive indices [5.18] and the interrogation of long period gratings [5.19].

Conventional FBGs have been interrogated with an impressive strain resolution of $17\,\mathrm{n}\varepsilon/\sqrt{\mathrm{Hz}}$ at 30 Hz using an unbalanced Mach-Zehnder interferometer in conjunction with an AWG. However, the bandwidth is not sufficient for dynamic strain measurements and the experimental setup is complex [5.20,5.21]. Another team used the ratio of the intensity in two AWG channels to successfully demonstrated impact detection. Several pairs of channels were used to extend the strain range to accurately reproduce dynamic impact signals with a sampling rate of 100 kHz; though no analysis of resolution or noise was carried out [5.22,5.23].

Although there have been numerous reports of using AWGs for the interrogation of FBG sensors, little has been reported regarding the *optimisation* of such a system. For a practical system, intensity ratio to wavelength calibration, noise levels, and long term stability are important to fully characterise the sensor system. In this chapter, the various system design parameters are investigated experimentally as well as their link to system performance indicators such as sensitivity and dynamic range for dynamic strain sensing. For an AWG interrogation system, there is a trade-off between sensitivity and dynamic range which is linked to the relative spectral widths of the FBG and AWG channels. A comparison is made between several FBG spectral widths in addition to a comparison between two commercially available AWG variants with bandwidths of 100 GHz and 200 GHz. The system performance is also investigated; this includes system stability over a long time period where temperature variation might be significant, as well as short-duration tests to verify the resilience of the ratiometric technique to intensity fluctuations either from the light source or due to bend losses. Finally, the impact of using a semiconductor optical amplifier (SOA) to increase the

light intensity is investigated. This is relevant as it offers advantages for addressing larger sensor networks.

When measuring dynamic strain signals, the physical length of the FBG is important because the grating must be short when compared to the strain wavelength in order to maximise sensitivity. The FBG length has implications for the FBG spectral width, and the effect of this when compared to the AWG spectral width needs to be considered. The effect of strain field wavelength on FBG sensitivity has been investigated previously using models based upon the transfer matrix method [5.24,5.25]. In this chapter this analysis is extended to include the specific case of the AWG interrogation scheme, compare results with experiment and show how we can use the results to inform decisions on the design of sensing FBGs.

5.1.1. Arrayed Waveguide Grating

An arrayed waveguide grating is a standard fibre-optic communications component used for wavelength division multiplexing (WDM) and demultiplexing signals. In one typical design an AWG is composed of two planar slab waveguides with an array of waveguides connecting them, this is illustrated in Figure 5.2. Broadband light entering the first slab waveguide is no longer laterally confined and diffracts into the waveguide array [5.21]. The light then propagates to the second slab waveguide which is the free propagation region. The arrayed waveguide is designed such that the optical length difference (OPD), ΔL, between adjacent waveguides ensures light emerges with different *wavelength dependent* relative phases. ΔL is given by the following equation:

$$\Delta L = m \frac{\lambda_c}{N_g} \tag{5.1}$$

where m is an integer called grating order, λ_c is central wavelength and N_g is the effective refractive index of the array waveguide [5.26].

Constructive interference therefore occurs at different points for different wavelengths, allowing the spatial separation of different wavelength channels to be achieved at the output waveguides [5.27].
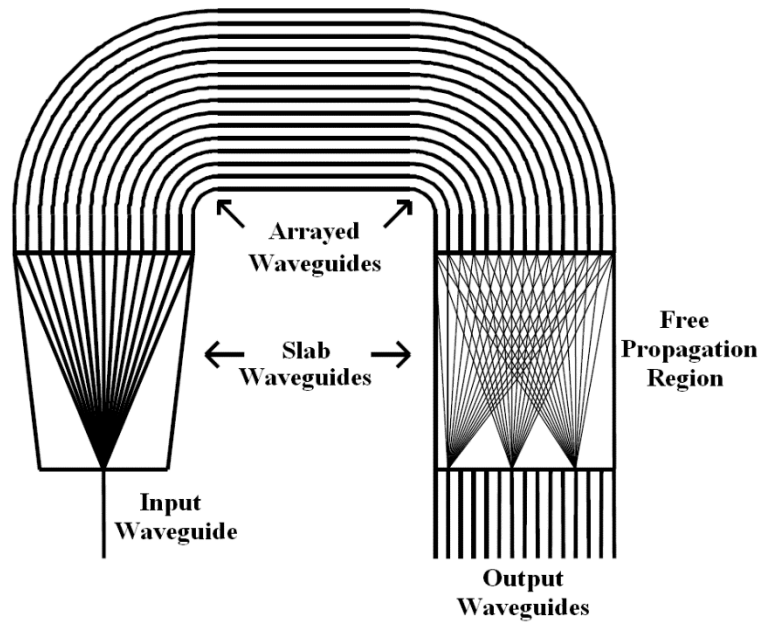
Figure 5.2. Schematic of an arrayed waveguide grating showing all waveguide components and free propagation region. The outputs for three different wavelength channels are shown. Adapted from [5.21]

5.2. Principle of Operation

The basic interrogation system is illustrated schematically in Figure 5.3. A broadband amplified spontaneous emission (ASE) source is used to illuminate a sensing FBG and the reflected spectrum enters the AWG via a 3 dB directional coupler. An optical circulator was not available at the time but would be preferable in place of the coupler as less light would be lost. The AWG is an Alcatel A1936AWG with a 100 GHz channel spacing (0.81 nm) containing 32 channels covering a wavelength range of 1536.1 − 1560.1 nm. The AWG is temperature controlled, which allows the AWG channel positions to be tuned by up to 1.68 nm. The AWG channels with spectra that flank the FBG spectrum are monitored using four photodetectors that were built from pigtailed InGaAs photodiodes. They are based on a transimpedence amplifier design using an op-amp and housed in a diecast box pictured in Figure 5.4. The circuit is shown in Figure 5.5 and the op-amp used had a device number of OPA604AP. The detectors have a 3 dB bandwidth of 175 kHz although this can be altered, along with the gain, by changing the resistor which is readily accessible in a chip holder.
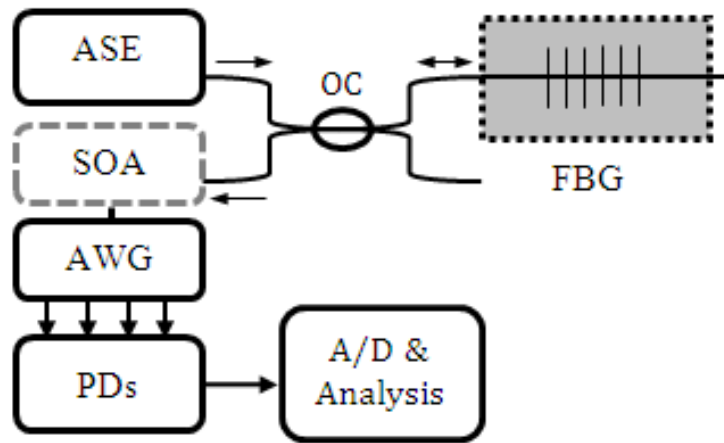
Figure 5.3. Schematic of the interrogation scheme. ASE: amplified spontaneous emission light source, OC: optical coupler, FBG: fibre Bragg grating, AWG: arrayed waveguide grating, PDs: InGaAs photodiode detectors. SOA: semiconductor optical amplifier, an optional addition to increase the light intensity.
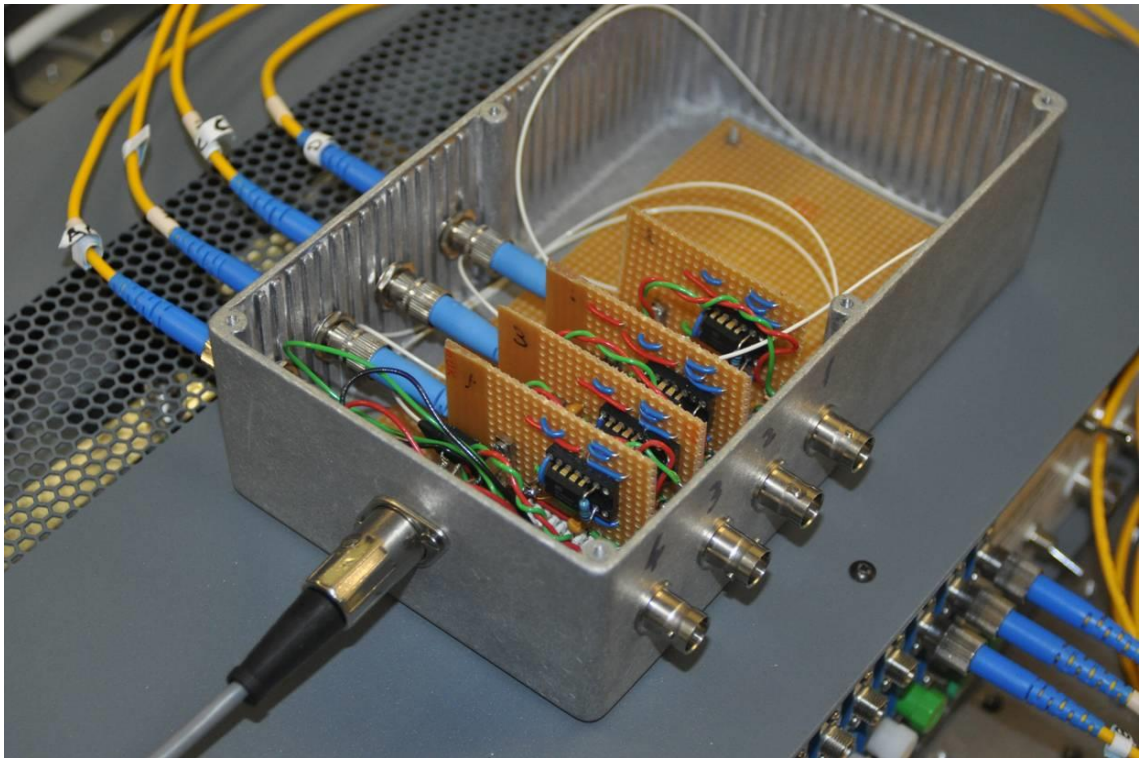

Figure 5.4. Four photodetectors constructed from InGaAs photodiodes and housed in a diecast box.
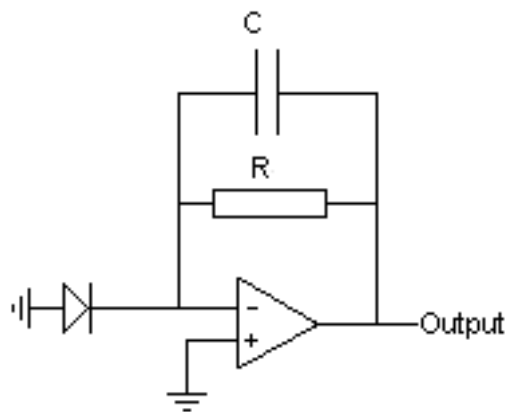

Figure 5.5. Diagram of the photodetecter circuit.

106

When the FBG is strained the spectrum will shift, altering its overlap with each of the AWG channels, thereby causing a change in the light intensity measured at each channel. We define the interrogation function, ρ

$$\rho = \log(\frac{I_n}{I_{n+1}}) \tag{5.2}$$

where I_n and I_{n+1} are the light intensities captured by the detectors for AWG channels n and $n + 1$ [5.14]. Figure 5.6 shows a typical FBG spectrum (full-width half-maximum (FWHM) 0.2 nm) overlaid over two AWG channel spectra measured separately with an optical spectrum analyser (OSA). The interrogation function ρ can be related to the grating wavelength and hence the applied strain. This relationship is not necessarily linear due to spectral features in the AWG channels and/or the FBG; therefore calibration experiments are used to determine the conversion from the interrogation function to FBG wavelength (or strain).
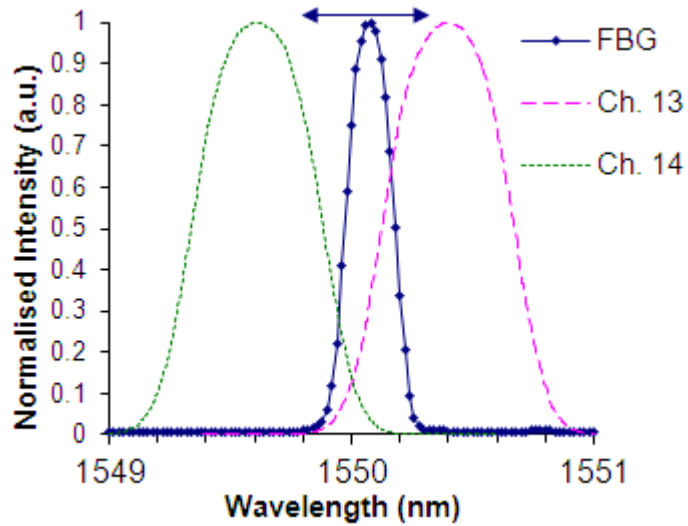

Figure 5.6. Normalised FBG spectrum along with the spectra from two AWG channels measured using an optical spectrum analyser. Arrow shows the wavelength shift of the FBG when subjected to strain.

5.2.1. Calibration of interrogation function

A calibration experiment can be performed in order to relate the arbitrary units of the interrogation function to the centre wavelength of the FBG and thereby the strain it experiences. This was carried out for three different FBGs, the details and results of which are reported in §5.3.1. One end of the fibre was fixed while the other was attached to a micrometer stage, allowing the centrally located grating to be strained linearly by a known amount. In addition to the setup in Figure 5.3, the grating was simultaneously monitored using an OSA in order to determine the grating's centre wavelength while it was strained, allowing the relationship between the interrogation

function and the grating wavelength to be determined. The grating centre wavelength was determined from the midpoint between the grating 3 dB points, which gives a more robust measure of the centre wavelength for flat-topped gratings and was observed to have an resolution of ± 1pm. The strain was calculated from the micrometer readings of the extension of the fibre, which is measured with an resolution of ±5 μm, producing a known strain resolution to ±10 με for a 50 cm length of fibre. The fibre was clamped firmly and the stage was moved back to the initial position at the end of each test to verify the repeatability, therefore indicating no system hysteresis and that no fibre slippage had occurred.
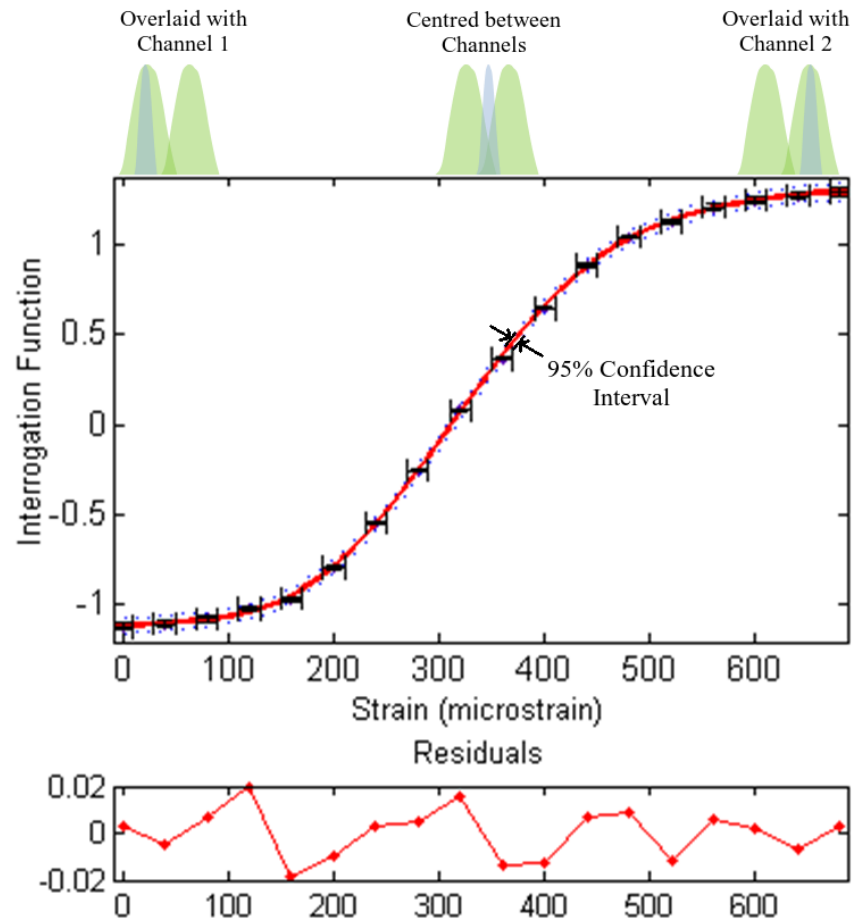

Figure 5.7. Calibration data for FBG with 0.20 nm spectral width and 'Sum of Sines' fit (red solid) along with 95% confidence bounds (blue dashed).

Figure 5.7 shows the resulting interrogation function as the FBG is strained in linear increments from a position where the FBG spectra fully overlaps one AWG channel to a position where it fully overlaps with the following channel (see top of Figure 5.7). This is the maximum strain range that can be detected using only two channels of the AWG; which, for this FBG, is ± 360 με. A curve fit was applied to the data in order to relate the interrogation function output of the system to the strain that the FBG was experiencing. Various types of fit were calculated and it was found that the most

accurate fit, in this example, was a sum of sine functions. The precise form of the interrogation function depends on many factors including the relative shapes of the FBG and the AWG channels. As such, the calibration is largely empirical and a practical way to relate the system output to the strain in the FBG is more important than the mathematical form of the fit. Figure 5.7 also shows the 95% confidence bounds (blue dashed lines), which are extremely close indicating the accuracy of the fit. In the central region (350 ± 100 µε) this fitting confidence corresponds to a strain error of only ± 5 µε; however, the overall system performance will also be influenced by the system intensity noise, AWG wavelength stability, the relative widths of the AWG and FBG spectra and the interaction between the transient strain field and the FBG. This calibration procedure was performed for three different FBGs with different FWHM, as described in §5.3.1.

5.2.2. Bonded Calibration Comparison

These initial calibrations were performed by straining a free fibre but in an actual application the FBG would be bonded onto or embedded within a host material in order to measure the strain in that material. It is possible that the effective strain sensitivity of the FBG may be altered when it is bonded down, for example the complete material strain might not be transferred to the FBG. Factors such as the bonded length, fibre coating, adhesive type and thickness can all effect the bond quality and the amount of strain transferred [5.28, 5.29]. To determine whether a free fibre calibration is still valid once the fibre has been bonded, a new grating was calibrated, as above, and then bonded onto a composite panel and re-calibrated.

A monolithic carbon fibre panel with a thickness of 4.5 mm was used and an aluminium 'C'-section frame was constructed to allow strain to be applied using a three point bend, shown in Figure 5.8. The panel is 0.86 m long and the sides of the frame clamp the sides of the panel firmly in place. The frame was then attached with tape onto blocks so that it is raised above the ground and able to bend freely. A bolt in the centre, shown in Figure 5.9, can be adjusted to deflect the panel away from the frame, with the pressure distributed along the line perpendicular to the frame.
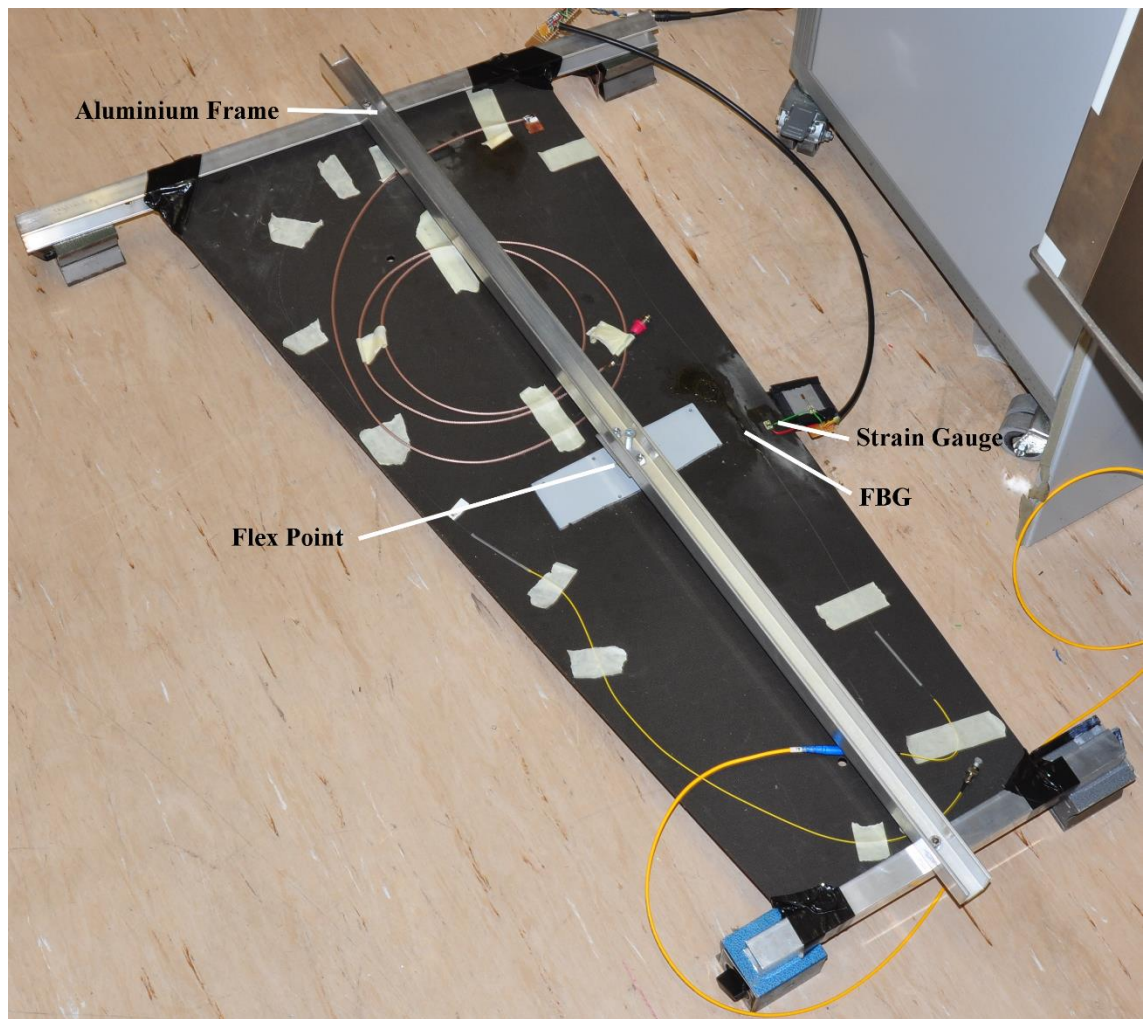
Figure 5.8. Top view of a composite panel with bonded FBG sensor and strain gauge. Static strain occurs from aluminium frame in a three point bend test.
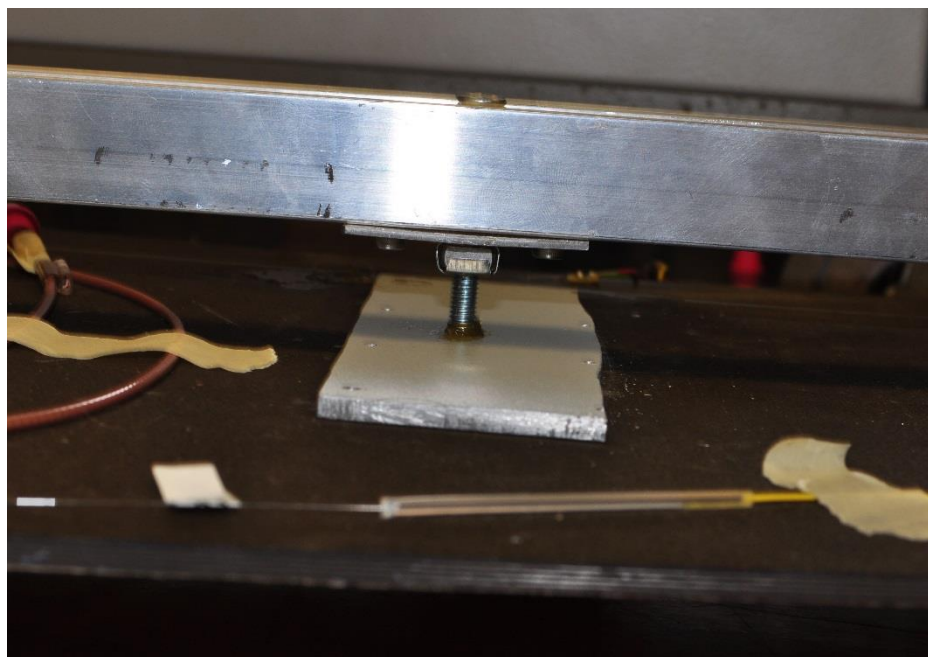

Figure 5.9. Side view of static strain apparatus. The bolt is adjusted to deflect the panel away from the frame in a three point bend.

A new FBG was used with a FWHM of 0.67 nm and a polyamide coating, it was calibrated similarly to the other gratings in the previous section before being bonded onto the panel. The grating was bonded to the panel using the same procedure as a strain gauge. The area was first sanded flat and smooth then cleaned with ethanol. A thin layer of quick setting epoxy resin was applied and then the grating was placed flush to the surface of the panel under a slight tension. It was ensured that the grating was then completely submerged in the adhesive over the whole of its length.

To measure the strain, a strain gauge was bonded onto the panel next to the FBG, the output was measured using a National Instruments 9219 24-bit universal analogue input device. The strain gauge was calibrated with a general tensile test using an Instron 4507 machine. The strain gauge was then used for comparison with the FBG.

The bonded FBG was gradually strained by increasing the deflection of the panel, the interrogation function was measured using the AWG as well as the strain registered by the strain gauge. The results are shown in Figure 5.10, it can be seen that the two calibration curves differ. The bonded FBG appears to have a lower strain sensitivity, as such it takes a larger strain to cause the FBG spectrum to shift over the whole wavelength range. This may be because the strain in the panel is not being perfectly transferred to the FBG. The differences in the calibration curves suggest that it is not always possible to assume that a calibration performed with a free fibre is valid for an FBG that has been bonded onto a structure.
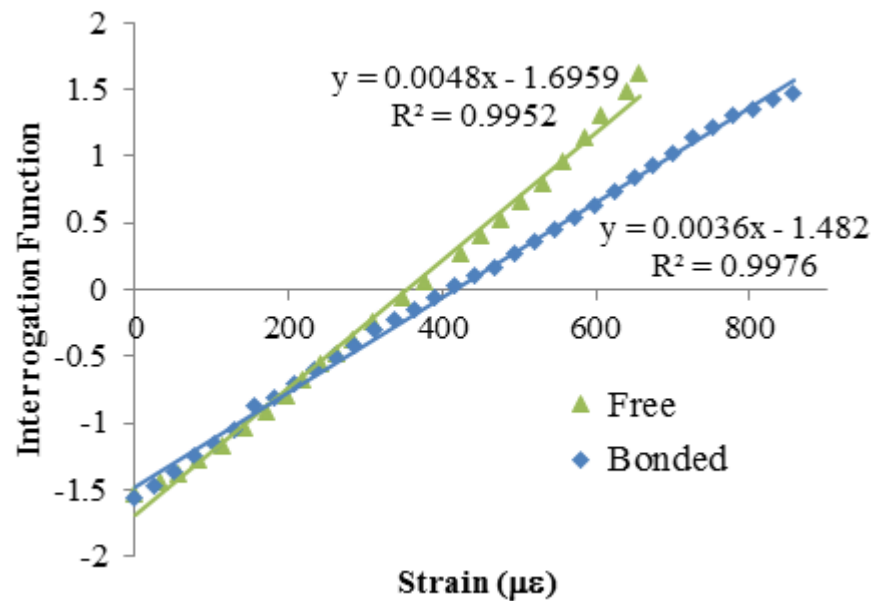

Figure 5.10. Calibration curves showing the relation between the interrogation function and strain for a free FBG under tension and for the same FBG strained after being bonded onto a composite panel.

111

5.3.   System Design Parameters

There are several factors to consider when designing a FBG interrogation system utilising an AWG in order to achieve the desired sensitivity and strain range at an appropriate cost. The strain range can be improved by increasing the AWG channel spectral width or by assigning more channels per sensor with the additional cost of detectors and signal processing. An increase in AWG spectral width will reduce the measurand resolution because the associated FBG wavelength shift will result in a lower change in intensity. The spectral width of the FBG is also important: a narrow grating will produce a greater sensitivity but if it is too narrow in comparison with the AWG channel width then there is the risk that the intensity measured in one of the AWG channels will be negligible making the calculation of the ratio in equation 5.1 highly susceptible to noise. A final, and related, consideration is that of the FBG physical length which must be small enough in order to allow the strain field wavelengths of interest to be resolved. Unfortunately, reducing the FBG length results in an increased spectral width for a given grating reflectivity which ultimately limits the options for this parameter. These parameters are investigated in the following sections using a combination of MATLAB simulation and validation experiments.

5.3.1. Effect of FBG spectral width

A MATLAB model was created that simulates the system output by combining a FBG reflection spectrum with modelled AWG channel spectra. The FBG center wavelength is iterated across the AWG channel spectra in order to relate it to the interrogation function for several different values of FBG spectral width. There is little modelling of such a system reported in the open literature and the models that do exist have assumed that the AWG passband is Gaussian. The first model follows that assumption and creates two Gaussian profiles offset by 0.8 nm with FWHM of 0.54 nm, values which correspond to the AWG used in §5.2.1. In this work the FBG spectrum is generated from a model refractive index profile based on chosen parameters such as grating length, refractive index modulation, Bragg wavelength and apodization function. The transfer matrix method is then used to compute the effect of light travelling through the FBG and compute the reflection spectrum [5.24]. The convolution of the FBG spectrum and the first AWG channel is then computed followed by the convolution with the second AWG channel. The approximate integral of each of the two convolutions is calculated using the trapezoidal method which corresponds to the signal which would be seen by a detector measuring the spectrum. Finally, the interrogation function is

calculated using equation 5.2. This is then repeated for every step of the FBG spectrum as it is iterated across the AWG spectra. The simulation was carried out for a range of FBG spectral widths to investigate the effect on measurand sensitivity and the shape (linearity) of the interrogation function, with the results shown in Figure 5.11.
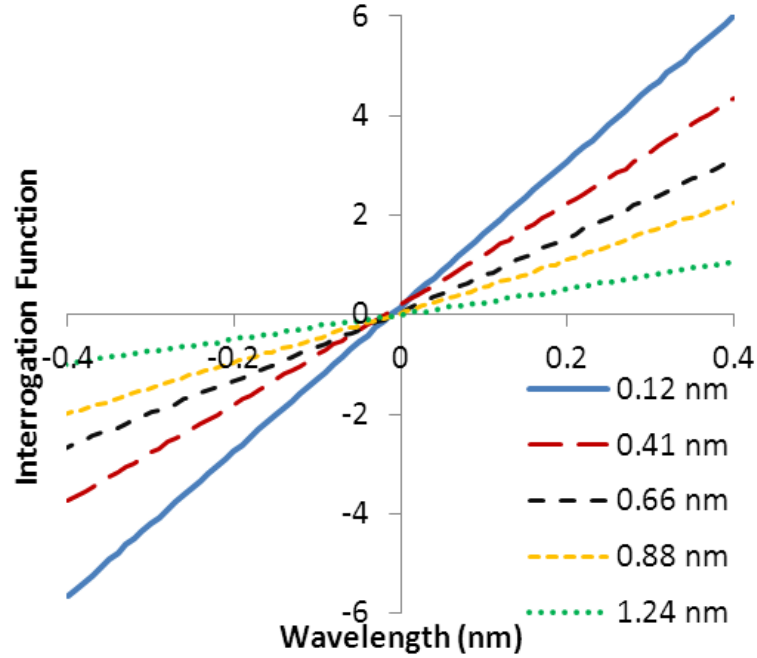

Figure 5.11. System model relating the interrogation function output to wavelength for different FBG spectral widths using apodized FBG model and Gaussian 100GHz AWG channel model.

These results agree with previous published results [5.14] that reducing the FBG FWHM improves the measurand sensitivity, i.e. the same shift in wavelength will cause a larger difference in light intensity transmitted by each AWG channel leading to a larger change in the interrogation function. To verify this, practical experiments were carried out with three different FBGs of different length and spectral width to allow comparison with the model, their details along with some results from the calibration are shown in Table 5.1. The FBGs are from different manufacturers which possibly caused the differences in the coefficient of strain, although they are all in the usual range. The reflected spectrum power was measured by illuminating the grating using a broadband source and measuring the optical power reflected back through a circulator. The same source was used for each grating and this can then be used to determine the power of light reflected from each grating relative to each other. The strain range is the amount of strain covered when the grating moves from fully overlapped with one AWG channel to the adjacent one. This is larger for the gratings with the highest coefficient of strain.

Table 5.1. FBG characteristics for the three investigated FBG sensors.

	FBG 1	FBG 2	FBG 3
Bragg Wavelength	1550.20 nm	1550.30 nm	1550.30 nm
Bandwidth/FWHM	0.20 nm	0.42 nm	0.66 nm
Reflected Spectrum Power[a]	11 µW	27 µW	42 µW
Grating Length	20 mm	~10 mm	3 mm
Coefficient of Strain	1.09 pm/µε	1.16 pm/µε	0.90 pm/µε
Strain Range	± 360 µε	± 310 µε	± 428 µε

[a] For comparison, using same source

Figure 5.12 shows normalized experimental results in order to compare linearity. The 0.20 nm FBG has the greatest sensitivity for small shifts in Bragg wavelength. However, once the grating spectrum has been strained away from the central region where both channel intensities are approximately equal the sensitivity drops dramatically therefore illustrating the relationship between range and resolution.
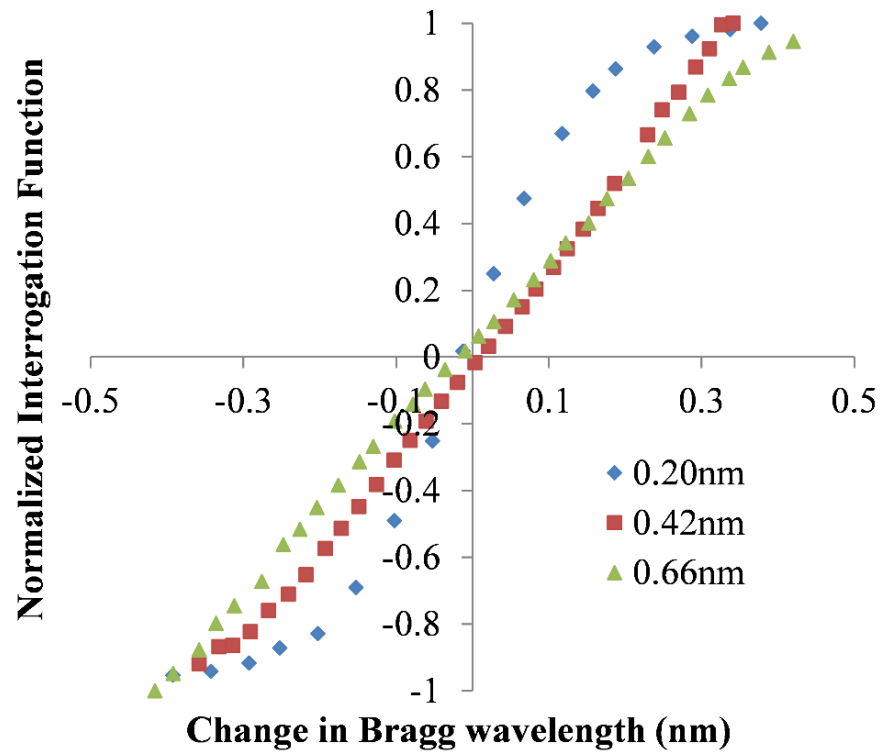

Figure 5.12. Comparison of the interrogation functions of 3 Bragg gratings as they are strained so that their spectra move from a position overlapping one AWG channel to overlap the next.

The 0.42 nm FBG gives a response closer to linearity as the FBG spectrum better spans the spectral gap between the two AWG channels. Comparatively, the 0.66 nm FBG has a similar linearity with a slightly reduced sensitivity. The FWHM of the AWG channels is 0.54 nm, and a FBG width similar to this will produce the most linear response.

A linear response is an advantage as it gives a consistent sensitivity across the measurable strain range. Although a lack of linearity can be compensated by calibrating the systems response as strain is applied, this can lead to larger errors as the calibration needs to be performed with a high level of accuracy and reliability in order to accurately describe a nonlinear curve. Strain calibrations performed on large, real structures such as aircraft wings can be difficult to perform accurately and as shown in §5.2.2, a calibration carried out on an unbonded grating may not be accurate once it has been bonded onto a structure. Due to these facts a linear response which is more resilient to slight deviations from the initial calibration may be preferable.
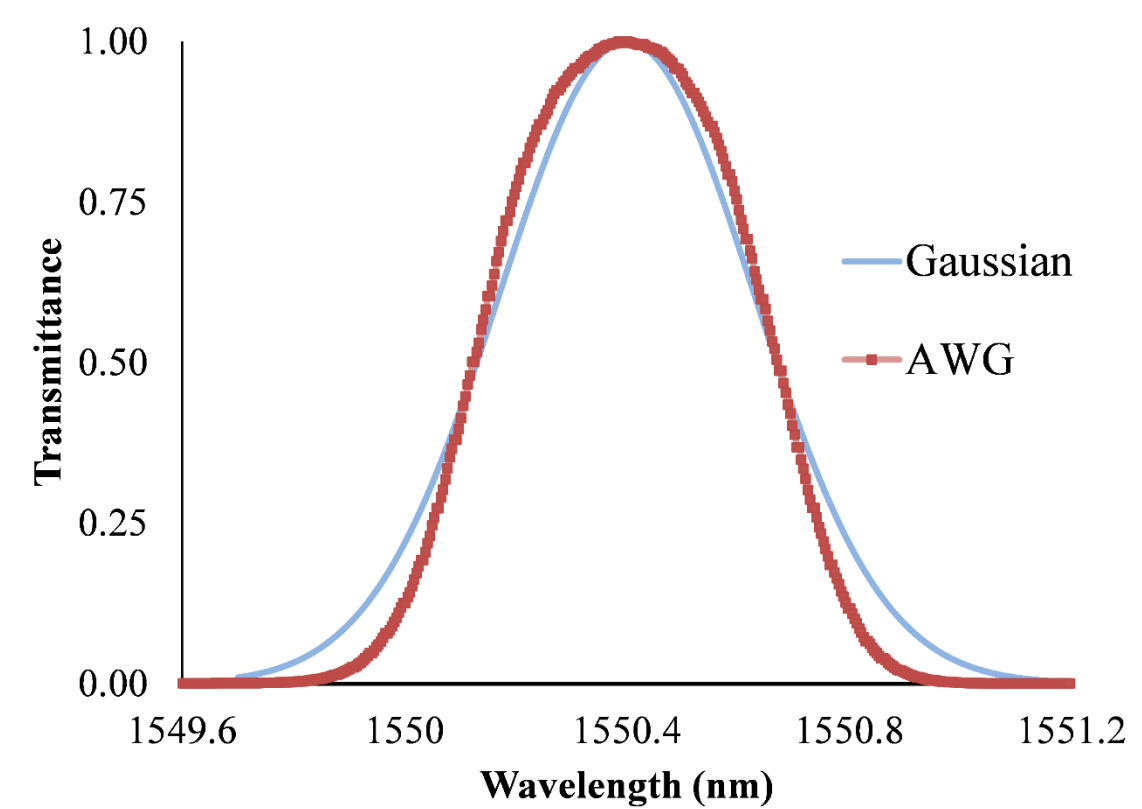

Figure 5.13. A comparison between the measured transmittance profile of an AWG channel and a Gaussian with the same FWHM.

To investigate the differences between the experimental results shown in figure 5.11 and the modelled results in figure 5.10 the measured transmittance profile of one of the AWG channels was compared to a standard Gaussian function of form

115

$$f(x) = a\,exp\left(-\frac{(x-b)^2}{2c^2}\right) \tag{5.3}$$

with $c \approx FWHM/2\sqrt{2\ln 2}$. This comparison is shown in Figure 5.13, it can be seen that the AWG does not possess a Gaussian profile but instead the passband falls off more sharply. This difference has a significant effect on the output of the system as demonstrated in Figure 5.14. This shows, for FBG 1, the difference between the experimental result, the Gaussian model previously described and a model incorporating the actual AWG spectra measured using an OSA. The latter was identical to that of the other model except that the modelled Gaussian profiles of the AWG channels were replaced by normalized AWG spectra obtained by measuring the AWG used in the practical experiment with an OSA. This deviation from a Gaussian profile clearly has a large effect: increasing the sensitivity for small wavelength shifts and causing a loss of linearity. Therefore, a thorough system design should include the consideration of the AWG passband profile rather than relying on the assumption that it is Gaussian with a quoted FWHM.
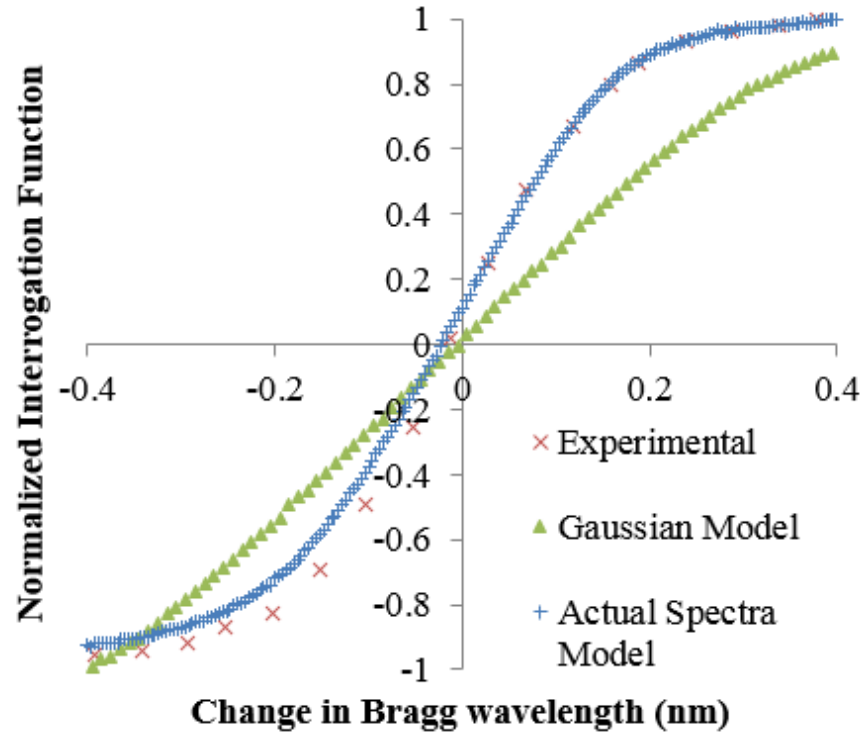

Figure 5.14. Comparison using FBG 1 of experimental data using an AWG, a model with Gaussian AWG passband and a model utilising actual AWG spectra. The experimental data and the actual spectra model data are completely overlaid in the positive change in Bragg wavelength direction.

5.3.2. Comparison of AWG Bandwidth

AWGs are commercially available in bandwidth variants including 50, 100 and 200 GHz, with 100 GHz being common. With many telecommunication technologies progressing towards denser multiplexing, narrower bandwidth AWGs are starting to be mass produced, leading to exciting possibilities for narrow bandwidth filters for high sensitivity applications. For a ratiometric AWG wavelength interrogation scheme, as described above, the channel passband bandwidth determines the maximum strain range when two channels are assigned to each FBG sensor. From first principles, increasing the number of channels, and associated detectors, assigned to each sensor increases the maximum strain range according to the expression

$$\pm \varepsilon_{\max} = \frac{1}{2(a-1)\,B_{3\mathrm{dB}}/C_\mathrm{s}} \tag{5.4}$$

where a is an even integer indicating the number of AWG channels assigned to each sensor, B_{3dB} is the 3 dB bandwidth of an average AWG channel and C_S is the coefficient of strain for the FBG sensor in units of pm $\mu\varepsilon^{-1}$. An analysis of this equation shows that increasing from two to four channels per sensor leads to a threefold increase in the maximum strain range, which must be weighed against the additional cost of the two more detectors and associated signal processing.

A comparison of the system response when using the 100 GHz AWG detailed above, which has a 3dB bandwidth of 0.54 nm, and a 200 GHz AWG with a 3 dB bandwidth of 1.10 nm. The same procedure was used as above for comparing the effect of varying FBG spectral width, and for this comparison, a single 3 mm length grating with a 3dB bandwidth of 0.616 nm (similar to FBG 3) was used. Figure 5.15 shows the results of this experiment; the 200 GHz AWG allows the measurement of the Bragg wavelength over double the range when compared to the 100 GHz variant. This however comes at the cost of the loss of sensitivity and linearity over this range; while a small deviation in Bragg wavelength has the same sensitivity as the 100 GHz case, this quickly falls away leaving a low change in light intensity with the Bragg wavelength shift over most of the range. The sensitivity for the 100 GHz AWG is 4.06 a.u./nm compared to 2.23 a.u./nm for the 200 GHz where the units are the dimensionless interrogation function units. Fitting a straight line to the 100 GHz data results in a fit with an r-squared value of 0.998 while the 200 GHz data results in a low value of 0.952. As noted in §5.3.1 the response can be linearized with the correct choice of the FBG 3 dB bandwidth which, for the case of the 200 GHz, would be close to 1.1 nm. However, even with the correct

choice of FBG bandwidth, the sensitivity would still be inherently lower. The choice of the AWG bandwidth would therefore be informed by the application, for instance, in an impact detection application, using a 200 GHz AWG would likely produce sufficient sensitivity, so a larger maximum strain range using less detectors and AWG channels would be preferable.
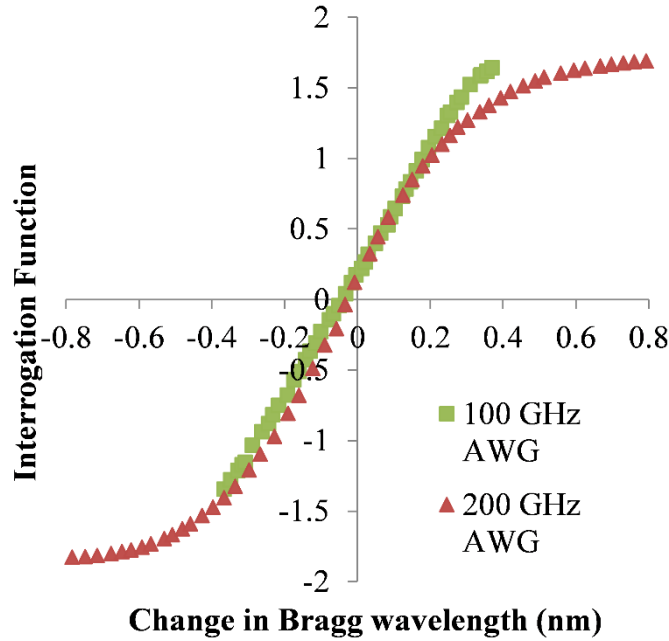

Figure 5.15. Comparison of 100 and 200 GHz AWGs showing how the interrogation function varies with the changing Bragg wavelength of the FBG sensor.

5.3.3. FBG Length Considerations

An important consideration for FBG sensor systems for dynamic events is the physical length of the grating, L. When plate waves are produced by impacts or acoustic emission in a material, such as a composite panel, the wavelength of the highest significant frequency component must be considered. Impact events may produce vibrations with frequencies upto ~100 kHz and detecting such frequencies is useful for some applications [5.30]. For such waves, a composite material typically has a wave velocity of ~1100 ms^{-1}, giving a typical wavelength of ~11 mm. Commercially available FBGs usually have lengths between 1 and 20 mm. The wavelength of the strain wave of interest may be of comparable size. If as a result, the sensor grating does not experience a uniform strain along its length then the resultant wavelength shift is likely to be reduced. This is demonstrated in Figure 5.16 showing how strain waves of different wavelengths overlay on an FBG. This effect can be defined by the ratio of the strain wavelength to the grating length; for the cases where the ratio is equal to 1 or 0.5, the grating is strained equally in both directions leading to no effect. However, in the

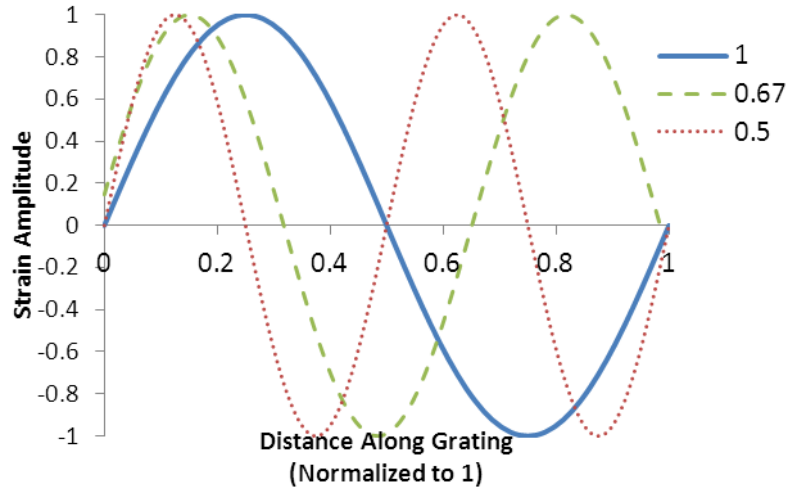special case where the ratio is 0.67, there is a net effect as the wave is not symmetric across the grating.

Figure 5.16. **The effect of strain wavelength on fibre Bragg gratings for different relative lengths given by the ratio of strain wavelength/grating length.**

To investigate the limits set on the FBG length by this effect, the MATLAB model was extended to simulate the effect of a strain wave on an FBG using the transfer matrix method. The refractive index profile of the grating is first modelled as a many layered structure, each layer with a constant refractive index value before being perturbed by the spatially varying strain field. In order for the technique to work, the thickness of a layer, d, has to be much less than the grating period Λ. Therefore the number of layers the grating length is divided into is given by, μ,

$$\mu = a\frac{L}{\Lambda} \tag{5.5}$$

where a is a numerical constant $\gg 1$. Experimentation showed that reducing a from the initial choice of 100 to 10 did not cause any significant loss of accuracy but allowed the model to be completed an order of magnitude faster and was therefore chosen. This means that for a 1 mm long grating at 1550 nm, μ would be approximately 18850 layers.

Each layer is perturbed by the strain wave which is the sum of two contributions: the mechanical contribution due to the modulation of the grating pitch and the optical contribution due to the change in refractive index via the elasto-optic effect. The fibre axis, z, is deformed by the mechanical action of the perturbation and becomes

$$z' = f(z,t) = z + \varepsilon_m \sin\left(\frac{2\pi}{\lambda_s}z - w_s t\right) + \varepsilon_m \frac{2\pi}{\lambda_s}\sin(w_s t) \tag{5.6}$$

119

where ε_m is strain wave amplitude, ω_s is its angular frequency and λ_S is its wavelength [5.24]. The strain wave perturbing the grating was assumed to be sinusoidal with a magnitude of 50 $\mu\varepsilon$.

The effective refractive index modulation from the perturbation is given by

$$n'_{eff}(z',t) = n_{eff\,0} - \Delta n \sin\left\{\frac{\pi z}{\Lambda}\right\}$$
$$-\left(\frac{n^3_{eff\,0}}{2}\right)[P_{12} - \nu(P_{11} + P_{12})]\varepsilon_m \cos\left(\frac{2\pi}{\lambda_s}z' - w_s t\right)$$

(5.7)

where P_{ij} are the stress-optic coefficients and ν is the Poisson's ratio, $n_{eff\,0}$ is the effective unperturbed refractive index.

Once this perturbed profile has been computed the reflectivity as a function of wavelength can be computed from the transfer matrix of the whole structure which is computed by multiplying the transfer matrices of all of the individual layers.

Thus far, this follows the method work by Minardo et al. in [5.24], the following extends from that work and applies it to the case of the AWG interrogation system.

The AWG channels were also modelled, allowing the output of the system, in the form of the interrogation function, to be calculated from the overlap of the calculated grating spectrum with the AWG channels as before. To make the model as close to the real system as possible a noise factor was added during integration of the final light spectrum which is representative of the detector. Measurements of the noise level were made using the real system, it was found to be approximately equal to 2% of the DC signal level. The noise was implemented using a pseudo-random normal distribution.

This whole procedure produces the system response at a moment in time while the FBG is subject to a strain wave. To provide the full picture of the time evolving system response this procedure is carried out for 16 different times ranging from zero to T, the time period of the strain wave, is given by

$$T = \frac{\lambda_s}{\upsilon}$$

(5.8)

where λ_s is the strain wavelength and υ is its wavespeed.

This was computed for both apodized and non-apodized gratings for many values of the ratio λ_s/L. The interrogation function is shown for some of these values for non-apodized gratings in Figure 5.17 and apodized gratings in Figure 5.18.
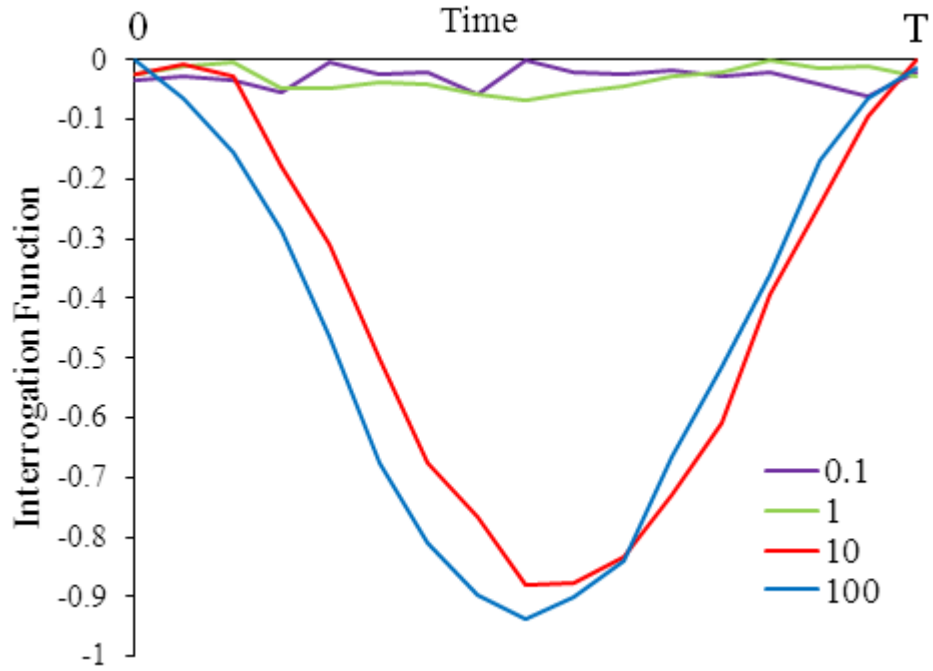
Figure 5.17. Modelled change in the interrogation function for a non-apodised FBG interacting with a strain wave over one time period, *T*, of the wave. Each curve corresponds to a different value of the strain wavelength/grating length ratio.
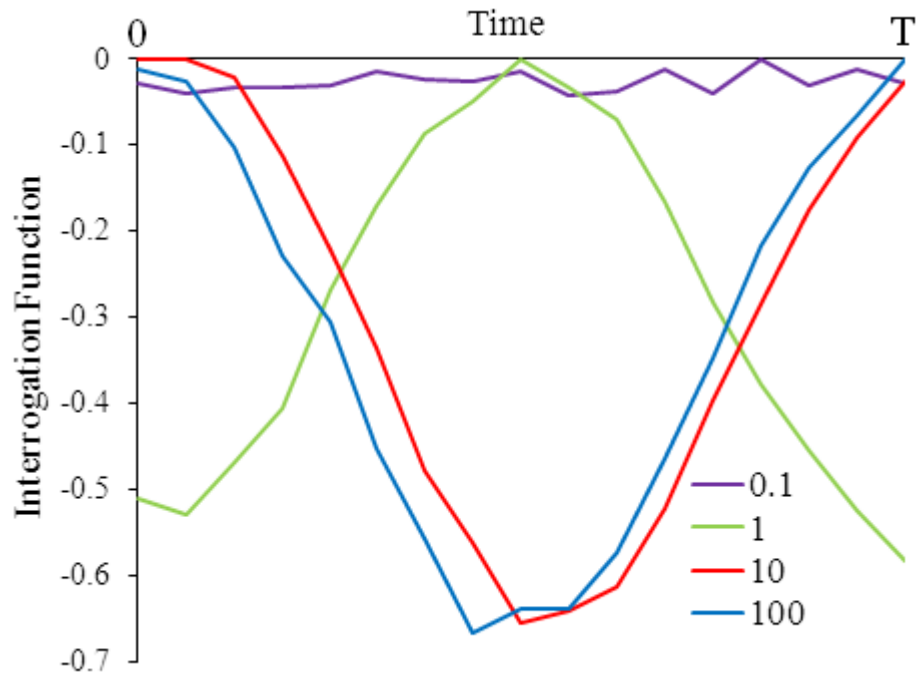
Figure 5.18. Modelled change in the interrogation function for an apodised FBG interacting with a strain wave over one time period, *T*, of the wave. Each curve corresponds to a different value of the strain wavelength/grating length ratio.

The maximum change in the interrogation function was then calculated for each of these curves which correspond to a different value of the ratio λ_s/L. All of these values were used to create Figure 5.19, which relates the change in interrogation function to the strain wavelength/grating length ratio.
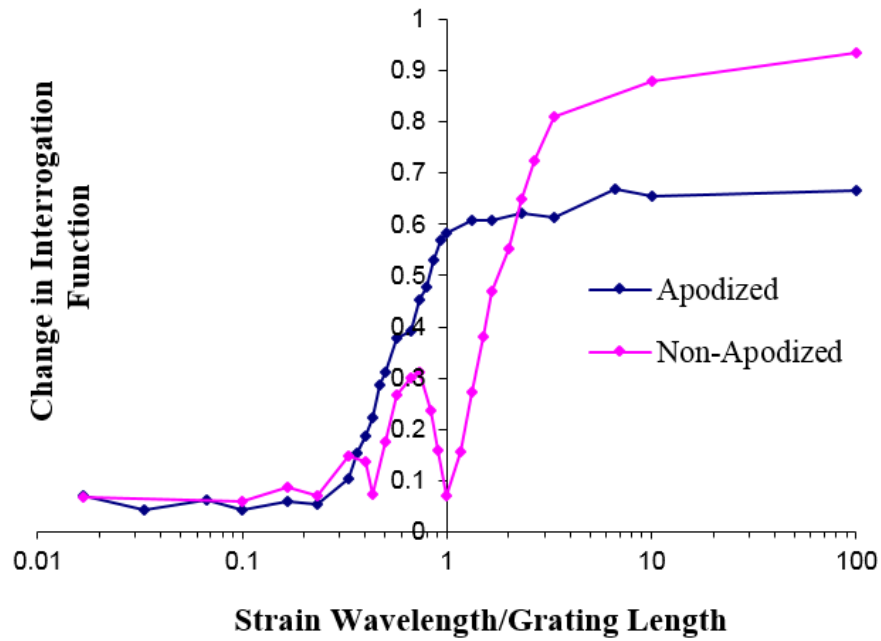
Figure 5.19. Comparing the sensitivity of the AWG interrogation system for many values of the ratio between the perturbing strain wavelength and the grating length for both apodized and non-apodized gratings.

As expected for the non-apodized case, the sensitivity approaches zero as the strain wavelength approaches the grating length because the two halves of the strain wave will cause opposite shifts in the grating and therefore cancel with each other. The sensitivity recovers marginally when the ratio approaches 0.67 as an odd number of half wavelengths will create a sizable net effect. These results suggest that in order to be sensitive to the maximum amount of signal the grating length should approach a tenth of the wavelength of the highest frequency component of interest.

For the apodized case, the sensitivity falls away at a shorter wavelength. This can be qualitively explained by considering that the apodized grating has a gradual refractive index profile over the full length of the grating and as such the 'effective' length of the grating is shorter. Theoretically, a greater change in interrogation function can be achieved with the non-apodized grating, due to the effect of the FBG side lobes, but this is dependent on the side lobe intensity and comparative width of the grating and AWG channels. In addition, it complicates the calibration relation and leads to non-linearity; it is therefore advisable to use apodized FBGs, which will maintain a high sensitivity down to a strain wavelength to grating length ratio of 1.

5.3.4. Effect of Grating Length on Grating FWHM

The primary concern when choosing the grating length should be the frequency components of interest in the measured signal. In addition, the grating length indirectly affects the FBG spectral width. The reflectivity, R, of the grating is given by [5.4]

$$R = tanh^2\Omega \tag{5.9}$$

where

$$\Omega = \pi n \, (L/\lambda_B) \, (\Delta n/n) \, \eta(V). \tag{5.10}$$

The refractive index is given by n and $\eta(V)$ is the fraction of the integrated fundamental mode intensity contained in the core. R, therefore, varies in relation to both the length of the grating L and the refractive index perturbation ($\Delta n/n$). Therefore, the shorter the FBG length the greater the refractive index perturbation must be in order to obtain a high reflectivity grating which is desirable for a system of this nature. This has the consequence of broadening the FBG spectrum with the 3dB bandwidth approximated by the equation

$$B_{3dB} = \lambda_B s \, \sqrt{\left(\left(\frac{\Delta n}{n}\right)^2 + \left(\frac{1}{N}\right)^2\right)} \tag{5.11}$$

where s is a factor ~ 1 for strong gratings and ~ 0.5 for weak gratings and N is the number of grating planes [5.31]. Hence, both the shortening of the grating and the increased refractive index perturbation lead to an increase in the 3 dB bandwidth, with the length change being the dominant factor. The refractive index modulation is varied to determine the level required for a high reflectivity grating which then determines the 3 dB bandwidth. Figure 5.20 illustrates this using the model described earlier to produce spectra for 1 mm and 3 mm long, non-apodized gratings showing the increase in spectral width as the length of the grating is reduced. The required refractive index modulation to achieve high reflectivity is different for the 1mm and 3mm gratings which is why the shorter grating is modelled with higher values of the modulation.
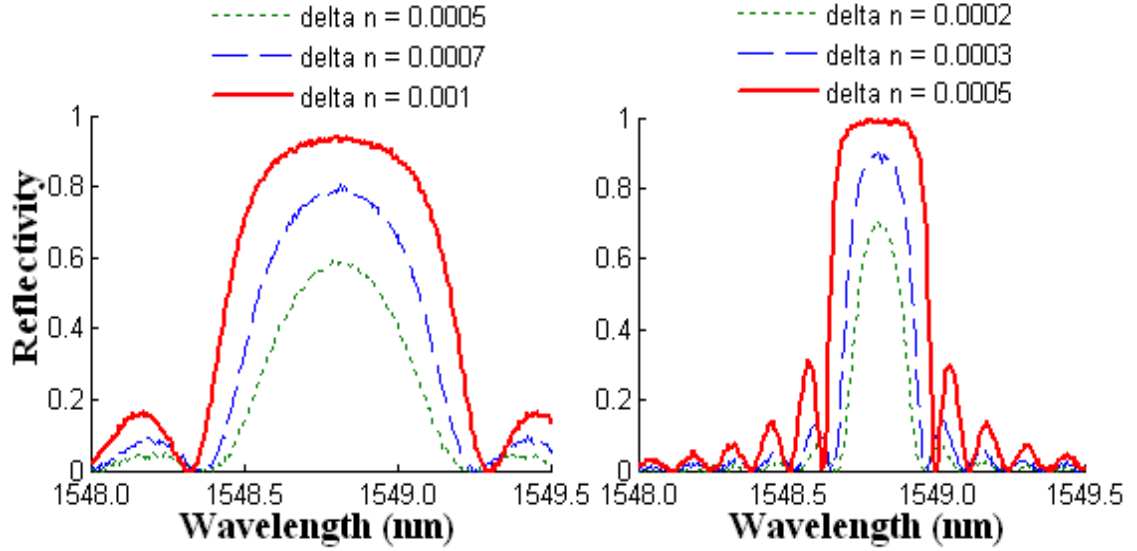
Figure 5.20. Models of FBG spectra for 1mm long gratings (left) and 3mm gratings (right) for various values of delta n, the refractive index modulation. They show the required modulation to reach a high reflectivity grating for each case.

5.3.5. Design summary based upon model with experimental evidence

Based on these results, the following considerations should be followed when designing an AWG based FBG interrogation system. The sensing requirements should first be established including the maximum signal frequency to be detected, the maximum deviation of the FBG spectrum (based on maximum expected wavelength shift e.g. strain in this example), the number of multiplexed sensors and the sensitivity required. If the maximum frequency to be detected places any restrictions on the length of the grating, and therefore the grating spectral width, this should be determined first. The AWG bandwidth should then be chosen based on the number of sensors required, the maximum wavelength shift to be accommodated and the sensitivity. More AWG channels can be assigned to each sensor to increase the range while preserving the sensitivity, but this requires more detectors and signal processing per sensor and reduces the amount of sensors which can be multiplexed. Finally, the FBG spectral width (FWHM) should then be set to be similar to the spectral width of the AWG channel to improve linearity and put less reliance on an accurate and reproducible calibration. If measurement sensitivity is of particular importance then the width may have to be reduced at the risk of greater nonlinearity.

5.4.   System Performance and Stability

For a system such as the one described above, there are various sources of potential error including thermal noise, shot noise, temperature variations of components and the error due to nonlinearity in the system. While the system can be calibrated to produce a

124

linear relation between strain and the interrogation function, this still produces errors especially in the low sensitivity regions when the FBG spectrum is completely overlapped with one AWG channel. As discussed in §5.3.1 this can be minimised by ensuring that the FBG FWHM is well matched to that of the AWG channel FWHM.

In order to quantify the other sources of error listed, experiments were carried out for each of the sensors without strain being applied. This was performed for two different time periods in order to assess the effect that temperature fluctuations and long-period drifts have on system stability as well as short timescale events. Data were captured for 1 hour at 1 Hz sample rate to determine long-term stability and for 20 ms at a 200 kHz sample rate to evaluate the noise over the duration of a typical transient impact detection event.
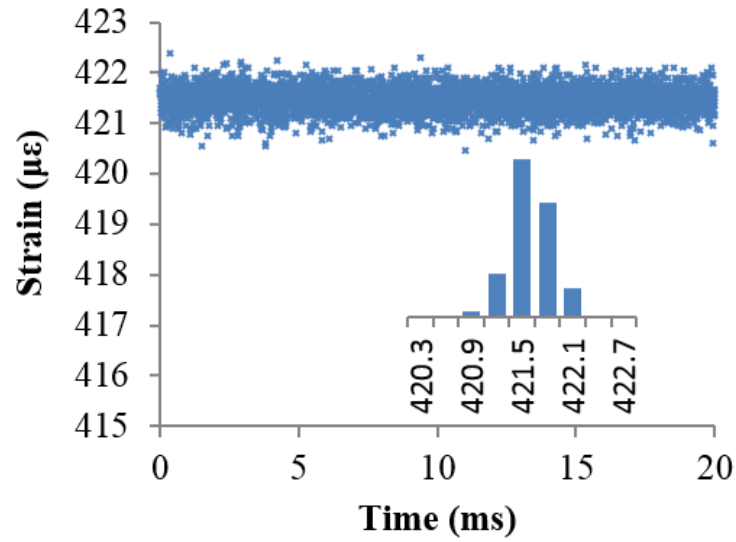
Figure 5.21. Stability test for FBG 3 over 20 ms with a sample rate of 200 kHz. Displayed is the strain as a function of time along with a histogram showing the distribution of points (inset).

Figure 5.21 shows one such stability test for FBG 3, carried out over 20 ms with a sample rate of 200 kHz, showing the time evolution of the signal as well as a histogram displaying the spread of the data points. The strain was calculated from the interrogation function using the calibration obtained earlier;

$$strain = (i.f. + 1.482) / 0.0036 \qquad (5.12)$$

Figure 5.22. Stability test for FBG 3 over an hour with a sample rate of 1Hz.

The long term stability test for FBG 3 is shown in Figure 5.22, data was captured over an hour with a sample rate of 1 Hz.

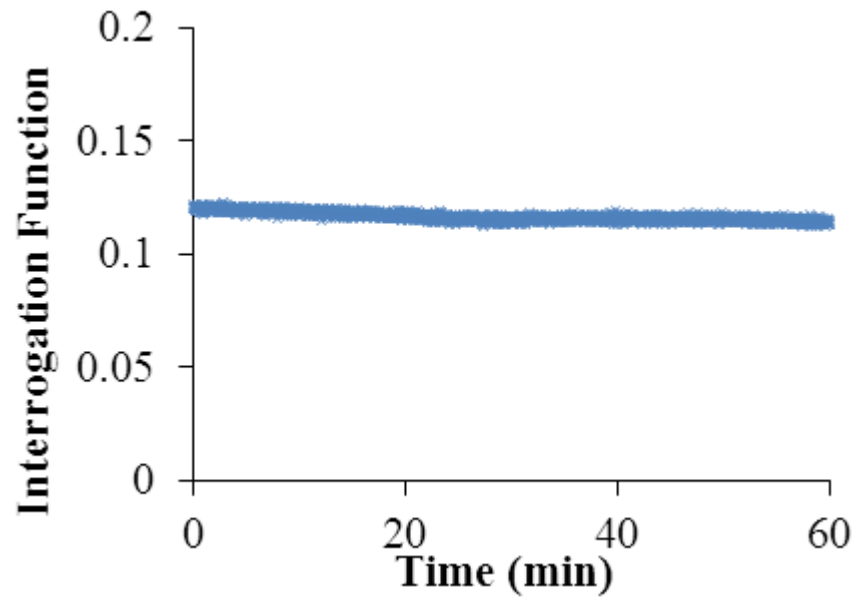Using the calibration curves determined in §5.2.1, the standard deviations (σ) of these data were converted to strain values in order to determine the strain resolution of the system. These data are summarised in Table 5.2.

Table 5.2. Comparison of the standard deviation of the system over a 20 ms as well as a 1 h time period for each of the FBGs.

Time Period	Standard Deviation ($\mu\varepsilon$)		
	FBG 1	FBG 2	FBG 3
20 ms	1.83	1.38	1.00
1 h	3.67	3.62	2.11

To further characterize system performance, the signal-to-noise ratio (SNR) was calculated using the calibration data for each of the three FBGs. This was computed for the equal case where the FBG spectrum is between two AWG channel spectra giving an equal signal in each, and for the overlapped case where the FBG is fully overlapped with one AWG channel leaving the adjacent channels with very low signals. These cases correspond respectively to the central point on the calibration curve and to the edges. The SNR was calculated using a value of 2σ for the noise which, assuming a normal distribution, would account for over 95% of the data. Table 5.3 presents the SNR data along with the associated strain resolution for the two cases. For the equal signal case, the average SNR over the 3 FBGs for each individual channel was 32.9 with the combined SNR for the interrogation function of 23.2. For the overlapped case, the overlapped channels had an average SNR of 58.8, while the neighbouring channels

126

had an average of 7.4. The dramatic loss of signal-to-noise in the neighbouring channels is due to the very low light level caused by the small overlap between the FBG and AWG spectra. Due to the low SNR of one of the two channels, the overall SNR is on average 7.3. There is therefore a significant variation in SNR across the calibration curve which is detrimental to system performance. This is very evident in the strain resolution which falls from 2.5 in the equal position to 20.5 when the FBG completely overlaps an AWG channel.

Table 5.3. Comparison of the signal-to-noise ratio (SNR) and strain resolution for both the case where the FBG spectrum is directly between two AWG channels and the case where it is completely overlayed with one of them.

	SNR			Strain
	Ch. 1	Ch. 2	Combined	Resolution ($\mu\varepsilon$)
Equal	33.2	32.6	23.2	2.5
Overlapped	58.8	7.4	7.3	20.5

To address this low SNR, a semiconductor optical amplifier (SOA) was added to the system, shown in the dashed box of Figure 5.3. An SOA is an optical amplifier using a semiconductor gain medium which is electrically pumped. Anti-reflection elements such as anti-reflective coatings are used on the end faces to prevent lasing.

The SOA, with a gain of ~ 19 dB is used to amplify the optical spectrum reflected by the FBG to create a spectrum power of ~ 5.7 dBm utilising FBG 3. The electrical gain in the detector circuit was reduced in order to avoid saturating the detector meaning that most of the amplification was optical. This technique should significantly increase the optical signal in each of the AWG channels with a sizeable signal even for the neighbouring channels of the overlapped case mentioned previously. The SNR experiments were then repeated with the SOA incorporated in order to determine whether an increase in SNR had resulted.

For the equal case, the average signal-to-noise over the 3 FBGs for each individual channel was 35.6 with the combined SNR for the interrogation function of 25.0, this is a modest increase in the SNR of 8%. For the overlapped case, the overlapped channels had an average SNR of 37.3 while the neighbouring channels had an average of 27.9. This is a dramatic improvement over the non-SOA system with a large SNR in both channels. The overall SNR for the overlapped case is on average 21.8 which is a dramatic increase of ~300% over the system without the SOA included.

It has been shown that the inclusion of an SOA can significantly improve the SNR of the system, especially for the case where one channel has significantly more signal than the other. This has been investigated with a small system in a laboratory environment; it is anticipated that the improvement may be greater in a real system which may suffer light losses through imperfect connections, badly routed fibres or large sensor networks. Further work could establish the exact improvement in strain resolution through calibration of FBGs using the SOA system and allow determination of the optimum strain resolution.

5.5. Conclusion

An AWG based interrogation scheme for measurement of dynamic strain events using fibre Bragg gratings has been demonstrated. Key performance indicators have been identified including temporal bandwidth, strain range, resolution, linearity and number of multiplexed sensors. In order to design a system for a given application, the requirements for each of these parameters should first be determined. Achieving this specification requires careful choice of factors including the FBG grating length, FBG spectral width, AWG spectral width and the amount of AWG channels to be assigned to each grating. Through the use of modelling and experimentation, these parameters were investigated and their relationships with the key performance indicators identified. It was shown that an AWG channel cannot always be accurately described by a simple Gaussian profile and that the actual form can produce significant differences in the expected system response. In addition, increased linearity in the system response can be achieved by matching the FWHM of the FBG and AWG channels.

Through modelling the effect of high frequency strain waves on an FBG it was found that in order to maximise the dynamic signal captured by the sensor the grating length should be, at most, a tenth of the wavelength of the highest frequency component of interest.

The system performance was investigated with both short term (20 ms) fluctuations and long term (1 hour) drifts being measured, demonstrating a system resolution of a few microstrain. A comparison of the signal-to-noise ratio (SNR) of the system was drawn for the case when the FBG spectrum is midway between the AWG channels and the case where the FBG spectrum is directly overlaid with one channel. It was found that the average SNR in the former case was 23.2, while only 7.3 in the latter, producing a strain resolution of 2.5 $\mu\varepsilon$ and 20.5 $\mu\varepsilon$, respectively. Inclusion of a semiconductor

optical amplifier into the system produced an 8% improvement in the signal-to-noise ratio of the equal case, while in the overlapped case where there is a low light intensity in one channel there was dramatic improvement of ~ 300%.

5.6.   Discussion

An AWG based FBG interrogation system has several advantages when compared to other techniques for dynamic interrogation such as edge filters or demodulating with a narrow line-width laser. These include larger numbers of multiplexed sensors, larger strain range and a reduction in errors resulting from intensity variations due to source fluctuations or bend loss. However, there are several trade-offs between strain sensitivity, strain range, number of sensors and temporal bandwidth which must be carefully considered for the intended application. Without consideration of factors such as the AWG channel spectral width, FBG spectral width and physical length the resulting system could be unfit for purpose. If the physical length of the FBG is too long then it will be insensitive to higher frequency strain waves which may be of interest. Therefore this is the first parameter of the system that should be set in order to ensure it is sensitive to all frequencies of interest. The second parameter to determine is the AWG channel bandwidth; there are only a small number of values commercially available, larger values will allow a larger strain range per channel but will reduce the strain sensitivity. Larger values, such as that of a 200GHz AWG, will be most appropriate to applications that require a large strain range but only average sensitivity such impact detection. Finally the spectral width should be chosen, the closer the value is to the AWG channel spectral width the more linear the system response will be. Higher strain sensitivity over a shorter strain range can be achieved by reducing the FBG spectral width which will be preferable applications with small strain amplitudes such as acoustic emission. The FBG grating length will, for a high reflectivity grating, place restrictions on its spectral width so it may not be possible to achieve the optimal value for the system. If a narrower grating is desired then a semiconductor optical amplifier could be used to obtain a large optical signal from a lower reflectivity grating.

5.7. References

[5.1] H. B. Liua, H. Y. Liua, G. D. Penga, P. L. Chu, "*Strain and temperature sensor using a combination of polymer and silica fibre Bragg gratings*", Optics Communications **219** pp. 139–142 (2003).

[5.2] M. A. Davis and A. D. Kersey, "*Application of a Fiber Fourier Transform Spectrometer to the Detection of Wavelength-Encoded Signals from Bragg Grating Sensors*" Electron. Lett. Vol. **31** No. 10 (1995).

[5.3] Y. Zhu, and A. Wang, "*Miniature Fiber-Optic Pressure*", Sensor IEEE Photonics Technology Letters, Vol. **17**, No. 2 (2005).

[5.4] Y. –J. Rao, "*In-fibre Bragg grating sensors*" Meas. Sci. Technol. **8** pp. 355–375 (1996).

[5.5] A. D. Kersey, M. A. Davis, H. J. Patrick, M. LeBlanc, K. P. Koo, C. G. Askins, M. A. Putnam, and E. J. Friebele, "*Fiber Grating Sensors*" Journal of Lightwave Technology, Vol. **15**, No. 8 (1997).

[5.6] C. Rodrigues, C. Félix, A. Lage, J. Figueiras, "*Development of a long-term monitoring system based on FBG sensors applied to concrete bridges*" Engineering Structures **32** pp. 1993-2002 (2010).

[5.7] C. C. Chan, W. Jin, H. L. Ho, and M. S. Demokan, "*Performance Analysis of a Time-Division-Multiplexed Fiber Bragg Grating Sensor Array by Use of a Tunable Laser Source*", IEEE Journal Of Selected Topics In Quantum Electronics, Vol. **6**, No. 5 (2000).

[5.8] G. A. Ball, W. W. Morey and P. K. Cheo, "*Fibre laser source/analyzer for Bragg grating sensor array interrogation*" Journal of Lightwave Technol. **12** pp. 700–3 (1994).

[5.9] M. A. Davis, D. G. Bellemore, M. A. Putnam and A. D. Kersey, "*Interrogation of 60 fibre Bragg grating sensors with microstrain resolution capability*" Electron. Lett. Vol. **32** No. 15 (1996).

[5.10] Ibsen Photonics, Ryttermarken 15-21, DK-3520 Farum, Denmark http://www.ibsen.dk/

[5.11] Fiberpro Inc, 26-55 Gajeongbuk-ro, Yuseong-gu, Dae-Jeon, Korea http://www.fiberpro.com/

[5.12] A. B. Lobo Ribeiro, L. A. Ferreira, J. L. Santos, and D. A. Jackson, *"Optical Fiber Sensor Technology in Portugal"* Appl. Opt. **36**, pp. 934-939 (1997).

[5.13] D. C. Betz, G. Thursby, B. Culshaw and W. J. Staszewski, *"Acousto-ultrasonic sensing using fiber Bragg gratings"*, Smart Mater. Struct. **12** pp. 122–128 (2003).

[5.14] Y. Sano and T. Yoshino, *"Acousto-ultrasonic sensing using fiber Bragg gratings"* Journal Of Lightwave Technology, Vol. **21**, No. 1 (2003).

[5.15] P. Niewczas, A. J. Willshire, L. Dziuda, and J. R. McDonald, *"Performance Analysis of the Fiber Bragg Grating Interrogation System Based on an Arrayed Waveguide Grating"*, IEEE Transactions On Instrumentation And Measurement, Vol. **53**, No. 4 (2004).

[5.16] D. Robertson, P. Niewczas, and J. R. McDonald, *"Interrogation of a Dual-Fiber-Bragg-Grating Sensor Using an Arrayed Waveguide Grating"* IEEE Transactions On Instrumentation And Measurement Vol. **56**, No. 6 (2007).

[5.17] G. Fusiek, P. Niewczas, A. J. Willshire, and J. R. McDonald, *"Nonlinearity Compensation of the Fiber Bragg Grating Interrogation System Based on an Arrayed Waveguide Grating"*, IEEE Transactions on Instrumentation and Measurement Vol. **57**, No. 11 (2008).

[5.18] P. Cheben, E. Post, S. Janz, J. Albert, A. Laronche, J. H. Schmid, D. –X. Xu, B. Lamontagne, J. Lapointe, A. Delâge, and A. Densmore, *"Tilted fiber Bragg grating sensor interrogation system using a high-resolution silicon-on-insulator arrayed waveguide grating"*, Opt. Lett. **33** (22) (2008).

[5.19] H. Guo, G. Xiao, and J. Yao, *"Interrogation of a Long Period Grating Fiber Sensor With an Arrayed-Waveguide-Grating-Based Demultiplexer Through Curve Fitting"*, IEEE Sensors Journal **8** (11) (2008).

[5.20] D. C. C. Norman, D. J. Webb and R. D. Pechstedt, *"Extended range interrogation of wavelength division multiplexed fibre Bragg grating sensors using arrayed waveguide grating"* Electron. Lett. **39** (24) (2003).

[5.21] D. C. C. Norman, D. J. Webb and R. D. Pechstedt, *"Interrogation of Fibre Bragg Grating Sensors Using an Arrayed Waveguide Grating"*, Meas. Sci. Technol. **16** pp. 691–698 (2005).

[5.22] N. Watanabe, M. Shimanzaki, Y. Okabe, H. Soejima, and T. Ogisu, *"Impact detection in composite laminates by high-speed FBG measurement system using AWG filters"* Asia-Pacific Workshop on Structural Health Monitoring (Tokyo) (2010).

[5.23] Y. Okabe, N. Watanabe, M. Shimazaki, H. Soejima and T. Ogisu, *"Detection of Impact Strain Waves in Composites by High-Speed FBG Sensor System with AWG Filter"*, Proceedings of IWSHM Conf., (Stanford University) (2011).

[5.24] A. Minardo, A. Cusano, R. Bernini, L. Zeni, and M. Giordano, *"Response of Fiber Bragg Gratings to Longitudinal Ultrasonic Waves"* IEEE Transactions on Ultrasonics, Ferroelectrics, and Frequency Control, Vol. **52** No. 2 (2005).

[5.25] M. A. Muriel, and A. Carballar, *"Internal Field Distributions in Fiber Bragg Gratings"* IEEE Photonics Technology Letters, Vol. **9**, No. 7 (1997).

[5.26] F. G. Sun, G. Z. Xiao, Z. Y. Zhang, and Z. G. Lu, *"Modelling of arrayed waveguide grating for wavelength interrogation application"*, Optics Communications **271** pp. 105–108 (2007).

[5.27] M. K. Smit, and C. Van Dam, *"PHASAR-Based WDM devices: Principles, design and applications"* IEEE J. Topics Quantum Elec. **2** pp. 236-250 (1996).

[5.28] W.Y. Li, C.C. Cheng, Y.L. Lo, *"Investigation of strain transmission of surface-bonded FBGs used as strain sensors"*, Sensors and Actuators A: Physical, Vol. **149**, No. 2, pp. 201-207 (2009).

[5.29] J. -R. Lee, H. -M. Jeong, *"Design of resonant acoustic sensors using fiber Bragg gratings"*, Meas. Sci. Technol. 21 (2010).

[5.30] R. John, I. Read, and W. MacPherson, *"Impact Damage Assessment by Sensor Signal Analysis"*, Proceedings of IWSHM Conf., (Stanford University) (2011).

[5.31] P. S. Russell, J. Archambault and L. Reekie, *"Fibre gratings"*, Phys. World **6 pp.** 41–6 (1993).

Chapter 6 - Two Wave Mixing Interrogator

6.1.   Introduction

One method of interrogating FBG sensors with high measurement bandwidth is to use a matched filter, such as another FBG, in the readout unit (described in §5.1).   This matched grating does not experience the shift in wavelength due to strain and the system is designed such that the sensing grating spectrum is slightly shifted in the wavelength domain with respect to the filter grating so that in the sensor neutral position it is spectrally located at the full-width at half-maximum point of the matched grating [6.1, 6.2].   As the sensing grating spectrum shifts due to applied strain the intensity of light reflected via the sensor and filter FBG changes and is therefore used as a measure for the wavelength shift.   This technique has no practical measurement rate limit and can achieve high sensitivity.   However in an array of FBG sensors, each sensing grating needs a corresponding matched filter grating and a complex optical routing configuration (i.e. coupler tree) must be used to ensure the array return signals are incident on the appropriate filter gratings.   This results in increased complexity and price of the system.   This configuration is also vulnerable to intensity fluctuations from the source, or connecting lead bend losses, both of which risk being interpreted as a change in strain unless care is taken with referencing.   It will also stop working when the sensing grating shifts away from the matched grating due to quasi-static strain or temperature changes.

An alternative approach uses an arrayed waveguide grating instead of the matched gratings, as described in the previous chapter.   Several channels can be used per sensor to produce a coarse spectrometer by fitting a parabola to the data with no practical limit on measurement speed [6.3, 6.4, 6.5].   Alternatively, two adjacent channels of the AWG can be made to overlap with an FBG spectrum and used in a similar manner to the matched grating technique with a ratio of the two channels calculated to counteract the effect of common mode intensity noise [6.6].   Using this technique, impacts have been successfully detected and the detectable strain range extended by increasing the number of pairs of channels used for each sensor [6.7, 6.8].

While this technique has many advantages such as wavelength multiplexing, high temporal bandwidth and good sensitivity it does, however, have a limited range due to the FBG spectrum shifting too much such that it no longer overlaps a monitored AWG channel.   Each channel must have a separate photodiode and associated signal processing to make the measurement, for example, for a standard 100 GHz AWG with 4

channels assigned to each sensor the stain range would be $\pm 736\ \mu\epsilon$. The typical requirements for an aerospace structural health monitoring application specify a strain range of $\pm 3500\ \mu\epsilon$ [6.9, 6.10] along with an operational temperature range of -60 °C to 160 °C [6.9] or -60 °C to 100 °C [6.10]. Even with the latter, less stringent, requirement each sensor would require 22 channels of an AWG to be able to deal with the changes in quasi-static strain and temperature expected in an aerospace environment. Some temperature compensation may be possible by temperature tuning the AWG in accordance with the aircraft temperature but any inhomogeneity of the temperature across the airframe, for instance near the engines, cannot be compensated in this manner. For a dynamic strain sensing system therefore, the cross sensitivity to both quasi-static strain and temperature is a problem for certain applications using this demodulation technique.

This chapter will investigate the possibility of a dynamic strain sensing system that remains functional while simultaneously undergoing large quasi-static strain and temperature fluctuations. A dynamic fibre Bragg grating interrogation scheme is investigated using two-wave mixing in erbium-doped fibre. An interference pattern set up in the erbium-doped fibre creates, due to the photorefractive effect, a dynamic grating capable of wavelength demodulating the FBG signal. The presence of a dynamic grating was verified and then dynamic strain signals from a fibre stretcher were measured. The adaptive nature of the technique was successfully demonstrated by heating the FBG while it underwent dynamic straining leading to detection unlike an alternative arrayed waveguide grating system which simultaneously failed detection. Two gratings were then wavelength division multiplexed with the signal grating receiving approximately 30 dB greater signal showing that there was little cross talk in the system.

6.2.   Theory

6.2.1.   Two-wave mixing

Two wave mixing (TWM) is a non-linear process by which two electromagnetic waves couple together and exchange energy in a non-linear optical medium. An interference pattern formed by two laser beams will lead to a periodic spatial variation in intensity in a non-linear medium this will induce a refractive index variation. This process is similar to that of hologram formation and such an index variation pattern is often called a volume grating. When the two waves propagate through the grating induced by them they undergo Bragg scattering and exchange energy [6.11].

Two coherent beams, termed the signal and the pump, made to interfere in a photorefractive crystal (PRC) such as InP:Fe can produce two-wave mixing. This results in a dynamic grating being formed with a grating spacing related to that of the wavelength of the two beams. The mechanism can be understood as (i) interference of the interacting beams leading to the creation of intensity gratings which, in turn, causes (ii) nonuniform photoexcitation of charges in the PRC that then diffuse or drift to create (iii) a space-charge field within the PRC. This leads to creation of (iv) a refractive index grating via the electrooptical effect, and which causes (v) diffraction of the interacting beams [6.12, 6.13, 6.14, 6.15, 6.16]. A proportion of the pump beam is diffracted into the path of the signal beam and interferes with it, which results in phase matching between the two beams. The created grating is dynamic and will adapt to any changes in the signal beam wavelength which are slower than the PRC response time. This causes the diffracted pump beam to track the signal beam for any quasi-static shifts and only dynamic changes faster than the photorefractive response time will result in a net phase change which can then be detected.

6.2.2. Erbium-doped fibre

A dynamic grating can also be formed in an erbium-doped fibre (EDF) when the bright fringes of an interference pattern in the fibre cause spatial hole burning due to the local saturation of the fibre-optic absorption (or gain if the fibre is optically pumped) [6.17]. Absorption or gain gratings have been proposed as controllable filters for distributed feedback-lasers or in various optical communications applications including high-speed optical radio frequency signal processing [6.18, 6.19]. Other studies have applied this technique to structural health monitoring by utilising a section of EDF as the sensing element in which the gain grating will be perturbed by a dynamic event in a similar manner to that of an FBG [6.20, 6.21, 6.22].

6.3. Experiment

6.3.1. Static testing

In this work the dynamic grating is used as a means of interrogating conventional fibre Bragg gratings in a standard piece of fibre. Figure 6.1 shows the optical setup of the interrogation system.
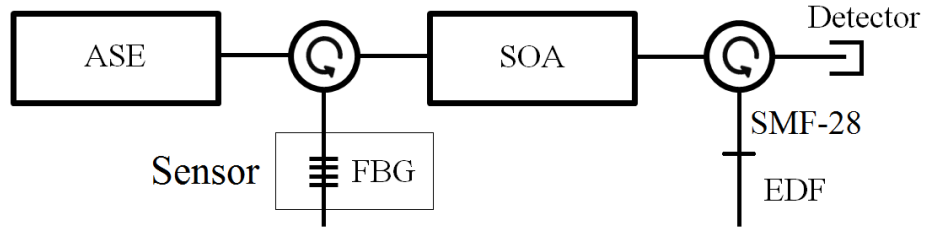
Figure 6.1. Optical diagram of proposed setup, ASE: amplified stimulated emission source, FBG: fibre Bragg grating, SOA: semiconductor optical amplifier, EDF: erbium doped fibre

An amplified spontaneous emission (ASE) broadband source is used to illuminate an FBG via a circulator. The reflected grating spectrum, which has a power of −16.07 dBm, then enters a semiconductor optical amplifier (SOA) and is amplified to a power of 6.40 dBm. This passes through a second circulator into a length of standard SMF-28 fibre with a short length (defined later) of EDF fibre (Metrogain M12-980-125) fusion spliced onto the end. The end face of the EDF is cleaved in order to create a reflection that is approximately 4%. This reflected wave then interferes with the incoming wave (Figure 6.2a) causing fringes of high and low optical intensity which leads to the formation of a dynamic grating due to the photorefractive effect (Figure 6.2b). This grating will then cause backward diffraction of some of the incoming wave creating the signal of interest (Figure 6.2c). Any quasi-static shifts in the FBG wavelength will result in a readjustment of the grating spacing with a time response related to the lifetime of the erbium excited state (between 1 to 10 ms) [6.20]. Dynamic shifts in the FBG wavelength will cause it to differ from the spacing of the dynamic grating leading to destructive interference and therefore the strain signal will be measurable as a varying light intensity at the detector (Figure 6.2d).

To ensure that there is sufficient coherence length in order to cause interference in the EDF, FBGs have been chosen with the narrowest practical linewidth, 0.1 nm. This corresponds to a coherence length given by equation (6.1) [6.23]:

$$l_c \cong \frac{\lambda_0^2}{\Delta\lambda} \qquad (6.1)$$

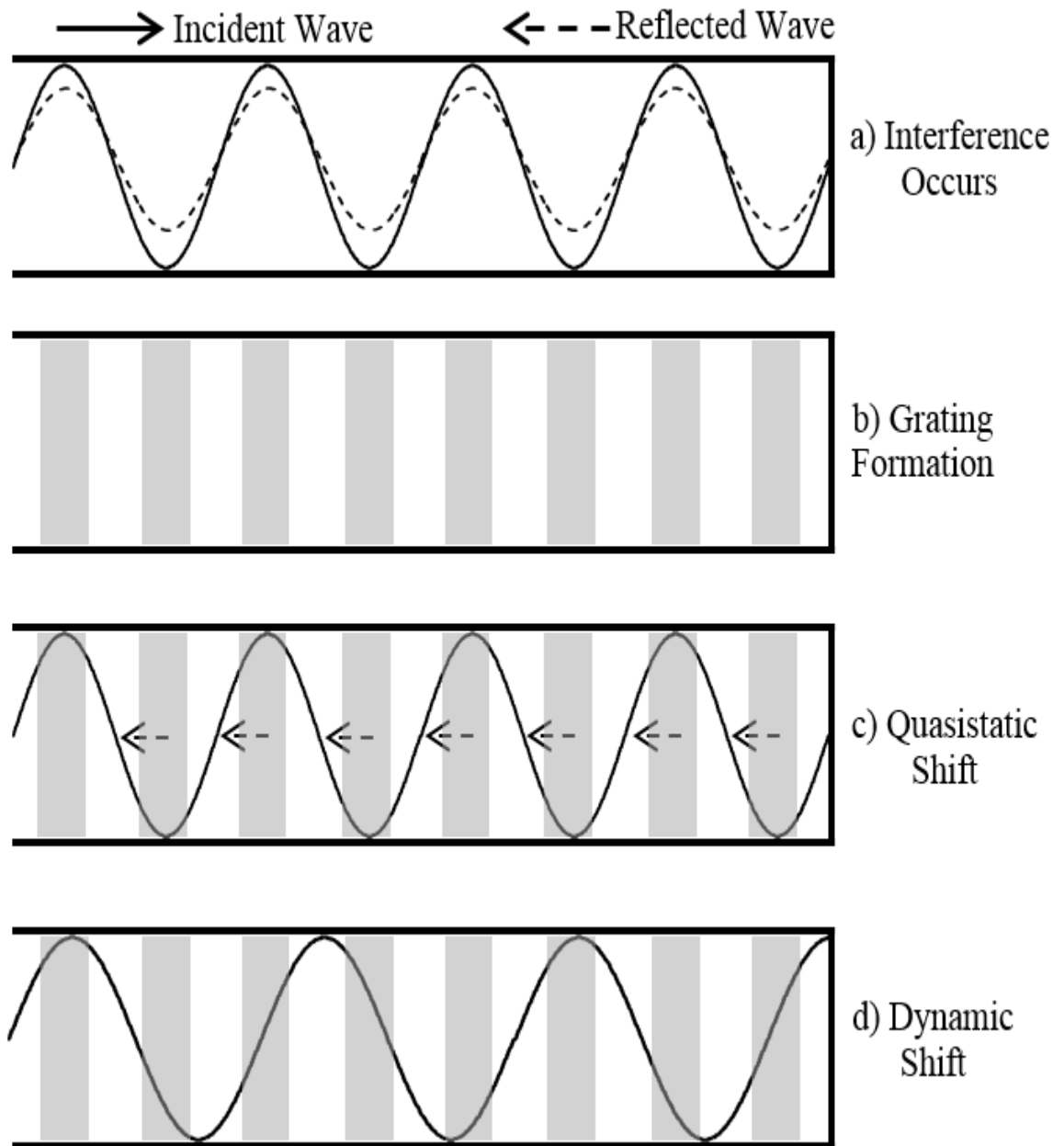which, for an FBG centred at 1550 nm, gives a coherence length of 24.0 mm.

Figure 6.2. Interrogation principle showing incident wave creating a reflected wave on the fibre end face (a). This leads to areas of high and low optical intensity and the creation of a dynamic grating (b). For the case of a quasi-static shift, this causes diffraction of some of the incident wave backwards, coherently with the reflected wave (c). This dynamic grating adapts to correspond with quasi-static shifts but dynamic shifts in the incident wavelength will cause it to differ from the dynamic grating leading to destructive interference and a reduction in reflected light (d).
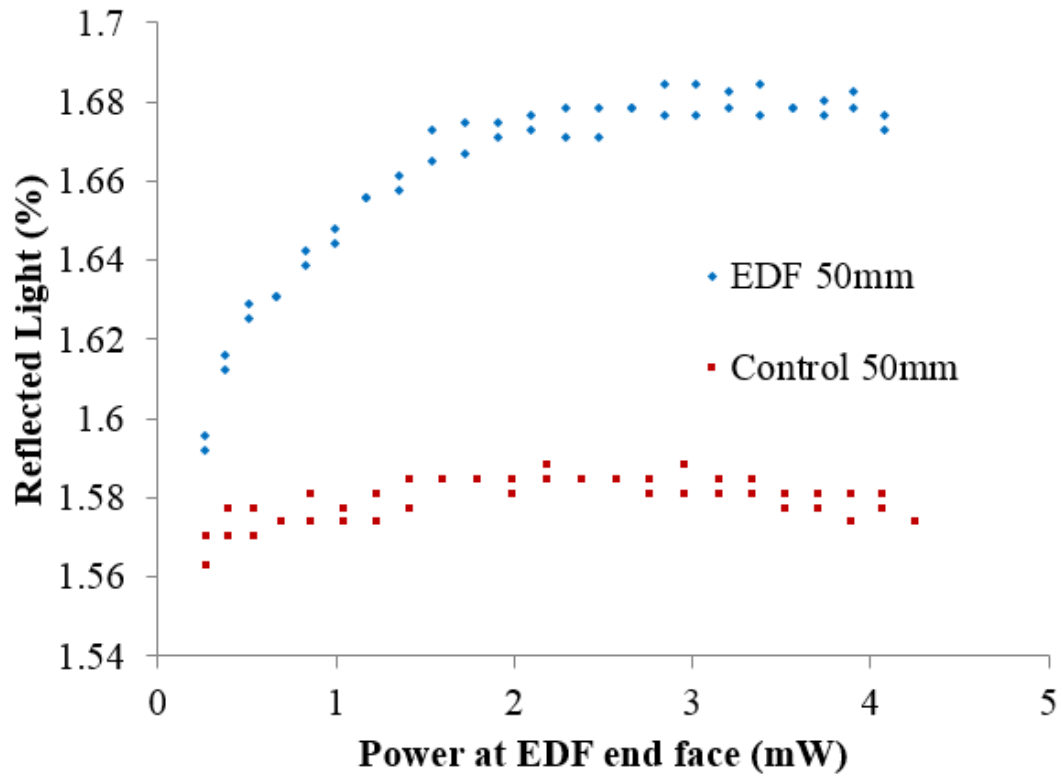
Figure 6.3. The percentage of reflected light returning from 50mm of EDF as the input light intensity is varied. Control experiment replaces EDF with the same length of SMF-28.
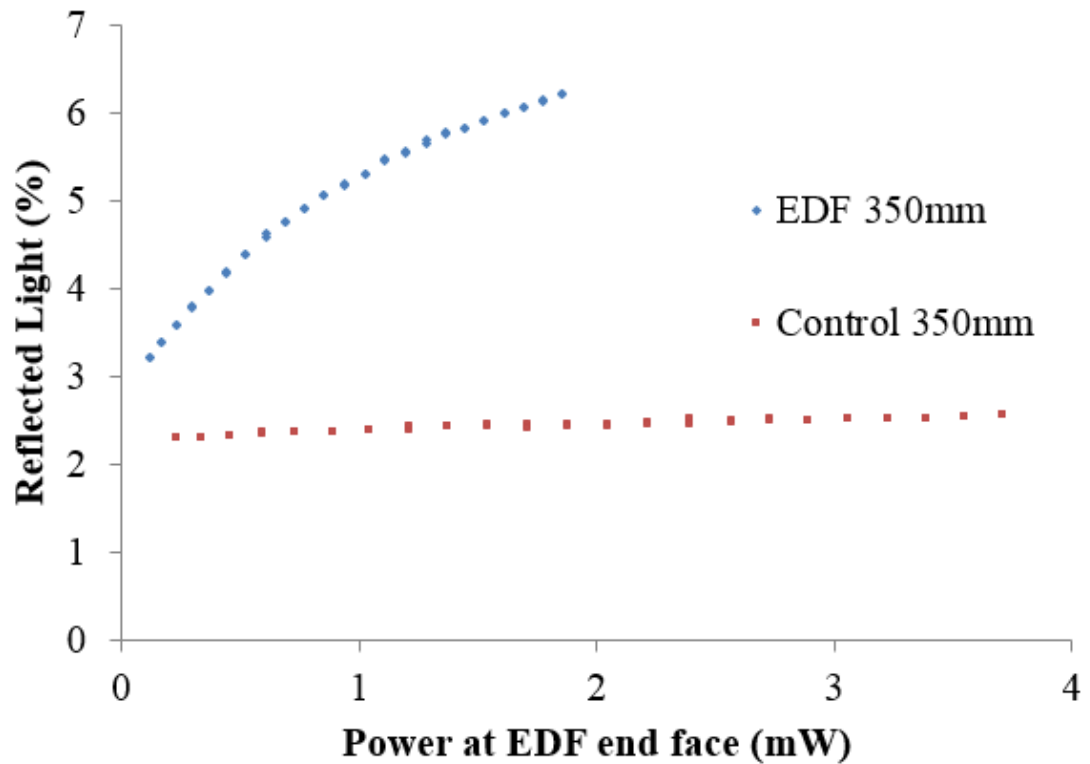

Figure 6.4. The percentage of reflected light returning from 350mm of EDF as the input light intensity is varied. Control experiment replaces EDF with the same length of SMF-28.

Firstly, to confirm the existence of an absorption grating, the input light intensity into the EDF is varied while measuring the percentage of light reflected to the detector. If a

grating is present then the percentage of reflected light should increase with input power, at low power there will be a weak grating, but as the input power increases the grating will approach saturation. To maximise the amount of coherent light used, two lengths of EDF were compared: 50 mm and 350 mm. In addition, as a control experiment the EDF was replaced by the same length of standard SMF-28 which is not expected to form a dynamic grating and can be used for comparison. The percentage of light reflected is slightly lower and more variable than might be expected due to the additional splice losses and possible variability in end cleave quality. The input light intensity was varied using the drive current to the SOA which was increased to maximum and then decreased back to minimum to test repeatability and hysteresis. The results, in Figure 6.3, show a subtle increase in the percentage of reflected light for the 50 mm fibre indicating the presence of a weak dynamic grating. The 350 mm fibre, Figure 6.4, shows a significant increase as the input power increases to the point that almost twice the initial percentage of light returns. Due to the high absorption in the EDF (8 dB/m at 1550 nm) the maximum input power at the fibre endface was lower and the data is corrected for absorption on the return trip to the detector. The shorter length of EDF saturated at around 2 – 3 mW input power but the longer fibre did not saturate as the input power was limited by the output of the SOA and increased amount of absorption caused by the longer EDF. These results suggest that a dynamic grating is indeed being formed and that the 350 mm fibre produces the strongest effect.

6.3.2. *Dynamic testing*

To test the EDF systems ability to reproduce dynamic strain signals, a dynamic fibre stretcher was built using a speaker driven by a function generator. One end of the fibre containing the FBG was clamped firmly while the other was attached to the centre of the speaker allowing it to be strained axially. The system has a limited frequency range but can perform well upto around 200 Hz after which the response diminishes. In order to compare the EDF system response with that of a known system, a 99:1 coupler was inserted immediately following the SOA and 1% of the light intensity routed to a 100 GHz AWG (Alcatel A1936AWG). The system was set up so that the FBG spectrum was at the full-width-at-half-maximum point of the AWG channel in order to demodulate the wavelength as the FBG spectrum moves. Both systems were measured using InGaAs photodetectors with a 3 dB bandwidth of 175 kHz. Measuring the 1% signal directly with the photodetector showed no intensity modulation while the grating is strained and therefore only by measuring the wavelength shift can the signal be

captured. Figure 6.5 shows the results of the dynamic testing with both the AWG and EDF systems reproducing the 200 Hz signal accurately. Due to the nature of the different interrogation schemes one system produces an increase in intensity as the wavelength increases while the other produces a decrease leading to the π phase offset observed in Figure 6.5.
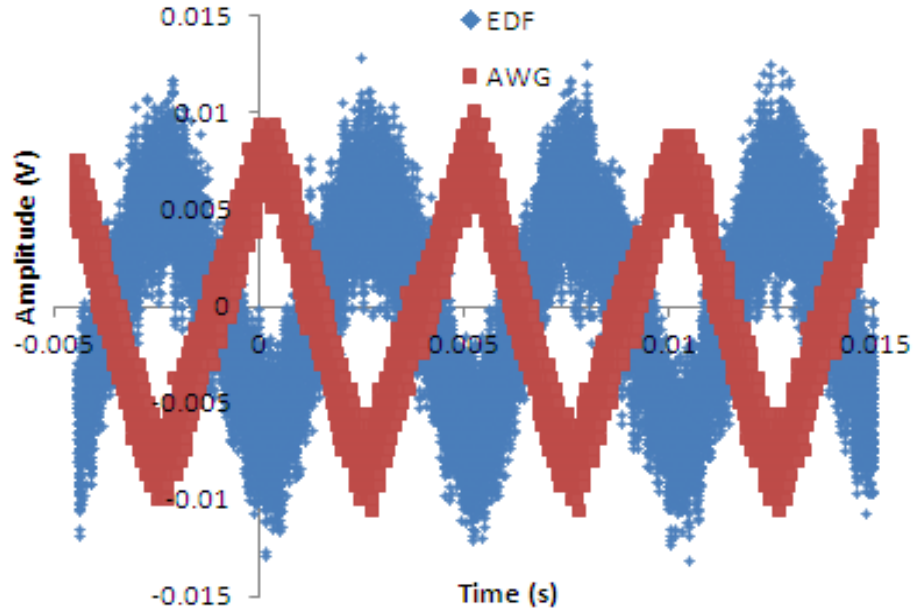

Figure 6.5. The output from the EDF interrogation system measured simultaneously with the AWG system while the FBG undergoes dynamic strain at 200 Hz at ambient temperature, 22.5 °C.

To demonstrate the advantages of the EDF over the AWG based scheme the FBG was heated axially with a soldering iron (non-contact) while simultaneously being strained dynamically.
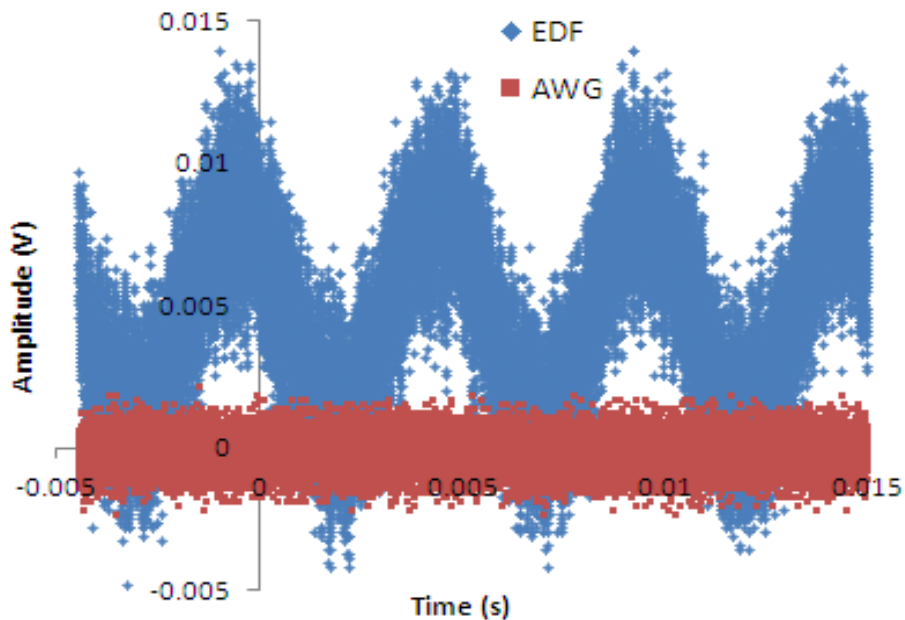

Figure 6.6. The output from the EDF interrogation system measured simultaneously with the AWG system while the FBG undergoes dynamic strain at 200 Hz after heating to 31 °C.

Figure 6.6 shows the comparison of the system responses once the FBG has been heated by approximately 8.5 °C to 31 °C. The EDF system response is unchanged while the AWG system only registers noise as the FBG spectrum has shifted away from the channel being interrogated. This result equally applies for static strain and as discussed earlier the large quasi-static shifts possible in an aerospace environment cannot be economically dealt with by the addition of extra AWG channels and detectors.

6.3.3.   *Multiplexing*

It would be beneficial to be able to simultaneously interrogate several FBG sensors using this technique in order to cover a larger area or to enable localisation of events through time of flight methods.
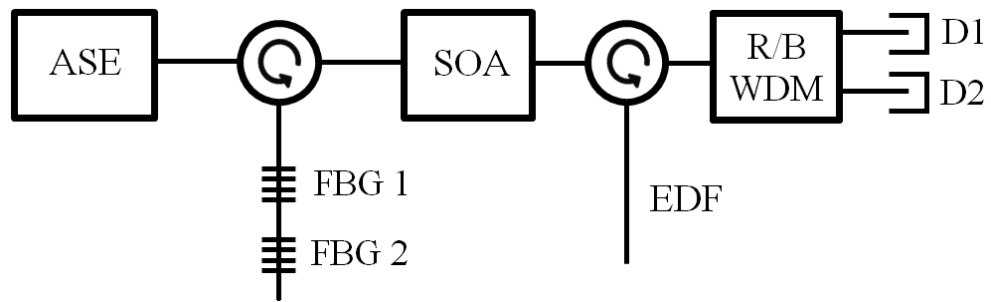

Figure 6.7. Optical diagram of multiplexing setup, ASE: amplified stimulated emission source, FBG: fibre Bragg grating, SOA: semiconductor optical amplifier, EDF: erbium doped fibre, R/B WDM: red/blue C-Band wavelength division multiplexing coupler, D1 and D2: InGaAs fibre coupled detectors.

Other studies such as Qiao *et al*.[6.13] have demonstrated dynamic strain measurement from several multiplexed FBG sensors using two-wave mixing in a photorefractive crystal. In order to demonstrate this with erbium-doped fibre the experimental setup was extended as shown in Figure 6.7 with a red/blue C-band wavelength division multiplexing coupler used to split out the signals of two different FBG sensors. FBG 1 was the same as previously used and was centred under tension at 1555nm while FBG 2 was at 1536 nm, both approximately centred in one of the couplers 17.5 nm 3 dB passbands. The ASE source has a higher emission at 1536 nm leading to a higher signal at detector 2 compared to detector 1.
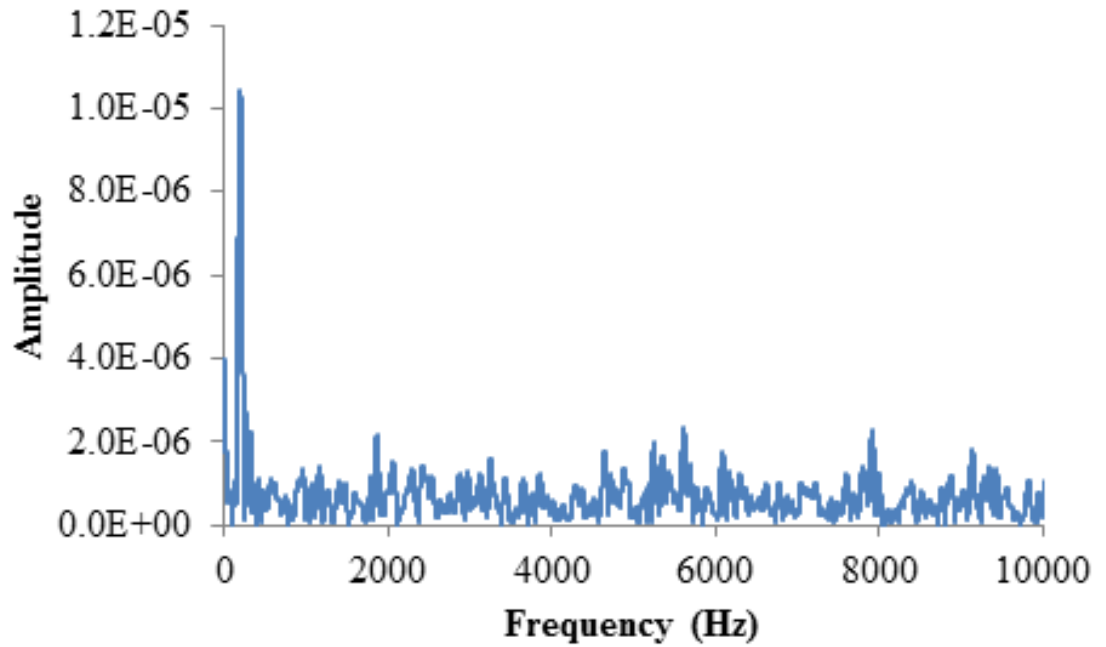
Figure 6.8. Fast Fourier transform of the multiplexed FBG 1 sensor output while it was dynamically strained at 200 Hz and FBG 2 is left unstrained
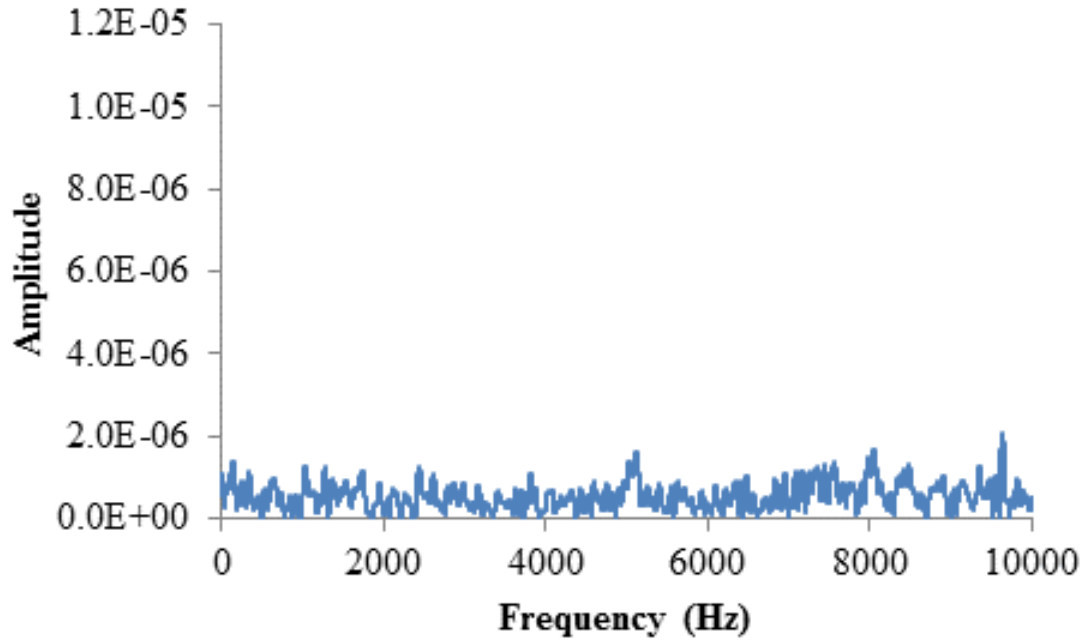

Figure 6.9. Fast Fourier transform of the multiplexed FBG 2 sensor output which was left unstrained as FBG 1 was dynamically strained at 200 Hz, as shown in Figure 6.8.

Figure 6.8 shows the fast Fourier transform results when FBG 1 was dynamically strained at 200 Hz while FBG 2 was left unstrained, Figure 6.9. A large peak can clearly be seen at 200 Hz in the data from FBG 1 while there is no corresponding peak in the data from the unstrained FBG 2. The signal peak at 200 Hz is over 16 dB larger than the noise level of the unstrained grating. Given that this measurement is limited by the noise it is likely that the crosstalk is significantly less than this level. This shows

that an erbium doped fibre two-wave mixing interrogator can be successfully wavelength division multiplexed without any significant crosstalk between the channels.

6.4. Conclusions

In this chapter we have demonstrated an adaptive wavelength demodulation technique utilising two-wave mixing in an erbium-doped fibre. The creation of a dynamic grating was determined by the percentage increase in reflected light back from the end face of the fibre as the input light intensity is increased. Dynamic strain sensing was demonstrated at 200 Hz using a FBG fibre stretcher which produced results consistent with an arrayed waveguide grating (AWG) interrogation scheme. The adaptive nature of the system was proven by heating the FBG by 8.5 °C resulting in the loss of the AWG signal while the erbium-doped fibre system remained functional. Two FBGs were then successfully wavelength division multiplexed and it was shown that the cross talk was almost 30 dB below the signal level.

6.5. Discussion

This technique has many potential advantages due to its self-referencing nature, the ability to intrinsically cope with quasi-static strain and temperature variations would be extremely beneficial in harsh and variable environments. However, the system demonstrated above had a low sensitivity and requires a high optical intensity. In contrast, the AWG system that was used as a comparison measured the signal with lower noise using only 1% of the light intensity that formed the input to the two-wave mixing interrogator. A potential line of enquiry to address this issue is described in §6.6.

The wavelength multiplexing of two FBG sensors was successfully demonstrated in §6.3.3. This is an important feature of the interrogator but relying on wavelength division multiplexing negates some of the benefits of the self-referencing which is the main advantage of the system. The multiplexor channels have to be spectrally wide and each have a flat topped passband in order to prevent intensity variations as the FBG spectrum shifts with quasi-static strain or temperature changes.

6.6. Future Work

In order to progress with a two wave mixing interrogator based on erbium doped fibre, greater sensitivity must be achieved. The signal to noise ratio must be improved which can be achieved by improving some features of the interrogator design utilised so far in this chapter. The dynamic grating is created from the incoming wave and a 4%

reflection of this wave, an optical setup that allowed two waves with similar intensity to interfere would create a much stronger dynamic grating. In the current setup, the light that reflects from the end face of the EDF also reaches the detector along with the signal of interest dramatically reducing the signal to noise ratio. Increasing the amount of light reflected, for instance, with a mirror, merely increases both the signal and the noise levels and produces no overall improvement. A design which could isolate the light that reflects from the dynamic grating would allow this signal to be measured accurately and dramatically increase the signal to noise ratio.

A proposed design to address these concerns is presented in Figure 6.10. The broadband source illuminates the fibre Bragg grating sensor via the circulator which then enters a two by two 50:50 polarization insensitive coupler. The top arm of this circuit delivers the light directly into the erbium doped fibre, the bottom arm enters a two by two polarization splitter which splits the light into its horizontally and vertically polarized components. The vertical component is removed from the system while the horizontal component enters the EDF to interfere with the light counter-propagating along the top arm. The lengths of the top and bottom arms are matched in order to create an interference pattern within the EDF. The detector is placed on the vertically polarized arm of a second polarization splitter meaning that the only light that can reach the detector must travel clockwise along the top arm before being reflected by the dynamic grating and returning anticlockwise along the top arm. This is the signal of interest and all other paths will lead the light elsewhere through the use of the polarization splitters.
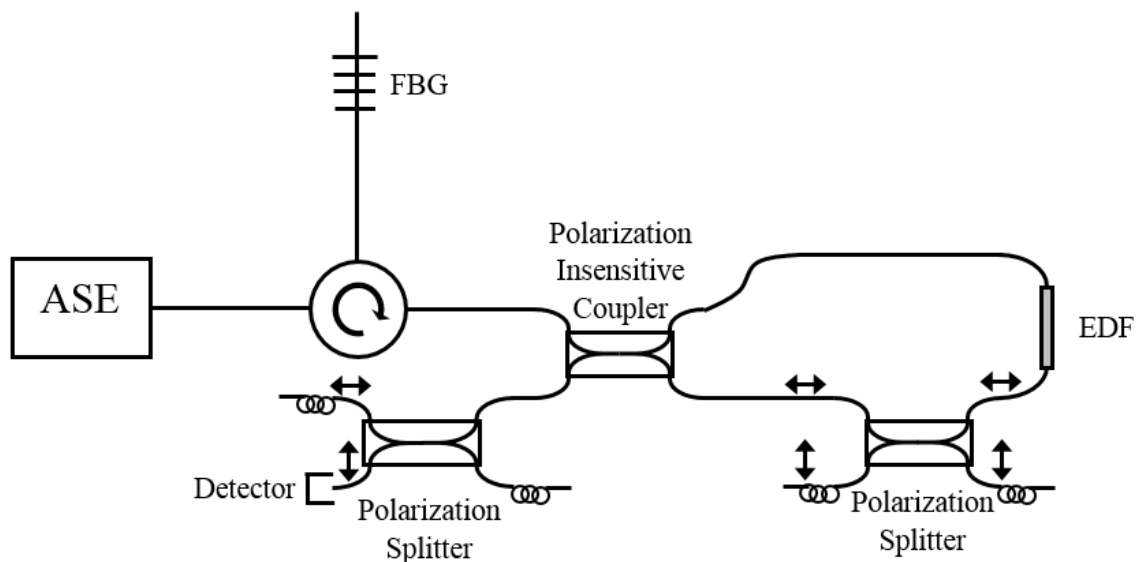

Figure 6.10. Proposed optical design for a two wave mixing interrogator using polarization components to separate out the signal of interest. ASE: amplified spontaneous emission broadband source, FBG: fibre Bragg grating sensor, EDF: erbium doped fibre.

This design should create a stronger dynamic grating due to the similar intensity of the two interfering waves as well as separate out the signal of interest. While half of the light will be lost through splitting the polarized components and further light to polarization fading this is not significant as the large amount of light that just contributed to noise in the previous design is removed. These features should dramatically increase the signal to noise ratio leading to a more sensitive system.

6.7. References

[6.1]   A. B. Lobo Ribeiro, J. L. Santos, J. M. Baptista, L. A. Ferreira, F. M. Araújo, and A. P. Leite, *"Optical Fiber Sensor Technology in Portugal"*, Fiber and Integrated Optics Vol. **24** pp. 171-199 (2005).

[6.2]   M. S. Melle, K. Lui, and R. M. Measures, *"A Passive Wavelength Demodulation System for Guided-Wave Bragg Grating Sensors"*, IEEE Photonics Technology Letters Vol. **4**, No. 5 (1992).

[6.3]   P. Niewczas, A. J. Willshire, L. Dziuda, and J. R. McDonald, *"Performance Analysis of the Fiber Bragg Grating Interrogation System Based on an Arrayed Waveguide Grating"*, IEEE Transactions on Instrumentation and Measurement Vol. **53**, No. 4, (2004).

[6.4]   D. Robertson, P. Niewczas, and J. R. McDonald, *"Interrogation of a Dual-Fiber-Bragg-Grating Sensor Using an Arrayed Waveguide Grating",* IEEE Transactions on Instrumentation and Measurement., Vol. **56**, No. 6, (2007).

[6.5]   G. Fusiek, P. Niewczas, A. J. Willshire, and J. R. McDonald, *"Nonlinearity Compensation of the Fiber Bragg Grating Interrogation System Based on an Arrayed Waveguide Grating"* IEEE Transactions on Instrumentation and Measurement Vol. **57**, No. 11, (2008).

[6.6]   Y. Sano, and T. Yoshino, *"Fast Optical Wavelength Interrogator Employing Arrayed Waveguide Grating for Distributed Fiber Bragg Grating Sensors"*, Journal of Lightwave Technology Vol. **21**, No. 1 (2003).

[6.7]   N. Watanabe, M. Shimanzaki, Y. Okabe, H. Soejima, and T. Ogisu, *"Impact detection in composite laminates by high-speed FBG measurement system using AWG filters",* Asia-Pacific Workshop on Structural Health Monitoring, November 30, to December 2, 2010, The University of Tokyo, Tokyo, Japan (2010).

[6.8]   Y. –G. Lee, B. –W. Jang, Y. –Y. Kim, C. –G. Kim, C. -Y. Park, B. –W. Lee, "*Detection of Impact Locations on Composite Wing Structure Using FBG Sensors*", Asia-Pacific Workshop on Structural Health Monitoring, November 30, to December 2, 2010, The University of Tokyo, Tokyo, Japan (2010).

[6.9]   I. J. Read, and P. D. Foote, "*Sea and flight trials of optical fibre Bragg grating strain sensing systems*", Smart Mater. Struct. **10**, pp. 1085–1094 (2001).

[6.10] H. Guo, G. Xiao, N. Mrad, and J. Yao, "*Fiber Optic Sensors for Structural Health Monitoring of Air Platforms*", Sensors 2011, **11**, pp. 3687-3705 (2011).

[6.11] P. Yeh, "*Two-Wave Mixing in Nonlinear Media*", IEEE Journal of Quantum Electronics, Vol. **25**, No. 3 (1989).

[6.12] G. Kirikera, O. Balogun, and S. Krishnaswamy, "*Fiber Bragg Gratings and Two Wave Mixing Spectral Demodulator System for Impact Detection and Localization*", 4th European Workshop on Structural Health Monitoring, Crakow, Poland, (2008).

[6.13] Y. Qiao, Y. Zhou, and S. Krishnaswamy, "*Adaptive demodulation of dynamic signals from fiber Bragg gratings using two-wave mixing technology*", Appl. Opt., Vol. **45**, No. 21 (2006).

[6.14] P. Delaye, A. Blouin, D. Drolet, L. –A. de Montmorillon, G. Roosen, and J. –P. Monchalin, "*Detection of ultrasonic motion of a scattering surface by photorefractive InP:Fe under an applied dc field*", J. Opt. Soc. Am. B. Vol. **14**, No. 7 (1997).

[6.15] P. Delaye, L. –A. de Montmorillon, and G. Roosen, "*Transmission of time modulated optical signals through an absorbing photorefractive crystal*", Optics Communications pp. 154-164 (1995).

[6.16] P. Fomitchov, T. W. Murray, and S. Krishnaswamy, "*Intrinsic fiber-optic ultrasonic sensor array using multiplexed two-wave mixing interferometry*", Appl. Opt., Vol. **41**, No. 7 (2002).

[6.17] S. Stepanov, E. Hernández, and M. Plata, "*Two-wave mixing by means of dynamic Bragg gratings recorded by saturation of absorption in erbium-doped fibers*", Opt. Lett. Vol. **29**. No. 12 (2004).

[6.18] B. Fischer, J. L. Zyskind, J. W. Sulhoff, D. J. DiGiovanni, *"Nonlinear wave mixing and induced gratings in erbium-doped fiber amplifiers"*, Opt. Lett. Vol. **18**. No. 24 (1993).

[6.19] S. A. Havstad, B. Fischer, A. E. Willner, and M. G. Wickham, *"Loop-mirror filters based on saturable-gain or -absorber gratings"*, Opt. Lett. Vol. **24**, No. 21 (1999).

[6.20] S. Molin, I. Abada, D. Dolfi, J. −P. Huignard, and M. Doisy, *"Dynamic strain sensor based on two wave mixing in optical fibers"*, Proc. SPIE 20th Int. Conf. on Optical Fibre Sensors, Edinburgh, UK, Vol. 7503 (2009).

[6.21] S. Stepanov, and F. P. Cota, *"Transient two-wave mixing in a linear configuration of an adaptive interferometer based on Er-doped fiber with saturable absorption"*, Opt. Lett. Vol. **32**, No. 17 (2007).

[6.22] S. Stepanov, *"Dynamic population gratings in rare-earth-doped optical fibres"*, J. Phys. D: Appl. Phys. **41** 224002 (2008).

[6.23] A. S. Marathay, *"Elements of optical coherence theory"*, Wiley, 139 (1982).

Chapter 7 – Demonstrator System

7.1. Introduction

Many different aspects of dynamic strain sensing and impact detection have been researched for this thesis. The purpose of this chapter is to describe the development of a demonstrator system bringing together aspects of this research in order to produce a capable FBG impact detection and location system. A key objective of this work is to produce an optical system that allows interrogation of multiplexed sensors, is scalable and could be adapted for a real world application. The system must be sufficiently sensitive to measure the acoustic waves produced during an impact event even after they have travelled through a complex, highly attenuating composite structure as well as have sufficient range to measure the maximum wavelength change caused by the impact. Once the dynamic strain signals have been acquired for an impact the location should be determined as accurately as possible and displayed or recorded to demonstrate the capability.

To accomplish this, an AWG based system has been chosen as it offers the possibility for multiplexed sensor operation, high strain sensitivity and sufficient strain range. The current implementation of the two-wave mixing based interrogator may perhaps lack the required sensitivity to accurately measure the highly attenuated signals that occur on the curved composite structure. The system will be influenced by the design considerations identified in chapter 5 and extended to simultaneous interrogate multiple FBG sensors.

The signal acquisition and impact location determination will build on the work from chapter 3. The LabVIEW program will be extended to acquire more channels and a neural network will be trained to determine the impact location as it was found to noticeably outperform the triangulation method.

As such, this demonstration system brings together the different areas of research presented in this thesis in order to show their applicability and visually demonstrate the technologies.

7.2. System Implementation

The leading edge structure used for the impact location work in chapter 3 was utilised again for this demonstrator system. Four new FBG sensors were bonded onto the structure near to the corners. At each of the sensor locations, the fibre axis was aligned with the centre of the curved surface in order to maximise sensitivity for the largest proportion of the surface, illustrated in Figure 7.1. The FBG sensors used were of the

same type as FBG 3 in chapter 5, supplied by Aston University, they have a physical length of 3mm and an average FWHM of 0.63 nm. A 100 GHz AWG was chosen to maximise the sensitivity of the system while still providing sufficient strain range, it has an FWHM of 0.54 nm which is well matched to the sensors' FWHM and will thus result in good linearity. The four FBG sensors were fusion spliced to create an array multiplexed into a single optical fibre, which was then bonded onto the underside of the structure using quick set epoxy resin.
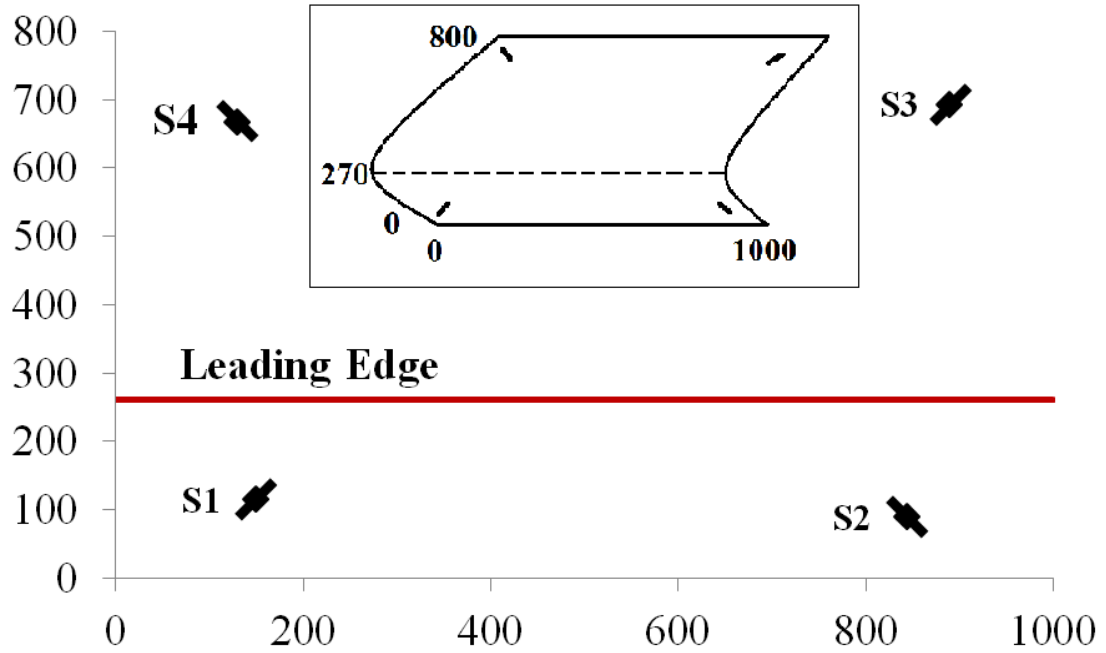

Figure 7.1. Diagram showing the FBG sensor positions and orientations on a 2D representation of the leading edge structure. The sensors are angled to provide greatest sensitivity to the largest proportion of the structure possible.

Figure 7.2 shows the optical diagram for the demonstrator system featuring an amplified spontaneous emission broadband source (ASE) which illuminates four multiplexed FBG sensors via a circulator. The FBG reflection spectra are then optically amplified using the semiconductor optical amplifier (SOA) and then enter the arrayed waveguide grating (AWG) via the common channel. The four sensors had their Bragg wavelength carefully chosen so that there is approximately 3.2 nm separating each one. This allows each sensor to be placed between two different AWG channels as it is a multiple of its 0.8nm channel spacing. As the FBG spacing is four times larger than the AWG channel spacing allows a separation to be maintained and thus ensure there is no crosstalk between sensors. The AWG was temperature tuned to place each of the FBG spectral peaks directly between two AWG channels and then the temperature was held constant.
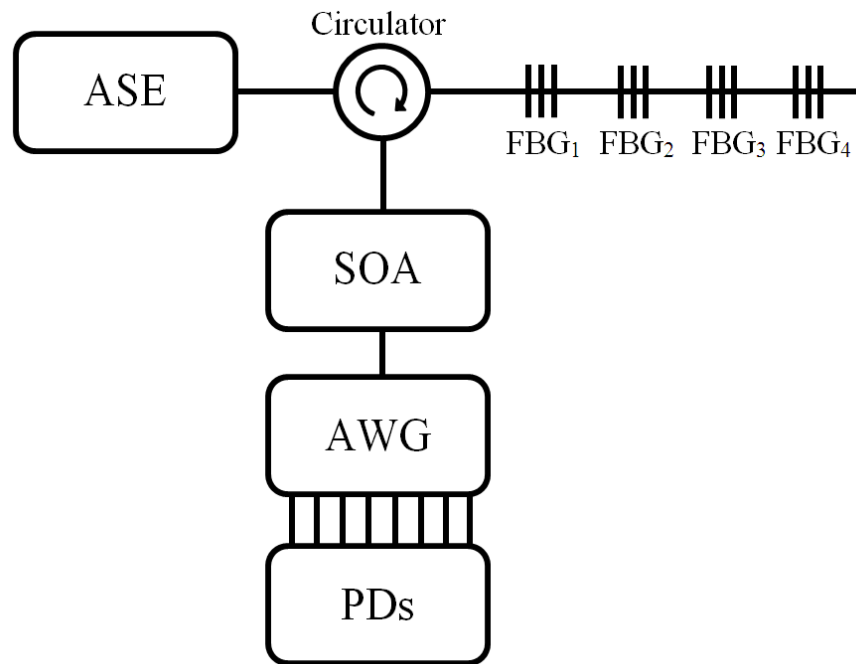
149

Figure 7.2. Optical diagram for the demonstrator system featuring an amplified spontaneous emission broadband source (ASE), four multiplexed FBG sensors, semiconductor optical amplifier (SOA), arrayed waveguide grating (AWG) and set of eight fibre coupled photodetectors (PDs).
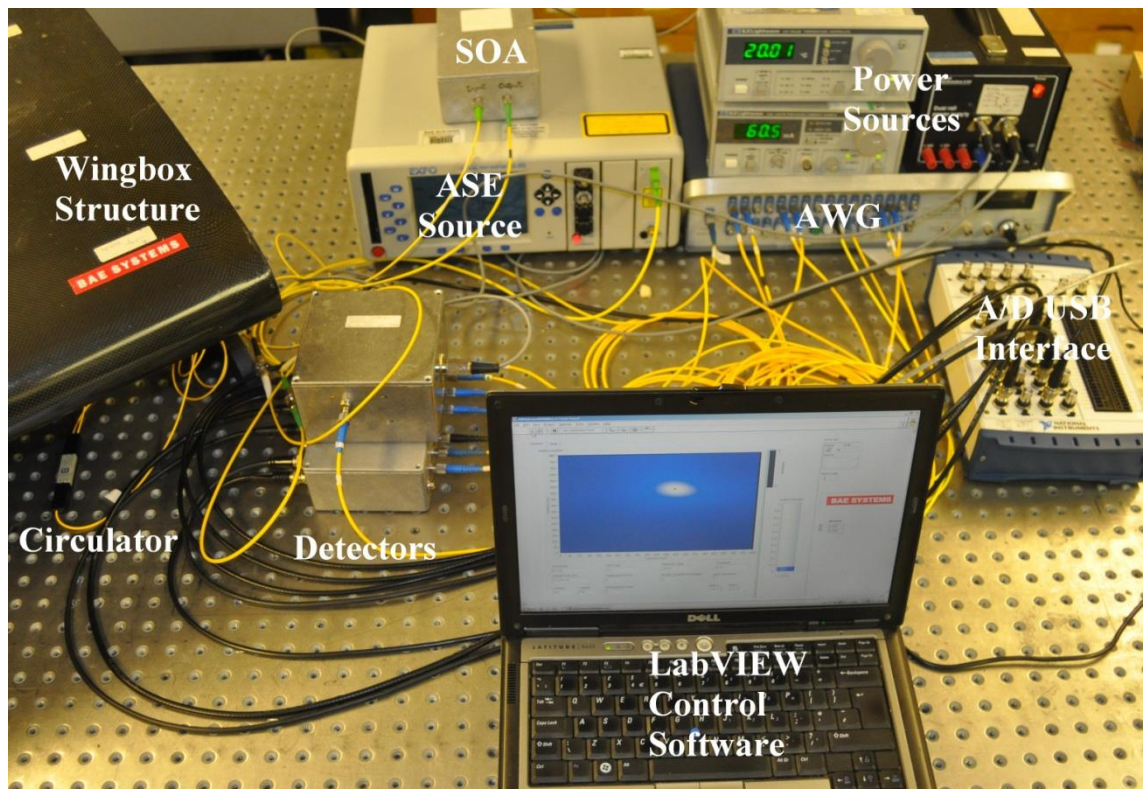

Figure 7.3. Demonstrator setup with all parts of the system labelled.

The full demonstrator system is pictured in Figure 7.3 showing the leading edge structure, optical setup, analogue-to-digital USB interface and LabVIEW control software. A further four detectors were built using the same type of photodiodes and circuit design to those created for the original AWG system, described in §5.2. This

expanded the system to eight detector channels allowing the simultaneous monitoring of eight AWG channels so that ratios can be taken to recover the four FBG signals.

The reflection spectrum for the multiplexed fibre is shown in Figure 7.4 and demonstrates the consistent wavelength separation as well as the variation in intensity due to a combination of splice losses and FBG variability. The spectra are shown both before and after they were bonded onto the composite structure, the spectra have shifted slightly but have maintained their consistent separation. Figure 7.5 shows the spectra after amplification by the SOA, it can be seen that the amplitude has increased by over three orders of magnitude and leaves the output less noisy. However, it has increased the size of a notch in FBG 2, but this should not pose a problem for the system. There was also some variation in each detectors response to a set light intensity, possibly because the photodiodes have been used previously in other circuits for different purposes and may be in differing physical condition. In order to mitigate these differences the detectors were paired up according to the most similar response and then the weakest responding pair was used to measure the sensor with the most intense reflection spectrum (FBG 4). Conversely, the strongest responding detector pair was used to measure the sensor with the least intense spectrum (FBG 1). The fibre was connected to the circulator at the high wavelength end as the FBG peak intensities are a closer match to the detector pair responses than when the fibre is interrogated from the other end.
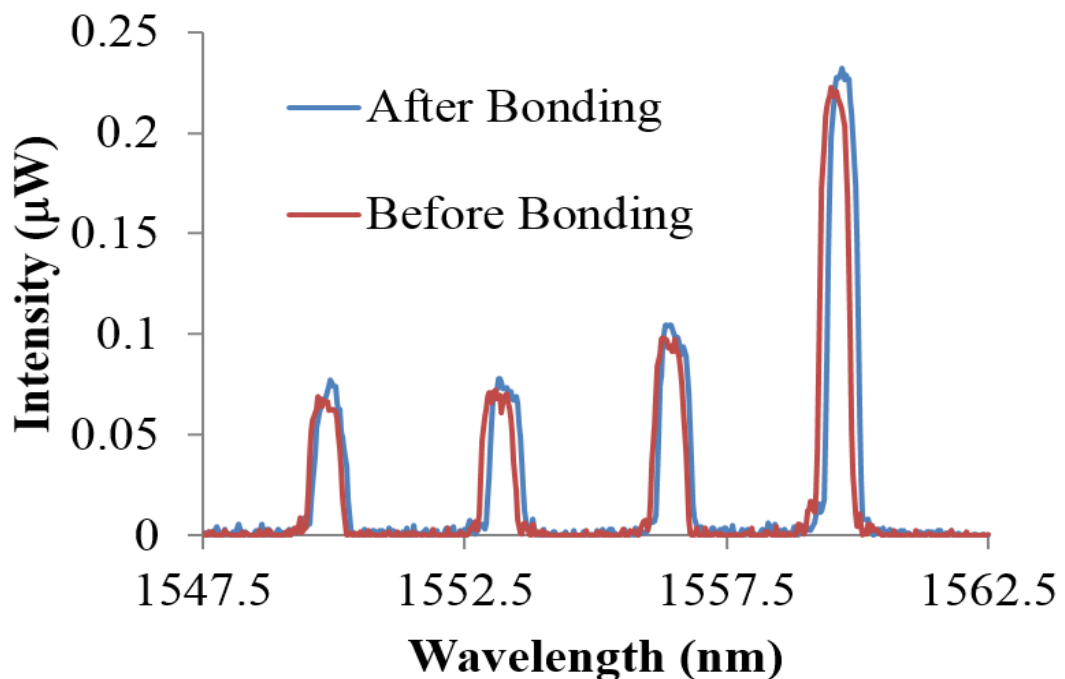

Figure 7.4. Reflection spectra from the multiplexed set of 4 FBG sensors with approximately 3.2nm spacing both before and after bonding onto the composite structure.
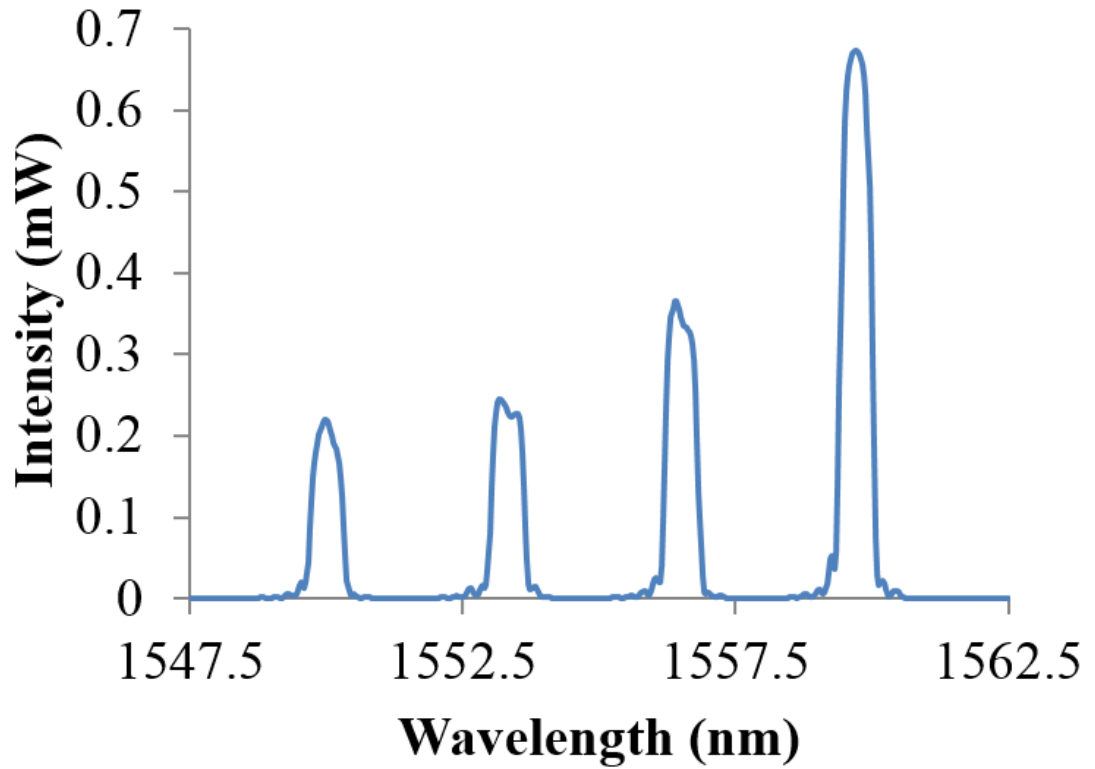
151

Figure 7.5. Reflection spectra from the multiplexed set of 4 FBG sensors after bonding onto the panel and after amplification by the semiconductor optical amplifier. Notice the change in units when compared to Figure 7.4.

The LabVIEW program used in chapter 3 to acquire signals from 4 channels was expanded to measure all 8 detector channels and reconstruct the FBG signal, ρ, using the following equation (see §5.2)

$$\rho = \log \frac{I_n}{I_{n+1}} \qquad (7.1)$$

where I_n and I_{n+1} are the light intensities captured by the detectors for AWG channels n and $n + 1$.

Three hundred impacts were then carried out, fifteen at each of the twenty marked locations on the structure. From these impacts, 283 valid data sets were captured, the remaining impacts did not have a signal measured by all four sensors and were therefore unsuitable for training. This data set was used to train a new neural network using the Matlab neural network toolbox. Initially, the neural network had an identical architecture as that used for the electrical sensors and used the same training algorithm. However, the results were unsatisfactory so a wider range of network architectures were trained and compared in order to find the optimal solution for this problem, see §7.3.3. The difference in performance may be caused by the directionality of the FBG sensors which could mean that a neural network with more nodes in the hidden layer is required

152

to deal with the increased complexity of the problem. References to work utilising the directionality of FBG sensors were listed in §2.5.2.

7.3. System Results

7.3.1. Signal Capture

Figure 7.6 shows the signals captured from the four FBG sensors during a test impact near to sensor 3. The third sensor clearly measures the arrival of the acoustic wave caused by the impact first, as expected, as well as registering a larger signal amplitude. Sensor 2 is the second closest and measures a signal next, closely followed by the remaining two sensors. To give the most accurate and reliable measure of the arrival time at each sensor the following procedure is performed. The DC signal offsets are removed and then the modulus is taken so that both negative and positive strain changes are comparable. Each signal is then normalised to unity to allow easier comparison between signals and so that a constant peak detection threshold can be defined. A peak detection algorithm is then used to detect all peaks above 0.1 on the normalised scale, i.e. 10% of the max peak value, a threshold chosen to maximise the amount of peaks detected without falsely detecting those due to random noise. It was found that averaging the position of the first three peaks increased reliability and reduced the chance of a rogue peak dominating the measurement causing a completely incorrect location to be determined. Figure 7.7 shows the results of this method carried out for the sensor signals shown in Figure 7.6.
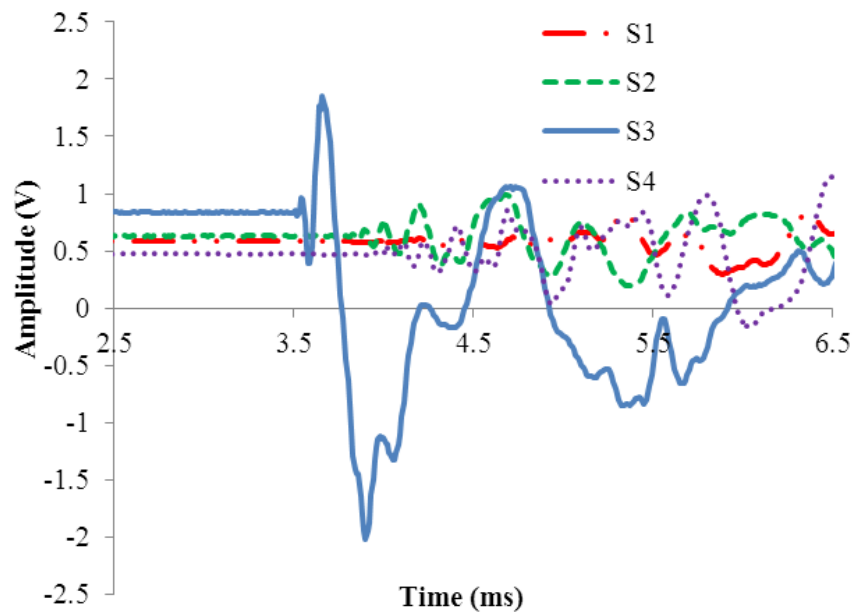

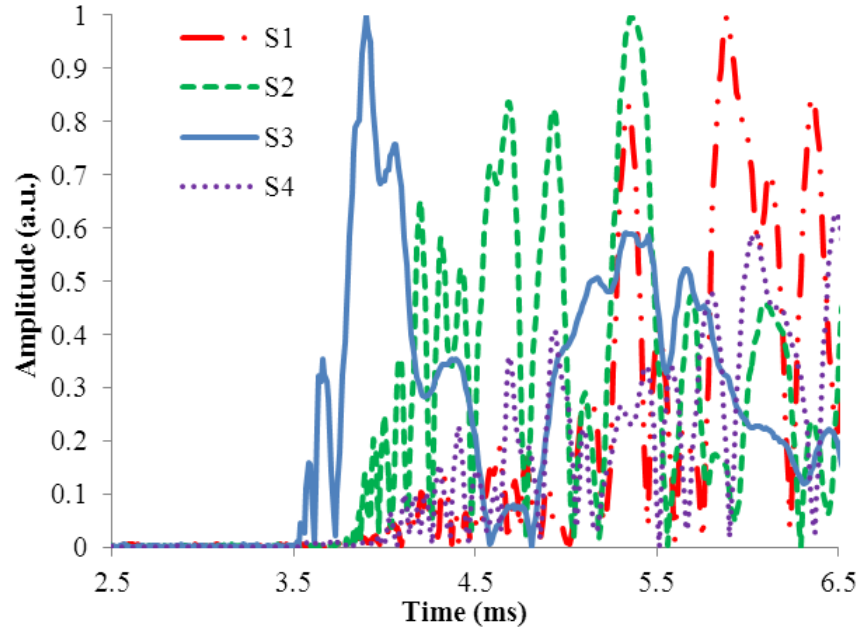**Figure 7.6. Signals captured from an impact close to sensor 3.**

Figure 7.7. Normalised signals shown in Figure 7.6. The signal offsets are removed, the modulus is taken and each signal is normalised to 1.

As well as capturing dynamic events, the system can also detect the load that the structure is undergoing. To test this, a 3.8 kg weight was placed on the structure within 100 mm of sensor 4 to place a load on the structure which the sensor will experience as a strain. Figure 7.8 shows the system response when the structure is unloaded (left) and loaded (right), the signal from sensor 4 shows a clear shift with a magnitude of 0.14 due to the load on the structure. The shift in the FBG spectrum was also measured with an optical spectrum analyser as 0.041 nm, which equates to a strain of around 46 $\mu\varepsilon$ using a conversion of 0.9 pm/$\mu\varepsilon$ measured for a similar grating in Chapter 5.
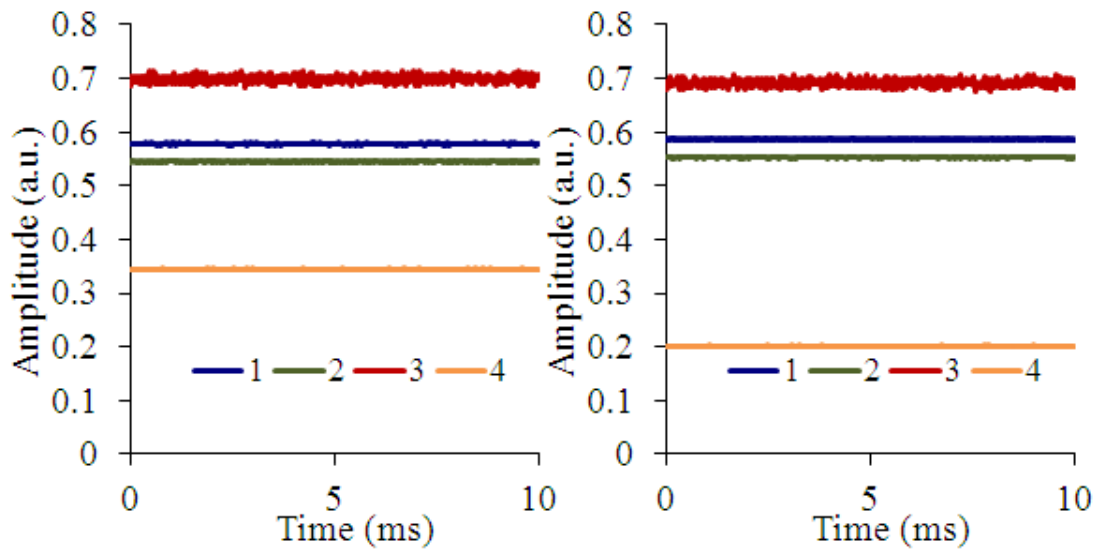

Figure 7.8. System response from the 4 FBG sensors while the structure is unloaded (left) and loaded (right) by a 3.8kg weight placed near sensor 4.

154

An impact was carried out while the structure was loaded with the weight and was successfully captured and displayed in Figure 7.9. From this data, the quasi-static strain could be determined from the D.C. signal level while simultaneously measuring the dynamic strain caused by the impact using the same system and sensors. The temperature could be easily determined with the addition of a strain isolated FBG on the structure that would then allow the quasi-static strain to differentiated from any temperature variations.
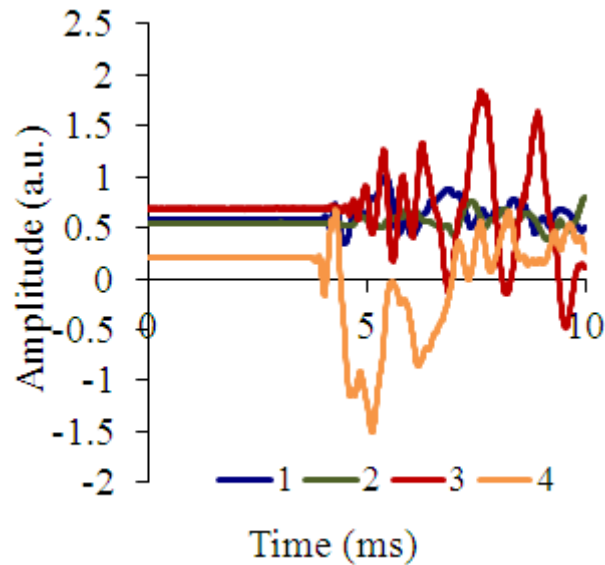

Figure 7.9. An impact captured while the structure is loaded with a 3.8kg weight.

7.3.2. *Initial Neural Network Results*

The three inputs to the neural network are the time differences between the average first peak locations for sensors 1 and 2, 2 and 3 and 3 and 4. Along with the actual impact locations as targets, these are used to train the neural network. This network implemented backpropagation learning using the gradient descent momentum method with an adaptive training rate. To test out the implemented network a further 300 impacts were performed, 15 at each of the 20 marked locations. The results for the first neural network are shown in Figure 7.10. It can be seen that the network is clustering all of the impact locations towards the centre of the structure and does not seem able to discriminate between them effectively. The error map for this data is shown in Figure 7.11, the largest errors occur at the top and bottom edges while in the middle the errors are quite low. This may be because the network could not adequately differentiate between locations so the largest minimisation of the error function was achieved by clustering the predictions towards the centre of the panel.
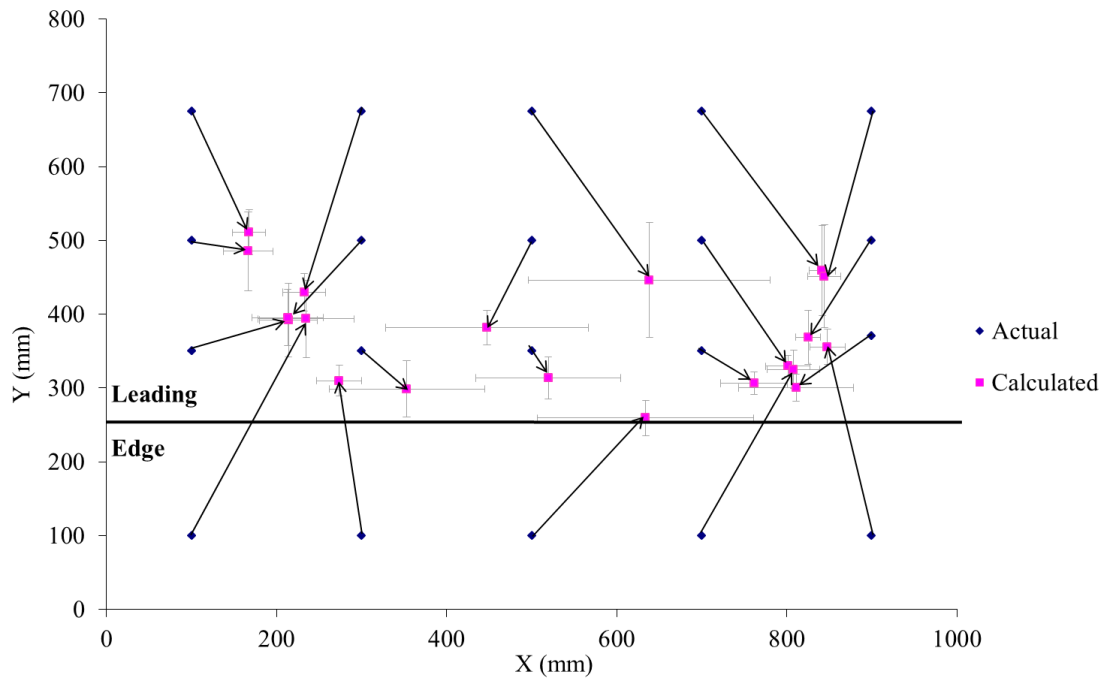
Figure 7.10. Location accuracy results using the neural network 1 which has 7 hidden layer nodes trained with 283 test inputs.
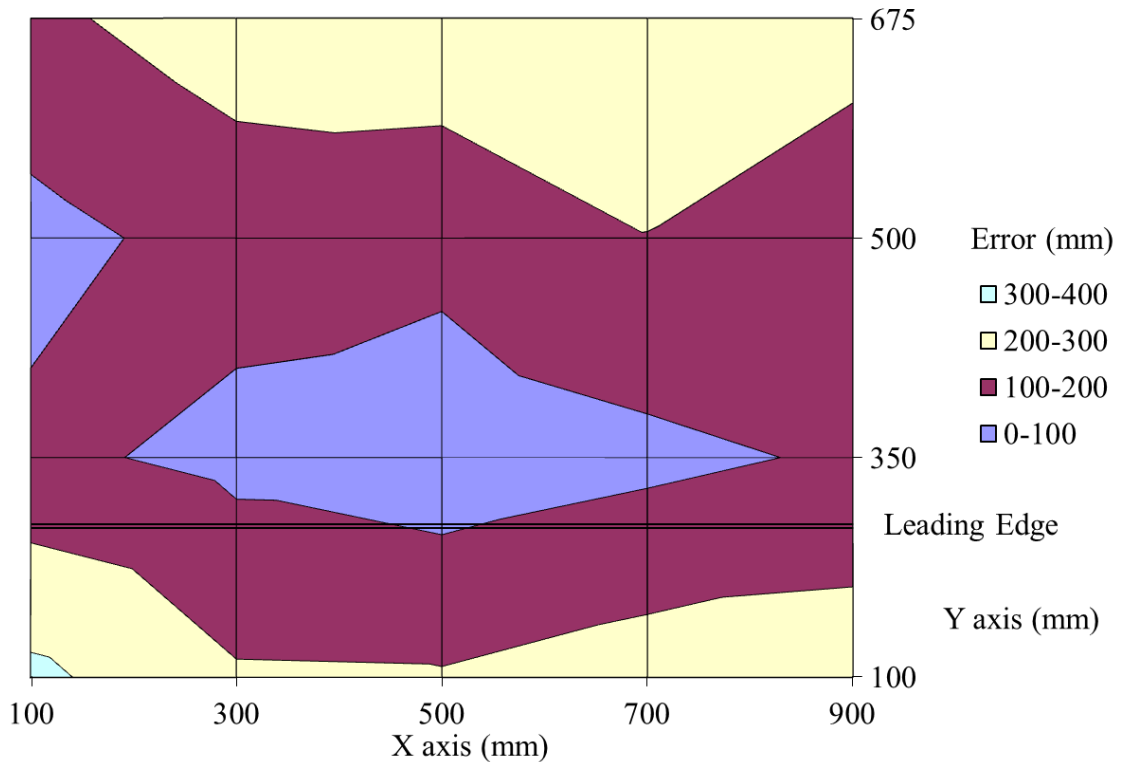
Figure 7.11. Error map for the data presented in Figure 7.10 showing larger errors towards the top corners and lowest errors in the centre.

7.3.3. Neural Network Testing

To improve on the results several different network architectures were trained and compared in order to find one that produced the best result. The training data set was almost doubled in size with the addition of the impact data that was used to test the first network. This data was only used as an input to the network and as such is unaffected

by the original network. The new expanded training set contained 514 signals captured on two different occasions that should help ensure that the network is sufficiently generalised. Two signals from each of the 20 locations were used to construct a data set to test the network after training and ensure that the network has not been overtrained. An overtrained network is a network that fits the training data very well but may lack generality in the same way that fitting a noisy sine wave dataset using a higher order polynomial will provide better results but this would not generalise to a second dataset.

Two parameters were varied to find the best network architecture:

1) Whether or not an adaptive learning rate is used; it dramatically reduces the number of training epochs required but may not work well for certain problems.

2) The number of hidden layer nodes; more nodes can increase the ability of the network to solve the problem more accurately but too many can lead to overtraining.

The training performance is a measure of the accuracy of the network using the data that was used to train it, the smaller the number the higher the accuracy. A more reliable test is using an independent test set, the previously described test set was used to produce the average x test performance and the average y test performance.

Table 7.1. Comparison of neural networks trained using different algorithms and number of hidden layer nodes.

Network	Adaptive Learning Rate	Hidden Layer Nodes	Training Epochs	Training Performance (a.u.)	X Test Performance (a.u.)	Y Test Performance (a.u.)
1	Yes	7	122		-0.0057	0.0066
2	Yes	10	135	0.0183	-0.0233	-0.0388
3	No	10	100000	0.0279	-0.0140	0.0240
4	No	10	100000	0.0134	0.0018	0.0048
5	No	10	1000000	0.0120	0.0018	0.0042
6	No	10	1000000	0.0107	0.0005	0.0009
7	No	7	1000000	0.0162	0.0018	0.0132
8	No	13	1000000	0.0102	0.0085	0.0011

The network that had the best results from the test data set was network 6; it was trained without an adaptive learning rate with a 10 node hidden layer over a million training epochs. This network was then implemented in the LabVIEW program and a new set of test impacts were carried out to compare its performance to network one. The results are displayed in Figure 7.12 and the error map for the same data is shown in Figure 7.13.
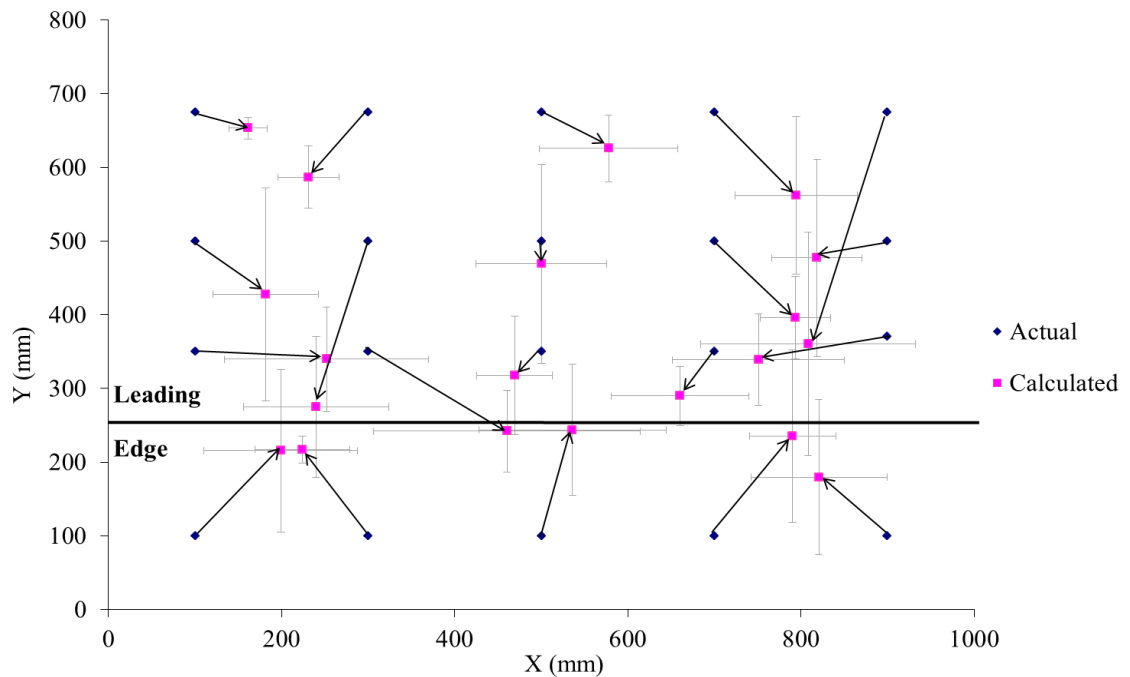

Figure 7.12. Final location accuracy results using the neural network 6 which has 10 hidden layer nodes and was trained with 514 test inputs.
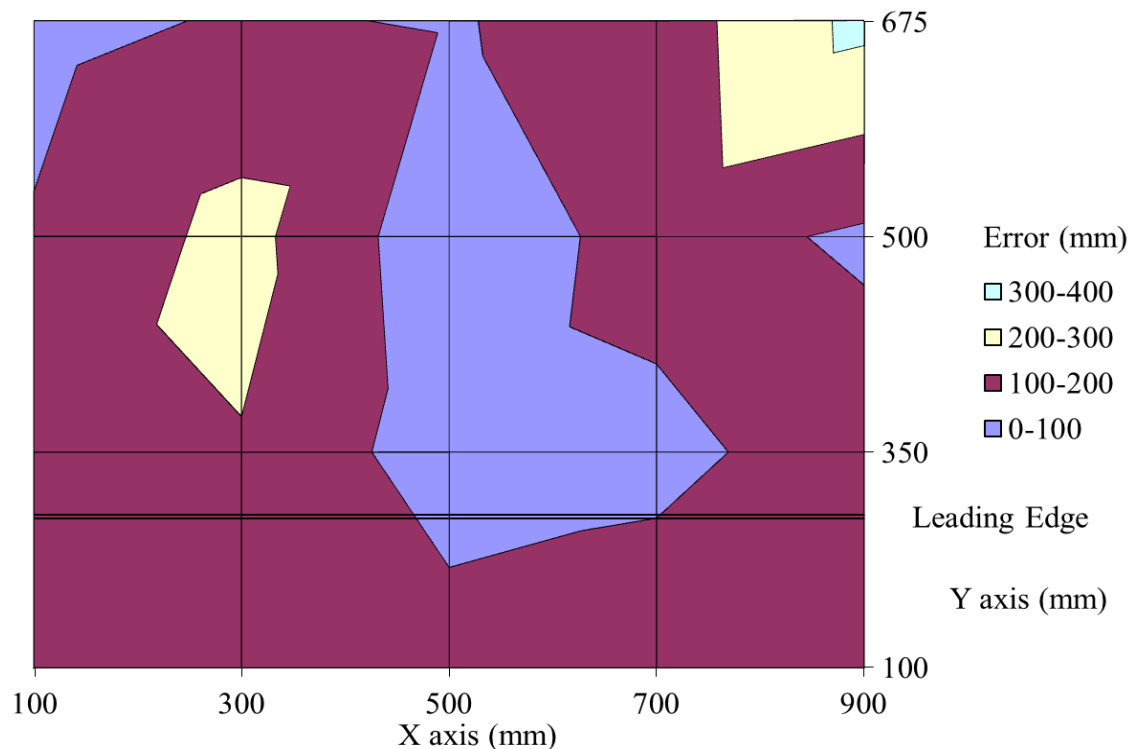

Figure 7.13. Error map for the data presented in Figure 7.12 showing larger errors towards the top corners and lowest errors in the centre.

158

The results are significantly better with this network, the lowest errors are still in the centre section with larger errors towards the corners but the magnitude of the errors has fallen significantly. The improved accuracy in the centre of the structure may be due to the directionality of the FBG sensors. They are most sensitive in the fibre direction which was directed towards the centre of the structure. The piezoelectric sensors used in chapter 3 have no directionality as they are composed of circular PZT discs and so this pattern was not observed.

The average error for network one was 177.6 mm while the error for network six was 133.6 mm which is an improvement of 25%. For comparison, Table 7.2, shows the average error for the impact location systems developed in chapter 3: piezoelectric sensors using the triangulation technique, piezoelectric sensors with a neural network and chirped fibre Bragg grating sensors (CFBG) using the triangulation technique.

Table 7.2. Comparison of impact location techniques by comparing the average location error from many impacts at 20 locations.

Sensor	Location Technique	Average Error (mm)	Average Standard Deviation (mm)
Piezoelectric	Triangulation	130.9	57.6
Piezoelectric	Neural Network	89.8	44.2
CFBG	Triangulation	143.0	123.1
FBG	Neural Network 1	177.6	67.2
FBG	Neural Network 6	133.6	82.6

This demonstrator system utilising neural network 6 was more accurate than the CFBG system although it was not as accurate as the piezoelectric system. The piezoelectric sensors are very sensitive and it is little surprise that they produced the most accurate system. However, the demonstrator system has many features that make it preferable to the piezoelectric system due to the advantages of fibre optic sensors and the multiplexed interrogation. In addition, the demonstrator system outperformed the CFBG system in terms of location accuracy but it also represents a more scalable system with multiplexed interrogation more suitable for real world applications.

7.4.   Conclusions and Discussion

A demonstrator system has been created which utilises the impact detection and location work in chapter 3 and the arrayed waveguide grating research undertaken in chapter 5. The system provides multiplexed interrogation of four FBG sensors bonded onto a complex leading edge structure allowing sensitive measurement of quasi-static strain as well as the detection and location of impacts using a neural network. It improves upon the previous systems investigated in this thesis due to its scalable nature. Each of the electrical sensors requires electrical amplification and an individual electric cable that can be long and heavy for a real application such as monitoring the wing of an aircraft. In a weight and space critical application such as this, routing many long cables to the wing is far from ideal. Furthermore, they pose an ignition risk if the wings are full of fuel as well as being a potential source of electromagnetic interference. While the CFBG system does not suffer from the issues inherent with electrical systems, the AWG system is much more scalable, provides the multiplexing feature that the CFBG lacks and improves on the location accuracy achieved.

Chapter 8 – Conclusions And Future Work

8.1.   Conclusions

The purpose of the work contained within this thesis was to investigate and develop techniques relating to impact detection in the aerospace and defence sectors. The increasing use of composite materials in the construction of both commercial and military aircraft as well as unmanned air vehicles has increased the need for onboard monitoring of impact events. This is due to the likelihood of barely-visible impact damage in composite materials that currently requires labour intensive non-destructive testing to detect.

If sensors such as fibre Bragg gratings or piezoelectric transducers are distributed across an aircraft wing they can detect that an impact has occurred through the acoustic wave that it creates. This wave will spread through the composite material and cause dynamic strain in the sensors. In order to make use of this information for maintenance purposes it would be highly beneficial to be able to locate the impact site as well as give an indication of impact severity. This task is more difficult for a composite wing when compared to a metallic wing, due to the high attenuation of acoustic waves and the anisotropic and inhomogeneous nature of the material.

In Chapter 3, a time of flight triangulation technique was used to locate impacts on a curved composite wing test structure. The speed of sound in the material was assumed to have a differing vertical and horizontal values aligned with the orientation of the woven fibres in the composite material and calibration tests were performed to determine the best values. Impacts were successfully located using the time-of-flight triangulation technique with an average error of 67 mm in the *x*-direction, 7% of the width of the structure. In the *y*-direction, the average error was 49 mm, 6% of the height of the structure. A neural network based system was implemented for comparison and improved the overall location accuracy from 130.9 mm to 89.8 mm; an improvement of over 30%. For the application case of locating impacts on an aircraft this accuracy would be sufficient to allow maintenance efforts to be concentrated into a small area and also allow impacts in critical areas to be identified. Finally, the energy of the impact was successfully estimated from the signal size at each of the sensors and accounting for the attenuation based on the distance between impact and sensor location.

Estimating impact intensity is useful to determine whether urgent action is required, for instance if an impact detection system registered a large impact in flight then an aircraft or UAV may be instructed to land at the nearest available location. This does mean that there is a potential to take unneeded action and it relies heavily on the energy estimate, which is in turn dependent on the location accuracy. Furthermore, the relationship between impact intensity and composite damage is not straightforward and depends on many factors; it is difficult to set an accurate energy threshold thought to be indicative of damage.

Chapter 4 addressed this issue by investigating the presence of features indicative of damage in the dynamic impact signals detected by the sensors. A large data set of impact signals was created containing non-damaging and damaging impacts on two large composite panels, each fitted with a piezoelectric sensor. This data was then analysed and a feature was identified that may correspond to the generation of acoustic emission as the composite gets damaged. This feature takes the form of significant secondary pulses in the 50 − 450 kHz filtered data. An automatic classification algorithm was successfully developed to analyse a signal and look for the presence of significant secondary pulses. This differentiates between non-damaging and damaging impacts based on a ratio termed the 'Damage Rating'; the ratio between the magnitudes of the largest secondary pulse and the initial pulse. This method produced a correct classification probability of 93-96% and a traffic light system was proposed to differentiate between non-damaging, potentially damaging and damaging impacts.

In Chapter 5, the focus moved on to the dynamic interrogation of fibre Bragg gratings in order to capture the impact signals which can then be analysed using the techniques developed in the previous two chapters. An FBG interrogator system was developed utilising an arrayed waveguide grating to demodulate wavelength shifts into intensity variations which can then be detected by a photodetector. Key performance indicators were identified including strain range, resolution, linearity, temporal bandwidth and number of multiplexed sensors. A number of different parameters affect the final system performance such as the FBG grating length, FBG spectral width, AWG channel spectral width and the number of AWG channels assigned to each sensor. These parameters were investigated both experimentally and through the use of modelling and their relationship to key performance indicators was determined. It was found that an AWG channel cannot always be accurately modelled by a simple Gaussian and the true form produces deviations from linearity as a Bragg grating spectral profile moves across

it. Additionally, it was determined that increased system linearity can be achieved by matching the FWHM of the FBG and AWG channels. The developed model forms a basis for designing and optimising an AWG interrogation system in order to ensure that the system fulfils its purpose.

The system performance was also investigated in relation to both short term (20 ms) fluctuations and long term (1 hour) drifts with a system resolution of a few microstrains achieved. A comparison of the signal-to-noise ratio was performed for the best and worst case scenarios: the FBG spectrum midway between the AWG channels and the FBG spectrum directly overlaid with one channel respectively. The average SNR in the former case was 23.2, while only 7.3 in the latter, producing a strain resolution of 2.5 $\mu\varepsilon$ and 20.5 $\mu\varepsilon$, respectively. Inclusion of a semiconductor optical amplifier into the system produced a modest 8% improvement in the signal-to-noise ratio of the equal case. However, for the overlapped case, where there is a low light intensity in one channel, there was dramatic improvement of ~ 300%.

An alternative, adaptive interrogation technique was investigated in Chapter 6. This technique utilised two-wave mixing in an erbium-doped fibre to create a dynamic grating which effectively optically high pass filters a signal from an FBG. This makes the system resistant to quasi-static strain signals and temperature drifts as the dynamic grating is being recreated on a time scale between 1 – 10 ms. The creation of a dynamic grating was detected by the percentage increase in reflected light back from the end face of the fibre as the input light intensity was increased. Dynamic strain sensing was demonstrated using a FBG fibre stretcher at 200 Hz which produced consistent results with the AWG interrogation scheme used simultaneously. The FBG was heated by 8.5 °C resulting in the loss of the AWG signal while the erbium-doped fibre system remained functional proving the adaptive nature of the technique. Finally, two FBGs were wavelength division multiplexed and it was shown that the crosstalk was almost 30 dB below the signal level.

A demonstrator system was created to bring together and exhibit some of the techniques developed in this thesis and was described in Chapter 7. This system expanded on the arrayed waveguide grating interrogator described in Chapter 5 by demonstrating multiplexed interrogation of four FBGs on a winglike structure Impacts were detected and then located by a neural network. It is believed that the directionality of the FBG sensors increased the complexity of the location problem when compared to the PZT

sensors. Hence, a different network architecture from that used in Chapter 3 was required.

8.2. Future Work

To further investigate the acoustic signatures detected during damaging impacts in Chapter 4 future work could focus on understanding the mechanism or mechanisms responsible for creating this feature. If the feature could be linked to specific damage types or failure mechanisms in composite materials it would enable the technique to be used with increased confidence to detect failure. In addition, more composite materials and panel types could be compared and contrasted to determine if the technique is equally successful in all of those cases.

This work can also be extended in combination with the arrayed waveguide grating interrogator to detect damage indicating impact signals using FBGs. They could also be used to investigate the directionality of the impact signals and determine whether there is any dependence on the composite fibre direction.

To progress the arrayed waveguide grating interrogator for use in an aerospace environment the issues related to quasi-static strain and temperature would have to be addressed. AWGs can be thermally tuned to wavelength shift the channel spectra, this feature could be used to compensate for temperature changes experienced by the sensors on the aircraft. Experiments would be carried out to determine the rate of temperature change, the effect on the stability of the system and the maximum spectral shift. As well as the thermal shifts experienced by the sensors, the AWG and other parts of the system would need to undergo environmental testing to determine whether thermal stabilisation or other ruggedisation would be required in order to maintain satisfactory operation in an aircraft environment.

As described in §6.6 in order to progress the erbium doped fibre interrogation technique the signal to noise ratio would have to be improved through an alternative optical design. The aim of this design would be to separate the signal of interest from the light that is creating the dynamic grating which currently adds a relatively large background light level causing a low signal to noise ratio. A proposed design is shown in Figure 6.10 that utilises polarisation selective components to separate out this signal of interest.